NUMERICAL ANALYSIS AND SIMULATIONS OF COUPLED PROBLEMS FOR THE CARDIOVASCULAR SYSTEM

Saverio Smaldone

▶ **To cite this version:**

Saverio Smaldone. NUMERICAL ANALYSIS AND SIMULATIONS OF COUPLED PROBLEMS FOR THE CARDIOVASCULAR SYSTEM. Mathematics [math]. L'UNIVERSITÉ PIERRE ET MARIE CURIE - Paris VI 2014. English. NNT : . tel-01287506

HAL Id: tel-01287506

https://theses.hal.science/tel-01287506v1

Submitted on 13 Mar 2016

HAL is a multi-disciplinary open access archive for the deposit and dissemination of scientific research documents, whether they are published or not. The documents may come from teaching and research institutions in France or abroad, or from public or private research centers.

L'archive ouverte pluridisciplinaire **HAL**, est destinée au dépôt et à la diffusion de documents scientifiques de niveau recherche, publiés ou non, émanant des établissements d'enseignement et de recherche français ou étrangers, des laboratoires publics ou privés.

ANALYSE NUMÉRIQUE ET SIMULATIONS DE PROBLÈMES COUPLÉS POUR LE SYSTÈME CARDIOVASCULAIRE

THÈSE DE DOCTORAT

Présentée par

Saverio SMALDONE

pour obtenir le grade de

DOCTEUR DE
L'UNIVERSITÉ PIERRE ET MARIE CURIE - Paris VI

Spécialité : MATHÉMATIQUES APPLIQUÉES

Soutenue publiquement le 10 Octobre 2014 devant le jury composé de :

Stéphanie SALMON	Président
Miguel Ángel FERNÁNDEZ	Directeur de thèse
Jean-Frédéric GERBEAU	Directeur de thèse
Christian VERGARA	Rapporteur
Laurence HALPERN	Examinateur
Frédéric HECHT	Examinateur
Nicolas MEUNIER	Examinateur

Après avis favorables des rapporteurs: Franck NICOUD et Christian VERGARA.

Thèse préparée au sein de l'équipe-projet REO
Laboratoire Jacques-Louis Lions
Université Pierre et Marie Curie - Paris 6
et **Centre de Recherche Inria Paris-Rocquencourt**
Domaine de Voluceau, BP 105
78153 Le Chesnay CEDEX

ACKNOWLEDGEMENTS

There are many acknowledgments that I would like to express but I'll write only few and sincere words.

I wish to thank my two supervisors, Jean-Frédéric Gerbeau et Miguel Fernández, for all the confidence that they give to me during this challenging thesis period and for all the occasions we spent together that let me grow up and become stronger.

I would like sincerely to thank the two reviewers Franck Nicoud and Christian Vergara for a thorough reading of the manuscript and for their estimate words about my work. I wish also to thank the other members of the PhD committee, Laurence Halpern, Frédéric Hecht, Nicolas Meunier and Stéphanie Salmon, to have accepted to participate to my defense and for all constructive questions they asked me.

Thank you to all my colleagues, students and researchers, for the moments of pleasure and of work we have shared at Inria during these years. Specials credits I would like to address to Marina, for her advices and support, and to Maryse for her patience and kindness.

This achievement could not be possible without the great and constant support of my parents, my brother and my sister. They never make me feel lack in anything. They always encouraged me in every choice I did, even in the most weird ones, like doing a PhD in Paris. I owe you the person I have become and I know that you will understand if the last words are for my friends.

Friends come and go but the most valuable ones remain forever.

Thanks to Annabelle. I do not think that some lines in this thesis could express all the huge gratefulness that I owe you and I would like to say you. You know, I'm not able to find the right words that you deserve but thanks for a lot of reasons. You have helped me in all possible ways in which a person could be helped and I'll never forget this.

Thanks to Alex. Thanks for your amazing friendship, thanks for all your precious teachings, thanks to have made me feel home in a foreign country, thanks for your words since the first day we met and, as you said, it was worth to do all this because we did it together.

My best moments in these years are thanks to you two, and what will happen in future does not matter, the memory of these moments will be always with me.

Thanks to Cora. Even from the US you have had always something to say to do not let me give up. I know that I can always count on you and I hope to give back all what I've received from you.

Thanks to all my friends, those ones who live far away, those ones of my childhood. Your every single word allowed me to go ahead. Thanks to the friends who were there in the most difficult days, the friends who did not make me feel alone. It's to all of you, the true friends, that I would like to dedicate this thesis.

Paris, October 2014 Saverio Smaldone

To my friends,
to those one who were, are
and always will be there

ANALYSE NUMÉRIQUE ET SIMULATIONS DE PROBLÈMES COUPLÉS POUR LE SYSTÈME CARDIOVASCULAIRE

Résumé : Dans cette thèse, nous proposons l'analyse numérique et le développement d'algorithmes partitionnés pour coupler l'écoulement du sang dans différents compartiments cardiovasculaires (3D-3D, 3D-0D).

Dans une première partie, un problème couplé fluide-fluide est introduit. Sur l'interface qui sépare les domaines, des conditions aux limites de type Robin-Robin dérivées de la formulation d'interface de Nitsche sont considérées. Nous proposons différents schémas explicites dont la stabilité est analysée dans la norme de l'énergie. Des simulations numériques illustrent le potentiel des méthodes présentées.

La deuxième partie propose des applications cardiovasculaires plus réalistes. Tout d'abord, un modèle d'ordre réduit pour les valves cardiaques est décrit. Sans traiter l'interaction fluide-structure avec le sang, les valves sont remplacées par des surfaces agissant comme des résistances immergées dans le fluide. Des simulations numériques montrent l'efficacité et la robustesse de ce modèle.

Pour finir, une formulation ALE est utilisée pour la résolution d'un modèle fluide sur un domaine mobile. Nous montrons qu'en ajoutant un terme consistent, une inégalité d'énergie stable peut être obtenue sans considérer aucune hypothèse de Loi de Conservation Géométrique. Le travail se termine avec des simulations numériques sur la dynamique du sang dans le ventricule gauche, couplé avec l'écoulement du sang dans l'aorte.

Mots-clés : Interaction fluide-fluide, méthodes d'interface de Nitsche, couplage explicite, conditions Robin-Robin, formulation de pression statique et totale, modèle RIS de valves, maillages fissurés, formulation ALE, stabilisation fluide en domaines mobiles.

NUMERICAL ANALYSIS AND SIMULATIONS OF COUPLED PROBLEMS FOR THE CARDIOVASCULAR SYSTEM

Abstract: In this thesis we present the numerical analysis and the development of partitioned algorithms in order to couple the blood dynamics in different cardiovascular compartments (3D-3D, 3D-0D).

In the first part a fluid-fluid coupled problem is introduced. On the interface between the domains Robin-Robin boundary conditions, derived from the Nitsche's interface formulation, are considered. We suggest different staggered explicit schemes whose stability is analyzed in the energy norm. Extensive numerical experiments illustrate the accuracy of the methods presented.

The second part deals with more realistic cardiovascular applications. First a reduced order model for the heart valves is described. Without dealing with fluid-structure interaction with the blood flow, the valves are replaced by immersed surfaces acting as resistances on the fluid. Numerical simulations show the efficiency and the robustness of this model in the framework of a fluid-fluid interaction scheme.

In the end, an ALE formulation is used to solve a fluid model in a moving domain. We show that adding a suitable consistent term, a stable energy inequality can be obtained without considering any Geometric Conservation Laws. The work ends with numerical simulations on blood dynamics in the left ventricle coupled with the blood flowing in the aorta.

Keywords: Fluid-fluid interaction, Nitsche's interface method, explicit coupling scheme, Robin-Robin conditions, static and total pressure formulations, RIS valve model, fissured meshes, ALE formulation, fluid stabilization in moving domains.

Contents

INTRODUCTION

I may never find all the answers,
... I may never prove
What I know to be true,
But I know that I still have to try.

"The Spirit Carries On" by Dream Theater.

CHAPTER 1
Thesis background and physiological overview

In this chapter, the general framework of the thesis is introduced. Our aim is to simulate and study, by coupling appropriate models and solvers, the behavior of the cardiovascular system starting from the blood that flows in it. First we give an overview on the current topic of research on cardiovascular problems (e.g. fluid-structure, electro-mechanics of the heart, 1D/0D model). Then we summarize the rest of the thesis by discussing the main results of each chapter. Finally we provide the basis of the physiology, structure and properties of the blood in the cardiovascular system.

Contents

1.1 Thesis general context

The goal of this thesis is to provide efficient and robust numerical methods to couple different cardiovascular compartments. This means to have the most realistic and physiological results with the less computationally expensive effort. The mid-term objective of this work is to study the multi-physics aspect arising in the cardiovascular system.

This PhD thesis is the result of the most relevant works I have accomplished in the REO project at Inria Paris-Rocquencourt.

1.1.1 Motivations

As more and more people switch to healthier lifestyles and with the progress of anti-hypertensives treatments, mortality from cardiovascular diseases has gone down in a number of countries. Yet despite this encouraging trend, diseases of the heart and arteries remain the number one killers at the global level. In cardiovascular diseases a unique cause is not detected. Various factors are well-known that increase the risk to develop the disease and manage the organism to become ill.

Heart attacks and strokes are major, but preventable, killers worldwide and the primary threat to human life in developed countries. They are mainly caused by a blockage of the blood from flowing to the heart or brain. Aortic aneurysm and dissection, i.e. dilatation and rupture of the aorta, damage of the heart valves in particular valve stenosis and regurgitation, also afflict thousands of people.

According the World Health Organization[1], over 80% of cardiovascular disease deaths take place in low and middle income countries and occur almost equally in men and women. General cardiovascular diseases have major human costs as well as economic costs. The cost for the health care systems of the European Union, for example, is just under €196 billion a year including direct health care costs, productivity losses and informal care of people [NTLF+12]. Ensuring that all people have a rapid access to appropriate treatment is essential to reducing disability and costs. A more careful knowledge of the structure of heart and its arteries is also an affordable method to prevent cardiovascular diseases.

For many centuries this has been the central objective of the studies of physicians and scientists from the arab Avicenna (980 - 1037) and Averroes (1126 - 1198) to Leonardo da Vinci (1452-1519), who represented very accurately the anatomy of the heart muscle (Figure 1.1). The physician and epidemiologist Giovanni Maria Lancisi (1654 - 1720) detailed the symptoms of heart failure, aneurysms, atherosclerosis.

Nowadays, clinicians use simple measurements such as heart rate, blood pressure or the electrocardiogram to diagnose cardiovascular pathologies. Subsequently, researchers have developed and are improving mathematical modeling techniques to help clinicians to interpret this kind of observations in a rational and systematic manner.

As the research in this direction is impressively improving, the comprehension and the modeling of the heart and the interplay between its principal functions still remains a challenging task. The resolution of coupled problems in a clinical environment is one of the primary objective, in part because of the prohibitive computational cost of the methods currently available. Coupling different physical compartments (fluid-solid, fluid 3D - fluid 1D, 0D - fluid 3D, etc.) raises many mathematical and numerical difficulties that are still the topics of active research.

It is generally admitted that the state-of-the-art commercial solvers are not yet able to solve large coupled problems, like fluid-solid interaction (FSI), in a time compatible with the

[1] http://www.who.int/mediacentre/factsheets/fs317/en/

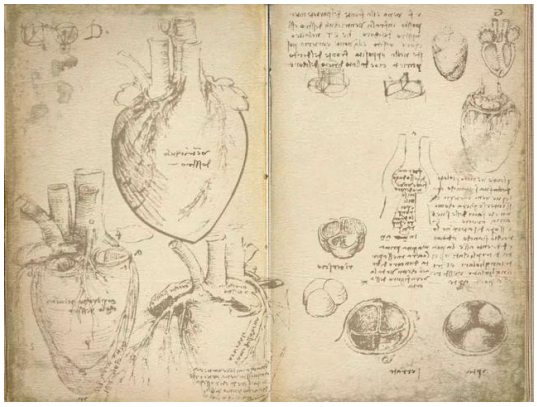

Figure 1.1: *Detailed analysis of the structure of the heart by Leonardo da Vinci.*

clinical practice. Progress is therefore needed in this respect. The main motivation is to solve the coupled problem without requiring too many expensive sub-iterations. The challenge in term of software development is to imagine a solution that would be versatile enough to couple together an arbitrary number of independent components of the cardiovascular system, with different coupling strategies, different physics or different representations of the same physics.

1.1.2 Multiphysics modeling of the cardiovascular system

A significant number of complex physical phenomena takes place in the heart [NNN+11], which is actually a treasure for modeling and objective of active research (Figure 1.2).

The mathematical analysis of biological phenomena that take place in the heart involves several areas of study: fluid mechanics, tissue mechanics, electrophysiology, suitable boundary conditions. To obtain a complete simulation of the heart, a deep analysis of these phenomena is necessary as well as a study of their impact on each other. The literature on this subject is abundant.

We can cite for example the pioneering work of [Pes77, WHS+02, WSKH04] on modeling the flow of blood through the heart with fluid-structure coupling. Complex fluid-structure interaction methods for the blood flow in general have been developed, e.g. [Ber12, CDFQ11, FGG07] where incompressible Navier-Stokes equations are coupled with the mechanical equations governing the dynamics of structure.

Another interesting and challenging area of study is the modeling of the heart valves. Different kind of models can be adopted to simulate the valve behavior. The simplest is the lumped parameter method, that reduces the valve behavior to the resolution of algebraic or differential equations [DZL07, JL06, KS06, SMCCS08, SSG+04, TW89]. Important progress have been realized in the simulations of the interaction between the blood fluid and the structure of the valves [AGPT09, LDSB10, MYWD07, SB09, HPSB03], however this type of problems still remains very challenging. A new approach has been recently pro-

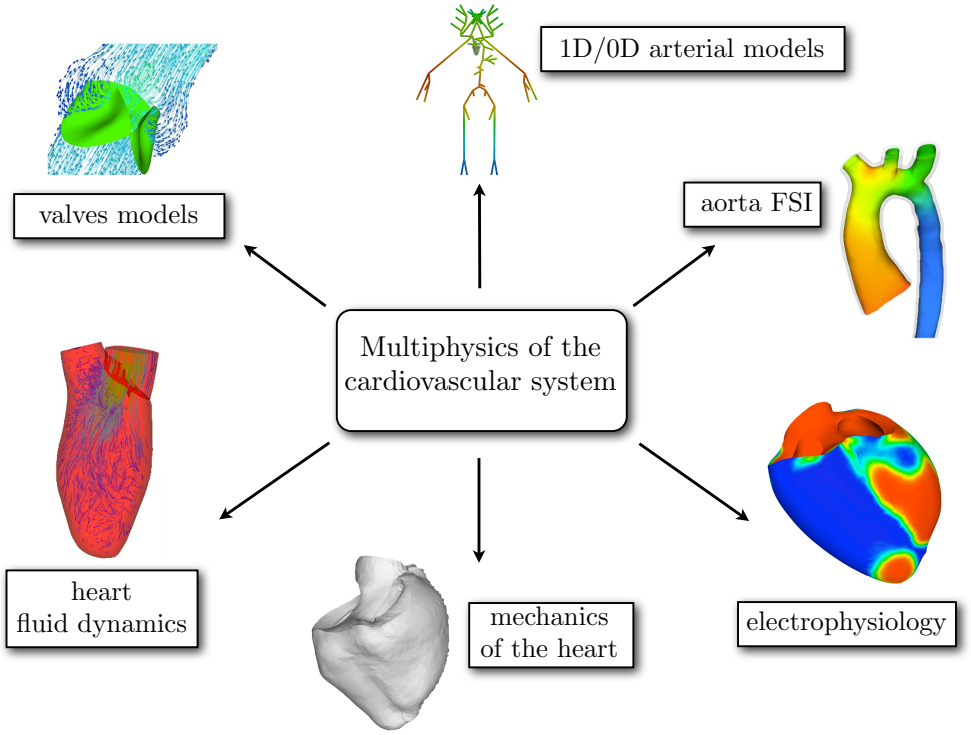

Figure 1.2: *Multiphysics aspect of the cardiovascular system: heart fluid dynamics (image form* [Ast10]*), valve models (image form* [dSGB08]*), 1D/0D arterial models (image form* [LMAD11]*), FSI in the aorta (image form* [Ber12]*), electrophysiology (image form* [Col14]), mechanics of the heart (image form [Imp13])

posed in [AHSG12] based on the resistive immersed surface (RIS) method, in which the valve surface acts as a resistance in the fluid.

Regarding cardiac mechanics, we can mention the work of [Hun75, Pes82] to whom we owe the first major contributions. More recently, various electro-mechanical heart models have been proposed, e.g. [CFG+09, GK10, NP04, Moi08]. In these studies, the constitutive law of the material is decomposed into a passive portion (visco-elastic properties of the myocardium) and an active portion (reactive with electrical activation).

First electrophysiology cellular models appear in the early 50s with the work of Hodgkin and Huxley [HH52a, HH52b], offering the first modeling of the action potential for the giant axon. This work will then be applied to the cardiac electrophysiology by Noble [Nob62] and many models of increasingly complexity follow. In cardiac electrophysiology several models which represent the evolution of the potential in the membrane have been developed. For example we cite [GK09] where the governing equations of electrophysiology are derived from the classical FitzHugh-Nagumo model [Fit61, NAY62, AP96].

The therapeutic procedures on patients suffering from cardiovascular or arterial disease requires sometimes the simulation of the entire closed-loop system, i.e. heart-aorta-arteries-peripheral circulation-veins. For this purpose many 3D-1D coupled models for blood

flow have been proposed in the literature, e.g. [BFU07, BPUF09, FGNQ01, OPK+00]. While, 3D-0D coupling [BCF13, MXA+12, VC06, WLW09] is a classical strategies to account for the neglected part of the cardiovascular system when 3D simulations are performed.

1.1.3 Personal contributions

The results presented in this work have been achieved by using, improving or developing different tools. In particular the following pieces of software have been largely employed:

- The 2D test cases are solved with the partial differential equations solver FreeFem++ [Hec12], written in a C++ idiom language. Specific C++ routines have been written in order to read the FreeFem results in suitable post-processing softwares.

- The finite element solver FELiScE (Finite Elements for Life Sciences and Engineering[2]) was used for the calculations. This is a C++ code based on the PETSc library for parallel scientific computing[3]. This code involves several students, engineers and researchers in a collaboration between the Inria team-projects REO and M∃DISIM. My personal contributions concerns the implementation of different functions, method and subroutines, to solve the models discussed in this work. In particular, all the functions employed for the resolution of the fluid-fluid models were implemented. The routines to fusion together the degrees of freedom of two different geometries and the specific class for the RIS valve model were coded. In addition, the ALE formulation was improved.

- The coupling between the two fluids codes, to perform fluid-fluid interaction, was done using a master code CVGraph (Cardio Vascular Graph) written in C++. This coupling code was started at the beginning of this thesis, and it allows to couple different solvers by message passing based on MPI, PVM and text-file protocols. We use the master/slave code to handle the communications between two fluid models implemented with FELiScE.

- A wide number of meshes has been processed by using the softwares 3-Matic (Materialise, Leuven, Belgium) [Mat13], Gmsh [GR09], MEDIT [Fre01] and other Inria routines. All geometries employed in this work are the result of several student's adaptation in different periods. All of them have been personally re-arranged, cut and smoothed with an accurate and painstaking work to obtain the simulations presented in this thesis. The realistic meshes used in Chapter 4 and Chapter 6 have been acquired by *Zygote Media Group* [Zyg11], they were obtained from the post-processing of highly resolved computer tomography data.

- For post-processing EnSight (CEI software) was employed by mean of Python interpreter [EnS06]. The open source software for scientific visualization ParaView[4] has

[2] http://felisce.gforge.inria.fr
[3] http://www.mcs.anl.gov/petsc/.
[4] http://www.paraview.org/.

been employed to extract the domains images. MATLAB was used to process the numerical data resulting from the simulations and to trace the different curves.

- An active participation to the development of several numerical schemes and their mathematical analysis, is the origin and the crucial point that drive all the numerical simulations of this thesis.

1.2 Thesis outline

We propose with this thesis, to analyze and simulate, by mean of the appropriate models, the cardiac hemodynamics that arises from the left atrium to the descending aorta (Figure 1.3).

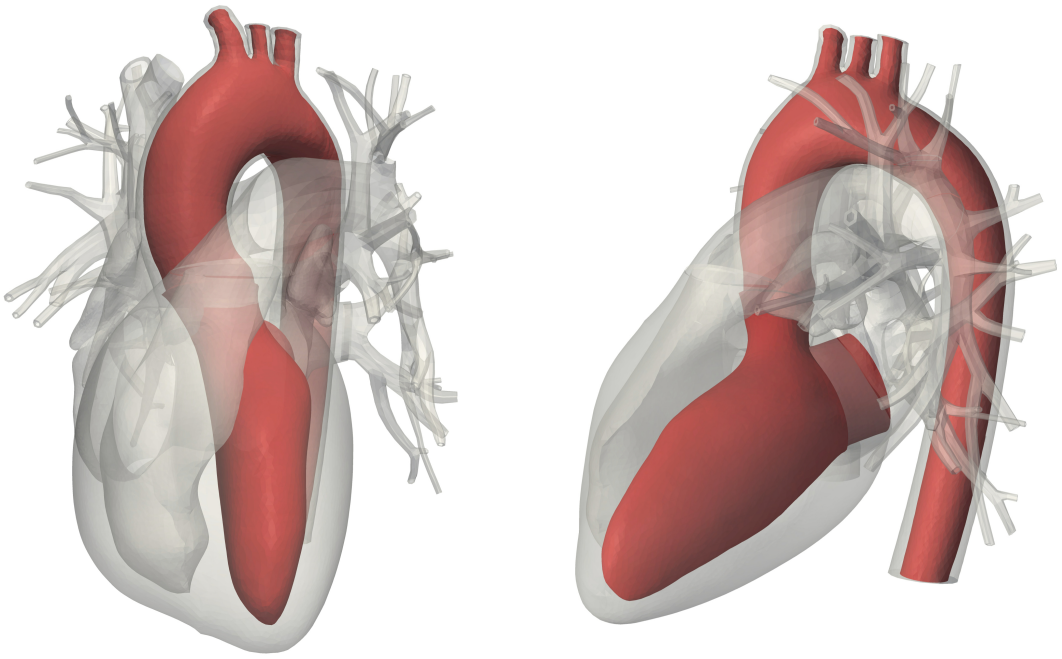

(a) *Front view* (b) *Left side view*

Figure 1.3: *Cardiac hemodaynamics modeling studied in this thesis*.

This work is essentially divided in two parts. The first one consists of 2 chapters, the second one has 3 chapters. Every chapter consists of

- An *abstract* summarizing the main ideas presented in the chapter.
- A *table of content* of the sections in which the chapter is divided.
- An *introduction* to the topics discussed in the chapter.
- *Final remarks* ending the chapter.
- The *Bibliography* of the chapter.

1.2.1 Part I: Fluid-Fluid interaction problem

The first part of this thesis deals with the numerical approximation of a fluid-fluid coupled problem which seems a model problem of a multi-compartment modeling of the cardiovascular system.

Chapter 2: Explicit coupling schemes for a fluid-fluid interaction problem We propose a new approach to the loosely coupled time-marching of a fluid-fluid interaction problems involving the incompressible Navier-Stokes equations. The time splitting schemes introduced in this chapter is derived from a space semi-discrete formulation based on Nitsche's interface method [Han05, BHS03]. This approach extends the loosely coupled schemes introduced in [BF09, BF14] for FSI problems to fluid-fluid interaction problems.

The method relies on a specific explicit Robin-Robin treatment of the coupling condition on the interface Σ:

$$\begin{cases} \boldsymbol{\sigma}(\mathbf{u}_1^n, p_1^n)\mathbf{n}_1 + \dfrac{\gamma\mu}{h}\mathbf{u}_1^n = \dfrac{\gamma\mu}{h}\mathbf{u}_2^{n-1} - \boldsymbol{\sigma}(\mathbf{u}_2^{n-1}, p_2^{n-1})\mathbf{n}_2, & \text{on} \quad \Sigma, \\ \boldsymbol{\sigma}(\mathbf{u}_2^n, p_2^n)\mathbf{n}_2 + \dfrac{\gamma\mu}{h}\mathbf{u}_2^n = \dfrac{\gamma\mu}{h}\mathbf{u}_1^n + \boldsymbol{\sigma}(\mathbf{u}_2^{n-1}, p_2^{n-1})\mathbf{n}_2, & \text{on} \quad \Sigma, \end{cases} \tag{1.1}$$

combined with a weakly consistent interface pressure stabilization in time:

$$S(p_{2,h}^n, q_{2,h}) \overset{\text{def}}{=} \frac{\gamma_0 h}{\gamma\mu}\int_\Sigma (p_{2,h}^n - p_{2,h}^{n-1})q_{2,h}. \tag{1.2}$$

Three different explicit formulations are proposed:

1. Algorithm 2.3 (on page 45), static pressure formulation: the formulation is consistent with the original coupled problem but the energy stability cannot a priori be guaranteed (Proposition 2.2).

2. Algorithm 2.4 (on page 50), static pressure formulation with skew-symmetric treatment of the convection: the energy stability can be recovered but it is not consistent with the original coupled problem.

3. Algorithm 2.6 (on page 52), total pressure formulation: consistent with the original coupled problem and an a priori energy estimate guaranties the stability of the splitting (Proposition 2.3).

Chapter 3: Numerical examples of fluid-fluid interaction problem in hemodynamics In this chapter we discuss the numerical simulations of the methods presented in Chapter 2.

We first perform 2D numerical tests, in order to shown the instabilities of a standard explicit Dirichlet-Neumann coupled scheme and to fix the Nitsche's method parameters. Then, with 3D numerical tests we observe that

1. *Algorithm 2.3*: even if the energy stability cannot a priori be guaranteed for the standard static pressure formulation, extensive numerical evidence has shown that the scheme is robust and accurate, with respect to a fully implicit method.
2. *Algorithm 2.4*: the numerical results have confirmed the poor accuracy of this scheme since it is not consistent with the original coupled problem.
3. *Algorithm 2.6*: the comparison with fully coupled solutions have shown that the method gives satisfactory results, in agreement with the energy estimate guaranteeing the stability of the splitting.

1.2.2 Part II: Toward cardiac hemodynamics

The second part of the thesis is mainly devoted to the numerical simulations of the cardiovascular system. By making use of the loosely coupled scheme presented in the first part, we obtain some results on the ventricle-valves-aorta coupled fluids problem. From a clinical standpoint the pathologies arising in the cardiovascular system have not a unique cause. The origin of a malfunctioning of the ventricle, valves or aorta can be strictly correlated. To best of our knowledge in literature, only few models couple these 3 aspects at same time.

Chapter 4: Fluid-fluid interaction problem and RIS model. Application to the aortic valve In this chapter we discuss the fluid-fluid problem in two cardiovascular compartments, in which one of them is represented by the valve. This is a prototype for left ventricle hemodynamics we discuss in Chapter 6.

A reduced model for heart valves, recently developed in [AHSG12], is integrated in the fluid problem. In this approach, the mechanics of valves is not considered. Instead, valves are replaced by immersed surfaces acting as resistances on the fluid which mimics the behavior of a real valve. The mathematical formulation is based on the model proposed in [FGM08] to deal with immersed stents. The geometry of the resistive surface is defined as the real three-dimensional valve geometry in its fully closed and fully open configuration. To capture the pressure jump across the immersed surface, a fissured mesh is introduced in the geometry (Section 4.3.1).

We have performed two kinds of numerical experiments:

1. A *template of the aorta* (Section 4.3.2), has been used to test the two-fluid coupled model with the RIS valve model. With respect to the simulations presented in Chapter 3, the aortic root domain without closed valve configuration, has been replaced by a fissured domain with closed and open valve configuration, while the aortic arc mesh is kept unchanged.
2. A *realistic aorta* (Section 4.3.3), whose geometry was obtained from medical images, is employed to investigate two stenotic valve cases. This pathological case is directly included in the mathematical model simply putting non-zero resistance on the stenotic leaflet during all the cardiac cycle, while keeping the same valve geometry with respect to the normal case.

Chapter 5: An energy stable time-marching scheme for fluid flows in moving domains This chapter is mainly focused on the energy stability of non-linear fluid model when it is solved in moving domains, through the so called Arbitrary Eulerian Lagrangian (ALE) formulation (Section 5.3). The new difficulty comes from those integrals, which are integrated over the moving domain at a given time-step.

In the same spirit of the Temam's trick, we show that, adding a weak consistent term ((5.26) on page 131)

$$\frac{1}{\delta t}\left(\int_{\Omega^n}\mathbf{u}^n\cdot\mathbf{v}-\int_{\Omega^{n-1}}\mathbf{u}^n\cdot\mathbf{v}\right)-\int_{\Omega^n}(\mathbf{u}^n\cdot\mathbf{v})(\nabla\cdot\mathbf{w}^{n-1})=\mathcal{O}(\delta t),$$

we can get a stable energy inequality without any Geometric Conservation Laws (*GCL*) (see [EGP09, TL79]), that were so far necessary to establish an energy balance for the fluid equations on a moving domain (see e.g. [FN99, TM01]).

A numerical test concludes the chapter. In this example the ALE non-stabilized formulation (Algorithm 5.1) is compared with the ALE stabilized formulation (Algorithm 5.2).

Chapter 6: Numerical examples in cardiac hemodynamics This chapter deals with the preliminary numerical simulations of the blood dynamics in the left ventricle coupled with the blood flow in the aorta via a staggered explicit algorithm. The simulations are performed taking into account the following elements

1. A fluid-fluid staggered scheme is used to couple the blood dynamics in the left ventricle with the blood dynamics in the aorta (Chapter 2 and Chapter 3).
2. RIS valve models account for both mitral and aortic valve (Chapter 4).
3. The stabilized ALE formulation for fluid flow in moving domain is used to model ventricle contraction (Chapter 5).
4. External displacements derived from an electro-mechanical simulation of the heart [SMCCS08, Imp13] are imposed on the ventricle wall.
5. Windkessel models are used in the outlets in order to take into account the neglected part of the cardiovascular system.

Chapter 7: Obtained results and perspectives This thesis is completed by concluding remarks. A list of conclusions and perspectives by chapter is discussed.

1.3 Anatomy and physiology of the cardiovascular system

In this section we provide to the reader with the essentially vocabulary and references concerning the main aspect of the cardiovascular system.

Although the cardiovascular system is essentially a network of vessels powered by a "pump", the heart, the complex anatomy and physiology that make it able to successfully keep a person alive is truly amazing. Add to that the influence of a variety of physical and chemical factors and we have a really complicated system of structures and events that need to operate correctly and efficiently to maintain its own internal stability. To understand how the heart accomplishes its important task, it is first necessary to consider the relationship between the structure and function of its components. The complexity of the cardiovascular system is just sketched here and for a more careful analysis we refer to a relevant bibliography, for example [Fun97, Kla11, TD12, Thi08a, Thi08b].

1.3.1 The circulatory loop

The cardiovascular system consists of the heart and vessels allowing blood circulation, that transport oxygen, nutrients, hormones, and cellular waste products throughout the body (Figure 1.4).

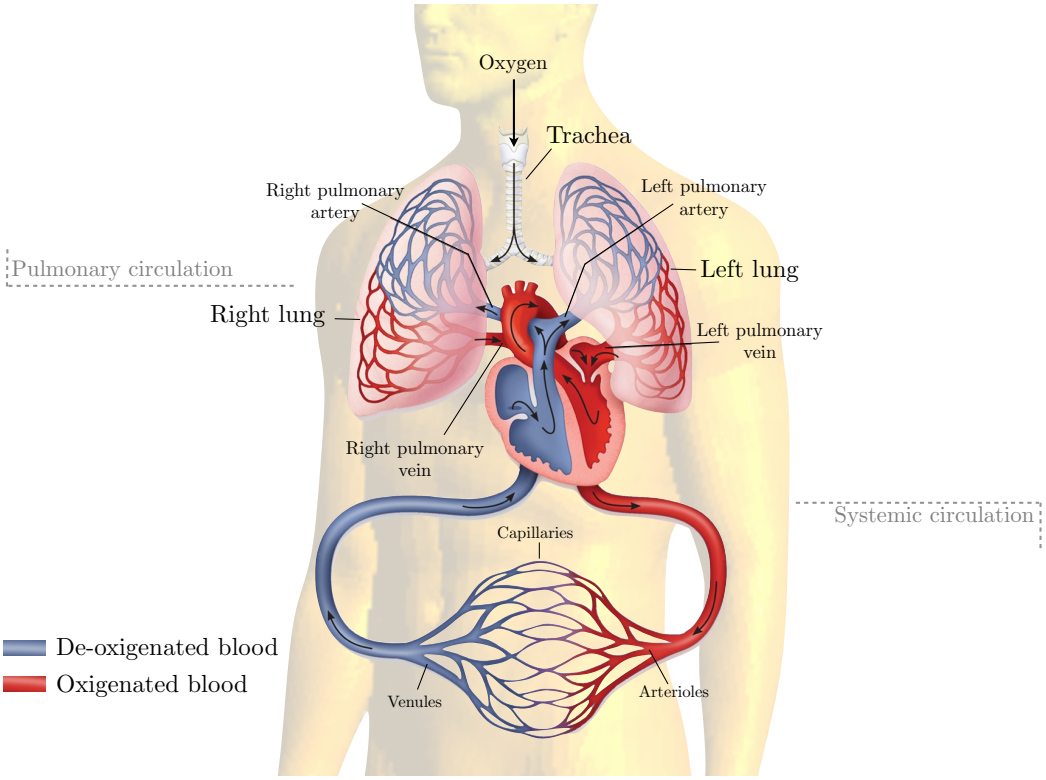

Figure 1.4: *Schematic view of the closed circulation of blood. Image adapted from* [Bio12].

There are two primary circulatory loops in the human body (e.g. see [Tay12]):

- *Pulmonary circulation*, transporting de-oxygenated blood from the right side of the heart to the lungs, where blood picks up oxygen and returns to the left side of the heart.
- *Systemic circulation*, carrying highly oxygenated blood from the left side of the heart to all of the tissues of the body. It removes wastes from body tissues and returns de-oxygenated blood to the right side of the heart.

Blood vessels are the body's highways that allow blood to flow quickly and efficiently from the heart to every region of the body and back again. There are three major types of vessels:

- *Arteries*, large vessels transporting blood away from the heart. They face high levels of blood pressure as they carry blood pushed from the heart under great forces.
- *Capillaries*, the smallest vessels, connecting the arterioles (small arteries) to the venules (small veins). They exchange gases, nutrients, and waste products with tissue cells.
- *Veins*, the large return vessels of the body, they transport the blood back to the heart. They are subjected to very low blood pressures.

1.3.2 The structure of the human heart

The heart is a muscular organ, body's hardest working organ, relatively small, about the size of a person's closed fist, that functions as the body's circulatory pump. It rests on the diaphragm between the lungs and extends from the sternum to the vertebral column. About two-thirds of the mass of the heart lies to the left of the body's mid-line.

The interior of the heart is divided into four compartments called chambers, or cavities (Figure 1.5). The two superior chambers are called *right atrium* and *left atrium*. The two inferior chambers are the *left ventricle* and the *right ventricle*. The right and left atria and ventricular chambers are separated by a *septal wall* or *septum*.

The external part of the heart is covered by a thin-membrane sac, the *pericardium*. Three layers surround the wall of the heart: *epicardium*, *myocardium* and *endocardium*. (Figure 1.6)

The heart consists of conducting tissue, blood vessels and extracellular media, but most of it is made up by *cardiac muscle tissue*. This is slightly different from the normal skeletal muscle tissue since it is striated but not under voluntary conscious control. The myocardium possesses a hierarchical micro-structure of

- *Myocytes*, cylindrical contractile cells, containing
  - *Sarcomeres* micro-anatomical units, composed of
    - *myosin*, thick filaments proteins,
    - *actin*, thin filaments proteins.

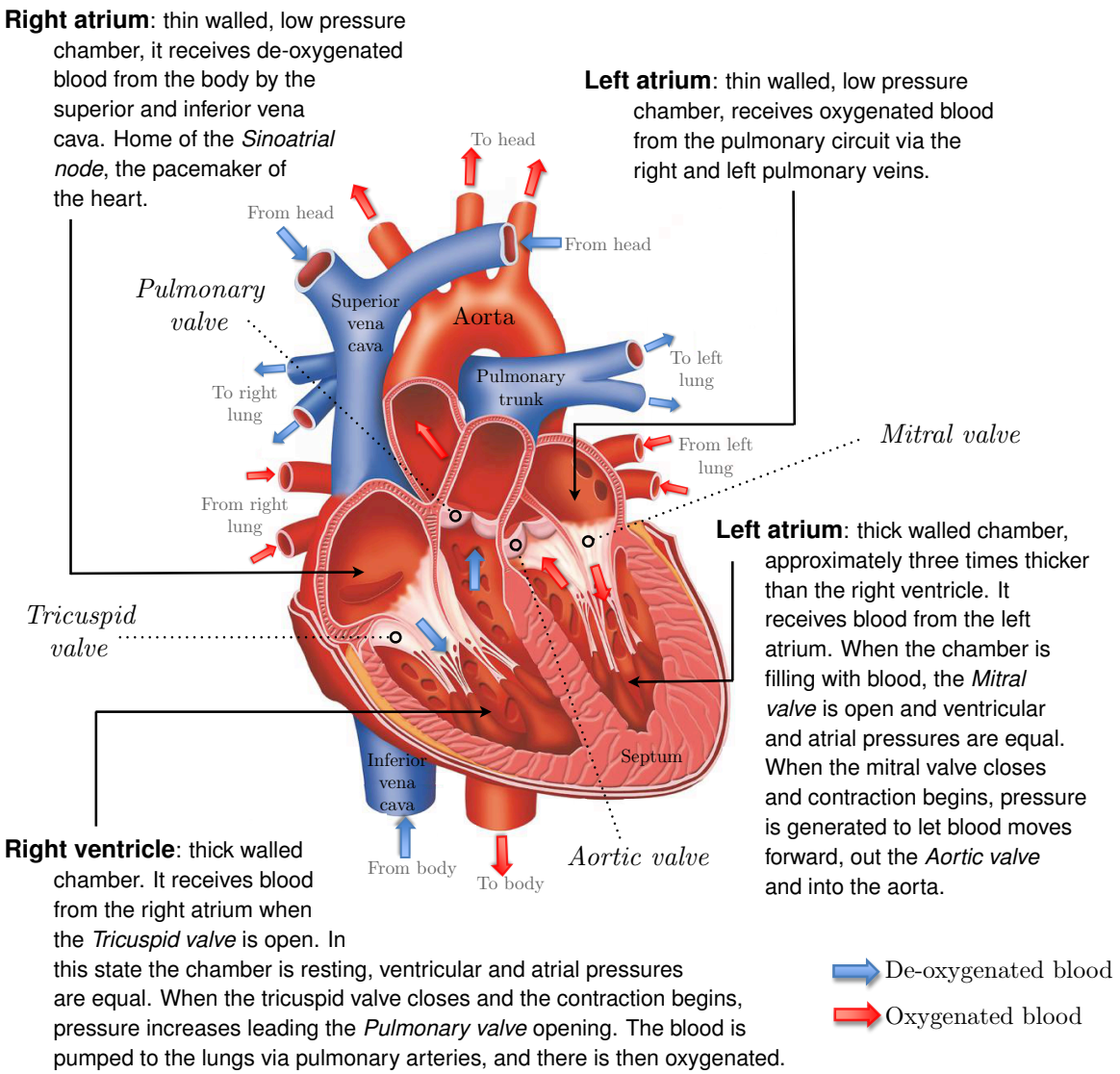

Figure 1.5: *Main components of the human heart and characteristics of its chambers. Front view. Heart image taken from* [O'C12].

Chemical and physical interactions between actin and myosin cause the sarcomere length to shorten, and therefore the myocyte to contract during the process of *excitation-contraction*.

1.3.3 Heart electro-physiology

The electrical impulse triggers the heart to beat. Between the interior and the exterior of a cardiac cell there holds a voltage difference, called transmembrane potential and its transient alteration is defined *action potential*.

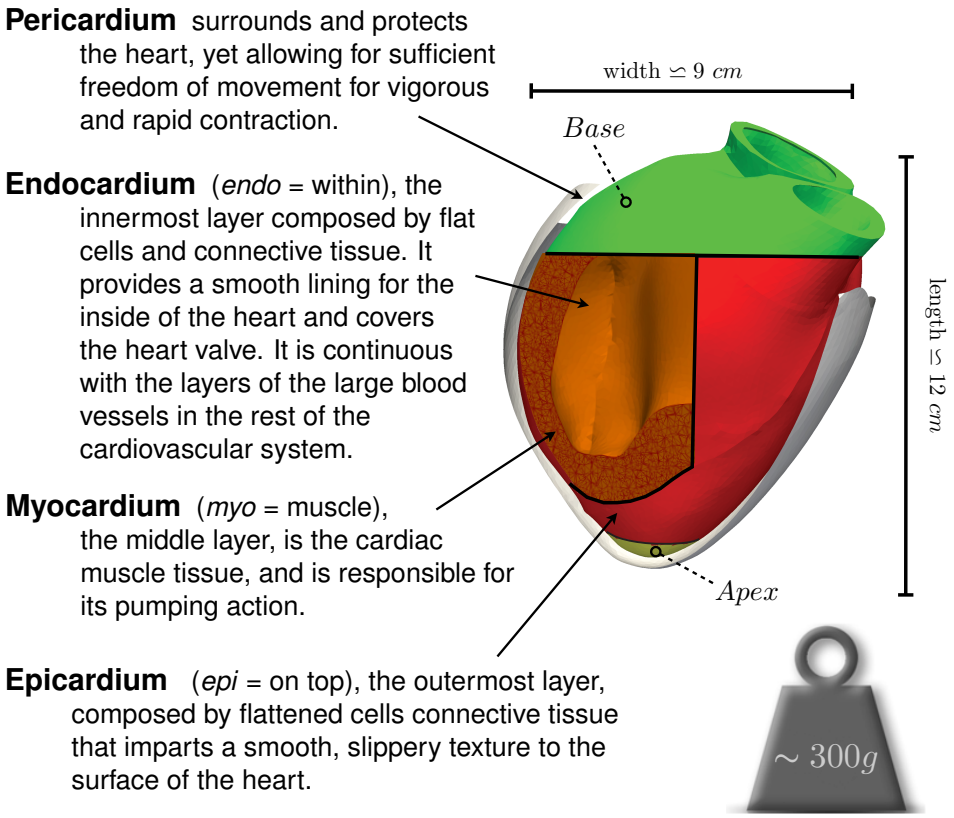

Figure 1.6: *Layers stratification and dimension of the heart in an adult healthy man. Front view with a section. Image modified from* [Imp13].

The changes in membrane potential during different phases are brought by changes in the movement of ions Ca^{2+}, Na^{+} and K^{+} across the membrane, through ion channels that open and close at different times (see [KS09] for more details). Without electrical stimuli, the transmembrane potential is negative, the cells are called to be *polarized*, due to the poor concentration of sodium and calcium ions in the cell. When the electrical stimuli arrive to the cell, the ion channels in the membrane open so that the transfer of sodium inwards the cell occurs. This is called *depolarization*, where the transmembrane potential becomes positive, leading to the contraction of the cardiac cells.

The electrical activity of the heart is summarized in Figure 1.7, with the Electrocardiogram (ECG) traces, called waves (P, QRS, T). The depolarization occurs throughout atria and thereafter the ventricles.

1.3.4 The cardiac valves

At the exit of each heart cavity, a valve prevents the back-flow of the blood into the corresponding chamber, see Figure 1.8.

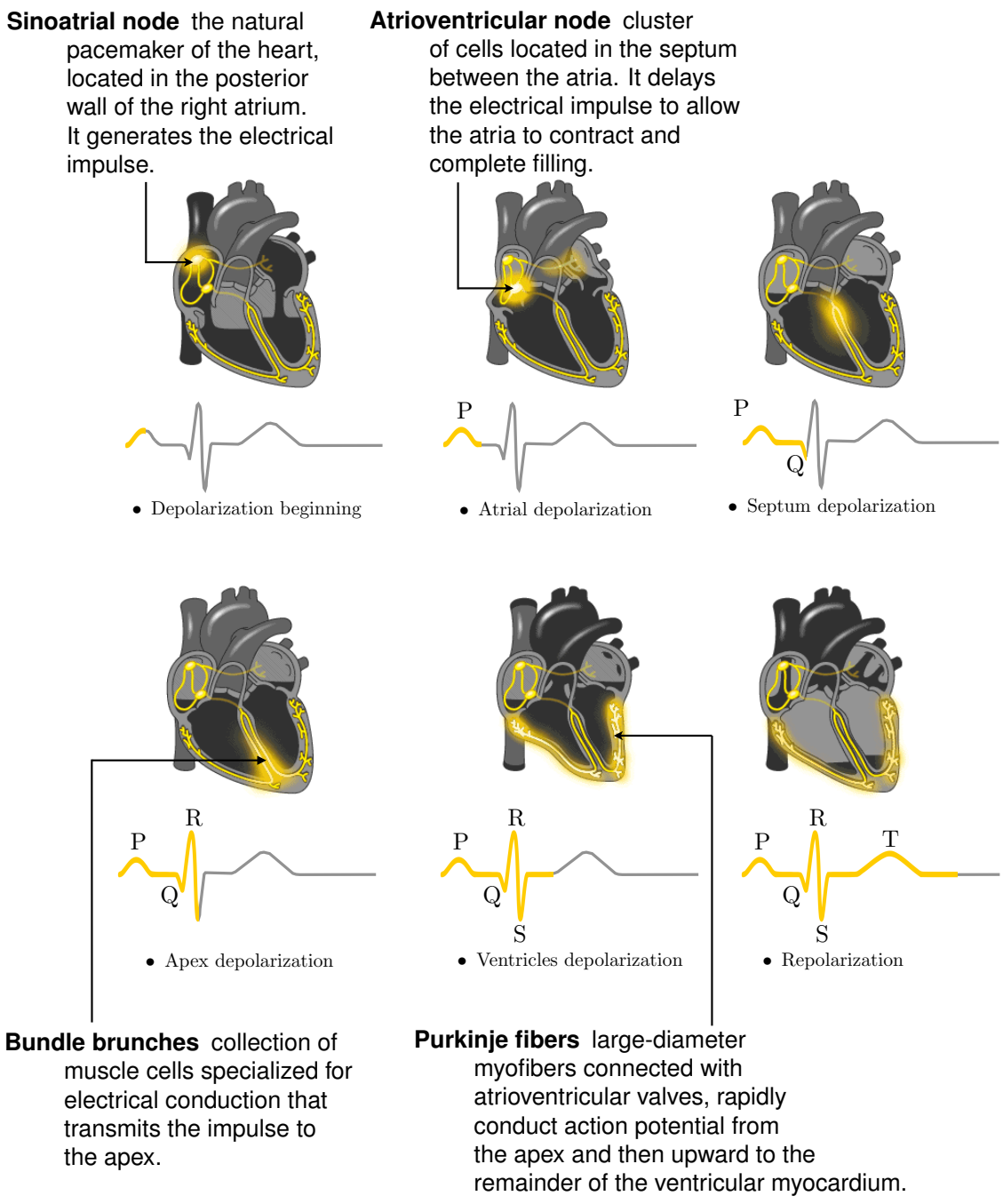

Figure 1.7: *Electrical activity of the heart and ECG trace. Heart images taken from* [Bio07].

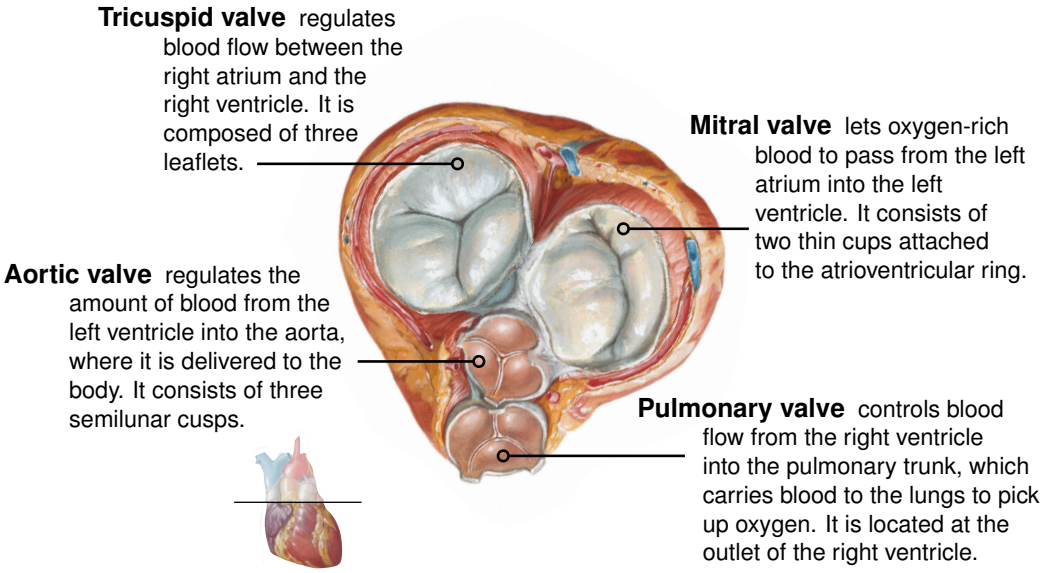

Figure 1.8: *The four heart valves sketched in an isovolumic phase. Top view. Image modified from* [Net94].

There are four valves: two ventriculo-arterial valves, the *tricuspid* and *mitral* - or bicuspid - valve and two atrio-ventricular valves, the *aortic* and *pulmonary* valves - both also termed semilunar valves. Biological attachments in both ventricles, *chordae tendinae*, prevent the atrio-ventricular valve to prolapse during their closures (see for example [IBHL13] for a general review).

1.3.5 The aorta

The aorta is the first and largest artery leaving the left side of the heart. It starts at the opening of the left ventricle, from which blood is pumped out of the heart through the aortic valve. In an adult, it is approximately $30 - 40\ cm$ long and has an average diameter of $2.5 - 3.5\ cm$ (see [HKRB+02, Mic12] for measurements). The wall of this artery is $2\ mm$ thick, giving it the strength and elasticity needed to receive blood at high pressure from the heart.

The elasticity of the aorta is of great importance because it helps to propel blood forward. As the heart pumps blood, the walls of the aorta stretch. When the heart relaxes, the aortic valve stops blood flowing, and as the aorta shrinks back, blood is pushed forward through the body[5].

The aorta subdivides in two parts: thoracic and abdominal aorta. The thoracic aorta loops up and then curls behind the heart to descend through the thorax (Figure 1.9). The first branches, right and left coronaries, come off the *sinus of Valsalva*, three anatomic dilatations of aortic root, in which the valve is located. These arteries supply the heart in

[5]This phenomenon is known also as the Windkessel effect.

oxygenated blood, hence they are extremely important and their blockage may cause an infarct.

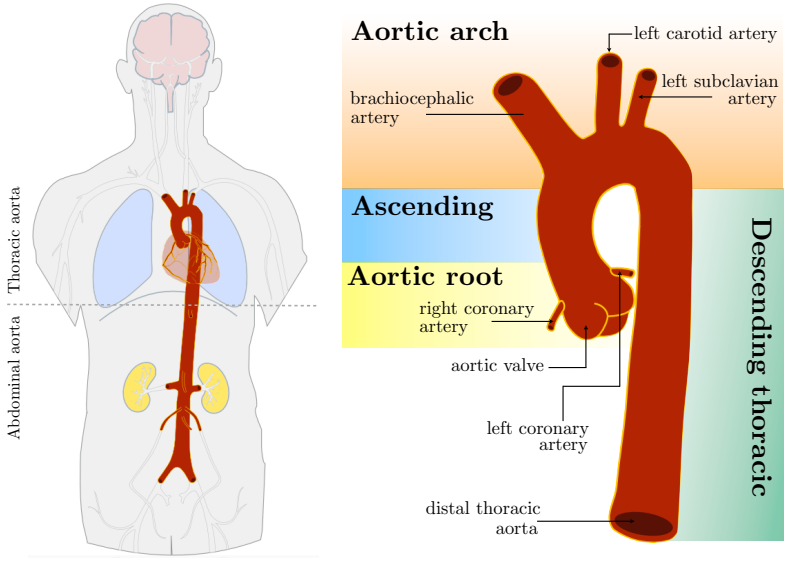

Figure 1.9: *Position in the human body, main parts and branches of the thoracic aorta. Images modified from* [Wik12].

The subsequent part is called the ascending aorta, the loop is the arch of the aorta, and it divides to become the brachiocephalic artery (that supplies of blood the right arm, the neck and the head), the left common carotid (suppling the head and the neck) and left subclavian arteries (suppling the left arm).

The aorta becomes abdominal as it reaches the appropriate region. Having emerged through the diaphragm, the aorta divides into numerous branches to supply blood to the surrounding organs as liver, stomach, spleen, intestines and kidneys. Finally the aorta splits into the left and right common iliac arteries, that mainly provide blood to the legs.

1.3.6 The cardiac cycle

The heart beat is a two-stage pumping action over a period of about $0.8\ s$, the longer period is called *diastole*, the shorter is the *systole*. More precisely, it consists of four main phases[6]: *isovolumic* (or *isovolumetric*) *relaxation*, *ventricular filling*, *isovolumic* (or *isovolumetric*) *contraction* and *systolic ejection* (Figure 1.10).

In between the filling and the isovolumic contraction, the atrial systole occurs, i.e. atria contract reversing a small quantity of blood in the ventricles.

A common representation of the cardiac cycle is the (left) ventricular pressure-volume loop (e.g. [Fun97]). The contraction and expansion of the volume in the heart produce an

[6]Some authors divide the cardiac cycle into seven phases: isovolumic relaxation and contraction, rapid and slow filling, rapid and slow ejection and atrial contraction (e.g. [Thi08a]).

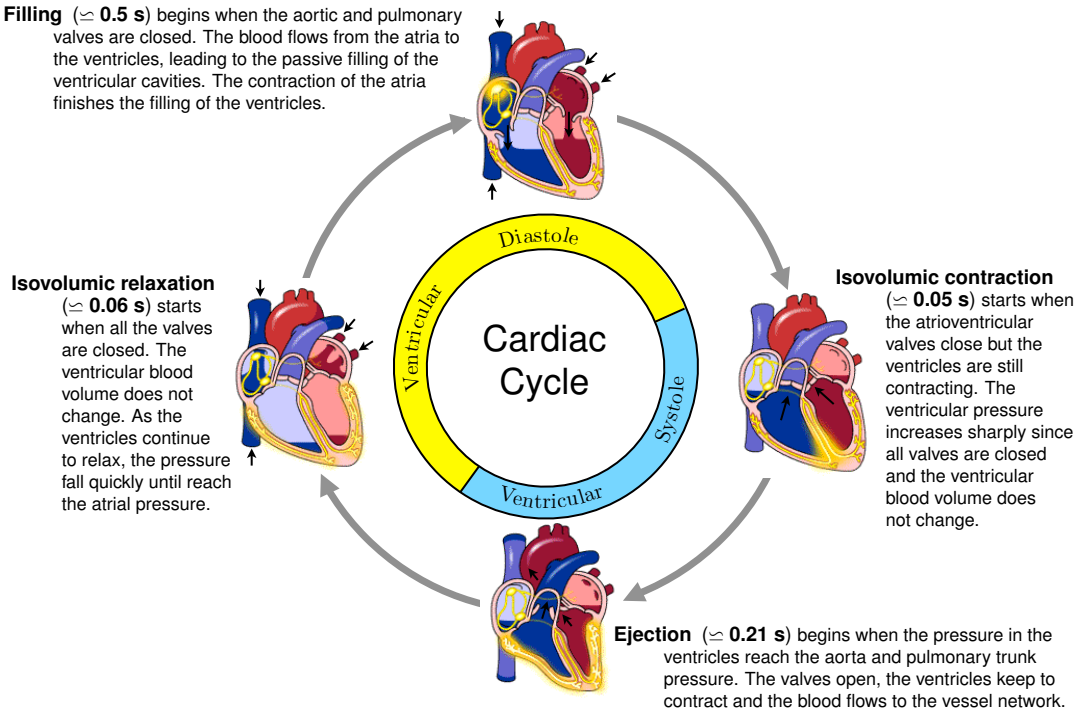

Figure 1.10: *The principal phases of a cardiac cycle. Heart images modified from* [Bio07].

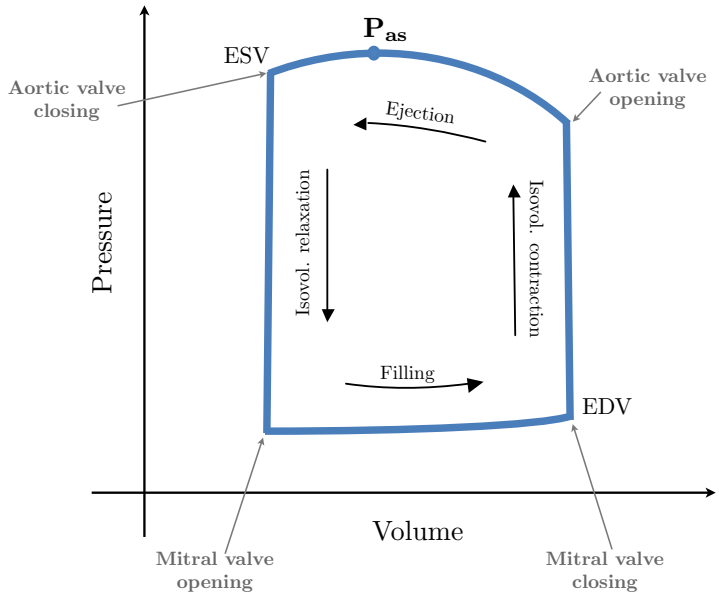

Figure 1.11: *Theoretical Pressure-Volume loop in the left ventricle:* P_{as} *is the aortic-systolic pressure, i.e. highest pressure if the aortic valve is opening properly. End Systolic Volume (ESV) and End Diastolic Volume (EDV) are the volumes of blood present in the ventricle at the end of systole and diastole respectively.*

increase and a reduction of the pressure that generate a closed curve. Figure 1.11 sketches out the theoretical course of the cardiac cycle in terms of pressure and volume change in the left ventricle. Several relevant hemodynamic parameters such as stroke volume, cardiac output, ejection fraction, myocardial contractility, etc. can be determined from this loop.

In Figure 1.12, the different phases of a cardiac cycle are represented by mean of the main cardiac indicators related to left atrium and ventricle activity. Clearly a similar cycle acts symmetrically also for the right atrium and ventricle.

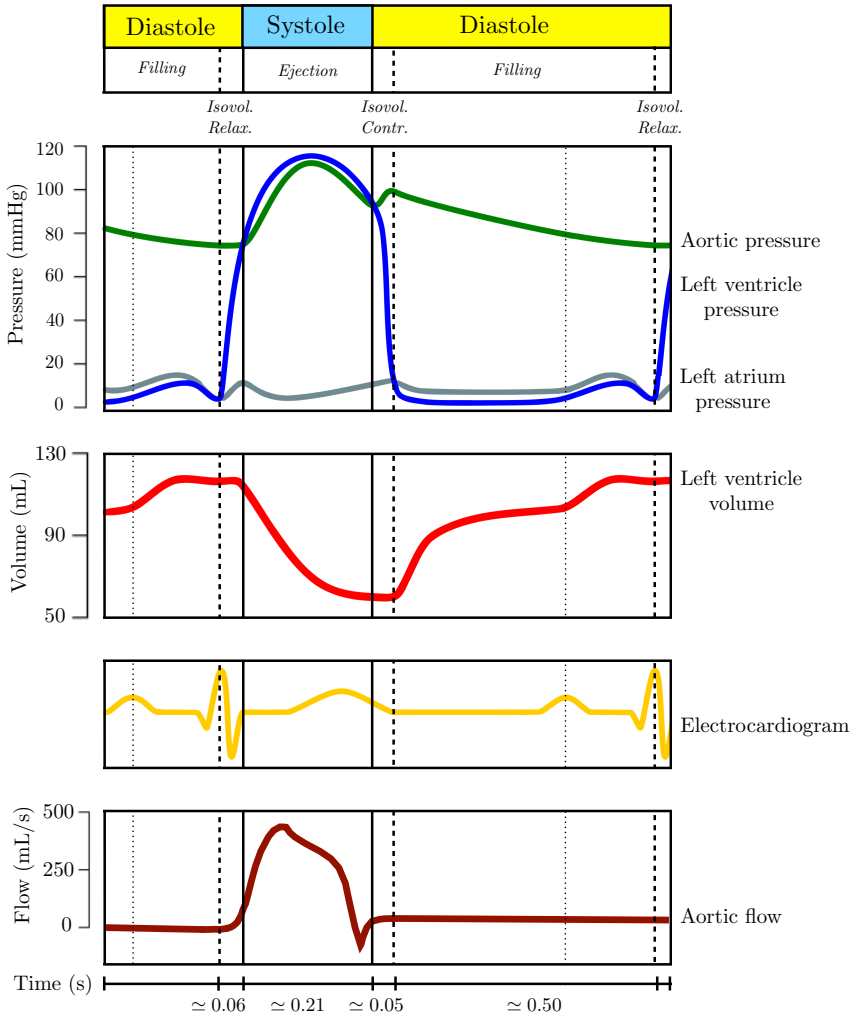

Figure 1.12: *Evolution of the principal cardiac indicators in a cycle: pressure in the left cardiac cavities and aorta, left ventricle volume, ECG trace and aortic flow.*

Bibliography of the Introduction

[AGPT09] M. Astorino, J.-F. Gerbeau, O. Pantz, and K.-F. Traoré. Fluid-structure interaction and multi-body contact. Application to the aortic valves. *Comput. Methods Appl. Mech. Engng.*, 198(45-46):3603–3612, 2009.

[AHSG12] M. Astorino, J. Hamers, S. C. Shadden, and J.-F. Gerbeau. A robust and efficient valve model based on resistive immersed surfaces. *Int. J. Numer. Meth. Biomed. Engng.*, 28:937–959, 2012.

[AP96] R. Aliev and A. Panfilov. A simple two-variable model of cardiac excitation. *Chaos, Solitons & Fractals*, 3(7):293–301, 1996.

[Ast10] M. Astorino. *Interaction Fluide-Structure dans le Systéme Cardiovasculaire. Analyse Numèrique et Simulation*. PhD thesis, Universitè Pierre et Marie Curie, Paris 6, 2010.

[BCF13] C. Bertoglio, A. Caiazzo, and M. A. Fernández. Fractional-step schemes for the coupling of distributed and lumped models in hemodynamics. *SIAM Journal on Scientific Computing*, 35:551–575, 2013.

[Ber12] C. Bertoglio. *Problémes Directs et Inverses en Interaction Fluide-Structure. Application á l'hèmodynamique*. PhD thesis, Universitè Pierre et Marie Curie, Paris 6, 2012.

[BF09] E. Burman and M. A. Fernández. Stabilization of explicit coupling in fluid-structure interaction involving fluid incompressibility. *Comput. Methods Appl. Mech. Engrg*, 198:766–784, 2009.

[BF14] E. Burman and M.A. Fernández. Explicit strategies for incompressible fluid-structure interaction problems: Nitsche type mortaring versus Robin-Robin coupling. *Int. J. Num. Meth. Engrg.*, 97(10):739–758, 2014.

[BFU07] P.J. Blanco, R.A. Feijóo, and S.A. Urquiza. A unified variational approach for coupling 3D-1D models and its blood flow applications. *Comp. Meth. Appl. Mech. Engrg.*, 196:4391 – 4410, 2007.

[BHS03] R. Becker, P. Hansbo, and R. Stenberg. A finite element method for domain decomposition with non-matching grids. *M2AN Math. Model. Numer. Anal.*, 37(2):209–225, 2003.

[Bio07] BioCoach. *Cardiovascular System I: The Beating Heart*. http://www.phschool.com/science/biology_place/biocoach/cardio1/intro.html, 2007.

[Bio12] Biological-forums. *The cardiovascular system. A schematic view of the closed circulation of blood*. http://biology-forums.com/index.php?action=gallery;sa=view;id=10020, 2012.

[BPUF09] P.J. Blanco, M.R. Pivello, S.A. Urquiza, and R.A. Feijóo. On the potentialities of 3d–1d coupled models in hemodynamics simulations. *Journal of Biomechanics*, 42(7):919 – 930, 2009.

[CDFQ11] P. Crosetto, S. Deparis, G. Fourestey, and A. Quarteroni. Parallel algorithms for fluid-structure interaction problems in haemodynamics. *SIAM Journal on Scientific Computing*, 33(4):1598–1622, 2011.

[CFG+09] D. Chapelle, M.A. Fernández, J.-F. Gerbeau, P. Moireau, J. Sainte-Marie, and N. Zemzemi. Numerical simulation of the electromechanical activity of the heart. In *Functional Imaging and Modeling of the Heart*, volume 5528, pages 357–365. Springer Berlin Heidelberg, 2009.

[Col14] A. Collin. *Analyse asymptotique en électrophysiologie cardiaque. Applications à la modélisation et à l'assimilation de données*. PhD thesis, Universitè Pierre et Marie Curie, Paris 6, 2014.

[dSGB08] N. Diniz dos Santos, J.-F. Gerbeau, and J.-F. Bourgat. A partitioned fluid-structure algorithm for elastic thin valves with contact. *Comput. Methods Appl. Mech. Engrg.*, 197(19-20):1750–1761, 2008.

[DZL07] V. Díaz-Zuccarini and J. LeFèvre. An energetically coherent lumped parameter model of the left ventricle specially developed for educational purposes. *Comput. Biol. Med.*, 37:774–784, 2007.

[EGP09] S. Étienne, A. Garon, and D. Pelletier. Perspective on the geometric conservation law and finite element methods for ALE simulations of incompressible flow. *Journal of Computational Physics*, 228(7):2313 – 2333, 2009.

[EnS06] EnSight CEI software. *EnSight Interface Manual*. http://www.ensight.com/, 2006.

[FGG07] M.A. Fernández, J.-F. Gerbeau, and C. Grandmont. A projection semi-implicit scheme for the coupling of an elastic structure with an incompressible fluid. *International Journal for Numerical Methods in Engineering*, 69(4):794–821, 2007.

[FGM08] M. Fernández, J.-F. Gerbeau, and V. Martin. Numerical simulation of blood flows through a porous interface. *Mathematical Modelling and Numerical Analysis*, 42:961–990, 2008.

[FGNQ01] L. Formaggia, J.F. Gerbeau, F. Nobile, and A. Quarteroni. On the coupling of 3D and 1D Navier - Stokes equations for flow problems in compliant vessels. *Comp. Meth. Appl. Mech. Engrg.*, 191:561–582, 2001.

[Fit61] R. Fitzhugh. Impulses and physiological states in theoretical models of nerve membrane. *Biophysical Journal*, 1(6):445–466, 1961.

[FN99] L. Formaggia and F. Nobile. A stability analysis for the arbitrary lagrangian eulerian formulation with finite elements. *East-West J. Numer. Math.*, 7(2):105–131, 1999.

[Fre01] P.J. Frey. MEDIT - An interactive mesh visualization software. Technical Report 0253, INRIA, 2001.

[Fun97] Y.C. Fung. *Biomechanics Circulation*. Springer, 2 edition, 1997.

[GK09] S. Göktepe and E. Kuhl. Computational modeling of cardiac electrophysiology: A novel finite element approach. *International Journal for Numerical Methods in Engineering*, 79(2):156–178, 2009.

[GK10] S. Göktepe and E. Kuhl. Electromechanics of the heart: a unified approach to the strongly coupled excitation-contraction problem. *Computational Mechanics*, 45:227–243, 2010.

[GR09] C. Geuzaine and J.-F. Remacle. Gmsh: A 3-d finite element mesh generator with built-in pre- and post-processing facilities. *International Journal for Numerical Methods in Engineering*, 79(11):1309–1331, 2009.

[Han05] P. Hansbo. Nitsche's method for interface problems in computational mechanics. *GAMM-Mitt.*, 28(2):183–206, 2005.

[Hec12] F. Hecht. New development in FreeFem++. *J. Numer. Math.*, 20(3-4):251–265, 2012.

[HH52a] A.L. Hodgkin and A. F. Huxley. Currents carried by sodium and potassium ions through the membrane of the giant axon of loligo. *Journal of Physiology*, 116(4):449–472, 1952.

[HH52b] A.L. Hodgkin and A. F. Huxley. A quantitative description of membrane current and its application to conduction and excitation in nerve. *Journal of Physiology*, 117(4):500–544, 1952.

[HKRB+02] A. Hager, H. Kaemmerer, U. Rapp-Bernhardt, S. Blücher, K. Rappa, T. M. Bernhardt, M. Galanski, and J. Hess. Diameters of the thoracic aorta throughout life as measured with helical computed tomography. *The Journal of thoracic and cardiovascular surgery*, 123:1060–1066, 2002.

[HPSB03] J. De Hart, G.W.M. Peters, P.J.G. Schreurs, and F.P.T. Baaijens. A three-dimensional computational analysis of fluid-structure interaction in the aortic valve. *Journal of Biomechanics*, 36:103–112, 2003.

[Hun75] P.J. Hunter. *Finite element analysis of cardiac muscle mechanics.* PhD thesis, University of Oxford, 1975.

[IBHL13] P. A. Iaizzo, R. W. Bianco, A. J. Hill, and J. D. St. Louis. *Heart Valves. From Design to Clinical Implantation*. Springer, 2013.

[Imp13] A. Imperiale. *Méthodes d'assimilation de la donnée image pour la personnalisation de modéles mécaniques*. PhD thesis, Universitè Pierre et Marie Curie, Paris 6, 2013.

[JL06] E. Jung and W. Lee. Lumped parameter models of cardiovascular circulation in normal and arrhythmia cases. *J. Korean Math. Soc.*, 43(4):885–897, 2006.

[Kla11] R. E. Klabunde. *Cardiovascular physiology concepts*. Lippincott Williams & Wilkins, http://www.cvphysiology.com/index.html, 2011.

[KS06] T. Korakianitis and Y. Shi. A concentrated parameter model for the human cardiovascular system including heart valve dynamics and atrioventricular interaction. *Medical Engineering & Physics*, 28:613–628, 2006.

[KS09] B. M. Koeppen and B. A. Stanton. *Berne & Levy Physiology*. Elsevier, 6 edition, 2009.

[LDSB10] K.D. Lau, V. Diaz, P. Scambler, and G. Burriesci. Mitral valve dynamics in structural and fluid-structure interaction models. *Medical Engineering & Physics*, 32:1057–1064, 2010.

[LMAD11] T. Lassila, A. C. I. Malossi, M. Astorino, and S. Deparis. Geometrical multiscale model of an idealized left ventricle with fluid-structure interaction effects coupled to a one-dimensional viscoelastic arterial network. In *Proceedings of the ECCOMAS Thematic International Conference on Simulation and Modeling of Biological Flows (SIMBIO 2011)*, September 2011.

[Mat13] Materialise. *3-Matic version 8*. http://biomedical.materialise.com/3-matic, 2013.

[Mic12] A. Micheau. *Normal adult aortic diameters*. Imaios, http://www.imaios.com/e-Cases/Channels/Radiology/Classifications/Anatomy-of-the-aorta, 2012.

[Moi08] P. Moireau. *Assimilation de données par filtrage pour les systèmes hyperboliques du second ordre. Applications à la mécanique cardiaque*. PhD thesis, Ecole Polytechnique, 2008.

[MXA+12] P. Moireau, N. Xiao, M. Astorino, C.A. Figueroa, D. Chapelle, C.A. Taylor, and J.F. Gerbeau. External tissue support and fluid-structure simulation in blood flows. *Biomech Model Mechanobiol*, 11:1–18, 2012.

[MYWD07] Y. S Morsi, W. W. Yang, C. S. Wong, and S. Das. Transient fluid-structure coupling for simulation of a trileaflet heart valve using weak coupling. *Journal of Artificial Organs*, 10(2):96–103, 2007.

[NAY62] J.S. Nagumo, S. Arimoto, and S. Yoshizawa. An active pulse transmission line stimulating nerve axon. *Proceedings of the IEEE*, 50:2061–2071, 1962.

[Net94] F. H. Netter. *The Netter collection of medical illustrations*, volume 4. Saunders, 1994.

[NNN+11] D.A. Nordsletten, S.A. Niederer, M.P. Nash, P.J. Hunter, and N.P. Smith. Coupling multi-physics models to cardiac mechanics. *Progress in Biophysics and Molecular Biology*, 104(1–3):77 – 88, 2011.

[Nob62] D. Noble. A modification of the Hodgkin-Huxley equation applicable to Purkinje fiber action and pacemaker potentials. *Journal of Physiology*, 160:317–352, 1962.

[NP04] M. P. Nash and A. V. Panfilov. Electromechanical model of excitable tissue to study reentrant cardiac arrhythmias. *Progress in Biophysics & Molecular Biology*, 85:501–522, 2004.

[NTLF+12] M. Nichols, N. Townsend, R. Luengo-Fernandez, J. Leal, A. Gray, P. Scarborough, and M. Rayner. *European Cardiovascular Disease Statistics*. European Heart Network, Brussels, European Society of Cardiology, Sophia Antipolis, 2012.

[O'C12] J. O'Callaghan. *How does the heart work?* http://www.howitworksdaily.com/whats-inside/inside-the-human-heart/, 2012.

[OPK+00] M. S. Olufsen, C. S. Peskin, W. Y. Kim, E. M. Pedersen, A. Nadim, and J. Larsen. Numerical simulation and experimental validation of blood flow in arteries with structured-tree outflow conditions. *Annals of Biomedical Engineering*, 28(11):1281–1299, 2000.

[Pes77] C. S. Peskin. Numerical analysis of blood flow in the heart. *Journal of Computational Physics*, 25(3):220–252, 1977.

[Pes82] C.S. Peskin. The fluid dynamics of heart valves: experimental, theoretical, and computational methods. *Annual Review of Fluid Mechanics*, 14:235–259, 1982.

[SB09] F. Sotiropoulos and I. Borazjani. A review of state-of-the-art numerical methods for simulating flow through mechanical heart valves. *Med Biol Eng Comput*, 47:245–256, 2009.

[SMCCS08] J. Sainte-Marie, D. Chapelle, R. Cimrman, and M. Sorine. Modeling and estimation of the cardiac electromechanical activity. *Computers and Structures*, 84:1743–1759, 2008.

[SSG+04] G. Szabóa, D. Soansb, A. Grafa, C. J. Bellera, L. Waiteb, and S. Hagla. A new computer model of mitral valve hemodynamics during ventricular filling. *European Journal of Cardio-thoracic Surgery*, 26:239–247, 2004.

[Tay12] T. Taylor. *Cardiovascular system*. InnerBody.com. HowToMedia, Inc., http://www.innerbody.com/image/cardov.html, 2012.

[TD12] G. J. Tortora and B. Derrickson. *Principles of Anatomy and Physiology*. Wiley, 2012.

[Thi08a] M. Thiriet. *Biology and Mechanics of Blood Flows. Part I: Biology*. Springer, New York, 2008.

[Thi08b] M. Thiriet. *Biology and Mechanics of Blood Flows: Part II: Mechanics and Medical Aspects of Blood Flows*. Springer, New York, 2008.

[TL79] P.D. Thomas and C.K. Lombard. Geometric conservation law and its application to flow computations on moving grids. *AIAA J.*, 17:1030–1037, 1979.

[TM01] P. Le Tallec and J. Mouro. Fluid structure interaction with large structural displacements. *Comput. Meth. Appl. Mech. Engrg.*, 190:3039–3067, 2001.

[TW89] J. D. Thomas and A. E. Weyman. Fluid dynamics model of mitral valve flow: Description with in vitro validation. *Journal of the American College of Cardiology*, 13(1):221–233, 1989.

[VC06] I. Vignon-Clementel. *A coupled multidomain method for computational modeling of blood flow*. PhD thesis, Stanford University, 2006.

[WHS+02] H. Watanabe, T. Hisada, S. Sugiura, J. Okada, and H. Fukunari. Computer simulation of blood flow, left ventricular wall motion and their interrelationship by fluid-structure interaction finite element method. *JSME International Journal Series C*, 45(4):1003–1012, 2002.

[Wik12] Wikipedia Encyclopedia. *Circulatory system*. http://en.wikipedia.org/wiki/Aorta, 2012.

[WLW09] N. Wetserhof, J.-W. Lankhaa, and B. E. Wetserhof. The arterial Windkessel. *Med. Biol. Eng. Comput.*, 47:131–141, 2009.

[WSKH04] H. Watanabe, S. Sugiura, H. Kafuku, and T. Hisada. Multiphysics simulation of left ventricular filling dynamics using fluid-structure interaction finite element method. *Biophys. J.*, 87(3):2074–2085, 2004.

[Zyg11] Zygote Media Group. *3D Human Anatomy for Animation, Illustration, CAD and Software Development*. http://www.zygote.com/, 2011. 3D Science project, http://www.3dscience.com/.

Part I

FLUID-FLUID INTERACTION PROBLEM

Your head will collapse
If there's nothing in it
And you'll ask yourself
Where is my mind?

"Where Is My Mind?" by Pixies.

CHAPTER 2

Explicit coupling schemes for a fluid-fluid interaction problem

In this chapter we propose a new approach to the loosely coupled time-marching of a fluid-fluid interaction problems involving the incompressible Navier-Stokes equations. The methods combine a specific explicit Robin-Robin treatment of the interface coupling with a weakly consistent interface pressure stabilization in time. A priori energy estimates guaranteeing stability of the splitting are obtained for a total pressure formulation of the coupled problem.

This chapter is part of:
Miguel Fernández, Jean-Frederic Gerbeau, Saverio Smaldone. **Explicit coupling schemes for a fluid-fluid interaction problem arising in hemodynamics**, published in SIAM Journal on Scientific Computing, 2014 [FGS14].

Contents

2.1 Introduction

Global and local features in hemodynamics are generally described by coupling dimensionally heterogeneous models of blood flow. In this geometrical multiscale paradigm, the three-dimensional (3D) Navier-Stokes equations are usually coupled with one-dimensional (1D) and/or zero-dimensional (0D) models that account for the parts before and after the 3D compartment (see, e.g., [BFU07, FGNQ01, QV03]). In this work, we are interested in coupling 3D compartments. Indeed, in some of them, it may be sufficient to consider a standard Navier-Stokes solver. But it is sometimes necessary to develop ad-hoc software to handle complex configurations. For instance, if a detailed modeling of blood flow in the left ventricle is sought for, the 3D model must incorporate additional features, such as the deformation of the cardiac cavity and the opening-closing dynamics of the aortic valves, which requires a very specific solver. Another example is provided by the simulation of endo-vascular devices (e.g., stents, coils) or vascular pathologies (e.g., aortic dissection, atherosclerotic plaques development, vascular wall remodeling) that may also require the development of specific software. In this context, it may be of practical interest to couple different 3D codes. The motivation of this work is therefore the partitioning of the 3D fluid computational domain into several complementary non-overlapping subdomains, in which these additional modeling features may take place. As an alternative to standard domain decomposition approaches, we propose to advance in time the system via specific explicit coupling (or *loosely coupled*) strategies that allow the uncoupled time-stepping of the sub-compartments.

As a preliminary step in this direction, in this work we focus on the case of two sub-compartments described by the incompressible Navier-Stokes equations. The two sub-problems are coupled, across their shared (artificial) interface, by standard kinematic/kinetic conditions, viz., continuity of velocity and stress. We address the uncoupled time-marching of the two sub-compartments via explicit coupling schemes. Note that this approach clearly differs from [MBDA11, BDM13], where partitioned iterative procedures acting on averaged/integrated interface quantities are proposed.

To this purpose, a major difficulty that has to be faced is related to the artificial energy transfers (unbalance of static and/or dynamic pressure power) induced by the interface time-splitting, which can lead to numerical instabilities. For instance, if a standard Dirichlet-Neumann scheme is foreseen (see [GK08]), the splitting introduces an unbalance of static powers across the interface. Relaxation of the kinematic constraint improves the situation, but with the payoff of an uncontrolled dynamic pressure power across the interface. This issue does not appear in fluid-fluid interaction models based on *rigid-lid* conditions, commonly used in oceanography modeling (see, e.g., [BK06, CHL09, CHL12, M̈79]), for which the normal velocity component vanishes on the interface.

In this work, the unbalanced static pressure power is controlled via a specific explicit Robin-Robin treatment of the interface coupling (based on Nitsche's interface method) and a weakly consistent interface pressure stabilization in time. Basically, this approach extends the loosely coupled schemes introduced in [BF09, BF14] for FSI problems to fluid-fluid interaction problems. We also show that the second source of instabilities (unbalanced dynamic pressure power) can be treated, in a natural way, by applying this method to a total pressure formulation of the Navier-Stokes equations.

Outline This chapter is organized as follows. In the next section, the incompressible Navier-Stokes equations are split into two sub-problems coupled across an artificial interface. The time discretization of the standard Dirichlet-Neumann approach is discussed in Section 2.3. A Nitsche's space semi-discrete formulation of this fluid-fluid interaction problem is presented in Section 2.4. Section 2.5 is devoted to the time-dicretization. We present different implicit (Paragraph 2.5.1) and explicit coupling strategies, in the static (Paragraph 2.5.2 and 2.5.3) and total pressure formulations (Paragraph 2.5.4), and state their corresponding discrete energy balances.

2.2 Coupled fluid-fluid problem

Let $\Omega \subset \mathbb{R}^d$, $d = 2, 3$ be a bounded fixed domain and a fluid modeled by the incompressible Navier-Stokes equations. The velocity $\mathbf{u} : \Omega \times \mathbb{R}^+ \to \mathbb{R}^d$ and the pressure $p : \Omega \times \mathbb{R}^+ \to \mathbb{R}$ satisfy:

$$\left\{ \begin{array}{rcll} \rho \partial_t \mathbf{u} + \rho \mathbf{u} \cdot \nabla \mathbf{u} - \nabla \cdot \boldsymbol{\sigma}(\mathbf{u}, p) & = & 0, & \text{in } \Omega, \\ \nabla \cdot \mathbf{u} & = & 0, & \text{in } \Omega, \\ \mathbf{u} & = & \mathbf{0}, & \text{on } \partial\Omega, \end{array} \right. \tag{2.1}$$

with the initial conditions $\mathbf{u}(0) = \mathbf{u}_0$. The term $\boldsymbol{\sigma}(\mathbf{u}, p) = -p\mathbf{I} + 2\mu\boldsymbol{\epsilon}(\mathbf{u})$, where $\boldsymbol{\epsilon}(\mathbf{u}) = (\nabla \mathbf{u} + \nabla^T \mathbf{u})/2$, is the fluid stress tensor, and ρ and μ stand for the fluid density and the dynamic viscosity respectively. For the sake of the analysis, homogeneous Dirichlet conditions are enforced on the whole boundary $\partial\Omega$. More realistic boundary conditions are considered in the numerical experiments of Section 3.3 of Chapter 3.

Problem (2.1) can be partitioned into two sub-problems defined in two non-overlapping sub-domains, $\Omega_1 \subset \mathbb{R}^d$ and $\Omega_2 \subset \mathbb{R}^d$, with $\overline{\Omega} = \overline{\Omega}_1 \cup \overline{\Omega}_2$ and $\Omega_1 \cap \Omega_2 = \emptyset$. The two sub-domains are separated by an interface $\Sigma \overset{\text{def}}{=} \partial\Omega_1 \cap \partial\Omega_2$, and $\Gamma_1 \overset{\text{def}}{=} \partial\Omega_1 \backslash \Sigma$, $\Gamma_2 \overset{\text{def}}{=} \partial\Omega_2 \backslash \Sigma$ (Figure 2.1).

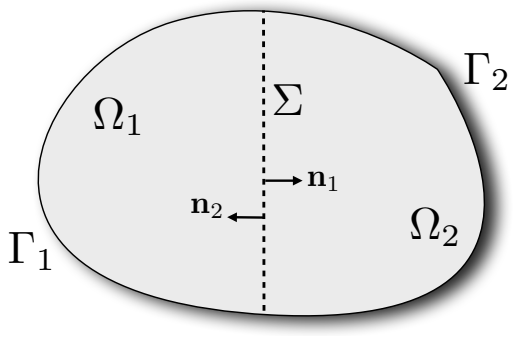

Figure 2.1: *Geometrical description of the fluid domains.*

The new formulation of the problem reads: find the velocity $\mathbf{u}_1 : \Omega_1 \times \mathbb{R}^+ \to \mathbb{R}^d$ and the

pressure $p_1 : \Omega_1 \times \mathbb{R}^+ \to \mathbb{R}$ such that

$$\left\{ \begin{array}{rcll} \rho\partial_t \mathbf{u}_1 + \rho\mathbf{u}_1 \cdot \nabla\mathbf{u}_1 - \nabla \cdot \boldsymbol{\sigma}(\mathbf{u}_1, p_1) & = & 0, & \text{in } \Omega_1, \\ \nabla \cdot \mathbf{u}_1 & = & 0, & \text{in } \Omega_1, \\ \mathbf{u}_1 & = & \mathbf{0}, & \text{on } \Gamma_1, \end{array} \right. \tag{2.2}$$

find the velocity $\mathbf{u}_2 : \Omega_2 \times \mathbb{R}^+ \to \mathbb{R}^d$ and the pressure $p_2 : \Omega_2 \times \mathbb{R}^+ \to \mathbb{R}$, such that

$$\left\{ \begin{array}{rcll} \rho\partial_t \mathbf{u}_2 + \rho(\mathbf{u}_2 \cdot \nabla)\mathbf{u}_2 - \nabla \cdot \boldsymbol{\sigma}(\mathbf{u}_2, p_2) & = & 0, & \text{in } \Omega_2, \\ \nabla \cdot \mathbf{u}_2 & = & 0, & \text{in } \Omega_2, \\ \mathbf{u}_2 & = & \mathbf{0}, & \text{on } \Gamma_2. \end{array} \right. \tag{2.3}$$

The solutions in the two sub-domains are coupled through the usual kinematic and kinetic conditions

$$\left\{ \begin{array}{rcll} \mathbf{u}_1 & = & \mathbf{u}_2, & \text{on } \Sigma, \\ \boldsymbol{\sigma}(\mathbf{u}_2, p_2)\mathbf{n}_2 & = & -\boldsymbol{\sigma}(\mathbf{u}_1, p_1)\mathbf{n}_1, & \text{on } \Sigma, \end{array} \right. \tag{2.4}$$

with $\mathbf{n}_1$, $\mathbf{n}_2$ the outward-pointing unit normal vectors on $\partial\Omega_1$ and $\partial\Omega_2$ respectively.

2.3 Dirichlet-Neumann coupling scheme

To fix the ideas we consider the time semi-discretized formulation of the previous models. A backward Euler scheme is used and the non-linear terms are linearized with a standard semi-implicit approach. The time derivatives in (2.1)-(2.3) are replaced by $\partial_{\delta t} x^n \stackrel{\text{def}}{=} (x^n - x^{n-1})/\delta t$, where $\delta t \stackrel{\text{def}}{=} T/N$ denotes the step size, the interval of interest is $(0, T)$, $N \in \mathbb{N}^+$ is a given integer and $x^n \approx x(n\delta t)$ with $0 \leq n \leq N$.

The fluid model (2.1) is discretized as:

$$\left\{ \begin{array}{rcll} \rho\partial_{\delta t} \mathbf{u}^n + \rho\mathbf{u}^{n-1} \cdot \nabla\mathbf{u}^n - \nabla \cdot \boldsymbol{\sigma}(\mathbf{u}^n, p^n) & = & 0, & \text{in } \Omega, \\ \nabla \cdot \mathbf{u}^n & = & 0, & \text{in } \Omega, \\ \mathbf{u}^n & = & \mathbf{0}, & \text{on } \partial\Omega \end{array} \right. \tag{2.5}$$

Hence, the corresponding coupled problem discretized in time results, for the first fluid model

$$\left\{ \begin{array}{rcll} \rho\partial_{\delta t} \mathbf{u}_1^n + \rho\mathbf{u}_1^{n-1} \cdot \nabla\mathbf{u}_1^n - \nabla \cdot \boldsymbol{\sigma}(\mathbf{u}_1^n, p_1^n) & = & 0, & \text{in } \Omega_1, \\ \nabla \cdot \mathbf{u}_1^n & = & 0, & \text{in } \Omega_1, \\ \mathbf{u}_1^n & = & \mathbf{0}, & \text{on } \Gamma_1, \end{array} \right. \tag{2.6}$$

likewise, for the second fluid model we have

$$\left\{ \begin{array}{rcll} \rho\partial_{\delta t} \mathbf{u}_2^n + \rho\mathbf{u}_2^{n-1} \cdot \nabla\mathbf{u}_2^n - \nabla \cdot \boldsymbol{\sigma}(\mathbf{u}_2^n, p_2^n) & = & 0, & \text{in } \Omega_2, \\ \nabla \cdot \mathbf{u}_2^n & = & 0, & \text{in } \Omega_2, \\ \mathbf{u}_2^n & = & \mathbf{0}, & \text{on } \Gamma_2. \end{array} \right. \tag{2.7}$$

The time discretization of the transmission conditions on Σ determines the implicit or explicit character of the coupling scheme.

2.3.1 Implicit interface treatment

The scheme is called implicit or strongly coupled scheme if (2.4) is enforced exactly at each time-step. The transmission condition on Σ are discretized as follow:

$$\left\{\begin{array}{rcll} \mathbf{u}_1^n & = & \mathbf{u}_2^n, & \text{on } \Sigma, \\ \boldsymbol{\sigma}(\mathbf{u}_2^n, p_2^n)\mathbf{n}_2 & = & -\boldsymbol{\sigma}(\mathbf{u}_1^n, p_1^n)\mathbf{n}_1, & \text{on } \Sigma. \end{array}\right. \tag{2.8}$$

Such transmission conditions amount to solve the monolithic problem (2.5), obtained by the time-discretization of (2.1). It is summarized in Algorithm 2.1.

ALGORITHM 2.1 (Monolithic fluid problem: static pressure formulation)

1. *Advance in time fluid problem* (2.1) *in the whole domain* Ω*;*
2. *Go to next time-step.*

The payoff of this scheme is that the Algorithm 2.1 yields a highly coupled system at each time-step.

2.3.2 Explicit interface treatment

The schemes whose coupling conditions are explicitly treated are called weakly or loosely coupled schemes. The following discretization on Σ is considered:

$$\left\{\begin{array}{rcll} \mathbf{u}_1^n & = & \mathbf{u}_2^{n-1}, & \text{on } \Sigma, \\ \boldsymbol{\sigma}(\mathbf{u}_2^n, p_2^n)\mathbf{n}_2 & = & -\boldsymbol{\sigma}(\mathbf{u}_1^n, p_1^n)\mathbf{n}_1, & \text{on } \Sigma. \end{array}\right. \tag{2.9}$$

Note the explicit treatment of the interface terms in (2.9), since the fluid 1 and fluid 2 velocities do not match at interface, indeed we have $\mathbf{u}_1^n = \mathbf{u}_2^{n-1} \neq \mathbf{u}_2^n$ on Σ. This uncoupled scheme is summarized in Algorithm 2.2.

ALGORITHM 2.2 (Explicit Dirichlet-Neumann fluid-fluid model)

1. *Advance in time fluid problem* (2.6) *in sub-domain* Ω_1 *with the Dirichlet condition* $(2.9)_1$*;*
2. *Advance in time fluid problem* (2.7) *in sub-domain* Ω_2 *with the Neumann condition* $(2.9)_2$*;*
3. *Go to next time-step.*

This procedure is particularly appealing in terms of computational cost, since allow

a sequential computation of $(\mathbf{u}_1^n, p_1^n)$ and $(\mathbf{u}_2^n, p_2^n)$, but this kind of coupling generates pressure instabilities at interface that can not be controlled. An example is reported in Section 3.2.1 in the next chapter. Similar instability also arise using Dirichlet-Neumann explicit scheme in fluid-structure interaction problems, in which the pressure instabilities are generated by the so called add-mass effect (see [CGN05, FWR07]), when fluid and solid density are comparable.

In the next sections we propose alternative splitting schemes with enhanced stability property.

2.4 Space discretization with Nitsche's interface method

The time splitting schemes introduced in the following sections are derived from a space semi-discrete formulation of (2.2)-(2.4) based on Nitsche's interface method (see, e.g., [Han05, BHS03]). In other words, conforming finite element approximations are used in each sub-system, which do not match at the interface, and the interface coupling (2.4) is enforced in a consistent fashion *à la* Nitsche. A salient feature of this approach, compared to a standard conforming finite element approximation, is that the artificial interface power, generated by the time splitting of the interface coupling, can be controlled directly by the consistent numerical dissipation of interface Nitsche's method (see [BF09, BF14]).

Nitsche's method, originally proposed to weakly enforce Dirichlet boundary conditions in elliptic problems (see [Nit71]), has been extended to a number of interface problems arising in computational mechanics (see, e.g., [Han05] for a review), including domain decomposition [BHS03], Stokes-Darcy coupling [BH07], elliptic-hyperbolic problems [BZ06], fluid-structure interaction [HH03, HHS04, BF09, BF14] and, more recently, interface problems with unfitted meshes (see, e.g., [HHL03, MLLR14, BF13]).

2.4.1 Monolithic formulation

Let be $\{\mathcal{T}_{1,h}\}_{0\leq h\leq 1}$ and $\{\mathcal{T}_{2,h}\}_{0\leq h\leq 1}$ two families of regular finite element triangulation for Ω_1 and Ω_2 respectively, with typical diameter h. Let $W_{i,h} \times Q_{i,h}$ denote an inf-sup stable, conforming finite element approximations of $[H^1(\Omega_i)]^d \times L^2(\Omega_i)$ for $i = 1, 2$. Let $V_{1,h} = W_{1,h} \cap [H^1_{\Gamma_1}(\Omega_1)]^d$ and $V_{2,h} = W_{2,h} \cap [H^1_{\Gamma_2}(\Omega_2)]^d$, where $H^1_\gamma(\Omega_i)$ denotes the space of $H^1(\Omega_i)-$functions vanishing on a part γ of $\partial\Omega_i$.

The considered space semi-discrete formulation of problem (2.2)-(2.4) reads: for all $t > 0$, find $(\mathbf{u}_{1,h},\ p_{1,h},\ \mathbf{u}_{2,h},\ p_{2,h}) \in W_{1,h} \times Q_{1,h} \times W_{2,h} \times Q_{2,h}$ satisfying the essential boundary conditions and such that

$$
\begin{aligned}
&A_1[\mathbf{u}_{1,h}; (\mathbf{u}_{1,h}, p_{1,h}), (\mathbf{v}_{1,h}, q_{1,h})] + A_2[\mathbf{u}_{2,h}; (\mathbf{u}_{2,h}, p_{2,h}), (\mathbf{v}_{2,h}, q_{2,h})] \\
&\quad + C_1[\mathbf{u}_{1,h}; (\mathbf{u}_{1,h}, \mathbf{u}_{2,h}), \mathbf{v}_{1,h}] + C_2[(\mathbf{u}_{2,h}, \mathbf{u}_{1,h}); (\mathbf{u}_{2,h}, \mathbf{u}_{1,h}), \mathbf{v}_{2,h}] \\
&\quad + \frac{\gamma\mu}{h} \int_\Sigma (\mathbf{u}_{2,h} - \mathbf{u}_{1,h}) \cdot (\mathbf{v}_{2,h} - \mathbf{v}_{1,h}) - \int_\Sigma \boldsymbol{\sigma}(\mathbf{u}_{2,h}, p_{2,h})\mathbf{n}_2 \cdot (\mathbf{v}_{2,h} - \mathbf{v}_{1,h}) \\
&\quad - \int_\Sigma (\mathbf{u}_{2,h} - \mathbf{u}_{1,h}) \cdot \mathbf{n}_2 q_{2,h} = 0,
\end{aligned}
\tag{2.10}
$$

for all $(\mathbf{v}_{1,h},\ q_{1,h},\ \mathbf{v}_{2,h},\ q_{2,h}) \in V_{1,h} \times Q_{1,h} \times V_{2,h} \times Q_{2,h}$, where

$$\begin{aligned} A_1[\mathbf{u}_{1,h};(\mathbf{u}_{1,h},p_{1,h}),(\mathbf{v}_{1,h},q_{1,h})] \overset{\text{def}}{=}\ & \rho\int_{\Omega_1}\partial_t\mathbf{u}_{1,h}\cdot\mathbf{v}_{1,h}+\int_{\Omega_1}2\mu\boldsymbol{\epsilon}(\mathbf{u}_{1,h}):\boldsymbol{\epsilon}(\mathbf{v}_{1,h}) \\ & -\int_{\Omega_1}p_{1,h}\nabla\cdot\mathbf{v}_{1,h}+\int_{\Omega_1}q_{1,h}\nabla\cdot\mathbf{u}_{1,h} \\ & +\rho\int_{\Omega_1}(\mathbf{u}_{1,h}\cdot\nabla\mathbf{u}_{1,h})\cdot\mathbf{v}_{1,h}, \end{aligned} \tag{2.11}$$

$$\begin{aligned} A_2[\mathbf{u}_{2,h};(\mathbf{u}_{2,h},p_{2,h}),(\mathbf{v}_{2,h},q_{2,h})] \overset{\text{def}}{=}\ & \rho\int_{\Omega_2}\partial_t\mathbf{u}_{2,h}\cdot\mathbf{v}_{2,h}+\int_{\Omega_2}2\mu\boldsymbol{\epsilon}(\mathbf{u}_{2,h}):\boldsymbol{\epsilon}(\mathbf{v}_{2,h}) \\ & -\int_{\Omega_2}p_{2,h}\nabla\cdot\mathbf{v}_{2,h}+\int_{\Omega_2}q_{2,h}\nabla\cdot\mathbf{u}_{2,h} \\ & +\rho\int_{\Omega_2}(\mathbf{u}_{2,h}\cdot\nabla\mathbf{u}_{2,h})\cdot\mathbf{v}_{2,h}, \end{aligned} \tag{2.12}$$

and the two terms C_1 and C_2 are defined by:

$$C_1[\mathbf{u};(\mathbf{w},\mathbf{z}),\mathbf{v}] \overset{\text{def}}{=} \frac{\rho}{2}\int_{\Omega_1}(\nabla\cdot\mathbf{u})\mathbf{w}\cdot\mathbf{v}+\frac{\rho}{2}\int_{\Sigma}\mathbf{u}\cdot\mathbf{n}_1(\mathbf{z}-\mathbf{w})\cdot\mathbf{v}, \tag{2.13}$$

$$\begin{aligned} C_2[(\mathbf{u},\boldsymbol{\xi});(\mathbf{w},\mathbf{z}),\mathbf{v}] \overset{\text{def}}{=}\ & \frac{\rho}{2}\int_{\Omega_2}(\nabla\cdot\mathbf{u})\mathbf{w}\cdot\mathbf{v}-\frac{\rho}{2}\int_{\Sigma}(\mathbf{u}\cdot\mathbf{n}_2)(\mathbf{w}\cdot\mathbf{v}) \\ & +\frac{\rho}{2}\int_{\Sigma}(\boldsymbol{\xi}\cdot\mathbf{n}_2)(\mathbf{z}\cdot\mathbf{v}). \end{aligned} \tag{2.14}$$

The first integral in (2.13) and (2.14) is nothing but the standard Temam's trick (see, e.g., [Tem68, Tem79]). The remaining interface terms are also strongly consistent terms, which are introduced to handle the convective energy contributions related to the discontinuous nature of the discrete solution on the interface.

The last three interface terms of (2.10) enforce the interface conditions (2.4) weakly, in a strongly consistent fashion, *à la* Nitsche. The interface stress term $-\int_\Sigma\boldsymbol{\sigma}(\mathbf{u}_{2,h},p_{2,h})\mathbf{n}_2\cdot(\mathbf{v}_{2,h}-\mathbf{v}_{1,h})$ results from the integration by parts in each subdomain and the application of the relation $(2.4)_2$. The remaining contributions, $\frac{\gamma\mu}{h}\int_\Sigma(\mathbf{u}_{2,h}-\mathbf{u}_{1,h})\cdot(\mathbf{v}_{2,h}-\mathbf{v}_{1,h})$ and $-\int_\Sigma(\mathbf{u}_{2,h}-\mathbf{u}_{1,h})\cdot\mathbf{n}_2 q_{2,h}$, are strongly consistent stabilization terms (thanks to $(2.4)_1$) which guarantee the stability of the resulting formulation. The dimensionless parameter $\gamma>0$ is chosen to ensure coercivity (see Lemma 2.1).

REMARK 2.1

The sixth term in (2.10), involving the stress tensor on the interface, is computed with the Fluid 2 variables. It could be replaced by

$$-\int_\Sigma\boldsymbol{\sigma}(\mathbf{u}_{1,h},p_{1,h})\mathbf{n}_1(\mathbf{v}_{1,h}-\mathbf{v}_{2,h}),$$

i.e. computed with Fluid 1 variables, without compromising the stability of the method. In

this case the seventh term (2.10) would be

$$\int_{\Omega_1} q_{1,h} \nabla \cdot \mathbf{u}_{1,h} = -\int_{\Sigma} (\mathbf{u}_{1,h} - \mathbf{u}_{2,h}) \cdot \mathbf{n}_1 q_{1,h}.$$

We could also consider a convex combination of both.

REMARK 2.2
This monolithic scheme is very similar to Discontinuous Galerkin formulations (see for example [GRW05] or the monography [DPE11, chap. 6]). The main contribution of this chapter is the partitioned schemes proposed below. For the sake of completeness, the stability analysis of the monolithic formulation is reminded in the next section.

2.4.1.1 Stability analysis

The following lemma shows the stability in the energy norm of the semi-discrete problem (2.10). It makes use of the standard local inverse trace inequality (see [Tho06] e.g.): for all $K \in \{\mathcal{T}_h\}_{h>0}$,

$$||\mathbf{u}_h||^2_{\partial K} \leq C_T h^{-1} ||\mathbf{u}_h||^2_K \qquad \forall\, \mathbf{u}_h \in W_h, \tag{2.15}$$

where $||\cdot||_K$ denotes the $L^2(K)$-norm.

LEMMA 2.1
Let $(\mathbf{u}_{1,h}, p_{1,h}, \mathbf{u}_{2,h}, p_{2,h})$ be solution of (2.10). If

$$\gamma > 2C_T, \tag{2.16}$$

where $C_T > 0$ is defined in (2.15), the following estimate holds

$$\frac{\rho}{2}\left(||\mathbf{u}_{1,h}(t)||^2_{\Omega_1} + ||\mathbf{u}_{2,h}(t)||^2_{\Omega_2}\right) + \frac{3\mu}{4}\int_0^t \left(||\boldsymbol{\epsilon}(\mathbf{u}_{1,h})||^2_{\Omega_1} + ||\boldsymbol{\epsilon}(\mathbf{u}_{2,h})||^2_{\Omega_2}\right)$$
$$+\frac{3\gamma\mu}{4h}\int_0^t ||\mathbf{u}_{2,h} - \mathbf{u}_{1,h}||^2_{\Sigma} \leq \frac{\rho}{2}(||\mathbf{u}_{1,h}(0)||^2_{\Omega_1} + ||\mathbf{u}_{2,h}(0)||^2_{\Omega_2}).$$

Proof. Taking $(\mathbf{v}_{1,h}, q_{1,h}, \mathbf{v}_{2,h}, q_{2,h}) = (\mathbf{u}_{1,h}, p_{1,h}, \mathbf{u}_{2,h}, p_{2,h})$ in A_1 and A_2 yields

$$\begin{aligned} A_1[\mathbf{u}_{1,h}; (\mathbf{u}_{1,h}, p_{1,h}), (\mathbf{u}_{1,h}, p_{1,h})] \;=\; & \frac{\rho}{2}\frac{d}{dt}||\mathbf{u}_{1,h}||^2_{\Omega_1} + 2\mu||\boldsymbol{\epsilon}(\mathbf{u}_{1,h})||^2_{\Omega_1} \\ & -\frac{\rho}{2}\int_{\Omega_1}(\nabla\cdot\mathbf{u}_{1,h})|\mathbf{u}_{1,h}|^2 + \frac{\rho}{2}\int_{\Sigma}(\mathbf{u}_{1,h}\cdot\mathbf{n}_1)|\mathbf{u}_{1,h}|^2 \end{aligned} \tag{2.17}$$

$$A_2[\mathbf{u}_{2,h};(\mathbf{u}_{2,h},p_{2,h}),(\mathbf{u}_{2,h},p_{2,h})] = \frac{\rho}{2}\frac{d}{dt}||\mathbf{u}_{2,h}||^2_{\Omega_2} + 2\mu||\boldsymbol{\epsilon}(\mathbf{u}_{2,h})||^2_{\Omega_2} - \frac{\rho}{2}\int_{\Omega_2}(\nabla\cdot\mathbf{u}_{2,h})|\mathbf{u}_{2,h}|^2 + \frac{\rho}{2}\int_{\Sigma}(\mathbf{u}_{2,h}\cdot\mathbf{n}_2)|\mathbf{u}_{2,h}|^2. \tag{2.18}$$

In addition, for the terms C_1 and C_2 we have

$$C_1[\mathbf{u}_{1,h};(\mathbf{u}_{1,h},\mathbf{u}_{2,h}),\mathbf{u}_{1,h}] = \frac{\rho}{2}\int_{\Omega_1}(\nabla\cdot\mathbf{u}_{1,h})|\mathbf{u}_{1,h}|^2 + \frac{\rho}{2}\int_{\Sigma}(\mathbf{u}_{1,h}\cdot\mathbf{n}_1)(\mathbf{u}_{2,h}\cdot\mathbf{u}_{1,h} - |\mathbf{u}_{1,h}|^2), \tag{2.19}$$

$$C_2[(\mathbf{u}_{2,h},\mathbf{u}_{1,h});(\mathbf{u}_{2,h},\mathbf{u}_{1,h}),\mathbf{u}_{2,h}] = \frac{\rho}{2}\int_{\Omega_2}(\nabla\cdot\mathbf{u}_{2,h})|\mathbf{u}_{2,h}|^2 - \frac{\rho}{2}\int_{\Sigma}(\mathbf{u}_{2,h}\cdot\mathbf{n}_2)|\mathbf{u}_{2,h}|^2 + \frac{\rho}{2}\int_{\Sigma}(\mathbf{u}_{1,h}\cdot\mathbf{n}_2)(\mathbf{u}_{1,h}\cdot\mathbf{u}_{2,h}). \tag{2.20}$$

Hence by inserting (2.17)–(2.20) into (2.10) we get the following energy equality

$$\frac{\rho}{2}\frac{d}{dt}(||\mathbf{u}_{1,h}||^2_{\Omega_1} + ||\mathbf{u}_{2,h}||^2_{\Omega_2}) + 2\mu\left(||\boldsymbol{\epsilon}(\mathbf{u}_{1,h})||^2_{\Omega_1} + ||\boldsymbol{\epsilon}(\mathbf{u}_{2,h})||^2_{\Omega_2}\right) + \frac{\gamma\mu}{h}||\mathbf{u}_{2,h}-\mathbf{u}_{1,h}||^2_{\Sigma} = 2\mu\int_{\Sigma}\boldsymbol{\epsilon}(\mathbf{u}_{2,h})\mathbf{n}_2\cdot(\mathbf{u}_{2,h}-\mathbf{u}_{1,h}). \tag{2.21}$$

The right-hand side of (2.21) is first treated with the Young's inequality and with the local inverse trace inequality (2.15):

$$2\mu\int_{\Sigma}\boldsymbol{\epsilon}(\mathbf{u}_{2,h})\mathbf{n}_2\cdot(\mathbf{u}_{2,h}-\mathbf{u}_{1,h}) \leq \frac{4\mu C_T}{\gamma}||\boldsymbol{\epsilon}(\mathbf{u}_{2,h})||^2_{\Omega_2} + \frac{\mu\gamma}{4h}||\mathbf{u}_{2,h}-\mathbf{u}_{1,h}||^2_{\Sigma}.$$

Using this inequality in (2.21) and integrating over $(0,t)$, it gives:

$$\frac{\rho}{2}\left(||\mathbf{u}_{1,h}(t)||^2_{\Omega_1} + ||\mathbf{u}_{2,h}(t)||^2_{\Omega_2}\right) + 2\mu\int_0^t||\boldsymbol{\epsilon}(\mathbf{u}_{1,h})||^2_{\Omega_1} + 2\mu\left(1-\frac{2C_T}{\gamma}\right)\int_0^t||\boldsymbol{\epsilon}(\mathbf{u}_{2,h})||^2_{\Omega_2} + \frac{3\gamma\mu}{4h}\int_0^t||\mathbf{u}_{2,h}-\mathbf{u}_{1,h}||^2_{\Sigma} \leq \frac{\rho}{2}(||\mathbf{u}_{1,h}(0)||^2_{\Omega_1} + ||\mathbf{u}_{2,h}(0)||^2_{\Omega_2}).$$

The last result, with condition (2.16), completes the proof. ■

2.4.2 Partitioned formulation

Our goal is to devise an algorithm that yields separate solutions in domain Ω_1 and Ω_2 via suitable transmission conditions on the interface Σ. Taking first $(\mathbf{v}_{2,h}, q_{2,h}) = (\mathbf{0}, 0)$ and

then $(\mathbf{v}_{1,h}, q_{1,h}) = (\mathbf{0}, 0)$, the monolithic formulation (2.10) can be split in two coupled sub-problems:

1. Fluid sub-problem 1: Given $(\mathbf{u}_{2,h},\, p_{2,h}) \in W_{2,h} \times Q_{2,h}$, find $(\mathbf{u}_{1,h},\, p_{1,h}) \in W_{1,h} \times Q_{1,h}$ such that

$$A_1[\mathbf{u}_{1,h}; (\mathbf{u}_{1,h}, p_{1,h}), (\mathbf{v}_{1,h}, q_{1,h})] + C_1[\mathbf{u}_{1,h}; (\mathbf{u}_{1,h}, \mathbf{u}_{2,h}), \mathbf{v}_{1,h}] + \frac{\gamma\mu}{h}\int_\Sigma (\mathbf{u}_{1,h} - \mathbf{u}_{2,h}) \cdot \mathbf{v}_{1,h} + \int_\Sigma \boldsymbol{\sigma}(\mathbf{u}_{2,h}, p_{2,h})\mathbf{n}_2 \cdot \mathbf{v}_{1,h} = 0$$

   for all $(\mathbf{v}_{1,h},\, p_{1,h}) \in V_{1,h} \times Q_{1,h}$.

2. Fluid sub-problem 2: Given $(\mathbf{u}_{1,h},\, p_{1,h}) \in W_{1,h} \times Q_{1,h}$, find $(\mathbf{u}_{2,h},\, p_{2,h}) \in W_{2,h} \times Q_{2,h}$ such that

$$A_2[\mathbf{u}_{2,h}; (\mathbf{u}_{2,h}, p_{2,h}), (\mathbf{v}_{2,h}, q_{2,h})] + C_2[(\mathbf{u}_{2,h}, \mathbf{u}_{1,h}); (\mathbf{u}_{2,h}, \mathbf{u}_{1,h}), \mathbf{v}_{2,h}] + \frac{\gamma\mu}{h}\int_\Sigma (\mathbf{u}_{2,h} - \mathbf{u}_{1,h}) \cdot \mathbf{v}_{2,h} - \int_\Sigma \boldsymbol{\sigma}(\mathbf{u}_{2,h}, p_{2,h})\mathbf{n}_2 \cdot \mathbf{v}_{2,h} - \int_\Sigma (\mathbf{u}_{2,h} - \mathbf{u}_{1,h}) \cdot \mathbf{n}_2 q_{2,h} = 0$$

   for all $(\mathbf{v}_{2,h},\, p_{2,h}) \in W_{2,h} \times Q_{2,h}$.

Note that, as in the standard Nitsche's method, all the interface terms are evaluated using face-wise integration. This partitioned formulation is the basis of the staggered algorithms presented in the next section.

Monolithic methods are, by construction, less modular than partitioned approaches and do not allow the use of legacy software. Partitioned methods, on the contrary, facilitate the reuse of existing code. Moreover, because of their inherent modularity, new models and numerical schemes can be introduced while keeping everything else the same.

2.5 Time-discretization: fully discrete formulations of the Nitsche's interface method

The present section is devoted to the time discretization of formulation (2.10). With the same notation introduced in Section 2.3 on page 36, i.e. backward Euler scheme and semi-implicit approach for the non-linear terms, the two discrete counterparts of operators A_1 and A_2 are defined by:

$$\begin{aligned} A_{1,\delta t}[\mathbf{u}_{1,h}^{n-1}; (\mathbf{u}_{1,h}^n, p_{1,h}^n), (\mathbf{v}_{1,h}, q_{1,h})] \overset{\text{def}}{=}\ & \rho\int_{\Omega_1} \partial_{\delta t}\mathbf{u}_{1,h}^n \cdot \mathbf{v}_{1,h} + 2\mu\int_{\Omega_1} \boldsymbol{\epsilon}(\mathbf{u}_{1,h}^n) : \boldsymbol{\epsilon}(\mathbf{v}_{1,h}) \\ & - \int_{\Omega_1} p_{1,h}^n \nabla\cdot\mathbf{v}_{1,h} + \int_{\Omega_1} q_{1,h}\nabla\cdot\mathbf{u}_{1,h}^n \\ & + \rho\int_{\Omega_1} (\mathbf{u}_{1,h}^{n-1}\cdot\nabla\mathbf{u}_{1,h}^n)\cdot\mathbf{v}_{1,h}, \end{aligned} \tag{2.22}$$

$$A_{2,\delta t}[\mathbf{u}_{2,h}^{n-1};(\mathbf{u}_{2,h}^{n},p_{2,h}^{n}),(\mathbf{v}_{2,h},q_{2,h})] \overset{\text{def}}{=} \rho\int_{\Omega_2}\partial_{\delta t}\mathbf{u}_{2,h}^{n}\mathbf{v}_{2,h}+2\mu\int_{\Omega_2}\boldsymbol{\epsilon}(\mathbf{u}_{2,h}^{n}):\boldsymbol{\epsilon}(\mathbf{v}_{2,h}) - \int_{\Omega_2}p_{2,h}^{n}\nabla\cdot\mathbf{v}_{2,h}+\int_{\Omega_2}q_{2,h}\nabla\cdot\mathbf{u}_{2,h}^{n} +\rho\int_{\Omega_2}(\mathbf{u}_{2,h}^{n-1}\cdot\nabla\mathbf{u}_{2,h}^{n})\cdot\mathbf{v}_{2,h}. \tag{2.23}$$

2.5.1 Implicit coupling

Before addressing the case of a staggered time-stepping, we start with the study of a monolithic scheme where the two sub-problems are solved simultaneously at each time instant t^n: find $(\mathbf{u}_{1,h}^{n},p_{1,h}^{n},\mathbf{u}_{2,h}^{n},p_{2,h}^{n})\in W_{1,h}\times Q_{1,h}\times W_{2,h}\times Q_{2,h}$ satisfying the essential boundary conditions and such that

$$\begin{aligned}&A_{1,\delta t}[\mathbf{u}_{1,h}^{n-1};(\mathbf{u}_{1,h}^{n},p_{1,h}^{n}),(\mathbf{v}_{1,h},q_{1,h})]+A_{2,\delta t}[\mathbf{u}_{2,h}^{n-1};(\mathbf{u}_{2,h}^{n},p_{2,h}^{n}),(\mathbf{v}_{2,h},q_{2,h})]+\\&+C_1[\mathbf{u}_{1,h}^{n-1};(\mathbf{u}_{1,h}^{n},\mathbf{u}_{2,h}^{n}),\mathbf{v}_{1,h}]+C_2[(\mathbf{u}_{2,h}^{n-1},\mathbf{u}_{1,h}^{n-1});(\mathbf{u}_{2,h}^{n},\mathbf{u}_{1,h}^{n}),\mathbf{v}_{1,h}]\\&+\frac{\gamma\mu}{h}\int_\Sigma(\mathbf{u}_{2,h}^{n}-\mathbf{u}_{1,h}^{n})\cdot(\mathbf{v}_{2,h}-\mathbf{v}_{1,h})-\int_\Sigma\boldsymbol{\sigma}(\mathbf{u}_{2,h}^{n},p_{2,h}^{n})\mathbf{n}_2\cdot(\mathbf{v}_{2,h}-\mathbf{v}_{1,h})\\&-\int_\Sigma(\mathbf{u}_{2,h}^{n}-\mathbf{u}_{1,h}^{n})\cdot\mathbf{n}_2q_{2,h}=0,\end{aligned} \tag{2.24}$$

for all $(\mathbf{v}_{1,h},q_{1,h},\mathbf{v}_{2,h},q_{2,h})\in V_{1,h}\times Q_{1,h}\times V_{2,h}\times Q_{2,h}$.

For the sake of conciseness, the strain rate tensors at time t^n are denoted by $\boldsymbol{\epsilon}_{1,h}^{m}\overset{\text{def}}{=}\boldsymbol{\epsilon}(\mathbf{u}_{1,h}^{m})$ and $\boldsymbol{\epsilon}_{2,h}^{m}\overset{\text{def}}{=}\boldsymbol{\epsilon}(\mathbf{u}_{2,h}^{m})$ and the following quantities are introduced:

$$\begin{aligned}E^n &\overset{\text{def}}{=} \frac{\rho}{2}\left(||\mathbf{u}_{1,h}^{n}||_{\Omega_1}^2+||\mathbf{u}_{2,h}^{n}||_{\Omega_2}^2\right)+\frac{3\gamma\mu}{4h}\delta t\sum_{m=1}^{n}||\mathbf{u}_{2,h}^{m}-\mathbf{u}_{1,h}^{m}||_\Sigma^2\\&\quad+\frac{2\mu}{3}\delta t\sum_{m=1}^{n}||\boldsymbol{\epsilon}_{1,h}^{m}||_{\Omega_1}^2+\frac{2\mu}{3}\delta t\sum_{m=1}^{n}||\boldsymbol{\epsilon}_{2,h}^{m}||_{\Omega_2}^2,\end{aligned} \tag{2.25}$$

$$E^0 \overset{\text{def}}{=} \frac{\rho}{2}\left(||\mathbf{u}_{1,h}^{0}||_{\Omega_1}^2+||\mathbf{u}_{2,h}^{0}||_{\Omega_2}^2\right). \tag{2.26}$$

The next proposition shows that this monolithic algorithm is stable without any condition on the discretization steps.

PROPOSITION 2.1
Let $(\mathbf{u}_{1,h}^{n},p_{1,h}^{n},\mathbf{u}_{2}^{n},p_{2}^{n})$ be the solution of the monolithic scheme (2.24). If

$$\gamma\geq 2C_T, \tag{2.27}$$

where $C_T>0$ is the constant of the inverse inequality (2.15), then

$$E^n\leq E^0.$$

Proof. The proof follows the same steps as the proof of Lemma 2.1. Choosing $(\mathbf{v}_{1,h}, q_{1,h}, \mathbf{v}_{2,h}, q_{2,h}) = (\mathbf{u}_{1,h}^n, p_{1,h}^n, \mathbf{u}_{2,h}^n, p_{2,h}^n)$ in (2.24), the interface terms resulting from the integration by parts of the advection in (2.22) and (2.23) cancel with interface stabilization terms (2.13) and (2.14). Then summing over $1 \leq m \leq n$ and multiplying by δt, we obtain:

$$
\begin{aligned}
&\frac{\rho}{2}\sum_{m=1}^{n}\left(||\mathbf{u}_{1,h}^m||_{\Omega_1}^2 - ||\mathbf{u}_{1,h}^{m-1}||_{\Omega_1}^2\right) + \frac{\rho}{2}\sum_{m=1}^{n}||\mathbf{u}_{1,h}^m - \mathbf{u}_{1,h}^{m-1}||_{\Omega_1}^2 + 2\mu\delta t\sum_{m=1}^{n}||\boldsymbol{\epsilon}_{1,h}^m||_{\Omega_1}^2 \\
&+\frac{\rho}{2}\sum_{m=1}^{n}\left(||\mathbf{u}_{2,h}^m||_{\Omega_2}^2 - ||\mathbf{u}_{2,h}^{m-1}||_{\Omega_2}^2\right) + \frac{\rho}{2}\sum_{m=1}^{n}||\mathbf{u}_{2,h}^m - \mathbf{u}_{2,h}^{m-1}||_{\Omega_2}^2 + 2\mu\delta t\sum_{m=1}^{n}||\boldsymbol{\epsilon}_{2,h}^m||_{\Omega_2}^2 \\
&+\frac{\gamma\mu}{h}\delta t\sum_{m=1}^{n}||\mathbf{u}_{2,h}^m - \mathbf{u}_{1,h}^m||_{\Sigma}^2 \\
&\leq \frac{4\mu C_T}{\gamma}\delta t\sum_{m=1}^{n}||\boldsymbol{\epsilon}_{2,h}^m||_{\Omega_2}^2 + \frac{\mu\gamma}{4h}\delta t\sum_{m=1}^{n}||\mathbf{u}_{2,h}^m - \mathbf{u}_{1,h}^m||_{\Sigma}^2,
\end{aligned}
$$

which can be reformulated as

$$
\begin{aligned}
&\frac{\rho}{2}\left(||\mathbf{u}_{1,h}^n||_{\Omega_1}^2 + ||\mathbf{u}_{2,h}^n||_{\Omega_2}^2\right) + 2\mu\delta t\sum_{m=1}^{n}||\boldsymbol{\epsilon}_{1,h}^m||_{\Omega_1}^2 \\
&+2\mu\left(1 - \frac{2C_T}{\gamma}\right)\delta t\sum_{m=1}^{n}||\boldsymbol{\epsilon}_{2,h}^m||_{\Omega_2}^2 + \frac{3\gamma\mu}{4h}\delta t\sum_{m=1}^{n}||\mathbf{u}_{2,h}^m - \mathbf{u}_{1,h}^m||_{\Sigma}^2 \\
&\leq -\frac{\rho}{2}\delta t\left(\sum_{m=1}^{n}||\mathbf{u}_{1,h}^m - \mathbf{u}_{1,h}^{m-1}||_{\Omega_1}^2 + \sum_{m=1}^{n}||\mathbf{u}_{2,h}^m - \mathbf{u}_{2,h}^{m-1}||_{\Omega_2}^2\right) \\
&+\frac{\rho}{2}(||\mathbf{u}_{1,h}^0||_{\Omega_1}^2 + ||\mathbf{u}_{2,h}^0||_{\Omega_2}^2),
\end{aligned}
$$

The last result, under the condition (2.27), completes the proof . ∎

2.5.2 Explicit coupling: a static pressure formulation

The monolithic scheme (2.24) involves the simultaneous computation of $(\mathbf{u}_{1,h}^n, p_{1,h}^n)$ and $(\mathbf{u}_{2,h}^n, p_{2,h}^n)$. In this section, a first staggered scheme (Algorithm 2.3) is proposed to solve problem (2.10). This method generalizes the explicit coupling schemes introduced in [BF09, BF14] for incompressible fluid-structure interaction.

As shown in Proposition 2.2, we are not able to prove its stability. We nevertheless present it because it allows us to introduce the main ideas that will be useful in the next section. In addition, this scheme was stable in most of the numerical simulations where it was tested (see Section 3.3.3 on page 68 in Chapter 3).

ALGORITHM 2.3 (Staggered scheme with static pressure)

1. *Find* $(\mathbf{u}_{1,h}^n, p_{1,h}^n) \in W_{1,h} \times Q_{1,h}$ *satisfying the essential boundary conditions and such that*

$$A_{1,\delta t}[\mathbf{u}_{1,h}^{n-1}; (\mathbf{u}_{1,h}^n, p_{1,h}^n), (\mathbf{v}_{1,h}, q_{1,h})] + C_1[\mathbf{u}_{1,h}^{n-1}; (\mathbf{u}_{1,h}^n, \mathbf{u}_{2,h}^{n-1}), \mathbf{v}_{1,h}] + \frac{\gamma\mu}{h}\int_\Sigma (\mathbf{u}_{1,h}^n - \mathbf{u}_{2,h}^{n-1}) \cdot \mathbf{v}_{1,h} + \int_\Sigma \boldsymbol{\sigma}(\mathbf{u}_{2,h}^{n-1}, p_{2,h}^{n-1}) \cdot \mathbf{n}_2 \mathbf{v}_{1,h} = 0, \tag{2.28}$$

   for all $(\mathbf{v}_{1,h}, q_{1,h}) \in V_{1,h} \times Q_{1,h}$.

2. *Find* $(\mathbf{u}_{2,h}^n, p_{2,h}^n) \in W_{2,h} \times Q_{2,h}$ *satisfying the essential boundary conditions and such that*

$$\begin{aligned} &A_{2,\delta t}[\mathbf{u}_{2,h}^{n-1}; (\mathbf{u}_{2,h}^n, p_{2,h}^n), (\mathbf{v}_{2,h}, q_{2,h})] + C_2[(\mathbf{u}_{2,h}^{n-1}, \mathbf{u}_{1,h}^{n-1}); (\mathbf{u}_{2,h}^n, \mathbf{u}_{1,h}^n), \mathbf{v}_{2,h}] \\ &+ \frac{\gamma\mu}{h}\int_\Sigma (\mathbf{u}_{2,h}^n - \mathbf{u}_{1,h}^n) \cdot \mathbf{v}_{2,h} - \int_\Sigma \boldsymbol{\sigma}(\mathbf{u}_{2,h}^{n-1}, p_{2,h}^{n-1}) \mathbf{n}_2 \cdot \mathbf{v}_{2,h} \\ &- \int_\Sigma (\mathbf{u}_{2,h}^n - \mathbf{u}_{1,h}^n) \cdot \mathbf{n}_2 q_{2,h} + S(p_{2,h}^n, q_{2,h}) = 0 \end{aligned} \tag{2.29}$$

   for all $(\mathbf{v}_{2,h}, q_{2,h}) \in V_{2,h} \times Q_{2,h}$.

3. *Go to next time-step.*

This scheme only yields one solution of each sub-problem at each time step. The terms involving the two forms $A_{1,\delta t}$ and $A_{2,\delta t}$ take the same expressions (2.22) and (2.23) as in the monolithic scheme. The differences between the two algorithms only lie in the interface terms. First, the stabilization term $C_1[\mathbf{u}_{1,h}^{n-1}; (\mathbf{u}_{1,h}^n, \mathbf{u}_{2,h}^n), \mathbf{v}_{1,h}]$ of the monolithic algorithm (2.24) is replaced by $C_1[\mathbf{u}_{1,h}^{n-1}; (\mathbf{u}_{1,h}^n, \mathbf{u}_{2,h}^{n-1}), \mathbf{v}_{1,h}]$ in order to uncouple the two sub-problems. Second, the weakly consistent term

$$S(p_{2,h}^n, q_{2,h}) \overset{\text{def}}{=} \frac{\gamma_0 h}{\gamma\mu}\int_\Sigma (p_{2,h}^n - p_{2,h}^{n-1}) q_{2,h}, \tag{2.30}$$

is added in sub-domain Ω_2 in order to control spurious pressure fluctuations which appear at the interface because of the explicit coupling between the two sub-domains. The dimensionless parameter $\gamma_0 > 0$ will be fixed to ensure the energy stability of the method.

It is interesting to note that this scheme, obtained from Nitsche's penalty formulation, can be seen as an explicit Robin-Robin scheme associated with the following boundary conditions:

$$\begin{cases} \boldsymbol{\sigma}(\mathbf{u}_1^n, p_1^n)\mathbf{n}_1 + \dfrac{\gamma\mu}{h}\mathbf{u}_1^n = \dfrac{\gamma\mu}{h}\mathbf{u}_2^{n-1} - \boldsymbol{\sigma}(\mathbf{u}_2^{n-1}, p_2^{n-1})\mathbf{n}_2, & \text{on} \quad \Sigma, \\ \boldsymbol{\sigma}(\mathbf{u}_2^n, p_2^n)\mathbf{n}_2 + \dfrac{\gamma\mu}{h}\mathbf{u}_2^n = \dfrac{\gamma\mu}{h}\mathbf{u}_1^n + \boldsymbol{\sigma}(\mathbf{u}_2^{n-1}, p_2^{n-1})\mathbf{n}_2, & \text{on} \quad \Sigma. \end{cases} \tag{2.31}$$

We attempt to prove the stability in the energy norm of the explicit formulation (2.28)-(2.29). Although the result is not conclusive, it is useful since it pinpoints the difficulty that will be addressed in Algorithm 2.6. In addition, most of the arguments of the proof are reusable for the stability analysis of Algorithm 2.6.

PROPOSITION 2.2
Let $(\mathbf{u}_{1,h}^n, p_{1,h}^n, \mathbf{u}_{2,h}^n, p_{2,h}^n)$ *be the solution of the staggered scheme* (2.28)-(2.29)*. Under the conditions:*

$$\gamma_0 > 4, \tag{2.32a}$$
$$\gamma\delta t \leq C_\Sigma h, \tag{2.32b}$$
$$\gamma \geq 4C_T, \tag{2.32c}$$

where $C_T > 0$ *is the constant of the inverse inequality* (2.15) *and* $C_\Sigma > 0$ *is given, the following estimate holds:*

$$\begin{aligned} E^n + \frac{\gamma\mu}{2h}\delta t||\mathbf{u}_{2,h}^n||_\Sigma^2 + \frac{\gamma_0 h}{2\gamma\mu}\delta t||p_{2,h}^n||_\Sigma^2 \leq\ & 3E^0 + \frac{3C_\Sigma\mu}{2}||\mathbf{u}_{2,h}^0||_\Sigma^2 \\ & + \frac{3\gamma_0 h}{2\gamma\mu}\delta t||p_{2,h}^0||_\Sigma^2 + 24\delta t||\boldsymbol{\epsilon}_{2,h}^0||_{\Omega_2}^2 \\ & + \frac{3}{2}\rho\delta t\sum_{m=1}^{n}\int_\Sigma \mathbf{u}_{1,h}^{m-1}\cdot\mathbf{n}_1\mathbf{u}_{1,h}^m\cdot(\mathbf{u}_{2,h}^m - \mathbf{u}_{2,h}^{m-1}). \end{aligned} \tag{2.33}$$

Proof. Let be $(\mathbf{v}_{1,h}, q_{1,h}, \mathbf{v}_{2,h}, q_{2,h}) = (\mathbf{u}_{1,h}^n, p_{1,h}^n, \mathbf{u}_{2,h}^n, p_{2,h}^n)$, the two forms $A_{1,\delta t}$ and $A_{2,\delta t}$ give

$$\begin{aligned} A_{1,\delta t}[\mathbf{u}_{1,h}^{n-1};(\mathbf{u}_{1,h}^n,p_{1,h}^n),(\mathbf{u}_{1,h}^n,p_{1,h}^n)] =\ & \frac{\rho}{2\delta t}\left(||\mathbf{u}_{1,h}^n||_{\Omega_1}^2 - ||\mathbf{u}_{1,h}^{n-1}||_{\Omega_1}^2 + ||\mathbf{u}_{1,h}^n - \mathbf{u}_{1,h}^{n-1}||_{\Omega_1}^2\right) \\ & + 2\mu||\boldsymbol{\epsilon}_{1,h}^n||_{\Omega_1}^2 - \frac{\rho}{2}\int_{\Omega_1}(\nabla\cdot\mathbf{u}_{1,h}^{n-1})|\mathbf{u}_{1,h}^n|^2 \\ & + \frac{\rho}{2}\int_\Sigma(\mathbf{u}_{1,h}^{n-1}\cdot\mathbf{n}_1)|\mathbf{u}_{1,h}^n|^2, \end{aligned}$$

$$\begin{aligned} A_{2,\delta t}[\mathbf{u}_{2,h}^{n-1};(\mathbf{u}_{2,h}^n,p_{2,h}^n),(\mathbf{u}_{2,h}^n,p_{2,h}^n)] =\ & \frac{\rho}{2\delta t}\left(||\mathbf{u}_{2,h}^n||_{\Omega_2}^2 - ||\mathbf{u}_{2,h}^{n-1}||_{\Omega_2}^2 + ||\mathbf{u}_{2,h}^n - \mathbf{u}_{2,h}^{n-1}||_{\Omega_2}^2\right) \\ & + 2\mu||\boldsymbol{\epsilon}_{2,h}^n||_{\Omega_2}^2 - \frac{\rho}{2}\int_{\Omega_2}(\nabla\cdot\mathbf{u}_{2,h}^{n-1})|\mathbf{u}_{2,h}^n|^2 \\ & + \frac{\rho}{2}\int_\Sigma(\mathbf{u}_{2,h}^{n-1}\cdot\mathbf{n}_2)|\mathbf{u}_{2,h}^n|^2. \end{aligned}$$

Similarly, for the terms C_1 and C_2 we get

$$\begin{aligned} C_1[\mathbf{u}_{1,h}^{n-1};(\mathbf{u}_{1,h}^n,\mathbf{u}_{2,h}^{n-1}),\mathbf{u}_{1,h}^n] &= \frac{\rho}{2}\int_{\Omega_1}(\nabla\cdot\mathbf{u}_{1,h}^{n-1})|\mathbf{u}_{1,h}^n|^2-\frac{\rho}{2}\int_\Sigma(\mathbf{u}_{1,h}^{n-1}\cdot\mathbf{n}_1)|\mathbf{u}_{1,h}^n|^2 \\ &\quad+\frac{\rho}{2}\int_\Sigma(\mathbf{u}_{1,h}^{n-1}\cdot\mathbf{n}_1)(\mathbf{u}_{2,h}^{n-1}\cdot\mathbf{u}_{1,h}^n), \\ C_2[(\mathbf{u}_{2,h}^{n-1},\mathbf{u}_{1,h}^{n-1});(\mathbf{u}_{2,h}^n,\mathbf{u}_{1,h}^n),\mathbf{u}_{2,h}^n] &= \frac{\rho}{2}\int_{\Omega_2}(\nabla\cdot\mathbf{u}_{2,h}^{n-1})|\mathbf{u}_{2,h}^n|^2-\frac{\rho}{2}\int_\Sigma(\mathbf{u}_{2,h}^{n-1}\cdot\mathbf{n}_2)|\mathbf{u}_{2,h}^n|^2 \\ &\quad+\frac{\rho}{2}\int_\Sigma(\mathbf{u}_{1,h}^{n-1}\cdot\mathbf{n}_2)(\mathbf{u}_{1,h}^n\cdot\mathbf{u}_{2,h}^n). \end{aligned}$$

By inserting these expressions into (2.28)-(2.29), summing over $1\le m\le n$ and multiplying by δt, we obtain

$$\begin{aligned} &\frac{\rho}{2}\sum_{m=1}^n\left(||\mathbf{u}_{1,h}^m||_{\Omega_1}^2-||\mathbf{u}_{1,h}^{m-1}||_{\Omega_1}^2\right)+\frac{\rho}{2}\sum_{m=1}^n||\mathbf{u}_{1,h}^m-\mathbf{u}_{1,h}^{m-1}||_{\Omega_1}^2+2\mu\delta t\sum_{m=1}^n||\boldsymbol{\epsilon}_{1,h}^m||_{\Omega_1}^2 \\ &+\frac{\rho}{2}\sum_{m=1}^n\left(||\mathbf{u}_{2,h}^m||_{\Omega_2}^2-||\mathbf{u}_{2,h}^{m-1}||_{\Omega_2}^2\right)+\frac{\rho}{2}\sum_{m=1}^n||\mathbf{u}_{2,h}^m-\mathbf{u}_{2,h}^{m-1}||_{\Omega_2}^2+2\mu\delta t\sum_{m=1}^n||\boldsymbol{\epsilon}_{2,h}^m||_{\Omega_2}^2 \\ &+\frac{\rho}{2}\delta t\sum_{m=1}^n\int_\Sigma\mathbf{u}_{1,h}^{m-1}\cdot\mathbf{n}_1\mathbf{u}_{1,h}^m\cdot(\mathbf{u}_{2,h}^{m-1}-\mathbf{u}_{2,h}^m) \\ =\ &\underbrace{\delta t\sum_{m=1}^n\int_\Sigma(p_{2,h}^m-p_{2,h}^{m-1})\mathbf{n}_2\cdot(\mathbf{u}_{2,h}^m-\mathbf{u}_{1,h}^m)-\frac{\gamma_0 h}{\gamma\mu}\delta t\sum_{m=1}^n\int_\Sigma(p_{2,h}^m-p_{2,h}^{m-1})p_{2,h}^m}_{T_1} \\ &\underbrace{-\frac{\gamma\mu}{h}\delta t\sum_{m=1}^n\int_\Sigma(\mathbf{u}_{2,h}^m-\mathbf{u}_{1,h}^m)\cdot\mathbf{u}_{2,h}^m+\frac{\gamma\mu}{h}\delta t\sum_{m=1}^n\int_\Sigma(\mathbf{u}_{2,h}^{m-1}-\mathbf{u}_{1,h}^m)\cdot\mathbf{u}_{1,h}^m}_{T_2} \\ &\underbrace{+2\mu\delta t\sum_{m=1}^n\int_\Sigma\boldsymbol{\epsilon}_{2,h}^{m-1}\mathbf{n}_2\cdot(\mathbf{u}_{2,h}^m-\mathbf{u}_{1,h}^m)}_{T_3}. \end{aligned} \tag{2.34}$$

We now proceed by adapting the arguments reported in [BF09]. Term T_1 involves the pressure fluctuations at the interface. Applying Young's inequality, it can be written as

$$\begin{aligned} T_1 &\le \frac{2h}{\gamma\mu}\delta t\sum_{m=1}^n||p_{2,h}^m-p_{2,h}^{m-1}||_\Sigma^2+\frac{\gamma\mu}{8h}\delta t\sum_{m=1}^n||\mathbf{u}_{2,h}^m-\mathbf{u}_{1,h}^m||_\Sigma^2 \\ &\quad-\frac{1}{2}\frac{\gamma_0 h}{\gamma\mu}\delta t||p_{2,h}^n||_\Sigma^2+\frac{1}{2}\frac{\gamma_0 h}{\gamma\mu}\delta t||p_{2,h}^0||_\Sigma^2-\frac{\gamma_0 h}{\gamma\mu}\frac{\delta t}{2}\sum_{m=1}^n||p_{2,h}^m-p_{2,h}^{m-1}||_\Sigma^2 \\ &= \frac{\gamma\mu}{8h}\delta t\sum_{m=1}^n||\mathbf{u}_{2,h}^m-\mathbf{u}_{1,h}^m||_\Sigma^2-\frac{1}{2}\frac{\gamma_0 h}{\gamma\mu}\delta t||p_{2,h}^n||_\Sigma^2+\frac{1}{2}\frac{\gamma_0 h}{\gamma\mu}\delta t||p_{2,h}^0||_\Sigma^2 \end{aligned}$$

$$+\frac{h}{2\gamma\mu}\left(4-\gamma_0\right)\delta t\sum_{m=1}^{n}||p_{2,h}^{m}-p_{2,h}^{m-1}||_{\Sigma}^{2}$$

the last term being negative (assumption of (2.32a)), it will be removed from the upper bound.

Term T_2 concerns the velocity fluctuations at the interface. Adding and subtracting $\mathbf{u}_{2,h}^{m}$ in the second integral of T_2, we have

$$\begin{aligned}
T_2 &= -\frac{\gamma\mu}{h}\delta t\sum_{m=1}^{n}\int_{\Sigma}(\mathbf{u}_{2,h}^{m}-\mathbf{u}_{1,h}^{m})\cdot\mathbf{u}_{2,h}^{m}+\frac{\gamma\mu}{h}\delta t\sum_{m=1}^{n}\int_{\Sigma}(\mathbf{u}_{2,h}^{m-1}-\mathbf{u}_{2,h}^{m})\cdot\mathbf{u}_{1,h}^{m}\\
&\quad+\frac{\gamma\mu}{h}\delta t\sum_{m=1}^{n}\int_{\Sigma}(\mathbf{u}_{2,h}^{m}-\mathbf{u}_{1,h}^{m})\cdot\mathbf{u}_{1,h}^{m}\\
&= -\frac{\gamma\mu}{h}\delta t\sum_{m=1}^{n}||\mathbf{u}_{2,h}^{m}-\mathbf{u}_{1,h}^{m}||_{\Sigma}^{2}-\frac{\gamma\mu}{h}\delta t\sum_{m=1}^{n}\int_{\Sigma}(\mathbf{u}_{2,h}^{m}-\mathbf{u}_{2,h}^{m-1})\cdot\mathbf{u}_{1,h}^{m}.
\end{aligned}$$

Adding and subtracting $\mathbf{u}_{2,h}^{m}$ in the second term of this relation, we obtain

$$\begin{aligned}
&-\frac{\gamma\mu}{h}\delta t\sum_{m=1}^{n}\int_{\Sigma}(\mathbf{u}_{2,h}^{m}-\mathbf{u}_{2,h}^{m-1})\cdot\mathbf{u}_{1,h}^{m}\\
&=-\frac{\gamma\mu}{h}\delta t\sum_{m=1}^{n}\left[\int_{\Sigma}(\mathbf{u}_{2,h}^{m}-\mathbf{u}_{2,h}^{m-1})\cdot\mathbf{u}_{2,h}^{m}-\int_{\Sigma}(\mathbf{u}_{2,h}^{m}-\mathbf{u}_{2,h}^{m-1})\cdot(\mathbf{u}_{2,h}^{m}-\mathbf{u}_{1,h}^{m})\right]\\
&=-\frac{\gamma\mu}{h}\delta t\sum_{m=1}^{n}\left[\int_{\Sigma}\frac{|\mathbf{u}_{2,h}^{m}|^2}{2}-\frac{|\mathbf{u}_{2,h}^{m-1}|^2}{2}+\frac{|\mathbf{u}_{2,h}^{m}-\mathbf{u}_{2,h}^{m-1}|^2}{2}\right.\\
&\quad\left.-\int_{\Sigma}(\mathbf{u}_{2,h}^{m}-\mathbf{u}_{2,h}^{m-1})\cdot(\mathbf{u}_{2,h}^{m}-\mathbf{u}_{1,h}^{m})\right]\\
&\leq-\frac{\gamma\mu}{2h}\delta t\sum_{m=1}^{n}\left[||\mathbf{u}_{2,h}^{m}||_{\Sigma}^{2}-||\mathbf{u}_{2,h}^{m-1}||_{\Sigma}^{2}-||\mathbf{u}_{2,h}^{m}-\mathbf{u}_{1,h}^{m}||_{\Sigma}^{2}\right].
\end{aligned}$$

Using assumption (2.32b) we finally get

$$T_2\leq-\frac{\gamma\mu}{2h}\delta t\sum_{m=1}^{n}||\mathbf{u}_{2,h}^{m}-\mathbf{u}_{1,h}^{m}||_{\Sigma}^{2}-\frac{\gamma\mu}{2h}\delta t||\mathbf{u}_{2,h}^{n}||_{\Sigma}^{2}+\frac{\mu C_{\Sigma}}{2}||\mathbf{u}_{2,h}^{0}||_{\Sigma}^{2}.$$

Applying Young's inequality and the local trace inequality (2.15), the term T_3 can be bounded as follows:

$$\begin{aligned}
T_3 &\leq \frac{8\mu C_T}{\gamma}\delta t\sum_{m=1}^{n}||\boldsymbol{\epsilon}_{2,h}^{m-1}||_{\Omega_2}^{2}+\frac{\gamma\mu}{8h}\delta t\sum_{m=1}^{n}||\mathbf{u}_{2,h}^{m}-\mathbf{u}_{1,h}^{m}||_{\Sigma}^{2}\\
&= \frac{8\mu C_T}{\gamma}\delta t\sum_{m=1}^{n-1}||\boldsymbol{\epsilon}_{2,h}^{m}||_{\Omega_2}^{2}+\frac{8\mu C_T}{\gamma}\delta t||\boldsymbol{\epsilon}_{2,h}^{0}||_{\Omega_2}^{2}+\frac{\gamma\mu}{8h}\delta t\sum_{m=1}^{n}||\mathbf{u}_{2,h}^{m}-\mathbf{u}_{1,h}^{m}||_{\Sigma}^{2}.
\end{aligned}$$

Inserting T_1, T_2 and T_3 in (2.34), we have:

$$\begin{aligned}
&\frac{\rho}{2}\left(||\mathbf{u}_{1,h}^n||_{\Omega_1}^2+||\mathbf{u}_{2,h}^n||_{\Omega_2}^2\right)+\frac{\gamma\mu}{4h}\delta t\sum_{m=1}^{n}||\mathbf{u}_{2,h}^m-\mathbf{u}_{1,h}^m||_{\Sigma}^2+2\mu\delta t\sum_{m=1}^{n}||\boldsymbol{\epsilon}_{1,h}^m||_{\Omega_1}^2\\
&+2\mu\left(1-\frac{4C_T}{\gamma}\right)\delta t\sum_{m=1}^{n}||\boldsymbol{\epsilon}_{2,h}^m||_{\Omega_2}^2+\frac{\gamma\mu}{2h}\delta t||\mathbf{u}_{2,h}^n||_{\Sigma}^2+\frac{1}{2}\frac{\gamma_0 h}{\gamma\mu}\delta t||p_{2,h}^n||_{\Sigma}^2\\
&\leq\frac{\rho}{2}\left(||\mathbf{u}_{1,h}^0||_{\Omega_1}^2+||\mathbf{u}_{2,h}^0||_{\Omega_2}^2\right)+\frac{\mu C_\Sigma}{2}||\mathbf{u}_{2,h}^0||_{\Sigma}^2+\frac{1}{2}\frac{\gamma_0 h}{\gamma\mu}\delta t||p_{2,h}^0||_{\Sigma}^2+\frac{8\mu C_T}{\gamma}\delta t||\boldsymbol{\epsilon}_{2,h}^0||_{\Omega_2}^2\\
&+\frac{\rho}{2}\delta t\sum_{m=1}^{n}\int_{\Sigma}\mathbf{u}_{1,h}^{m-1}\cdot\mathbf{n}_1\mathbf{u}_{1,h}^m\cdot(\mathbf{u}_{2,h}^m-\mathbf{u}_{2,h}^{m-1}).
\end{aligned}$$

Finally under the condition (2.32c) the assertion is proved. ■

REMARK 2.3
Another option could be to consider

$$C_2[(\mathbf{u}_{2,h}^{n-1},\mathbf{u}_{1,h}^{n-1});(\mathbf{u}_{2,h}^n,\mathbf{u}_{2,h}^{n-1}),\mathbf{v}_{2,h}]$$

in (2.29)*, i.e.* $\mathbf{u}_{2,h}^{n-1}$ *instead* $\mathbf{u}_{1,h}^n$ *or alternatively replace both* (2.28) *and* (2.29) *by*

$$C_1[\mathbf{u}_{1,h}^{n-1};(\mathbf{u}_{1,h}^n,\mathbf{u}_{1,h}^{n-1}),\mathbf{v}_{1,h}] \quad \textit{and} \quad C_2[(\mathbf{u}_{2,h}^{n-1},\mathbf{u}_{1,h}^{n-1});(\mathbf{u}_{2,h}^n,\mathbf{u}_{1,h}^{n-1}),\mathbf{v}_{2,h}],$$

i.e. $\mathbf{u}_{1,h}^{n-1}$ *in place of* $\mathbf{u}_{2,h}^{n-1}$ *in the first term, and* $\mathbf{u}_{1,h}^{n-1}$ *instead* $\mathbf{u}_{1,h}^n$ *in the second term. The formulations remain consistent, but a non-bounded term still appears in the energy balance.*

2.5.3 Explicit coupling: a stable but inconsistent formulation

Energy stability can be guaranteed if, instead of $C_1[\mathbf{u}_{1,h}^{n-1};(\mathbf{u}_{1,h}^n,\mathbf{u}_{2,h}^{n-1}),\mathbf{v}_{1,h}]$ and $C_2[(\mathbf{u}_{2,h}^{n-1},\mathbf{u}_{1,h}^{n-1});(\mathbf{u}_{2,h}^n,\mathbf{u}_{1,h}^n),\mathbf{v}_{2,h}]$ in Algorithm 2.3, we consider the following alternative terms:

$$c_1(\mathbf{u}_{1,h}^{n-1};\mathbf{u}_{1,h}^n,\mathbf{v}_{1,h}) \overset{\text{def}}{=} -\frac{\rho}{2}\int_{\Sigma}(\mathbf{u}_{1,h}^{n-1}\cdot\mathbf{n}_1)(\mathbf{u}_{1,h}^n\cdot\mathbf{v}_{1,h}), \tag{2.35}$$

$$c_2(\mathbf{u}_{2,h}^{n-1};\mathbf{u}_{2,h}^n,\mathbf{v}_{2,h}) \overset{\text{def}}{=} -\frac{\rho}{2}\int_{\Sigma}(\mathbf{u}_{2,h}^{n-1}\cdot\mathbf{n}_2)(\mathbf{u}_{2,h}^n\cdot\mathbf{v}_{2,h}). \tag{2.36}$$

The corresponding staggered scheme is presented in Algorithm 2.4.

ALGORITHM 2.4 (Staggered scheme with static pressure: inconsistent formulation)

1. *Find* $(\mathbf{u}_{1,h}^n,\, p_{1,h}^n) \in W_{1,h} \times Q_{1,h}$ *such that*

$$A_{1,\delta t}[\mathbf{u}_{1,h}^{n-1}; (\mathbf{u}_{1,h}^n, p_{1,h}^n)(\mathbf{v}_{1,h}, q_{1,h})] + c_1(\mathbf{u}_{1,h}^{n-1}; \mathbf{u}_{1,h}^n, \mathbf{v}_{1,h}) + \frac{\gamma\mu}{h}\int_\Sigma (\mathbf{u}_{1,h}^n - \mathbf{u}_{2,h}^{n-1})\cdot\mathbf{v}_{1,h} + \int_\Sigma \boldsymbol{\sigma}(\mathbf{u}_{2,h}^{n-1}, p_{2,h}^{n-1})\mathbf{n}_2\cdot\mathbf{v}_{1,h} = 0$$

   for all $(\mathbf{v}_{1,h},\, q_{1,h}) \in V_{1,h} \times Q_{1,h}$.

2. *Find* $(\mathbf{u}_{2,h}^n,\, p_{2,h}^n) \in W_{2,h} \times Q_{2,h}$ *such that*

$$A_{2,\delta t}[\mathbf{u}_{2,h}^{n-1}; (\mathbf{u}_{2,h}^n, p_{2,h}^n)(\mathbf{v}_{2,h}, q_{1,h})] + c_2(\mathbf{u}_{2,h}^{n-1}; \mathbf{u}_{2,h}^n, \mathbf{v}_{2,h}) + \frac{\gamma\mu}{h}\int_\Sigma (\mathbf{u}_{2,h}^n - \mathbf{u}_{1,h}^n)\cdot\mathbf{v}_{2,h} - \int_\Sigma \boldsymbol{\sigma}(\mathbf{u}_{2,h}^{n-1}, p_{2,h}^{n-1})\mathbf{n}_2\cdot\mathbf{v}_{2,h} - \int_\Sigma (\mathbf{u}_{2,h}^n - \mathbf{u}_{1,h}^n)\cdot\mathbf{n}_2 q_{2,h} + S(p_{2,h}^n, q_{2,h}) = 0$$

   for all $(\mathbf{v}_{2,h},\, q_{2,h}) \in V_{2,h} \times Q_{2,h}$.

3. *Go to next time-step.*

Note that this amounts to consider the skew-symmetric formulation of the convective term in each sub-domain, namely, for $i = 1, 2$

$$\frac{1}{2}\int_{\Omega_i} \mathbf{u}_i\cdot\nabla\mathbf{u}_i\cdot\mathbf{v}_i - \frac{1}{2}\int_{\Omega_i}\mathbf{u}_i\cdot\nabla\mathbf{v}_i\cdot\mathbf{u}_i. \tag{2.37}$$

Indeed, using integration by parts we have

$$\frac{1}{2}\int_{\Omega_i} \mathbf{u}_i\cdot\nabla\mathbf{u}_i\cdot\mathbf{v}_i - \frac{1}{2}\int_{\Omega_i}\mathbf{u}_i\cdot\nabla\mathbf{v}_i\cdot\mathbf{u}_i = \int_{\Omega_i} \mathbf{u}_i\cdot\nabla\mathbf{u}_i\cdot\mathbf{v}_i - \frac{1}{2}\int_\Sigma (\mathbf{u}_i\cdot\mathbf{n}_i)(\mathbf{u}_i\cdot\mathbf{v}_i). \tag{2.38}$$

A straightforward adaptation of Proposition 2.2 hence shows that Algorithm 2.4 is energy stable.

The skew-symmetrized form (2.37) is commonly used in the staggered time-marching of fluid-fluid interaction models based on *rigid-lid* coupling condition conditions (see, e.g., [CHL12] and the references therein), for which $\mathbf{u}_i\cdot\mathbf{n}_i = 0$ on Σ. The expression (2.37) is thus consistent, since the interface term in the right-hand side of (2.38) vanishes. Clearly, this does not hold for the coupled problem (2.2)-(2.4) and, therefore, Algorithm 2.4 involves an inconsistent treatment of (2.4). In fact, the following (inconsistent) Robin-Robin splitting

is enforced

$$\left\{\begin{array}{rcl} \boldsymbol{\sigma}(\mathbf{u}_1^n,p_1^n)\mathbf{n}_1-\frac{1}{2}(\mathbf{u}_1^{n-1}\cdot\mathbf{n}_1)\mathbf{u}_1^n+\frac{\gamma\mu}{h}\mathbf{u}_1^n &=& \frac{\gamma\mu}{h}\mathbf{u}_2^{n-1}-\boldsymbol{\sigma}(\mathbf{u}_2^{n-1},p_2^{n-1})\mathbf{n}_2, \text{ on } \Sigma,\\ \boldsymbol{\sigma}(\mathbf{u}_2^n,p_2^n)\mathbf{n}_2-\frac{1}{2}(\mathbf{u}_2^{n-1}\cdot\mathbf{n}_2)\mathbf{u}_2^n+\frac{\gamma\mu}{h}\mathbf{u}_2^n &=& \frac{\gamma\mu}{h}\mathbf{u}_1^n+\boldsymbol{\sigma}(\mathbf{u}_2^{n-1},p_2^{n-1})\mathbf{n}_2, \quad \text{on } \Sigma. \end{array}\right. \tag{2.39}$$

The numerical experiments reported in Section 3.3.3 in Chapter 3 confirm the expected poor accuracy of this method.

2.5.4 Explicit coupling: a total pressure formulation

We propose in this Section a provably stable staggered algorithm. The difficulty to establish the stability of Algorithm 2.3 came from the last term of (2.33) which resulted from the integration by parts of the advection. To get rid of this term, we suggest to use a formulation for which the advection cancels in the energy equation without any integration by parts. This can be achieved by introducing the total pressure $\pi \overset{\text{def}}{=} p+\rho\frac{|\mathbf{u}^2|}{2}$ and by reformulating the Navier-Stokes equation as:

$$\left\{\begin{array}{rcll} \rho\partial_t\mathbf{u}+\rho\mathbf{u}\cdot\nabla\mathbf{u}-\rho(\nabla\mathbf{u})^{\mathrm{T}}\mathbf{u}-\nabla\cdot\boldsymbol{\sigma}(\mathbf{u},\pi) &=& 0, & \text{in } \Omega,\\ \nabla\cdot\mathbf{u} &=& 0, & \text{in } \Omega,\\ \mathbf{u} &=& \mathbf{0}, & \text{on } \partial\Omega. \end{array}\right. \tag{2.40}$$

This formulation was in particular discussed in [HRT96, Page 337]. It simply results from the relation:

$$-\nabla\cdot\boldsymbol{\sigma}(\mathbf{u},p)=-\frac{\rho}{2}\nabla|\mathbf{u}|^2-\nabla\cdot\boldsymbol{\sigma}(\mathbf{u},\pi)=-\rho(\nabla\mathbf{u})^{\mathrm{T}}\mathbf{u}-\nabla\cdot\boldsymbol{\sigma}(\mathbf{u},\pi).$$

Note that the pressure unknown is now the total pressure π. This is not the case of the $curl\ \mathbf{u}\times\mathbf{u}$ *formulation* used in many works to enforce the total pressure in the boundary conditions, but which keeps the static pressure p as unknown (see, e.g., [BCMP88, FMN07, LMN+09, PZVP12, VV05]).

Using the same time discretization of Section 2.3, the monolithic scheme of the above model is reported in Algorithm 2.5

ALGORITHM 2.5 (Monolithic fluid problem: total pressure formulation)

1. *Advance in time fluid problem* (2.40) *in the whole domain* Ω*;*
2. *Go to next time-step.*

While, the partitioned formulation of the problem (2.40) reads:

find the velocity $\mathbf{u}_1 : \Omega_1 \times \mathbb{R}^+ \to \mathbb{R}^d$ and the pressure $\pi_1 : \Omega_1 \times \mathbb{R}^+ \to \mathbb{R}$ such that

$$\left\{ \begin{array}{rcll} \rho\partial_t \mathbf{u}_1 + \rho\mathbf{u}_1 \cdot \nabla\mathbf{u}_1 - \rho(\nabla\mathbf{u}_1)^{\mathrm{T}}\mathbf{u}_1 - \nabla \cdot \boldsymbol{\sigma}(\mathbf{u}_1, \pi_1) &=& 0, & \text{in } \Omega_1, \\ \nabla \cdot \mathbf{u}_1 &=& 0, & \text{in } \Omega_1, \\ \mathbf{u}_1 &=& \mathbf{0}, & \text{on } \Gamma_1, \end{array} \right. \tag{2.41}$$

find the velocity $\mathbf{u}_2 : \Omega_2 \times \mathbb{R}^+ \to \mathbb{R}^d$ and the pressure $\pi_2 : \Omega_2 \times \mathbb{R}^+ \to \mathbb{R}$, such that

$$\left\{ \begin{array}{rcll} \rho\partial_t \mathbf{u}_2 + \rho\mathbf{u}_2 \cdot \nabla\mathbf{u}_2 - \rho(\nabla\mathbf{u}_2)^{\mathrm{T}}\mathbf{u}_2 - \nabla \cdot \boldsymbol{\sigma}(\mathbf{u}_2, \pi_2) &=& 0, & \text{in } \Omega_2, \\ \nabla \cdot \mathbf{u}_2 &=& 0, & \text{in } \Omega_2, \\ \mathbf{u}_2 &=& \mathbf{0}, & \text{on } \Gamma_2. \end{array} \right. \tag{2.42}$$

The solutions in the two sub-domains are coupled through the kinematic and kinetic conditions:

$$\left\{ \begin{array}{rcll} \mathbf{u}_1 &=& \mathbf{u}_2, & \text{on } \Sigma, \\ \boldsymbol{\sigma}(\mathbf{u}_2, \pi_2)\mathbf{n}_2 &=& -\boldsymbol{\sigma}(\mathbf{u}_1, \pi_1)\mathbf{n}_1, & \text{on } \Sigma, \end{array} \right. \tag{2.43}$$

with $\mathbf{n}_1$, $\mathbf{n}_2$ the outward-pointing unit normal vectors on $\partial\Omega_1$ and $\partial\Omega_2$ respectively. The new staggered scheme, based on Nitsche's formulation, is presented in Algorithm 2.6.

ALGORITHM 2.6 (Staggered scheme with total pressure)

1. *Find* $(\mathbf{u}_{1,h}^n, \pi_{1,h}^n) \in W_{1,h} \times Q_{1,h}$ *satisfying the essential boundary conditions and such that*

$$\begin{aligned} &A_{1,\delta t}^{\pi}[\mathbf{u}_{1,h}^{n-1}; (\mathbf{u}_{1,h}^n, \pi_{1,h}^n), (\mathbf{v}_{1,h}, q_{1,h})] + \frac{\gamma\mu}{h}\int_\Sigma (\mathbf{u}_{1,h}^n - \mathbf{u}_{2,h}^{n-1}) \cdot \mathbf{v}_{1,h} \\ &+ \int_\Sigma \boldsymbol{\sigma}(\mathbf{u}_{2,h}^{n-1}, \pi_{2,h}^{n-1})\mathbf{n}_2 \cdot \mathbf{v}_{1,h} = 0, \end{aligned} \tag{2.44}$$

   for all $(\mathbf{v}_{1,h}, q_{1,h}) \in V_{1,h} \times Q_{1,h}$.

2. *Find* $(\mathbf{u}_{2,h}^n, \pi_{2,h}^n) \in W_{2,h} \times Q_{2,h}$ *satisfying the essential boundary conditions and such that*

$$\begin{aligned} &A_{2,\delta t}^{\pi}[\mathbf{u}_{2,h}^{n-1}; (\mathbf{u}_{2,h}^n, \pi_{2,h}^n), (\mathbf{v}_{2,h}, q_{2,h})] + S(\pi_{2,h}^n, q_{2,h}) \\ &+ \frac{\gamma\mu}{h}\int_\Sigma (\mathbf{u}_{2,h}^n - \mathbf{u}_{1,h}^n) \cdot \mathbf{v}_{2,h} - \int_\Sigma \boldsymbol{\sigma}(\mathbf{u}_{2,h}^{n-1}, \pi_{2,h}^{n-1})\mathbf{n}_2 \cdot \mathbf{v}_{2,h} \\ &- \int_\Sigma (\mathbf{u}_{2,h}^n - \mathbf{u}_{1,h}^n) \cdot \mathbf{n}_2 q_{2,h} = 0, \end{aligned} \tag{2.45}$$

   for all $(\mathbf{v}_{2,h}, q_{2,h}) \in V_{2,h} \times Q_{2,h}$.

3. *Go to next time-step.*

The variational formulation derived from (2.41)-(2.43) naturally leads to replace the two forms $A_{1,\delta t}$ and $A_{2,\delta t}$ used in the Algorithm 2.3 by the new forms $A^{\pi}_{1,\delta t}$ and $A^{\pi}_{2,\delta t}$ defined by

$$\begin{aligned} A^{\pi}_{1,\delta t}[\mathbf{u}^{n-1}_{1,h};(\mathbf{u}^{n}_{1,h},\pi^{n}_{1,h}),(\mathbf{v}_{1,h},q_{1,h})] \overset{\text{def}}{=} & \rho\int_{\Omega_1}\partial_{\delta t}\mathbf{u}^{n}_{1,h}\cdot\mathbf{v}_{1,h}+2\mu\int_{\Omega_1}\boldsymbol{\epsilon}(\mathbf{u}^{n}_{1,h}):\boldsymbol{\epsilon}(\mathbf{v}_{1,h}) \\ & -\int_{\Omega_1}\pi^{n}_{1,h}\nabla\cdot\mathbf{v}_{1,h}+\int_{\Omega_1}q_{1,h}\nabla\cdot\mathbf{u}^{n}_{1,h} \\ & +\rho\int_{\Omega_1}(\mathbf{u}^{n}_{1,h}\nabla\mathbf{u}^{n-1}_{1,h}\cdot\mathbf{v}_{1,h}-\mathbf{v}_{1,h}\nabla\mathbf{u}^{n-1}_{1,h}\cdot\mathbf{u}^{n}_{1,h}), \end{aligned} \tag{2.46}$$

$$\begin{aligned} A^{\pi}_{2,\delta t}[\mathbf{u}^{n-1}_{2,h};(\mathbf{u}^{n}_{2,h},\pi^{n}_{2,h}),(\mathbf{v}_{2,h},q_{2,h})] \overset{\text{def}}{=} & \rho\int_{\Omega_2}\partial_{\delta t}\mathbf{u}^{n}_{2,h}\mathbf{v}_{2,h}+2\mu\int_{\Omega_2}\boldsymbol{\epsilon}(\mathbf{u}^{n}_{2,h}):\boldsymbol{\epsilon}(\mathbf{v}_{2,h}) \\ & -\int_{\Omega_2}\pi^{n}_{2,h}\nabla\cdot\mathbf{v}_{2,h}+\int_{\Omega_2}q_{2,h}\nabla\cdot\mathbf{u}^{n}_{2,h} \\ & +\rho\int_{\Omega_2}(\mathbf{u}^{n}_{2,h}\nabla\mathbf{u}^{n-1}_{2,h}\cdot\mathbf{v}_{2,h}-\mathbf{v}_{2,h}\nabla\mathbf{u}^{n-1}_{2,h}\cdot\mathbf{u}^{n}_{2,h}). \end{aligned} \tag{2.47}$$

Note that with this new formulation, the last integral in (2.11) and (2.12) (Temam's trick) is no longer necessary. As with the previous formulation, the pressure fluctuation at the interface are controlled by the term

$$S(\pi^{n}_{2,h},q_{2,h}) \overset{\text{def}}{=} \frac{\gamma_0 h}{\gamma\mu}\int_{\Sigma}(\pi^{n}_{2,h}-\pi^{n-1}_{2,h})q_{2,h}, \tag{2.48}$$

in sub-domain 2. Again, the two sub-problems can be seen as coupled through the Robin-Robin transmission conditions:

$$\begin{cases} \boldsymbol{\sigma}(\mathbf{u}^{n}_{1},\pi^{n}_{1})\mathbf{n}_1+\dfrac{\gamma\mu}{h}\mathbf{u}^{n}_{1} &= \dfrac{\gamma\mu}{h}\mathbf{u}^{n-1}_{2}-\boldsymbol{\sigma}(\mathbf{u}^{n-1}_{2},\pi^{n-1}_{2})\mathbf{n}_2, \quad \text{on} \quad \Sigma, \\ \boldsymbol{\sigma}(\mathbf{u}^{n}_{2},\pi^{n}_{2})\mathbf{n}_2+\dfrac{\gamma\mu}{h}\mathbf{u}^{n}_{2} &= \dfrac{\gamma\mu}{h}\mathbf{u}^{n}_{1}+\boldsymbol{\sigma}(\mathbf{u}^{n-1}_{2},\pi^{n-1}_{2})\mathbf{n}_2, \quad \text{on} \quad \Sigma. \end{cases} \tag{2.49}$$

These are similar to (2.31), but the static pressure has been replaced by the total pressure.

REMARK 2.4

The total pressure formulation can be obviously used in the implicit case: find $(\mathbf{u}^{n}_{1,h},\pi^{n}_{1,h},\mathbf{u}^{n}_{2,h},\pi^{n}_{2,h}) \in W_{1,h}\times Q_{1,h}\times W_{2,h}\times Q_{2,h}$ *satisfying the essential boundary conditions and such that*

$$\begin{aligned} & A^{\pi}_{1,\delta t}[\mathbf{u}^{n-1}_{1,h};(\mathbf{u}^{n}_{1,h},\pi^{n}_{1,h}),(\mathbf{v}_{1,h},q_{1,h})]+A^{\pi}_{2,\delta t}[\mathbf{u}^{n-1}_{2,h};(\mathbf{u}^{n}_{2,h},\pi^{n}_{2,h}),(\mathbf{v}_{2,h},q_{2,h})]+ \\ & +\frac{\gamma\mu}{h}\int_{\Sigma}(\mathbf{u}^{n}_{2,h}-\mathbf{u}^{n}_{1,h})\cdot(\mathbf{v}_{2,h}-\mathbf{v}_{1,h})-\int_{\Sigma}\boldsymbol{\sigma}(\mathbf{u}^{n}_{2,h},\pi^{n}_{2,h})\mathbf{n}_2\cdot(\mathbf{v}_{2,h}-\mathbf{v}_{1,h}) \\ & -\int_{\Sigma}(\mathbf{u}^{n}_{2,h}-\mathbf{u}^{n}_{1,h})\mathbf{n}_2 q_{2,h}=0, \end{aligned}$$

for all $(\mathbf{v}_{1,h}, q_{1,h}, \mathbf{v}_{2,h}, q_{2,h}) \in V_{1,h} \times Q_{1,h} \times V_{2,h} \times Q_{2,h}$*. The proof of the stability analysis is performed in the same way as in Proposition 2.1, with the total pressure variable* $\pi_{i,h}$ *instead of* $p_{i,h}$*,* $i = 1, 2$ *but without the interface stabilization terms* (2.13) *and* (2.14)*.*

REMARK 2.5

If the proposed splitting schemes were used within a fluid-structure interaction framework, the fluid stress on the fluid-solid interface could not be directly obtained as the residual of the fluid variational formulation. Instead, this interface load should be explicitly computed via face-wise integration.

The next proposition shows that Algorithm 2.6 is conditionally stable in the energy norm.

PROPOSITION 2.3

Let $(\mathbf{u}_{1,h}^n, \pi_{1,h}^n, \mathbf{u}_{2,h}^n, \pi_{2,h}^n)$ *be the solution of* (2.44)-(2.45)*. With same the conditions* (2.32a)-(2.32c)*, i.e.:*

$$\gamma_0 > 4, \tag{2.50a}$$

$$\gamma\delta t \leq C_\Sigma h, \tag{2.50b}$$

$$\gamma \geq 4C_T, \tag{2.50c}$$

where $C_T > 0$ *is the constant of the inverse inequality* (2.15) *and* $C_\Sigma > 0$ *is given, the following estimate holds:*

$$\begin{aligned} E^n + \frac{\gamma\mu}{2h}\delta t||\mathbf{u}_{2,h}^n||_\Sigma^2 + \frac{1}{2}\frac{\gamma_0 h}{\gamma\mu}\delta t||\pi_{2,h}^n||_{\Omega_2}^2 \leq\ & 3E^0 + \frac{3}{2}C_\Sigma\mu||\mathbf{u}_{2,h}^0||_\Sigma^2 \\ & + \frac{3}{2}\frac{\gamma_0 h}{\gamma\mu}\delta t||\pi_{2,h}^0||_\Sigma^2 + 24\delta t||\boldsymbol{\epsilon}_{2,h}^0||_{\Omega_2}^2 \end{aligned}$$

where E^n*,* $n \geq 1$*, and* E^0 *are defined in* (2.25) *and* (2.26)*.*

Proof. Taking $(\mathbf{v}_{1,h}, q_{1,h}, \mathbf{v}_{2,h}, q_{2,h}) = (\mathbf{u}_{1,h}^n, \pi_{1,h}^n, \mathbf{u}_{2,h}^n, \pi_{2,h}^n)$, the terms related to advection in (2.46) and (2.47) cancel each others. Therefore, multiplying for δt and summing over

$1 \leq m \leq n$, the system (2.44)-(2.45) can be written as

$$\begin{aligned}
&\frac{\rho}{2}\sum_{m=1}^{n}\left(||\mathbf{u}_{1,h}^{m}||_{\Omega_1}^2 - ||\mathbf{u}_{1,h}^{m-1}||_{\Omega_1}^2\right) + \frac{\rho}{2}\sum_{m=1}^{n}||\mathbf{u}_{1,h}^{m}-\mathbf{u}_{1,h}^{m-1}||_{\Omega_1}^2 + 2\mu\delta t\sum_{m=1}^{n}||\boldsymbol{\epsilon}_{1,h}^{m}||_{\Omega_1}^2 \\
&+\frac{\rho}{2}\sum_{m=1}^{n}\left(||\mathbf{u}_{2,h}^{m}||_{\Omega_2}^2 - ||\mathbf{u}_{2,h}^{m-1}||_{\Omega_2}^2\right) + \frac{\rho}{2}\sum_{m=1}^{n}||\mathbf{u}_{2,h}^{m}-\mathbf{u}_{2,h}^{m-1}||_{\Omega_2}^2 + 2\mu\delta t\sum_{m=1}^{n}||\boldsymbol{\epsilon}_{2,h}^{m}||_{\Omega_2}^2 \\
&= \underbrace{\delta t\sum_{m=1}^{n}\int_{\Sigma}(\pi_{2,h}^{m}-\pi_{2,h}^{m-1})\mathbf{n}_2\cdot(\mathbf{u}_{2,h}^{m}-\mathbf{u}_{1,h}^{m}) - \frac{\gamma_0 h}{\gamma\mu}\delta t\sum_{m=1}^{n}\int_{\Sigma}(\pi_{2,h}^{m}-\pi_{2,h}^{m-1})\pi_{2,h}^{m}}_{T_1} \\
&\underbrace{-\frac{\gamma\mu}{h}\delta t\sum_{m=1}^{n}\int_{\Sigma}(\mathbf{u}_{2,h}^{m}-\mathbf{u}_{1,h}^{m})\cdot\mathbf{u}_{2,h}^{m} + \frac{\gamma\mu}{h}\delta t\sum_{m=1}^{n}\int_{\Sigma}(\mathbf{u}_{2,h}^{m-1}-\mathbf{u}_{1,h}^{m})\cdot\mathbf{u}_{1,h}^{m}}_{T_2} \\
&\underbrace{+2\mu\delta t\sum_{m=1}^{n}\int_{\Sigma}\boldsymbol{\epsilon}_{2,h}^{m-1}\mathbf{n}_2\cdot(\mathbf{u}_{2,h}^{m}-\mathbf{u}_{1,h}^{m})}_{T_3}. \qquad (2.51)
\end{aligned}$$

The terms in the right-hand side are bounded *mutatis mutandis* as in the proof of Proposition 2.2:

$$\begin{aligned}
T_1 &\leq \frac{\gamma\mu}{4h}\delta t\sum_{m=1}^{n}||\mathbf{u}_{2,h}^{m}-\mathbf{u}_{1,h}^{m}||_{\Sigma}^2 - \frac{1}{2}\frac{\gamma_0 h}{\gamma\mu}||\pi_{2,h}^{n}||_{\Sigma}^2 + \frac{1}{2}\frac{\gamma_0 h}{\gamma\mu}||\pi_{2,h}^{0}||_{\Sigma}^2 \\
T_2 &\leq -\frac{\gamma\mu}{2h}\delta t\sum_{m=1}^{n}||\mathbf{u}_{2,h}^{m}-\mathbf{u}_{1,h}^{m}||_{\Sigma}^2 - \frac{\gamma\mu}{2h}\delta t||\mathbf{u}_{2,h}^{n}||_{\Sigma}^2 + \frac{\mu C_\Sigma}{2}||\mathbf{u}_{2,h}^{0}||_{\Sigma}^2, \\
T_3 &\leq \frac{4\mu C_T}{\gamma}\delta t\sum_{m=1}^{n}||\boldsymbol{\epsilon}_{2,h}^{m}||_{\Omega_2}^2 + \frac{\gamma\mu}{4h}\delta t\sum_{m=1}^{n}||\mathbf{u}_{2,h}^{m}-\mathbf{u}_{1,h}^{m}||_{\Sigma}^2.
\end{aligned}$$

Inserting T_1, T_2 and T_3 in (2.51) and then under the conditions (2.50c) the assertion is proved. ∎

2.6 Final remarks

In this Chapter we have discussed several loosely coupled strategies for fluid-fluid interaction problems coupling the incompressible Navier-Stokes equations through standard kinematic/kinetic interface conditions. The main ingredients of the methods considered are:

1. an explicit Robin-Robin treatment of the interface coupling, (2.31), (2.39) and (2.49), and a suitable weakly consistent artificial compressibility on the interface, (2.30) and (2.48);

2. a specific formulation of the convective terms: static pressure (standard and skew-symmetric) and total pressure formulations.

The first controls the artificial power generated by the kinematic/kinetic splitting on the interface, while the second governs the unbalanced dynamic pressure power across the interface.

Energy stability cannot a priori be guaranteed for the standard static pressure formulation Algorithm 2.3, but it can be recovered with a static pressure formulation and a skew-symmetric treatment of the convection (Algorithm 2.4). Unfortunately, this formulation is not consistent with the original coupled problem due to its non-confirming character across the interface. For the total pressure formulation, an a priori energy estimate guaranteeing the stability of the splitting (Algorithm 2.6) has been derived.

In the next chapter we illustrate the performance of the methods introduced in the previous sections, via numerical experiment applied to an idealized geometry of a thoracic aorta.

Bibliography of Chapter 2

[BCMP88] C. Begue, C. Conca, F. Murat, and O. Pironneau. Les équations des stokes et de Navier-Stokes avec des conditions limites sur la pression (on Stokes and Navier-stokes equations with boundary condition on the pressure). *Non-linear partial differential equations and their applications, Lect. Coll. de France Semin., Paris/Fr. 1985-86, Pitman Res. Notes Math. Ser. 181*, IX:179–264, 1988.

[BDM13] P.J. Blanco, S. Deparis, and A.C.I. Malossi. On the continuity of mean total normal stress in geometrical multiscale cardiovascular problems. *Journal of Computational Physics*, 251:136–155, 2013.

[BF09] E. Burman and M. A. Fernández. Stabilization of explicit coupling in fluid-structure interaction involving fluid incompressibility. *Comput. Methods Appl. Mech. Engrg*, 198:766–784, 2009.

[BF13] E. Burman and M.A. Fernández. An unfitted Nitsche method for incompressible fluid-structure interaction using overlapping meshes. Research Report RR-8424, Inria, 2013. http://hal.inria.fr/hal-00918272.

[BF14] E. Burman and M.A. Fernández. Explicit strategies for incompressible fluid-structure interaction problems: Nitsche type mortaring versus Robin-Robin coupling. *Int. J. Num. Meth. Engrg.*, 97(10):739–758, 2014.

[BFU07] P.J. Blanco, R.A. Feijóo, and S.A. Urquiza. A unified variational approach for coupling 3D-1D models and its blood flow applications. *Comp. Meth. Appl. Mech. Engrg.*, 196:4391 – 4410, 2007.

[BH07] E. Burman and P. Hansbo. A unified stabilized method for Stokes' and Darcy's equations. *J. Comput. Appl. Math.*, 198:35–51, 2007.

[BHS03] R. Becker, P. Hansbo, and R. Stenberg. A finite element method for domain decomposition with non-matching grids. *M2AN Math. Model. Numer. Anal.*, 37(2):209–225, 2003.

[BK06] D. Bresch and J. Koko. Operator-splitting and Lagrange multiplier domain decomposition methods for numerical simulation of two coupled Navier-Stokes fluids. *Int. J. Appl. Math. Comput. Sci.*, 16:419–429, 2006.

[BZ06] E. Burman and P. Zunino. A domain decomposition method based on interior penalties for advection–diffusion–reaction problems. *Siam Jour. Num. Anal.*, 44:1612–1638, 2006.

[CGN05] P. Causin, J.-F. Gerbeau, and F. Nobile. Added-mass effect in the design of partitioned algorithms for fluid-structure problems. *Comput. Methods Appl. Mech. Engrg.*, 194(42-44):4506–4527, 2005.

[CHL09] J. M. Connors, J. S. Howell, and W. J. Layton. Partitioned time stepping for parabolic two domain problem. *SIAM J. Numer. Anal.*, 47(5):3526–3549, 2009.

[CHL12] J. M. Connors, J. S. Howell, and W. J. Layton. Decoupled time stepping methods for fluid-fluid interaction. *SIAM J. Numer Anal.*, 50(3):1297–1319, 2012.

[DPE11] Daniele Antonio Di Pietro and Alexandre Ern. *Mathematical aspects of discontinuous Galerkin methods*, volume 69. Springer, 2011.

[FGNQ01] L. Formaggia, J.F. Gerbeau, F. Nobile, and A. Quarteroni. On the coupling of 3D and 1D Navier - Stokes equations for flow problems in compliant vessels. *Comp. Meth. Appl. Mech. Engrg.*, 191:561–582, 2001.

[FGS14] M. Fernández, J. Gerbeau, and S. Smaldone. Explicit coupling schemes for a fluid-fluid interaction problem arising in hemodynamics. *SIAM Journal on Scientific Computing*, 36(6):A2557–A2583, 2014.

[FMN07] L. Formaggia, A. Moura, and F. Nobile. On the stability of the coupling of 3D and 1D fluid-structure interaction models for blood flow simulations. *ESAIM: Mathematical Modelling and Numerical Analysis*, 41(04):743–769, 2007.

[FWR07] C. Förster, W.A. Wall, and E. Ramm. Artificial added mass instabilities in sequential staggered coupling of nonlinear structures and incompressible viscous flows. *Comput. Methods Appl. Mech. Engrg.*, 7(196):1278–1293, 2007.

[GK08] L. Grinberg and G. E. Karniadakis. A scalable domain decomposition method for ultra-parallel arterial flow simulations. *Communications in Computational Physics*, 4(5):1151–1169, 2008.

[GRW05] Vivette Girault, Béatrice Rivière, and Mary Wheeler. A discontinuous galerkin method with nonoverlapping domain decomposition for the stokes and navier-stokes problems. *Mathematics of Computation*, 74(249):53–84, 2005.

[Han05] P. Hansbo. Nitsche's method for interface problems in computational mechanics. *GAMM-Mitt.*, 28(2):183–206, 2005.

[HH03] P. Hansbo and J. Hermansson. Nitsche's method for coupling non-matching meshes in fluid-structure vibration problems. *Comput. Mech.*, 32(1–2):134–139, 2003.

[HHL03] A. Hansbo, P. Hansbo, and M. G. Larson. A finite element method on composite grids based on Nitsche's method. *M2AN Math. Model. Numer. Anal.*, 37(3):495–514, 2003.

[HHS04] P. Hansbo, J. Hermansson, and T. Svedberg. Nitsche's method combined with space-time finite elements for ALE fluid-structure interaction problems. *Comput. Methods Appl. Mech. Engrg.*, 193:4195–4206, 2004.

[HRT96] J. G. Heywood, R. Rannacher, and S. Turek. Artificial boundaries and flux and pressure conditions for the incompressible Navier-Stokes equations. *International Journal for Numerical Methods in Fluids*, 22:325–352, 1996.

[LMN+09] W. Layton, C. C. Manica, M. Neda, M. Olshanskii, and L.G. Rebholz. On the accuracy of the rotation form in simulations of the Navier-Stokes equations. *Journal of Computational Physics*, 228:3433–3447, 2009.

[M̈79] P. Müller. *The equation of oceanic motion*, volume 2. Cambrige University Press, Cambrige, UK, 1979.

[MBDA11] A. C. I. Malossi, P. J. Blanco, S. Deparis, and A.Quarteroni. Algorithms for the partitioned solution of weakly coupled fluid models for cardiovascular flows. *International Journal for Numerical Methods in Biomedical Engineering*, 27:2035–2057, 2011.

[MLLR14] A. Massing, M.G. Larson, A. Logg, and M.E. Rognes. A stabilized Nitsche overlapping mesh method for the Stokes problem. *Numer. Math.*, 2014.

[Nit71] J. Nitsche. Über ein Variationsprinzip zur Lsung von Dirichlet-Problemen bei Verwendung von Teilräumen, die keinen Randbedingungen unterworfen sind. *Abh. Math. Semin. Univ. Hamb.*, 36:9–15, 1971.

[PZVP12] A. Porpora, P. Zunino, C. Vergara, and M. Piccinelli. Numerical treatment of boundary conditions to replace lateral branches in hemodynamics. *International Journal for Numerical Methods in Biomedical Engineering*, 28:1165–1183, 2012.

[QV03] A. Quarteroni and A. Veneziani. Analysis of a geometrical multiscale model based on the coupling of PDE's and ODE's for blood flow simulations. *SIAM J Multiscale Model Simul*, 1:173–195, 2003.

[Tem68] R. Temam. Une méthode d'approximation de la solution des équations de Navier-Stokes. *Bulletin de la Société Mathématique de France*, 96:115–152, 1968.

[Tem79] R. Temam. *Navier-Stokes Equations*, volume 2. Studies in Mathematics and its Applications. North-Holland Publishing Co., Amsterdam, 1979.

[Tho06] V. Thomée. *Galerkin Finite Element Methods for Parabolic Problems*. Springer Series in Computational Mathematics. Springer-Verlag, Berlin, 2006.

[VV05] A. Veneziani and C. Vergara. Flow rate defective boundary conditions in haemodynamics simulations. *International Journal for Numerical Methods in Fluids*, 47(8-9):803–816, 2005.

CHAPTER 3

Numerical examples of fluid-fluid interaction problem in hemodynamics

Here we illustrate the numerical results of the methods presented in the previous chapter. Numerical tests are carried out first to show the instability related to the explicit Dirichlet-Neumann scheme. Then we investigate the parameters sensibility to the proposed explicit coupling scheme. The performance of these methods is illustrated on several numerical experiments related to simulation of blood flow in an idealized geometry of an aorta, in which the aortic root and the aortic arch represent the two fluids domains. To consider the neglected part of the circulatory system, three elements Windkessel models are linked in the outlets. A comparison between the monolithic solutions, with static and total pressure formulation, ends this study.

This chapter is part of:
Miguel Fernández, Jean-Frederic Gerbeau, Saverio Smaldone. **Explicit coupling schemes for a fluid-fluid interaction problem arising in hemodynamics**, published in SIAM Journal on Scientific Computing, 2014 [FGS14].

Contents

3.1 Introduction

In this chapter, we present several numerical experiments of the blood dynamics in an idealized aorta in order to illustrate the accuracy and performance of the schemes proposed in Chapter 2.

Our computational domains consist of the aortic root and the aortic arch. In the aortic root, only open valve leaflets are included, with no valve model. A more accurate study, including a valve model is lead in Chapter 4, where we discuss the case of the fluid-fluid interaction problem with a reduced order model for the aortic valve and its applications to stenotic cases.

The coronary arteries attached to the aortic sinus, here are not considered as outlets, even if they play a key-role in heart function and in the study of the heart failure (e.g. [CPS+11, KVCC+10, SPH01]). In general the resistance in the coronaries increases during systole, when the heart muscle contracts, and decreases during diastole, when the heart muscle relaxes.

In each outlets of the aortic arch, a (0D) three-elements Windkessel model is placed (e.g. [BCF13, MXA+12, VC06, WLW09]), to take into account the blood pressure generated by the neglected part of the cardiovascular system.

The hemodynamics applications of the coupled fluids problem is preceded by 2D numerical tests. One regards the instability of the explicit Dirichlet-Neumann scheme (Section 2.3 on page 36) and the second one analyses the influence of the stabilization parameters γ and γ_0, introduced with the Nitsche's interface method (Section 2.4 on page 38).

For comparison purposes, in all the 2D and 3D numerical examples, the following error indicators will be used:

$$\varepsilon_{x_i} := \frac{||x_i - x_{\text{ref}}||_{L^2(\Gamma)}}{||x_{\text{ref}}||_{L^2(\Gamma)}}, \quad \varepsilon_x := \frac{||x_1 - x_2||_{L^2(\Sigma)}}{||x_{\text{ref}}||_{L^2(\Sigma)}}. \tag{3.1}$$

The first indicator measures the relative error on a part of the boundary $\Gamma \subset \partial\Omega_i$ for the physical quantity x_i (defined in Ω_i), $i = 1, 2$. The second indicator gives the relative interface drop of the variable x across the interface Σ. The subscript $_{\text{ref}}$ indicates a quantity from the reference solution, obtained by solving Algorithm 2.1 and Algorithm 2.5 in the whole domain Ω with a standard conforming finite element method.

Outline This chapter is organized as follows. Two classes of numerical experiments are discussed. The first one, in Section 3.2, is about 2D test cases that show the implicit and explicit treatment of the Dirichlet-Neumann coupling conditions and analyze the impact of the stabilization parameters derived by Nitsche's method. The second type of numerical simulations are 3D examples of hemodynamics application to the aorta, Section 3.3. In particular the definition of the domains and the boundary conditions are reported in Section 3.3.1. In Section 3.3.2 we discuss in brief the techniques and the solvers we use to implement the partitioned algorithm for the fluid-fluid model. In Section 3.3.3 and 3.3.4 the numerical simulation of the algorithm presented in the previous chapter are reported. The

last Section 3.3.6 concerns the comparison between the static and the total pressure formulation of the reference models.

3.2 Two-dimensional test cases

In this section we carry out two numerical tests in a 2D domain. The first one in order to investigate the instability of the Dirichlet-Neumann coupled problem, the second one to fix Nitsche's method parameters.

For all tests, the convective non-linear terms are neglected, hence we consider two coupled 2D Stokes problems in a rectangular domain $[0,3]\times[0,3]\cup[3,6]\times[0,3]$, with space units in cm. A constant velocity $(400,0)^{\mathrm{T}}\ cm/s$ is imposed on the left boundary and zero traction on the right boundary. A no-slip condition is enforced on the upper and lower sides of the domain (Figure 3.1).

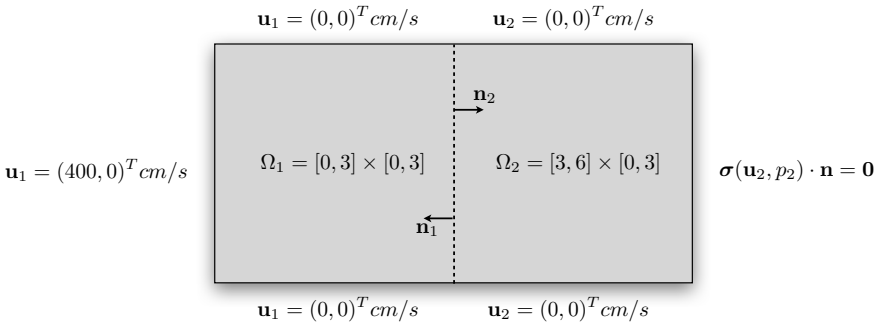

Figure 3.1: *Geometrical description and boundary conditions for the 2D test cases.*

The density $\rho = 1.06\ g/cm^3$ and the dynamic viscosity $\mu = 0.04\ poise$ are those typically encountered in blood flow simulations. The spatial discretization is based on $\mathbb{P}_1/\mathbb{P}_1$ stabilized finite elements. The time-step is $\tau = 10^{-4}\ s$, in a interval of $5.0\cdot 10^{-2}\ s$, and the space step is $h = 0.05\ cm$. All the numerical computations have been performed in FreeFem++ (see [Hec12]).

3.2.1 Implicit versus explicit Dirichlet-Neumann coupling conditions

Here the monolithic scheme reported in Algorithm 2.1 is compared with the Algorithm 2.2, whose kinetic/kinematic coupling conditions are explicitly treated.

Figure 3.2 compares the mean velocity and the mean pressure all over the domain obtained for the two algorithms. Notice the not stable behavior for velocity and pressure obtained with the explicit Dirichlet-Neumann coupled problem, Algorithm 2.2, due to the unbalance static powers across the interface.

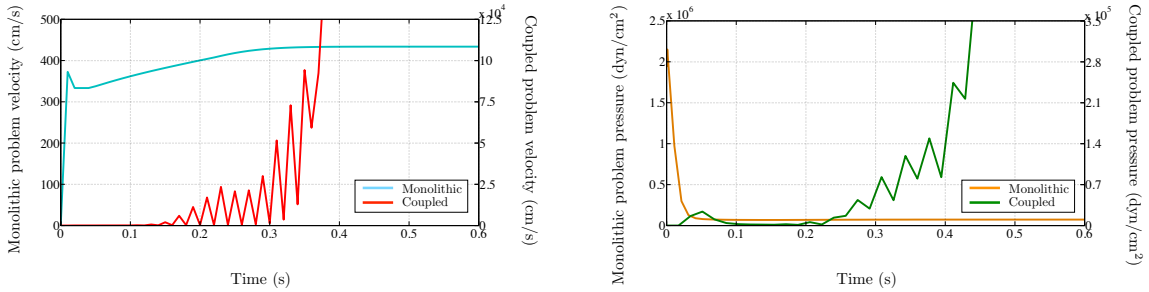

Figure 3.2: *Algorithm 2.1 (Monolithic) vs Algorithm 2.2 (Dirichlet-Neumann): mean velocity (left) and mean pressure (right).*

3.2.2 Impact of the stabilization parameters

We investigate now, the impact of the stabilization parameters γ and γ_0 on the accuracy of Algorithm 2.3.

We consider a two coupled 2D Stokes problems in the rectangular domain shown in Figure 3.1, with the same boundary condition described in the previous section. Note that in this case, only the interface pressure stabilization (2.30) is considered, since the convective non-linear terms are neglected. The tests are run with $\gamma_0 = 0,\ 1,\ 9,\ 16$ and $\gamma = 25,\ 250,\ 2500,\ 5000$.

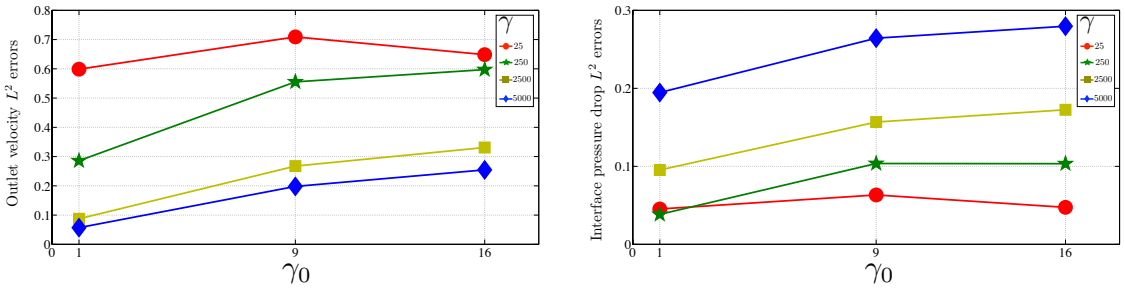

Figure 3.3: *Outlet velocity errors $\varepsilon_{\mathbf{u}_2}$ (left) and interface pressure drop errors ε_p (right).*

		γ			
		25	**250**	**2500**	**5000**
γ_0	**0**	X	X	X	X
	1	0.5987	0.2859	0.0873	0.0570
	9	0.7091	0.5554	0.2675	0.1980
	16	0.6485	0.5973	0.3310	0.2546

(a) *Outlet velocity errors $\varepsilon_{\mathbf{u}_2}$.*

		γ			
		25	**250**	**2500**	**5000**
γ_0	**0**	X	X	X	X
	1	0.0453	0.0384	0.0953	0.1946
	9	0.0633	0.1036	0.1568	0.2643
	16	0.0474	0.1034	0.1725	0.2796

(b) *Interface pressure drop errors ε_p.*

Table 3.1: *Stabilization parameters errors.*

In Figure 3.3, the relative error on the outlet velocity and on the pressure drop at the interface are plotted. These results suggest that the optimal choice of the parameters is $\gamma = 2500$ and $\gamma_0 = 1$, which gives a good compromise between the velocity and pressure errors (in particular $\varepsilon_{\mathbf{u}_2} = 0.0873$ and $\varepsilon_p = 0.0953$). The values for $\gamma_0 = 0$ are not reported

in Figure 3.3 since the corresponding numerical solution is unstable. This highlights the importance of the interface pressure stabilization (2.30).

The last 2D-test is performed in the same rectangular domain with the two optimal values of γ and γ_0 but neglecting the last term of (2.29), i.e. the consistent term that control the pressure contribution of the stress on the interface. In this case the outlet velocity error becomes $\varepsilon_{\mathbf{u}_2} = 0.1319$ and the interface pressure drop error is now $\varepsilon_p = 0.1082$. Even if the result remains stable, without considering this term an increasing of the errors can be noticed.

3.3 Three-dimensional aortic blood flow simulations

3.3.1 Domains and boundary condition

The computational domain is the 3D idealized geometry reported in Figure 3.4 (left), including the aortic root, with the valve, and the aortic arch. The two-domain partitioning is shown in Figure 3.4 (middle). This geometrical splitting is motivated by the fact that, in order to describe the blood dynamics through the valve, different modeling options can be incorporated within the aortic root Ω_1 (see, e.g., [AHSG12, dSGB08]). Here, for simplicity, the aortic valve is frozen in its open configuration (Figure 3.5). No-slip boundary conditions are imposed on the three leaflets of the valve.

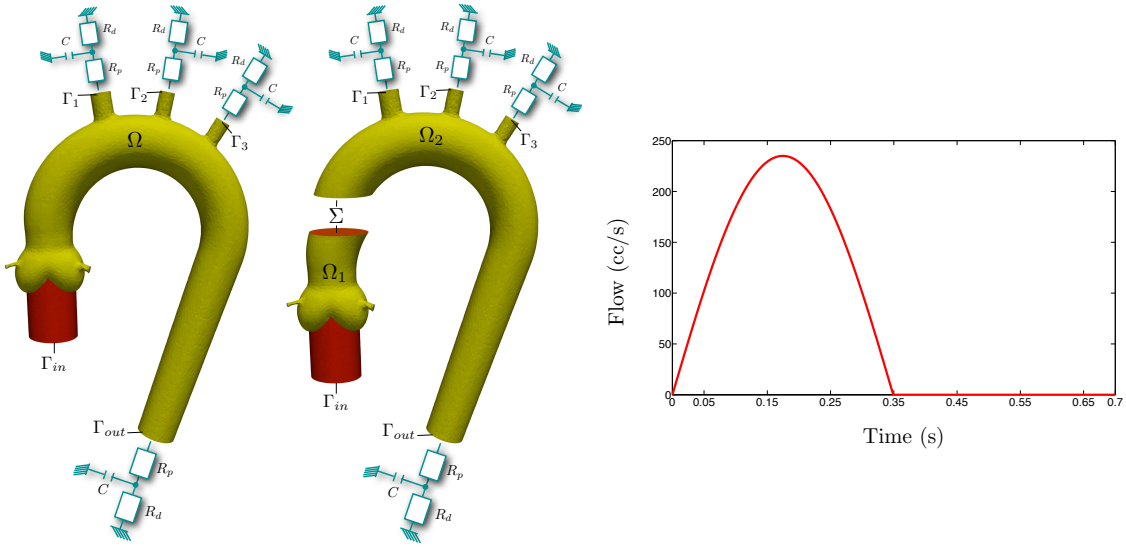

Figure 3.4: *Reference domain (left), sub-domains definition (middle) and inflow waveform (right).*

A sinusoidal waveform, see Figure 3.4 (right), is imposed on the inlet boundary Γ_{in}, this one has a diameter of $2\ cm$. The systolic phase, corresponding to the first half of the cardiac cycle, delivers a maximum flux of about $235\ cm^3/s$. In the second half (diastolic phase), the inlet flow is set to zero. The resulting cardiac output is approximatively $4.5\ dm^3/min$ and the heart rate is about 85 beats per minute.

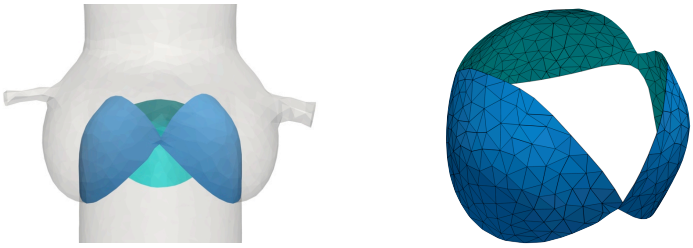

Figure 3.5: *Position in the sinus of the aortic root and mesh of the aortic valve in the open configuration.*

The outlets Γ_1, Γ_2 and Γ_3 correspond to the brachiocephalic artery, left common carotid and subclavian artery, respectively[1]. The outlet Γ_{out} is located in the descending aorta. The neglected portions of the circulation are taken into account by (explicitly) imposing the natural boundary condition $\boldsymbol{\sigma}\mathbf{n} = -P_p\mathbf{n}$ on each outlet. The proximal pressure P_p is described by a (0D) three-element Windkessel model (see, e.g., [BCF13, MXA+12, VC06, WLW09]) given by the ODE:

$$CR_d\frac{\mathrm{d}P_p}{\mathrm{d}t} + P_p = Q(R_d + R_p) + CR_pR_d\frac{\mathrm{d}Q}{\mathrm{d}t}, \tag{3.2}$$

obtained through analogies with electrical circuits (see Figure 3.6), where Q stands for the outlet flow rate, R_p and R_d denote the proximal and distal resistances and C is the capacitance representing the compliance of the blood vessels. The Windkessel parameters are reported in Table 3.2.

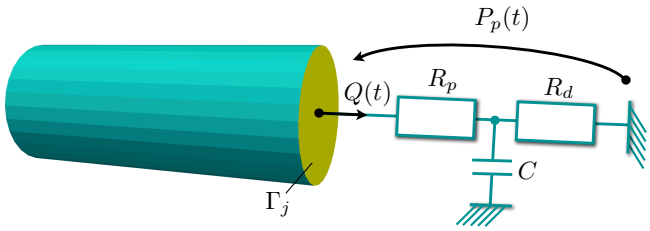

Figure 3.6: *Electric circuit modeling the Windkessel effect.*

	Γ_1	Γ_2	Γ_3	Γ_{out}
R_p $(dyn \cdot s \cdot cm^{-5})$	0.05×10^4	0.19×10^4	0.075×10^4	0.015×10^4
R_d $(dyn \cdot s \cdot cm^{-5})$	0.85×10^4	3.22×10^4	1.25×10^4	0.25×10^4
C $(cm^5 \cdot dyn^{-1})$	0.95×10^{-4}	0.25×10^{-4}	0.64×10^{-4}	3.17×10^{-4}

Table 3.2: *Windkessel parameters for idealized aorta test cases.*

[1] See also Figure 1.9 on page 20 for some details

For simplicity, the left and right coronaries, located in the aortic sinus, are closed. The physical parameters for blood are chosen as $\rho = 1.06\ g/cm^3$ and $\mu = 0.04\ poise$.

The space discretization is based on $\mathbb{P}_1/\mathbb{P}_1$ finite elements, stabilized with the SUPG/PSPG method (e.g. [Tez92, TO00]). The stabilization parameters are $\gamma = 2500$ and $\gamma_0 = 1$. For comparison purposes, the reference solution has been generated by solving Algorithm 2.1 and Algorithm 2.5. The meshes of Ω, Ω_1 and Ω_2 are, respectively, made of $177\ 651$, $53\ 960$ and $126\ 200$ tetrahedra. Six cardiac cycles have been simulated, using a time-step length of $\tau = 10^{-3}s$.

3.3.2 Master-slaves approach for two fluids coupled problem

Every compartment is supposed to be implemented as an independent software component, a master code, called CVGraph, takes care of the communications between the two compartments (Figure 3.7). This code has been started with the beginning of this thesis and is written in C++ language. The message passing between master and slaves solvers is done using MPI protocol.

The coupling is a two-way type: each compartment influences the other one at every time step. The coupling is a "Gauss-Seidel type", by analogy with the well-known method for the linear systems, i.e. the two solvers exchange their data simultaneously. Since we deal with loosely coupled schemes, the exchanges are done only once per time step.

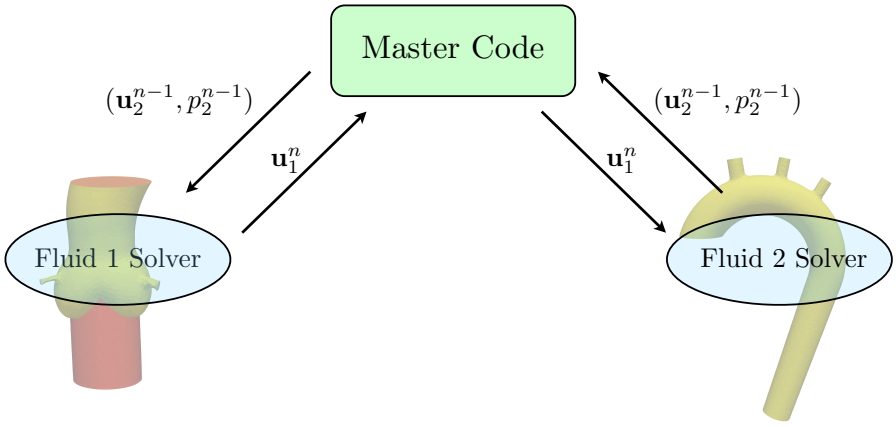

Figure 3.7: *Master-Slaves approach for fluid-fluid coupled model.*

Both the two fluid models are solved using the finite element solver FELiScE[2]. The connections between the two solvers are governed by the Robin-Robin conditions (e.g. (2.31)). In a generic time instant t^n, the velocity computed at interface by the Fluid 1 solver is sent, through the master code, to the Fluid 2 solver. The solution of this one computed on the interface is sent to the master code, who update time and send back it to the first solver to compute the solution in a new time step.

[2] http://felisce.gforge.inria.fr

The two solvers are supposed to be calibrated with the same time step or alternatively, the master code should take care of an interpolation in time as well. The interface mesh in the two domain is conform and the solution is imposed in each node of the interface.

3.3.3 Static pressure formulations

In this paragraph the results obtained with Algorithms 2.3 and Algorithms 2.4 are compared with the reference solution, obtained by solving (2.5) with a standard conforming finite element method. Its time-advancing scheme is summarized in Algorithm 2.1.

Figure 3.8 displays the snapshots of the velocity magnitude during the third cardiac cycle at two time instants in the systole, $t = 1.575\ s$ and $t = 1.662\ s$. While Figure 3.9 displays two time instants in the diastole, $t = 1.750\ s$ and $t = 1.925\ s$. The images depict the velocity profile, in a range of $0.0\ cm/s$ and $150.0\ cm/s$. The solution obtained with Algorithm 2.3 is close to the reference solution (Algorithm 2.1) on the interface and on the outlets. Note that even if we were not able to prove its energy stability (Proposition 2.2), the simulation is stable in this test case. Algorithm 2.4 yields a mass leak on the interface and has very poor results at the outlets. This is due to the non-consistent terms (2.35) and (2.36). This behavior is more visible at high velocity, i.e., in the systole phase.

Figures 3.10a and 3.10b show the interface flow rate and pressure in Ω_1 and Ω_2, obtained with Algorithms 2.3 and 2.4, respectively. The results provided by Algorithm 2.3 are clearly more accurate than those obtained with Algorithm 2.4. This can also be inferred from the error indicators reported in Table 3.3.

ε_{f_1}	0.0048	ε_{p_1}	0.0135
ε_{f_2}	0.0123	ε_{p_2}	0.0140
ε_f	0.0153	ε_p	0.0013

(a) *Algorithm 2.3.*

ε_{f_1}	0.0048	ε_{p_1}	0.1864
ε_{f_2}	0.1058	ε_{p_2}	0.1866
ε_f	0.1054	ε_p	0.0012

(b) *Algorithm 2.4 .*

Table 3.3: *Interface relative errors: flow ε_{f_1}, ε_{f_2} and pressure ε_{p_1}, ε_{p_2}. Interface drop errors: flow ε_f and pressure ε_p.*

The same behavior is observed for the flow rate and the pressure at the outlets. Figures 3.11a and 3.11b and Figures 3.12a and 3.12b compare the reference solution obtained from Algorithm 2.1, with the results obtained with the staggered algorithms in the three top arteries and the descending aorta. As shown by Table 3.4, the flow rate and pressure errors obtained with Algorithm 2.3 are between 1% and 5%, whereas with Algorithm 2.4 we get a 20% error.

REMARK 3.1
The results obtained with Algorithm 2.1 and with Algorithm 2.3 present spurious back flow phenomenon that does not impact the performance of the presented method. The reversal flow can be controlled using some of the techniques reported in the literature (e.g.[BGH+09, MBH+11, BC14]).

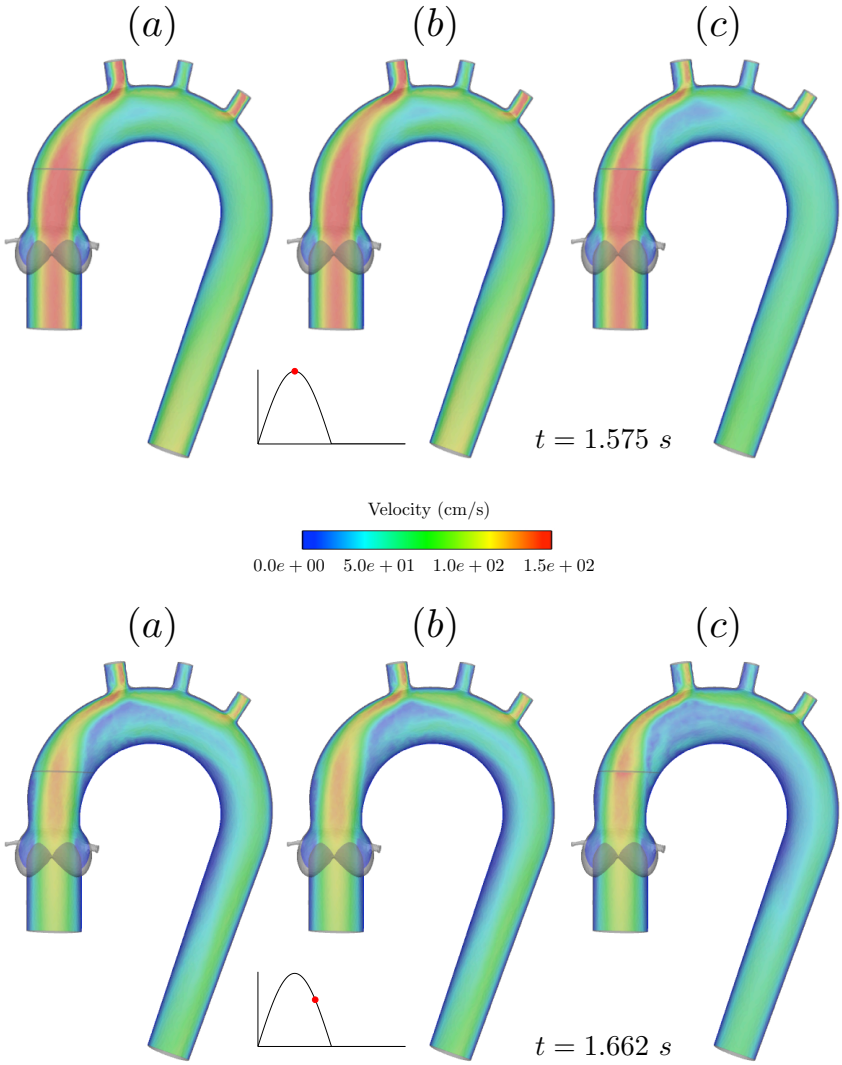

Figure 3.8: *Static pressure formulation. Snapshots of the velocity magnitude at two time instants in systole obtained with: (a) Algorithm 2.3; (b) Algorithm 2.1; (c) Algorithm 2.4.*

	Γ_1	Γ_2	Γ_3	Γ_{out}
ε_{f_2}	0.0589	0.0596	0.0488	0.0411
ε_{p_2}	0.0115	0.0121	0.0111	0.0122

(a) *Algorithm 2.3.*

	Γ_1	Γ_2	Γ_3	Γ_{out}
ε_{f_2}	0.2171	0.2237	0.2003	0.2185
ε_{p_2}	0.1822	0.1843	0.1797	0.1828

(b) *Algorithm 2.4*

Table 3.4: *Outputs flow ε_{f_2} and pressure ε_{p_2} errors.*

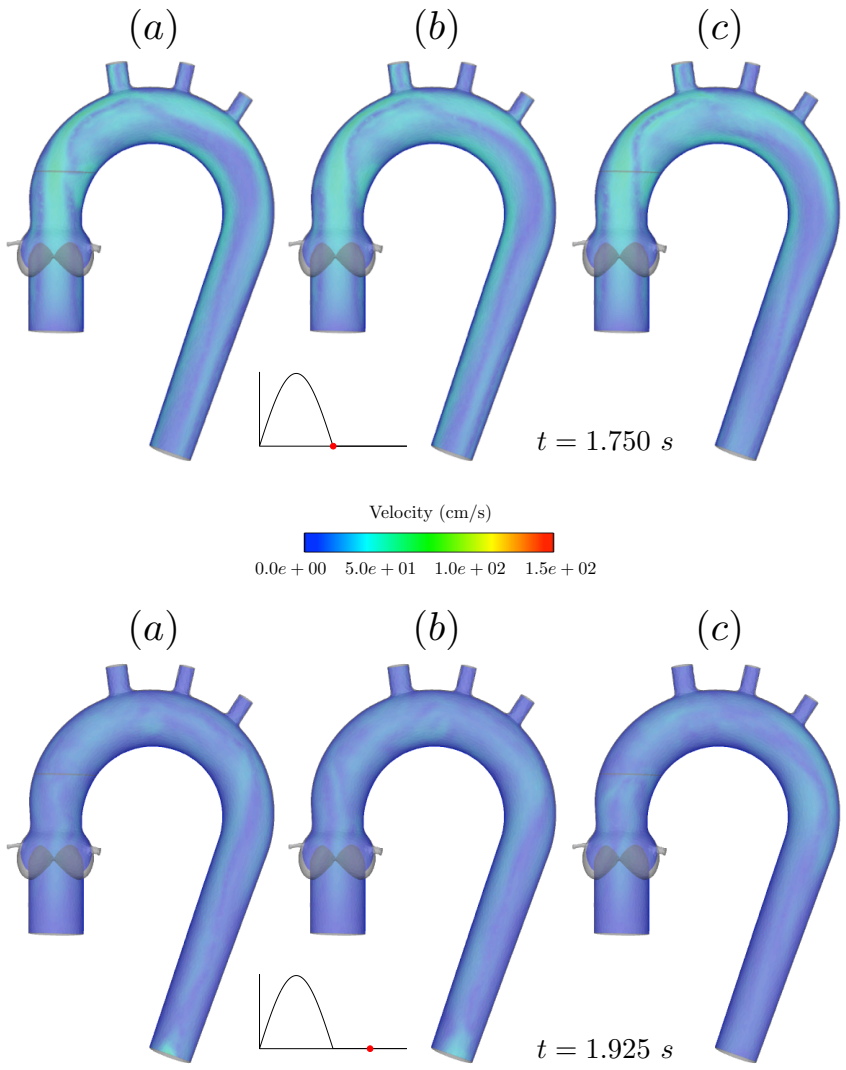

Figure 3.9: *Static pressure formulation. Snapshots of the velocity magnitude at two time instants in diastole obtained with: (a) Algorithm 2.3; (b) Algorithm 2.1; (c) Algorithm 2.4.*

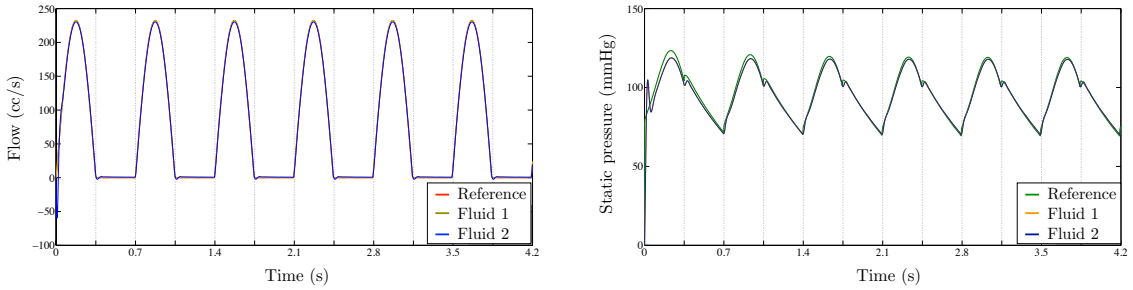

(a) *Algorithm 2.1 vs Algorithm 2.3.*

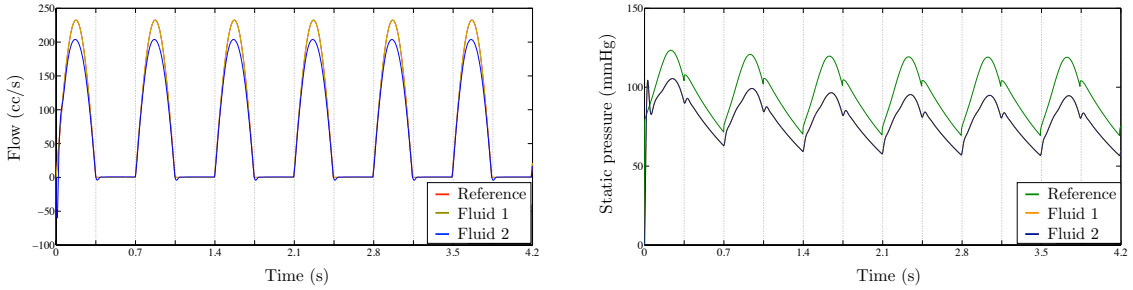

(b) *Algorithm 2.1 vs Algorithm 2.4.*

Figure 3.10: *Interface flows and pressures.*

3.3.4 Total pressure formulation

The results obtained with Algorithm 2.6 are presented in this paragraph. Figure 3.13 shows snapshots taken at two time instants in the systole and two time instant in the diastole in the third cardiac cycle, for the explicit algorithm with the total pressure and the reference solution obtained by the discretization of (2.40), using a standard conforming finite element method. Its time-advancing scheme is reported in Algorithm 2.5. Note the good agreement of the results on the interface and at the outlets.

ε_{f_1}	0.0053	ε_{π_1}	0.0321
ε_{f_2}	0.0266	ε_{π_2}	0.0415
ε_f	0.0286	ε_π	0.0113

Table 3.5: *Interface relative errors: flow ε_{f_1}, ε_{f_2} and total pressure ε_{π_1}, ε_{π_2}. Interface drop errors: flow ε_f and total pressure ε_π.*

	$\boldsymbol{\Gamma_1}$	$\boldsymbol{\Gamma_2}$	$\boldsymbol{\Gamma_3}$	$\boldsymbol{\Gamma_{\text{out}}}$
ε_{f_2}	0.0853	0.0926	0.0714	0.0670
ε_{π_2}	0.0295	0.0311	0.0276	0.0284

Table 3.6: *Algorithm 2.6: Outlet flow ε_{f_2} and total pressure ε_{π_2} errors.*

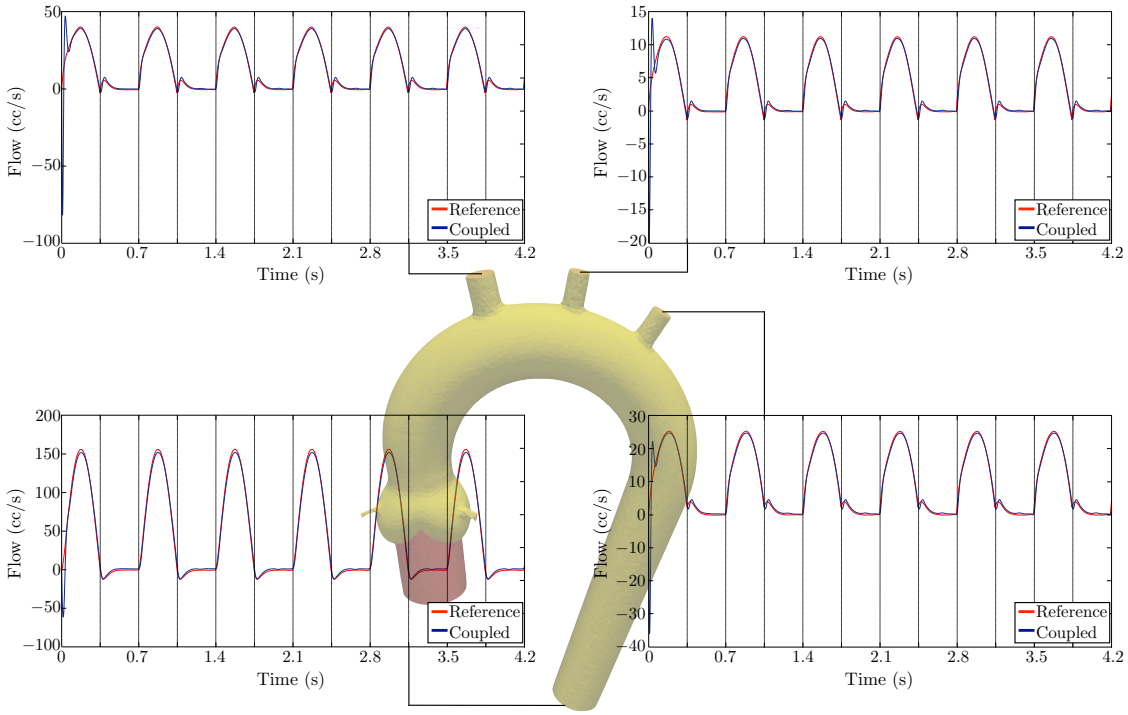

(a) *Flows.*

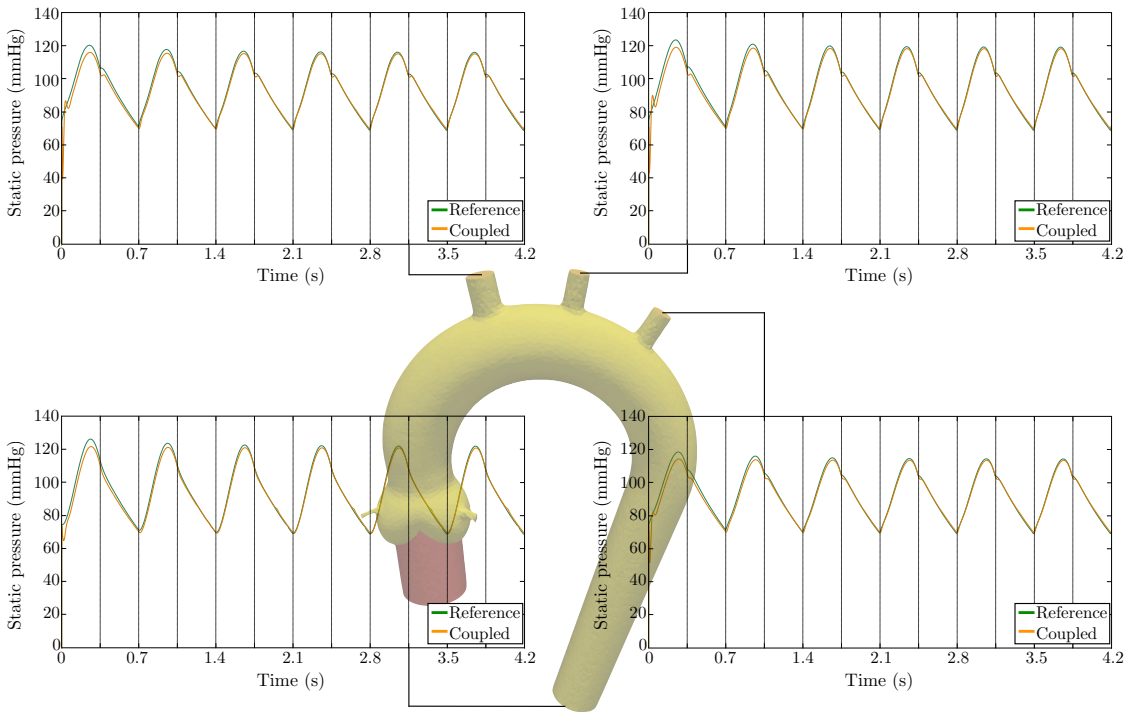

(b) *Static pressures.*

Figure 3.11: *Algorithm 2.1 vs. Algorithm 2.3 Outputs.*

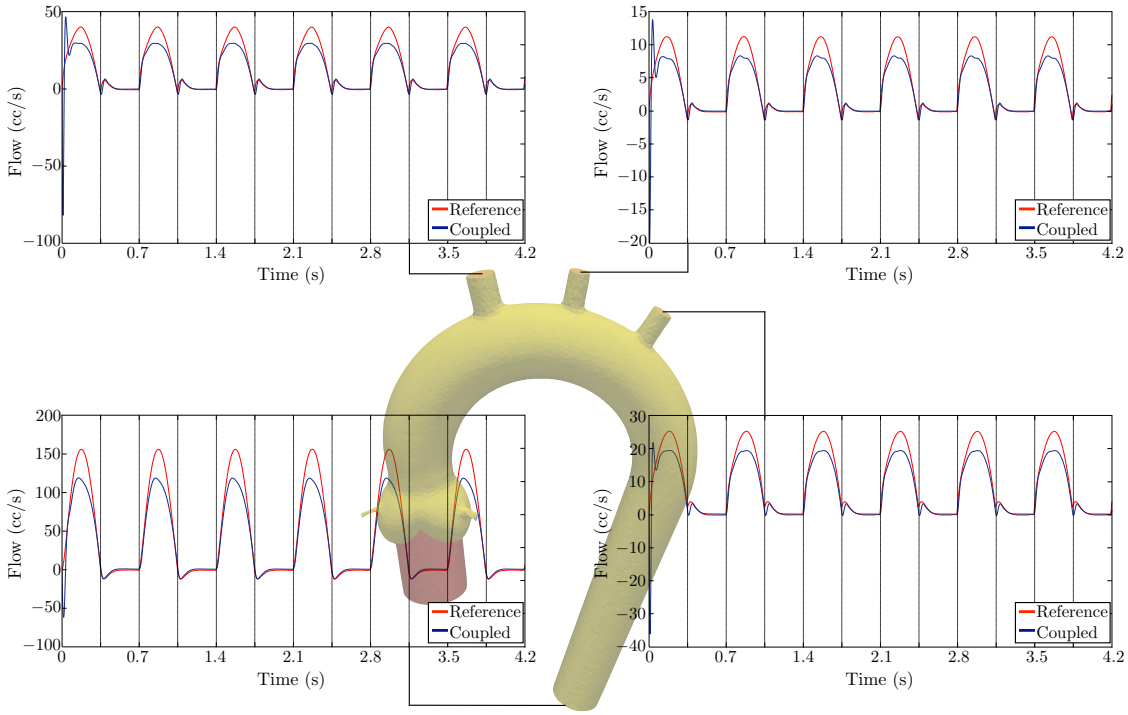

(a) *Flows.*

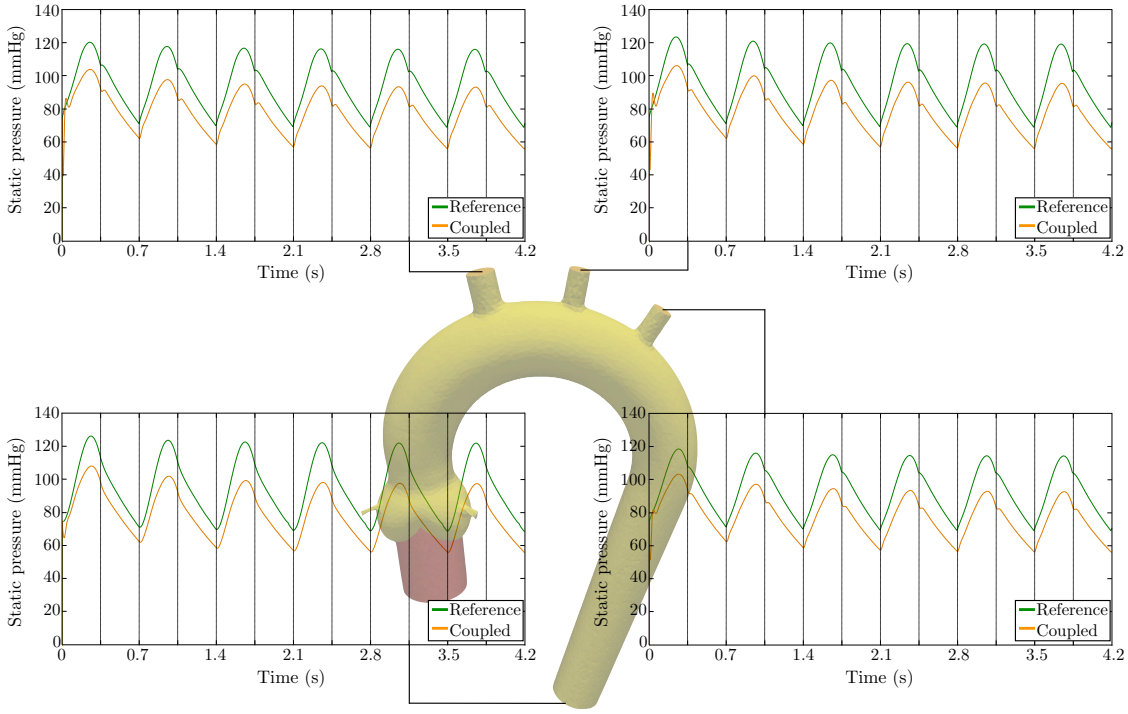

(b) *Static pressures.*

Figure 3.12: *Algorithm 2.1 vs. Algorithm 2.4 Outputs.*

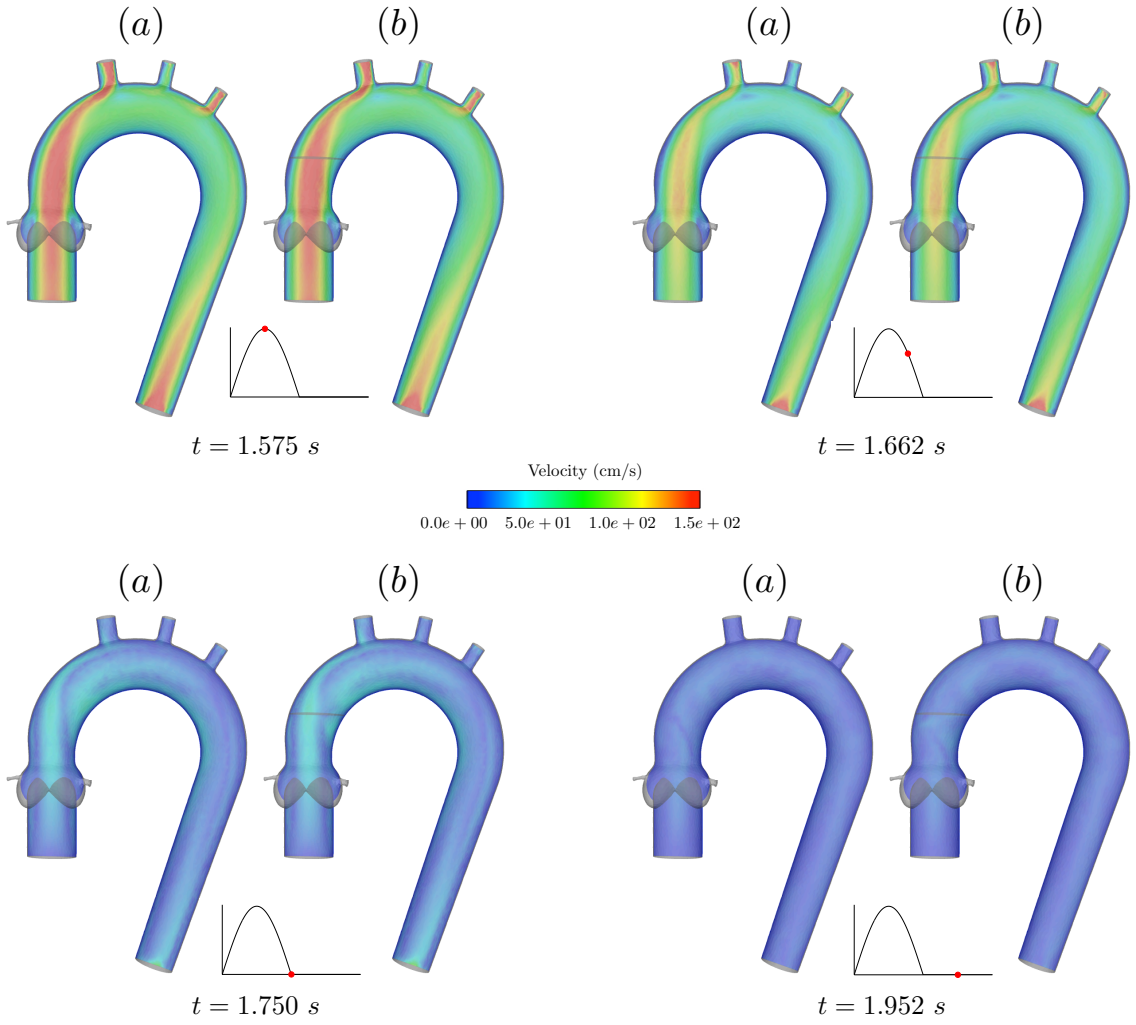

Figure 3.13: *Total pressure formulation. Snapshots of the velocity magnitude at two time instants in systole (top) and two time instant in diastole (bottom) obtained with: (a) Algorithm 2.5 and (b) Algorithm 2.6.*

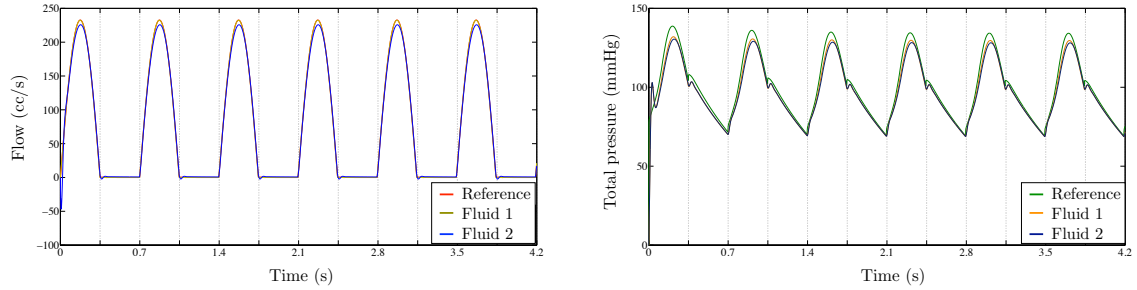

Figure 3.14: *Algorithm 2.5 vs Algorithm 2.6: interface flows (left) and total pressures (right).*

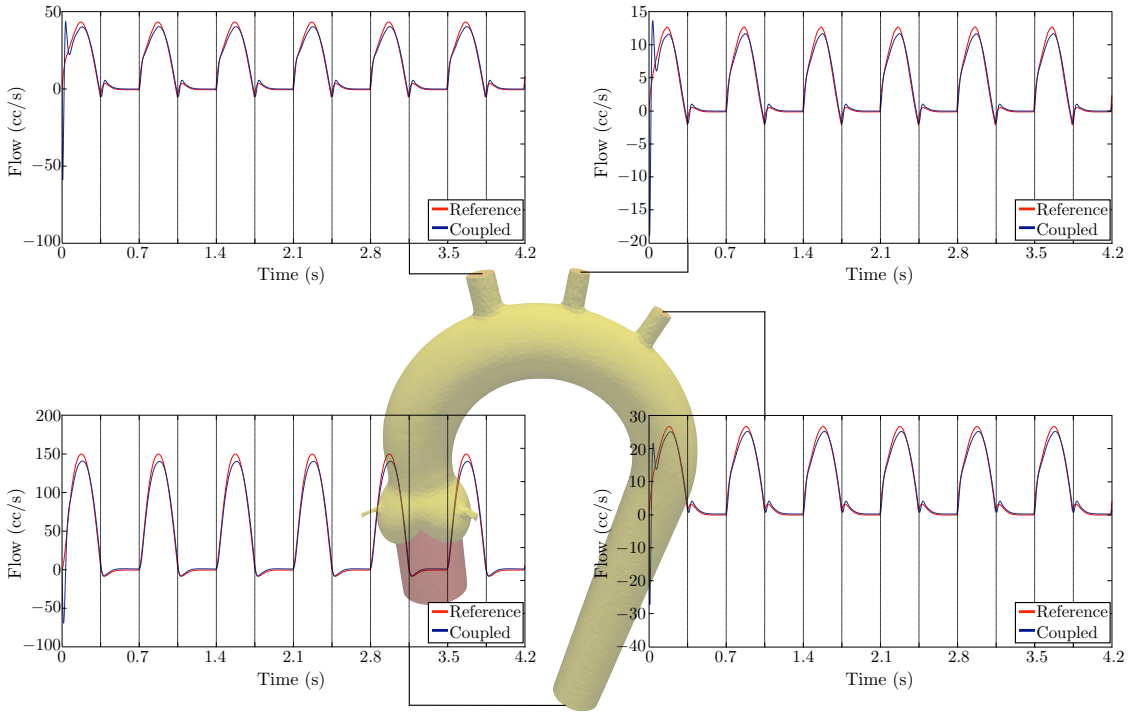

(a) *Flows.*

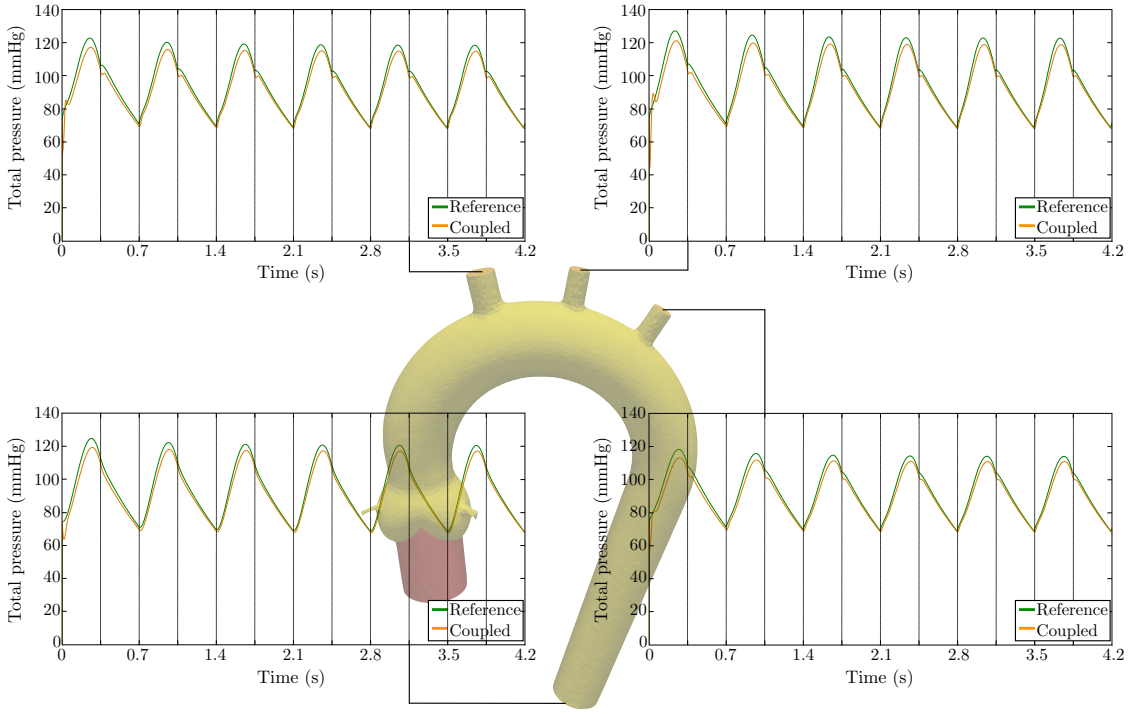

(b) *Total pressures.*

Figure 3.15: *Algorithm 2.6 Outputs.*

Figure 3.14 depicts the flow rate, on the left, and the pressure, on the right, for Fluid 1 and the Fluid 2, compared with the reference solution on the interface. Except very slight differences for Fluid 2 in the peak of the systole and at the beginning of the diastole, the flow rate and the pressure drop between the two fluids are around 2.28% and 1.33% respectively (Table 3.5).

The same behavior can be observed for the flow rate and the pressure at the outlets (Figure 3.15a and 3.15b). Discrepancies still arise at the maximum of the systoles and at the beginning of the diastoles. The errors in these cases remain between 6% and 9% for the flow rate and around 3% for the pressure (Table 3.6).

In our implementation, and for this specific test case (with an unbalanced number of degrees of freedom in the two sub-domains), the staggered solutions were typically 30% faster than the monolithic ones.

3.3.5 Inverted sub-problems and three sub-domains test cases

As additional tests, the staggered Algorithm 2.3 is tested in the physical configuration described in Section 3.3.3 but with two different repartitions of the sub-domains. The first one is obtained inverting the two sub-problems, i.e the Fluid 1 (2.28) is solved in the aortic arch and and the Fluid 2 (2.29) is solved in the aortic root. In the second test case the domain Ω is split in three non-overlapping sub-domains, the Fluid 1 is solved in the aortic arch, and the Fluid 2 in the aortic root and in the descending aorta. These two new tests are compared with the two-domain test case of Section 3.3.3. The velocity magnitude is shown in two instants of time in systole (Figure 3.16) and two instants of time during diastole (Figure 3.17).

The three numerical examples are in very good agreement. This is confirmed if we look at Figure 3.18a and Figure 3.18b, in which the flow and pressure course in the outlets are compared. The flow and pressure errors in the outlets are reported in Table 3.7.

Inverted sub-problems

	Γ_a	Γ_b	Γ_c	Γ_{out}
ε_{f_2}	0.0707	0.0729	0.0583	0.0583
ε_{p_2}	0.0237	0.0248	0.0230	0.0240

Three sub-domains

	Γ_a	Γ_b	Γ_c	Γ_{out}
ε_{f_2}	0.0875	0.0940	0.0777	0.0838
ε_{p_2}	0.0279	0.0317	0.0276	0.0318

Table 3.7: *Outlet flow ε_{f_2} and static pressure ε_{p_2} errors.*

With respect to ε_{f_2} and ε_{p_2} of Algorithm 2.3 presented in Table 3.4, a slight increasing of the errors can be observed. As expected the error increases with the number of the domain partitions.

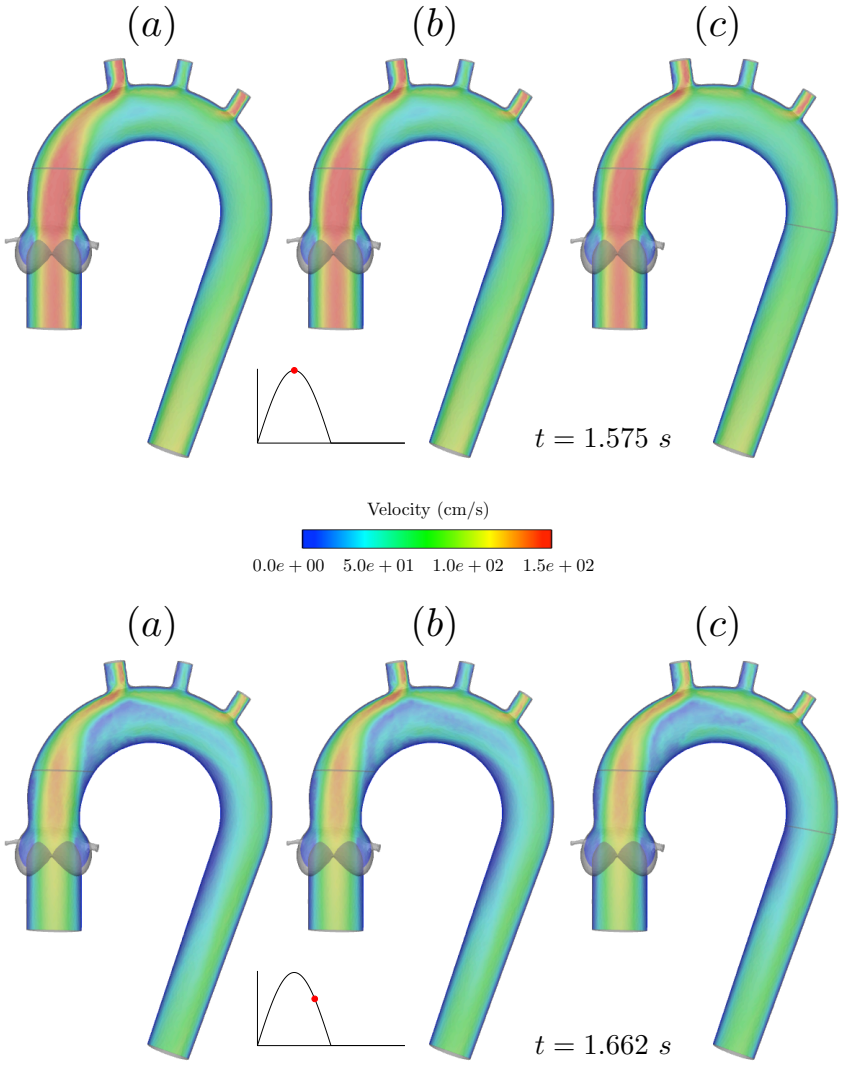

Figure 3.16: *Static pressure formulation. Snapshot of the velocity magnitude at two time instants in systole obtained with Algorithm 2.3 in two non-overlapping sub-domains (a), with inverted sub-problems (b) and in three non-overlapping sub-domains (c).*

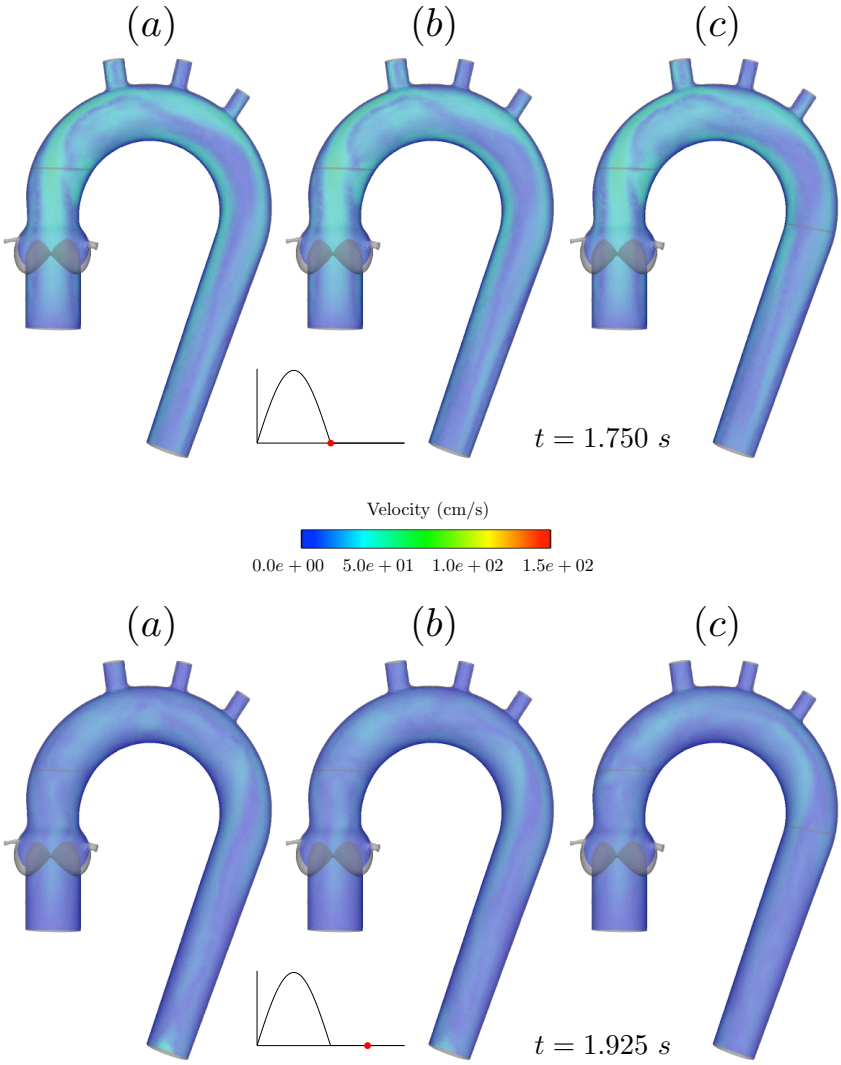

Figure 3.17: *Static pressure formulation. Snapshot of the velocity magnitude at two time instants in diastole obtained with Algorithm 2.3 in two non-overlapping sub-domains (a), with inverted sub-problems (b) and in three non-overlapping sub-domains (c).*

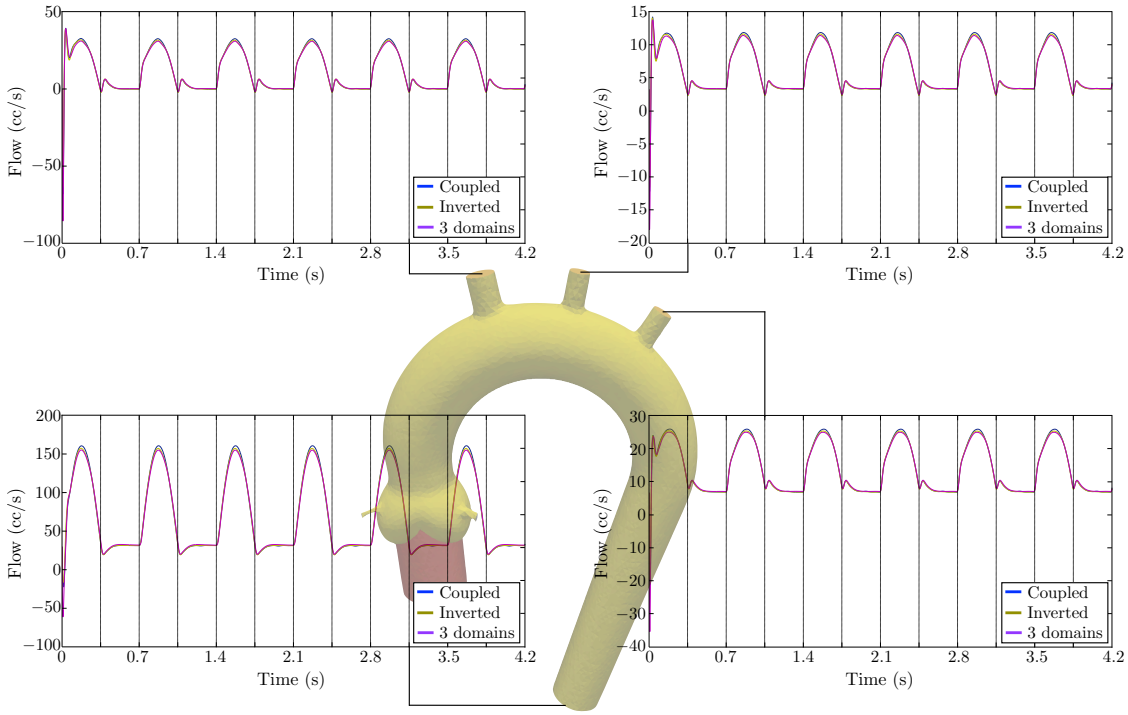

(a) *Flows.*

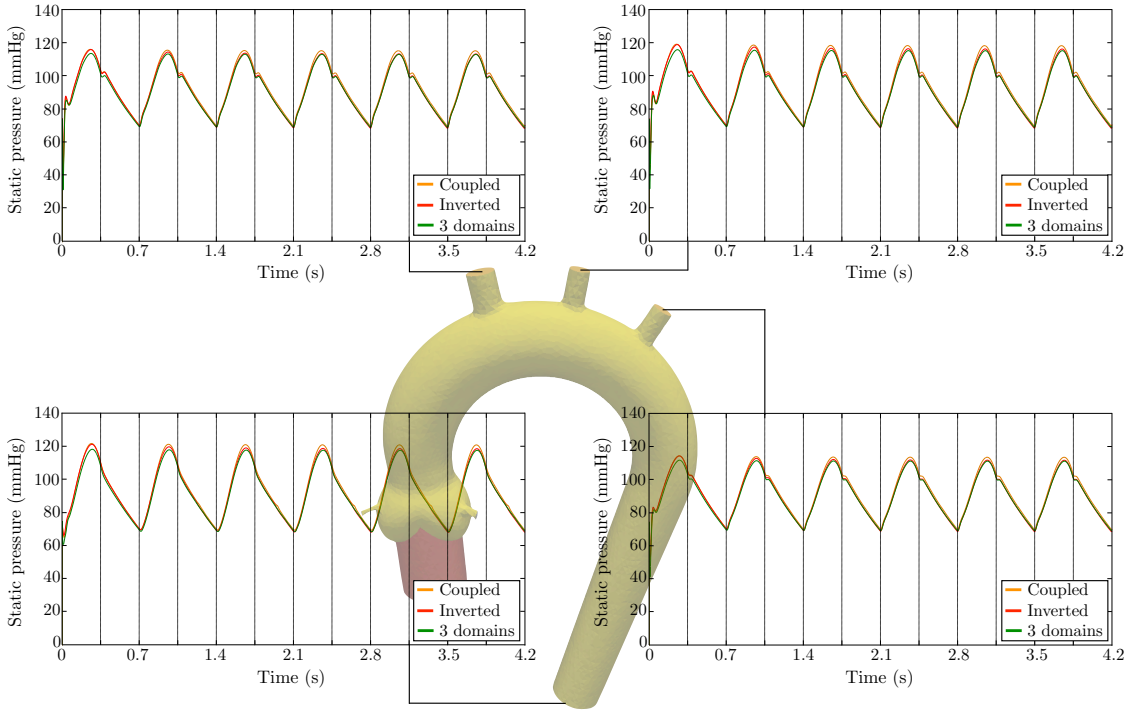

(b) *Total pressures.*

Figure 3.18: *Algorithm 2.3, inverted sub-problems and three sub-domains outlets*

3.3.6 Static pressure versus total pressure formulation

We conclude the numerical examples of the present chapter with the comparison between the two reference models. The first one is obtained discretizing the static pressure problem (2.1) (page 35 of Chapter 2), and the second one obtained from the discretization of the total pressure problem (2.40) (page 51 of Chapter 2). Both models are discretized with standard finite element method and computed in the one-piece domain shown in Figure 3.4 (left). Their time-advancing scheme are reported in Algorithm 2.1 and Algorithm 2.5, respectively.

Figure 3.19 shows the velocity vectors for the two reference models in two time instants of systole and two of diastole. Note the velocity vectors in the outputs during diastole. The total pressure formulation presents the intersection of the vectors caused by the kinetic energy in the pressure variable (see [HRT96]).

This feature is more visible in Figure 3.20 where the velocity patterns of the two reference models are plotted in the four outlets. During the diastole the total pressure formulation presents higher velocities respect the static pressure formulation. During the systole the velocity magnitude is similar in the three top arteries. In Γ_{out}, the descending aorta, back-flow effects appear with the static pressure reference model while they can be controlled if we use the total pressure formulation.

The total pressure formulation is commonly used to stabilize back-flow phenomena when present in the outlets, for this reason the *curl* $\mathbf{u} \times \mathbf{u}$ *formulation* is generally preferred because it changes the static pressure variable only on the outlets and not in all the domain, on this topic see for example the already cited works [BCMP88, FMN07, LMN+09, PZVP12, VV05]. The formulation used in this work, also said "Bernoulli pressure" formulation from the well known principle, is applied to obtain an energy estimation, as we did in the fluid-fluid model presented in Section 2.5.4 on page 51.

3.4 Final remarks

In this chapter we have discussed the numerical simulations of the methods presented in Chapter 2.

With the first 2D numerical test, we have shown the instability generated by an explicit Dirichelet-Neumann coupled scheme. The second 2D numerical test highlights the importance of the interface pressure stabilization (2.30), introduced in Paragraph 2.5.2, governed by the parameter γ_0: the numerical solutions corresponding to $\gamma_0 = 0$ are unstable, for any values of the parameters γ.

For the non-linear 3D numerical tests the parameters are choses as $\gamma = 2500$ and $\gamma_0 = 1$. The first one is within the range predicted by the stability condition (2.32c) and (2.50c), for the static and total pressure case, respectively. For the pressure penalty parameter γ_0, the numerical tests showed that the stability condition (2.32a) and (2.50a) overestimates its critical value. In practice, we can take a lower value without compromising stability.

After having shown the numerical simulation of the several explicit scheme presented in Chapter 2, we can conclude that

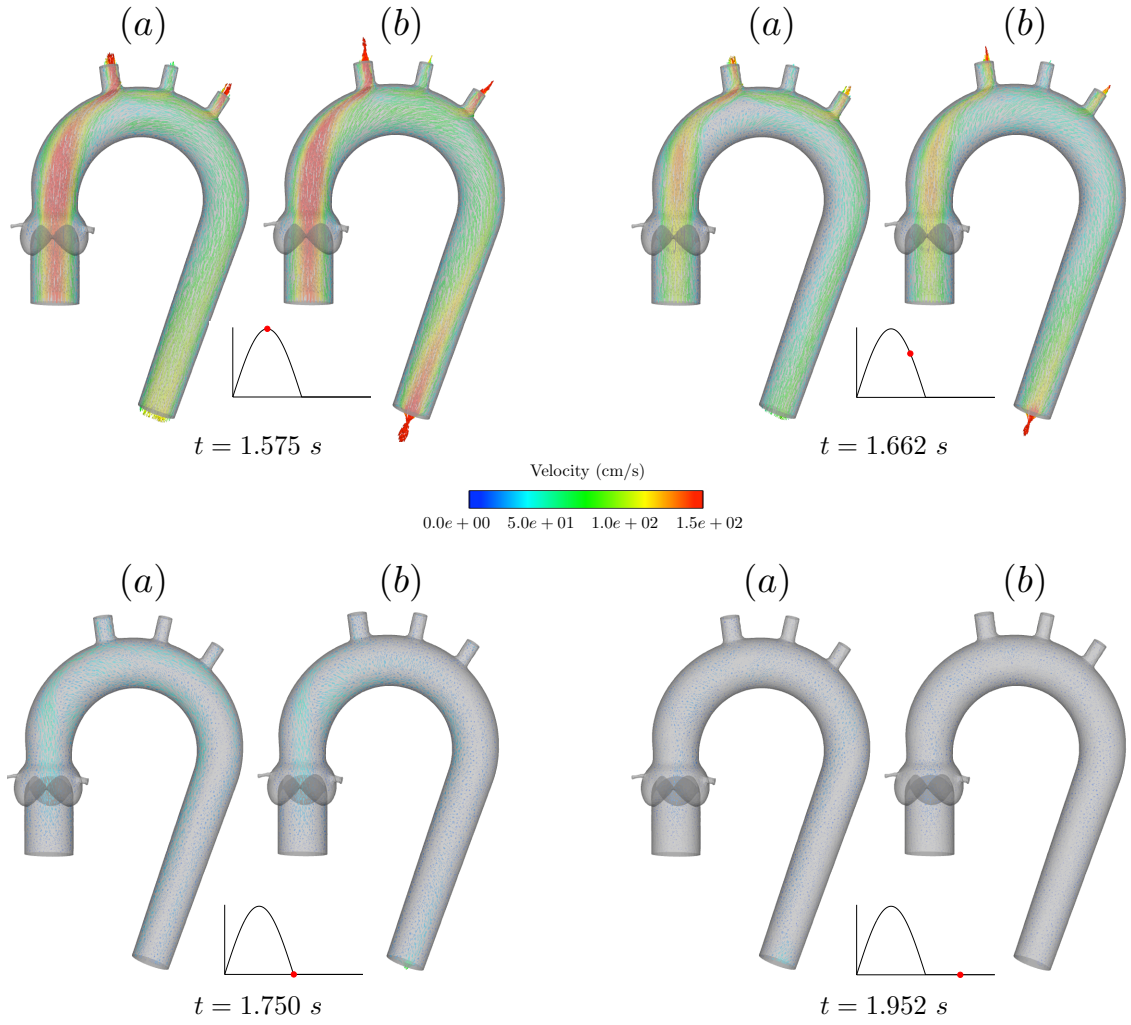

Figure 3.19: *Reference solutions. Snapshot of the velocity vectors at two time instants in systole (top) and two time instant in diastole (bottom), obtained with: (a) Algorithm 2.1 (static pressure formulation) and (b) Algorithm 2.5 (Total pressure formulation).*

- *Algorithm 2.3* (on page 45 in Paragraph 2.5.2): even if the energy stability cannot a priori be guaranteed for the standard static pressure formulation, extensive numerical evidence has shown that the scheme is robust and accurate, with respect to a fully implicit method. In addition, if in the Algorithm 2.3 the two terms $C_1[\mathbf{u}_{1,h}^{n-1}; (\mathbf{u}_{1,h}^{n}, \mathbf{u}_{2,h}^{n-1}), \mathbf{v}_{1,h}]$ and $C_2[(\mathbf{u}_{2,h}^{n-1}, \mathbf{u}_{1,h}^{n-1}); (\mathbf{u}_{2,h}^{n}, \mathbf{u}_{1,h}^{n}), \mathbf{v}_{2,h}]$ are not considered, the energy stability remains not verified and the numerical simulations have shown that in this case the accuracy of the method is not changed (see Table 3.8 for the interface errors and Table 3.3a on page 68 for comparisons).

- *Algorithm 2.4* (on page 50 in Paragraph 2.5.3): the numerical results have confirmed the poor accuracy of this scheme since it is not consistent with the original coupled problem.

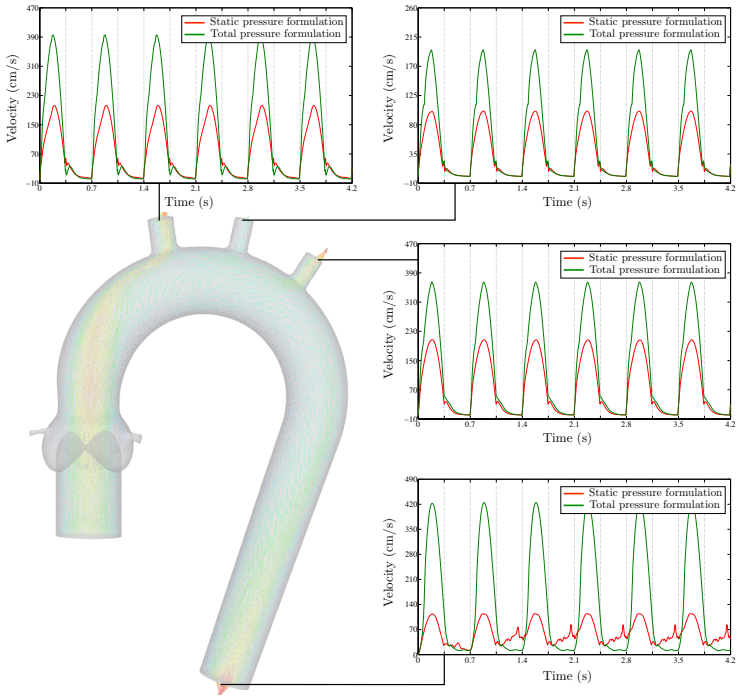

Figure 3.20: *Reference solutions. Outlets maximum velocity obtained with Algorithm 2.1 (static pressure formulation) and Algorithm 2.5 (total pressure formulation).*

ε_{f_1}	0.0048	ε_{p_1}	0.0146
ε_{f_2}	0.0138	ε_{p_2}	0.0152
ε_f	0.0168	ε_p	0.0015

Algorithm 2.3 without C_1 and C_2.

Table 3.8: *Interface relative errors: flow ε_{f_1}, ε_{f_2} and pressure ε_{p_1}, ε_{p_2}. Interface drop errors: flow ε_f and pressure ε_p.*

- *Algorithm 2.6* (on page 52 in Paragraph 2.5.3): the comparison with fully coupled solutions have shown that the method gives satisfactory results, in agreement with the energy estimate guaranteeing the stability of the splitting.

The staggered algorithms are not symmetric from the point of view of the boundary conditions. The overall accuracy of the schemes is not expected to be perturbed since the ordering of the sub-problems does not change the numerical dissipation of the scheme. Nevertheless, a test case has been discussed in Section 3.3.5. In this experiment, we compared the results of Algorithm 2.3 presented in Section 3.3.3 with the results obtained by inverting the two sub-problems, i.e the Fluid 1 is solved in the aortic arch and and the Fluid 2 is solved in the aortic root. For this test case, in spite of strong geometrical asymmetry, swapping the two sub-problems gave almost the same result with a slight increase of the errors.

We have considered Algorithm 2.3, which has the best accuracy among the schemes presented, in a computational domain partitioned in three non-overlapping sub-domains (Section 3.3.5). The results have shown that the error is slightly larger in this case. In fact, although not addressed, the overall convergence rate of the schemes is not expected to be affected by the number of sub-domains. But the constant of the error (and hence accuracy) would actually depend on this and becomes more visible for a relatively large number of sub-domains.

In the end in paragraph 3.3.6 we have shown how a total pressure formulation in the hemodynamics study can generate non-physiological results caused by the velocity in the outlets. For this reason, in the following study we use Algorithm 2.3 rather than Algorithm 2.4.

In the Chapters which follow, we will show that the domain representing the aortic root could be replaced by a fluid model of the heart, based on a different code. In this configuration, the weak coupling strategy proposed and the master-slave approach presented in Section 3.3.2 would be particularly appealing.

Bibliography of Chapter 3

[AHSG12] M. Astorino, J. Hamers, S. C. Shadden, and J.-F. Gerbeau. A robust and efficient valve model based on resistive immersed surfaces. *Int. J. Numer. Meth. Biomed. Engng.*, 28:937–959, 2012.

[BC14] C. Bertoglio and A. Caiazzo. A tangential regularization method for backflow stabilization in hemodynamics. *Journal of Computational Physics*, 261:162–171, 2014.

[BCF13] C. Bertoglio, A. Caiazzo, and M. A. Fernández. Fractional-step schemes for the coupling of distributed and lumped models in hemodynamics. *SIAM Journal on Scientific Computing*, 35:551–575, 2013.

[BCMP88] C. Begue, C. Conca, F. Murat, and O. Pironneau. Les équations des stokes et de Navier-Stokes avec des conditions limites sur la pression (on Stokes and Navier-stokes equations with boundary condition on the pressure). *Nonlinear partial differential equations and their applications, Lect. Coll. de France Semin., Paris/Fr. 1985-86, Pitman Res. Notes Math. Ser. 181*, IX:179–264, 1988.

[BGH+09] Y. Bazilevs, J.R. Gohean, T.J.R. Hughes, R.D. Moser, and Y. Zhang. Patient-specific isogeometric fluid-structure interaction analysis of thoracic aortic blood flow due to implantation of the Jarvik 2000 left ventricular assist device. *Comput. Methods Appl. Mech. Engng.*, 198:3534–3550, 2009.

[CPS+11] P. Chuchard, T. Puapansawat, T. Siriapisith, Y. H. Wu, and B. Wiwatanapataphee. Numerical simulation of blood flow through the system of coronary

arteries with diseased left anterior descending. *International Journal of Mathematics and Computers in Simulation*, 5:334–341, 2011.

[dSGB08] N. Diniz dos Santos, J.-F. Gerbeau, and J.-F. Bourgat. A partitioned fluid-structure algorithm for elastic thin valves with contact. *Comput. Methods Appl. Mech. Engrg.*, 197(19-20):1750–1761, 2008.

[FGS14] M. Fernández, J. Gerbeau, and S. Smaldone. Explicit coupling schemes for a fluid-fluid interaction problem arising in hemodynamics. *SIAM Journal on Scientific Computing*, 36(6):A2557–A2583, 2014.

[FMN07] L. Formaggia, A. Moura, and F. Nobile. On the stability of the coupling of 3D and 1D fluid-structure interaction models for blood flow simulations. *ESAIM: Mathematical Modelling and Numerical Analysis*, 41(04):743–769, 2007.

[Hec12] F. Hecht. New development in FreeFem++. *J. Numer. Math.*, 20(3-4):251–265, 2012.

[HRT96] J. G. Heywood, R. Rannacher, and S. Turek. Artificial boundaries and flux and pressure conditions for the incompressible Navier-Stokes equations. *International Journal for Numerical Methods in Fluids*, 22:325–352, 1996.

[KVCC+10] H. J. Kim, I. E. Vignon-Clementel, J. S. Coogan, C. A. Figueroa, K. E. Jansen, and C. A. Taylor. Patient-specific modeling of blood flow and pressure in human coronary arteries. *Annals of Biomedical Engineering*, 38(10):3195 – 3209, 2010.

[LMN+09] W. Layton, C. C. Manica, M. Neda, M. Olshanskii, and L.G. Rebholz. On the accuracy of the rotation form in simulations of the Navier-Stokes equations. *Journal of Computational Physics*, 228:3433–3447, 2009.

[MBH+11] M. E. Moghadam, Y. Bazilevs, T.-Y. Hsia, I. E. Vignon-Clementel, and Al. L. Marsden. A comparison of outlet boundary treatments for prevention of backflow divergence with relevance to blood flow simulations. *Computational Mechanics*, 48(3):277–291, 2011.

[MXA+12] P. Moireau, N. Xiao, M. Astorino, C.A. Figueroa, D. Chapelle, C.A. Taylor, and J.F. Gerbeau. External tissue support and fluid-structure simulation in blood flows. *Biomech Model Mechanobiol*, 11:1–18, 2012.

[PZVP12] A. Porpora, P. Zunino, C. Vergara, and M. Piccinelli. Numerical treatment of boundary conditions to replace lateral branches in hemodynamics. *International Journal for Numerical Methods in Biomedical Engineering*, 28:1165–1183, 2012.

[SPH01] N. P. Smith, A. J. Pullan, and P. J. Hunter. An anatomically based model of transient coronary blood flow in the heart. *SIAM J. APPL. MATH*, 62(3):990–1018, 2001.

[Tez92] T. E. Tezduyar. Stabilized Finite Element Formulation for Incompressible Flows Computations. *Advanced in Applied Mechanics*, 28:1–44, 1992.

[TO00] T. E. Tezduyar and Y. Osawa. Finite element stabilization parameters computed from element matrices and vectors. *Comp. Meth. Apl. Mech. Engrg.*, 28:411–430, 2000.

[VC06] I. Vignon-Clementel. *A coupled multidomain method for computational modeling of blood flow*. PhD thesis, Stanford University, 2006.

[VV05] A. Veneziani and C. Vergara. Flow rate defective boundary conditions in haemodynamics simulations. *International Journal for Numerical Methods in Fluids*, 47(8-9):803–816, 2005.

[WLW09] N. Wetserhof, J.-W. Lankhaa, and B. E. Wetserhof. The arterial Windkessel. *Med. Biol. Eng. Comput.*, 47:131–141, 2009.

Part II

TOWARD CARDIAC HEMODYNAMICS

My charade is the event of the season,
And if I claim to be a wise man,
Well, it surely means that I don't know.
... There'll be peace when you are done.

"Carry On My Wayward Son" by Kansas.

CHAPTER 4

Fluid-fluid interaction problem and RIS model. Application to the aortic valve

We present in this chapter the numerical simulations obtained by coupling the blood dynamics in the arch of the aorta and the blood flow in the aortic root in which a reduced order model describes the valve behavior. Without dealing with the fluid-structure interaction between the blood flow and the valve leaflets, the valve is replaced by immersed surfaces acting as resistance on the fluid. The resistive immersed surfaces (RIS) introduce additional dissipative terms in the momentum equation of the Navier-Stokes model. This approach represents a compromise between lumped parameters and multiphysics models. Numerical simulations are performed in two geometries of aorta, one idealized the other obtained from medical imaging.

Contents

4.1 Introduction

The study of the heart valves is a research topic which is receiving great attention (e.g. [NWY06, NKI+13, RFS+12, WM07]), owing to their complex mechanism and to the interest in their damage assessment. Valves geometry, functioning and interactions with the blood flow make the numerical simulations very challenging.

The aortic valve is the most representative for the numerical simulation of heart valves. The mechanism of the aortic valve occurs at high pressures, and it has the important task to

let the blood flow directly into the aorta and to prevent back-flow to the heart. Three semilunar *leaflets* compose the aortic valve. Behind them, three anatomic dilatations generate the *Valsalva sinus* in which the two coronary arteries, left and right, supply the heart with blood[1].

One of the main reasons that motivates numerical simulations of the aortic valve is a better comprehension of their potential malfunctioning (e.g. [KS06b, MKR+13, VCA+10, WM08]). Valve surgery reparation has a seminal interest in the medical community. In this direction, mechanic-artificial aortic valve has been studied [HNP+06, SB09, TCBV09]. In addition numerical simulations can be non-invasive techniques for the evaluation of a valve damage (e.g. [CdSG+05, GD06, GPD+00, GPL+04, vL09]). In [vL09] simulations obtained from a 3D FSI model of the aortic valve were used to compare different clinical indexes for various stenotic geometries. Another diagnostic parameter has been proposed in [GPD+00] based on the amount of the loss of energy caused by a stenosis on the overall hemodynamics. Among the aortic valve diseases, valve stenosis and valve regurgitation are the most common. In valve stenosis the resistance to forward flow is increased whereas in regurgitation the closed valves are leaking, leading blood flow back from the aorta to the ventricles. Regurgitation from a computational point of view can be more difficult to retrieve, since it impacts the left ventricular cavity performance [RKM+99].

Different kind of models can be adopted to simulate heart valve. The simplest is the lumped parameter method, that reduces the valve behavior to the resolution of algebraic or differential equations [DZL07, JL06, KS06a, SMCCS08, SSG+04, TW89]. Despite the important progress realized in the simulations of the interaction between the blood fluid and the structure of the valves (e.g. [AGPT09, HPSB03, vLABvdV05, LDSB10]), this type of problems still remains very challenging. A new approach has been recently proposed in [AHSG12, Ast10] based on the resistive immersed surface (RIS) method, in which the valve surface acts as a resistance in the fluid.

In the framework of coupling different cardiovascular compartments with their own solver, the fluid-structure method can be computationally expensive and the standard lumped parameters approach can perturb too much the flow owing to unphysical boundary conditions. Hence, we consider the RIS model to describe the heart valve as resistance components only in two positions, in the fully open and fully closed. Discontinuity pressures are considered in order to capture the pressure jump on the immersed surfaces (see [FGM08]).

In this chapter we discuss the fluid-fluid problem in two cardiovascular compartments, in which one of them is represented by the valve region. This is a prototype for left ventricle hemodynamics we will discuss in the next chapters. Here we present some examples to test and motivate the coupling of the blood dynamics in the left ventricle and including reduced order valves model with the blood flow in the aorta.

The main contribution of this chapter is the implementation of this method in the parallel solver FELiScE[2] and the set up of numerical experiments physiologically relevant.

[1] Section 1.3 for some details and references.

[2] http://felisce.gforge.inria.fr

Outline This chapter is organized as follows. Section 4.2 deals with the mathematical model while Section 4.3 presents the numerical experiments. In details, paragraph 4.2.1 and 4.2.2 present the mathematical description of the RIS valve model and its integration in the explicit fluid-fluid interaction problem. The geometry of the valve and the inlet conditions for the numerical simulations are presented in 4.3.1. Two test cases, idealized and realistic, are shown in paragraph 4.3.2 and 4.3.3. Paragraph 4.3.4 ends the discussion with the derivation of the principal medical indexes applied to the RIS stenotic valve model.

4.2 A reduced order model for heart valves

We present in this section the RIS model [FGM08] applied to the heart valves. The presentation of the model is largely inspired from the work proposed in [AHSG12] and [Ast10, Chapter 7]. We integrate this model into our fluid-fluid problem studied in the previous part.

4.2.1 RIS valve model and the space discretization

The main ingredients of the RIS model studied in the present chapter are essentially twofold. The first one is to consider the valve only in two configurations, the completely closed and the completely opened configuration. The second ingredient is to introduce an additional dissipative term in the momentum equation of the fluid model.

Let $\mathcal{S}_o \subset \mathbb{R}^{d-1}$ and $\mathcal{S}_c \subset \mathbb{R}^{d-1}$ be two co-dimensional surfaces representing respectively the open and closed valve configuration, the resulting computational domain is then $\Omega = \Omega^f \cup \mathcal{S}_c \cup \mathcal{S}_o$, with the fluid domain $\Omega^f \subset \mathbb{R}^d$, $d = 2, 3$, and $\partial\Omega$ is the boundary of the entire domain. The immersed surfaces $\mathcal{S}_i$ subdivides the fluid domain Ω in two sub-domains Ω^+ and Ω^- (Figure 4.1).

Denoting by $\partial\Omega$ the artery wall, the incompressible Navier-Stokes equations (2.1), now reads: find the velocity $\mathbf{u} : \Omega \times \mathbb{R}^+ \to \mathbb{R}^d$ and the pressure $p : \Omega \times \mathbb{R}^+ \to \mathbb{R}$ satisfying

$$\left\{ \begin{array}{rcll} \rho\partial_t \mathbf{u} + \rho\mathbf{u}\cdot\nabla\mathbf{u} - \nabla\cdot\boldsymbol{\sigma}(\mathbf{u},p) + \displaystyle\sum_{i=o,c} R_i \mathbf{u}\delta_{\mathcal{S}_i} &=& 0, & \text{in } \Omega, \\ \nabla\cdot\mathbf{u} &=& 0, & \text{in } \Omega, \\ \mathbf{u} &=& \mathbf{0}, & \text{on } \partial\Omega, \end{array} \right. \tag{4.1}$$

with the initial conditions $\mathbf{u}(0) = \mathbf{u}_0$ and appropriate boundary conditions at the inlet and the outlet. The term $\boldsymbol{\sigma}(\mathbf{u}, p) = -p\mathbf{I} + 2\mu\boldsymbol{\epsilon}(\mathbf{u})$, with $\boldsymbol{\epsilon}(\mathbf{u}) = (\nabla\mathbf{u} + \nabla^T\mathbf{u})/2$, is the fluid stress tensor. While ρ is the fluid density and μ is the dynamic viscosity, both assumed to be constant. For each surface $\mathcal{S}_i$, we denote by $\delta_{\mathcal{S}_i}$, the Dirac measure and by R_i, the associated resistance, representing the dissipation due to the presence of the immersed surface.

The space discretization is based on the conforming stabilized finite element method proposed in [FGM08]. We define $\{\mathcal{T}_h\}_{0\leq h\leq 1}$ a family of triangulation of Ω, with diameter h, conforming with the immersed surfaces $\mathcal{S}_i$.

We consider equal order approximations for the velocity and the pressure. Both velocity and pressure approximations will be continuous at inter-element boundaries, except for

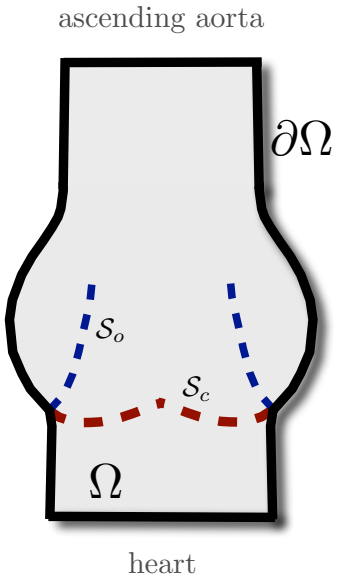

Figure 4.1: *Sketch of the domain Ω with the immersed surfaces $\mathcal{S}_c$ and $\mathcal{S}_o$.*

the pressure that will be discontinuous on the faces of the immersed surfaces (see Section 4.3.1). Hence the space W_h defines an inf-sup stable and conforming finite element approximations of $[H^1(\Omega)]^d$ while the space $\mathcal{Q}$ defines inf-sup stable and conforming finite element approximations of the L^2-functions continuous in Ω^+ and Ω^- and discontinuous over $\mathcal{S}_i$. While the space Q_h will denote a finite element approximations of $L^2(\Omega)$.

Then we denote by $V_h = W_h \cap [H^1_\Gamma(\Omega)]^d$, with $H^1_\Gamma(\Omega)$ the space of $H^1(\Omega)-$functions vanishing on $\partial\Omega$. The space discretization of (4.1) reads: for all $t > 0$, find $(\mathbf{u}_h,\ p_h) \in V_h \times \mathcal{Q}_h$ such that

$$A[\mathbf{u}_h; (\mathbf{u}_h, p_h), (\mathbf{v}_h, q_h)] + \sum_{i=\{o,c\}} R_i \int_{\mathcal{S}_i} \mathbf{u}_h \cdot \mathbf{v}_h = 0, \tag{4.2}$$

for all $(\mathbf{v}_h,\ q_h) \in V_h \times \mathcal{Q}_h$. The form $A[\mathbf{u}_h; (\mathbf{u}_h, p_h), (\mathbf{v}_h, q_h)]$ has the expression

$$\begin{aligned} A[\mathbf{u}_h; (\mathbf{u}_h, p_h), (\mathbf{v}_h, q_h)] \ \stackrel{\text{def}}{=}\ & \rho \int_\Omega \partial_t \mathbf{u}_h \cdot \mathbf{v}_h + \int_\Omega 2\mu\boldsymbol{\epsilon}(\mathbf{u}_h) : \boldsymbol{\epsilon}(\mathbf{v}_h) \\ & - \int_\Omega p_h \nabla \cdot \mathbf{v}_h + \int_\Omega q_h \nabla \cdot \mathbf{u}_h + \rho \int_\Omega \mathbf{u}_h \cdot \nabla \mathbf{u}_h \cdot \mathbf{v}_h. \end{aligned}$$

The extra terms on the momentum equation preserve the continuity of the velocity $\mathbf{u}$ on the immersed surfaces and induce jumps of the normal stresses when $R_i \neq 0$. In other terms, (4.2) is the variational formulation obtained providing the incompressible Navier-Stokes equations (2.1) of further boundary conditions on the immersed surfaces $\mathcal{S}_i$

$$\begin{cases} [\![\mathbf{u}]\!] &= \mathbf{0}, & \text{on } \mathcal{S}_i, \\ [\![\boldsymbol{\sigma}(\mathbf{u}, p) \cdot \mathbf{n}]\!] &= -R_i \mathbf{u}, & \text{on } \mathcal{S}_i, \end{cases} \tag{4.3}$$

where the quantity $[\![\cdot]\!]$ correspond to the jump between the distal (+) and proximal (-) side of each immersed surfaces. Then we have

$$[\![\mathbf{u}]\!] \stackrel{\text{def}}{=} \mathbf{u}^+ - \mathbf{u}^-, \qquad [\![\boldsymbol{\sigma}(\mathbf{u}, p) \cdot \mathbf{n}]\!] \stackrel{\text{def}}{=} \boldsymbol{\sigma}(\mathbf{u}^+, p^+) \cdot \mathbf{n}^+ + \boldsymbol{\sigma}(\mathbf{u}^-, p^-) \cdot \mathbf{n}^-$$

with $\mathbf{n}^+$ and $\mathbf{n}^-$ the outgoing normals on $\mathcal{S}_i$, with $i = \{o, c\}$.

REMARK 4.1
Note that (4.1) *can be equivalently reformulated on two connected sub-domains, where the domain* $\Omega = \Omega^+ \cup (\mathcal{S}_o \cup \mathcal{S}_c) \cup \Omega^-$ *with* $\Omega^+ \cap \Omega^- = \emptyset$*. On each sub-domain the Navier-Stokes problem* (2.1) *is solved with the conditions on the immersed surfaces* $\mathcal{S}_o$ *and* $\mathcal{S}_c$ *represented by the* (4.3) *(see [Ast10, FGM08]).*

The key-role of this model is played by the resistances on the immersed surfaces. For each immersed surface, R_i can be interpreted as penalization parameter that regulates the opening and the closing of the valve. Indeed when R_i is large, the value $\mathbf{u} = \mathbf{0}$ is enforced on $\mathcal{S}_i$ and when R_i is zero, no dissipative term is added, thus the surface is invisible to the flow and there is no pressure drop across it. If R_i assumes non-zero small values, the surface acts as a porous medium [CFGM11].

The magnitude of the resistance mimics the behavior of a real valve and in our case it varies according the following conditions:

- The valve *closes* if $Q < 0$, i.e. $R_c \neq 0$ and $R_o = 0$. Indeed, the valve is open as long as a positive flow occurs in the direction of the valves opening. Therefore the closure of the valve happens when a flow reversal acts on the immersed surface.

- The valve *opens* if $\Delta p = p^- - p^+ > 0$, i.e. $R_c = 0$ and $R_o \neq 0$. Indeed the valve is closed until the ventricular pressure, i.e the mean pressure on the proximal surface (-), is less than the aortic pressure, i.e. the mean pressure in the distal surface (+). The valve opens when the ventricular pressure overtakes the aortic pressure, i.e. when the valve is subjected to a positive pressure difference.

The same physiological conditions for opening/closure is used in [FLTV06] and applied to a 0D model of the valve in lumped parameter model of the heart integrated in a 1D description of the arterial network.

REMARK 4.2
Not that the previous conditions cannot be commuted. In other terms, the evaluation of a positive flow could not be considered as test condition for the opening of the valves, since at this point the flow across the valve is zero, and only after the valve opening it will be positive. On the other hand, the information on the pressure across the valve could not be used to establish the valve closure, because when the valve is open the pressure difference would always be zero across the surface representing the closed valve.

4.2.2 Explicit fluid-fluid problem and time discretization of RIS model

In this section we discuss the time discretization of the RIS valve model in the framework of the fluid-fluid coupled problem.

Problem (4.1) can be partitioned into two sub-problems defined in two non-connected sub-domains, $\Omega_1 \subset \mathbb{R}^d$ and $\Omega_2 \subset \mathbb{R}^d$. The two sub-domains are separated by an interface $\Sigma \stackrel{\text{def}}{=} \partial\Omega_1 \cap \partial\Omega_2$. In addition the immersed surface splits a domain in two connected sub-domains Ω^- and Ω^+, the proximal and the distal one. Thus the fluid domain with the fluid-fluid model and the RIS valve model results

$$\begin{aligned} \Omega &= \Omega_1 \cup \Omega_2 \\ &= [\Omega_1^+ \cup (\mathcal{S}_o \cup \mathcal{S}_c) \cup \Omega_1^-] \cup \Omega_2, \end{aligned}$$

with $\Omega_1 \cap \Omega_2 = \emptyset$ and $\Omega_1^+ \cap \Omega_1^- = \emptyset$ (Figure 4.2).

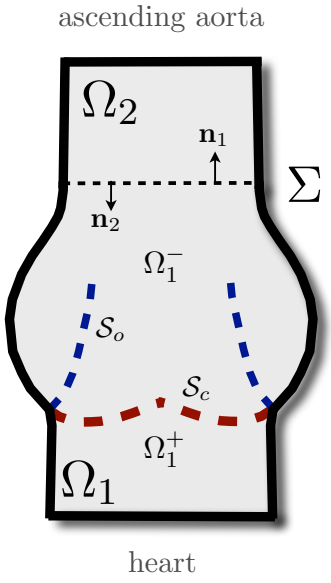

Figure 4.2: *Sketch of the sub-domains Ω_1 and Ω_2 with the immersed surfaces $\mathcal{S}_c$ and $\mathcal{S}_o$.*

The resulting explicit scheme, summarized in Algorithm 4.1, is based on Algorithm 2.3, page 45.

ALGORITHM 4.1 (Staggered scheme 2.3 with RIS model)

1. *Find* $(\mathbf{u}_{1,h}^n,\, p_{1,h}^n) \in W_{1,h} \times \mathcal{Q}_{1,h}$ *satisfying the essential boundary conditions and such that*

$$\begin{aligned} &A_{1,\delta t}[\mathbf{u}_{1,h}^{n-1}; (\mathbf{u}_{1,h}^n, p_{1,h}^n), (\mathbf{v}_{1,h}, q_{1,h})] + C_1[\mathbf{u}_{1,h}^{n-1}; (\mathbf{u}_{1,h}^n, \mathbf{u}_{2,h}^{n-1}), \mathbf{v}_{1,h}] \\ &+\frac{\gamma\mu}{h}\int_\Sigma (\mathbf{u}_{1,h}^n - \mathbf{u}_{2,h}^{n-1})\cdot\mathbf{v}_{1,h} + \int_\Sigma \boldsymbol{\sigma}(\mathbf{u}_{2,h}^{n-1}, p_{2,h}^{n-1})\cdot\mathbf{n}_2\mathbf{v}_{1,h} \\ &+\sum_{i=o,c} R_i^n \int_{\mathcal{S}_i} \mathbf{u}_1^n \cdot \mathbf{v}_1 = 0, \end{aligned} \tag{4.4}$$

for all $(\mathbf{v}_{1,h},\, p_{1,h}) \in V_{1,h} \times \mathcal{Q}_{1,h}$. *With the resistances*

$$R_c^n = R_{\text{off}}(1-\delta_c^n) + R_{\text{on}}\delta_c^n \quad \textit{and} \quad R_o^n = R_{\text{on}}(1-\delta_c^n) + R_{\text{off}}\delta_c^n; \tag{4.5}$$

2. *Find* $(\mathbf{u}_{2,h}^n,\, p_{2,h}^n) \in W_{2,h} \times Q_{2,h}$ *satisfying the essential boundary conditions and such that*

$$\begin{aligned} &A_{2,\delta t}[\mathbf{u}_{2,h}^{n-1}; (\mathbf{u}_{2,h}^n, p_{2,h}^n), (\mathbf{v}_{2,h}, q_{2,h})] + S(p_{2,h}^n, q_{2,h}) \\ &+C_2[(\mathbf{u}_{2,h}^{n-1}, \mathbf{u}_{1,h}^{n-1}); (\mathbf{u}_{2,h}^n, \mathbf{u}_{1,h}^n), \mathbf{v}_{2,h}] + \frac{\gamma\mu}{h}\int_\Sigma (\mathbf{u}_{2,h}^n - \mathbf{u}_{1,h}^n)\cdot\mathbf{v}_{2,h} \\ &-\int_\Sigma \boldsymbol{\sigma}(\mathbf{u}_{2,h}^{n-1}, p_{2,h}^{n-1})\cdot\mathbf{n}_2\mathbf{v}_{2,h} - \int_\Sigma (\mathbf{u}_{2,h}^n - \mathbf{u}_{1,h}^n)\cdot\mathbf{n}_2 q_{2,h} = 0 \end{aligned} \tag{4.6}$$

for all $(\mathbf{v}_{2,h},\, p_{2,h}) \in V_{2,h} \times Q_{2,h}$.

3. *Go to next time-step.*

The two forms $A_{1,\delta t}[\mathbf{u}_{1,h}^{n-1}; (\mathbf{u}_{1,h}^n, p_{1,h}^n), (\mathbf{v}_{1,h}, q_{1,h})]$ and $A_{2,\delta t}[\mathbf{u}_{2,h}^{n-1}; (\mathbf{u}_{2,h}^n, p_{2,h}^n), (\mathbf{v}_{2,h}, q_{2,h})]$ have the expression as in (2.22) and (2.23), likewise the terms $C_1[\mathbf{u}_{1,h}^{n-1}; (\mathbf{u}_{1,h}^n, \mathbf{u}_{2,h}^{n-1}), \mathbf{v}_{1,h}]$ and $C_2[(\mathbf{u}_{2,h}^{n-1}, \mathbf{u}_{1,h}^{n-1}); (\mathbf{u}_{2,h}^n, \mathbf{u}_{1,h}^n), \mathbf{v}_{2,h}]$ are defined in (2.13) and (2.14), and the pressure stabilization term $S(p_{2,h}^n, q_{2,h})$ has the form (2.30).

The evolution in time of the resistance magnitude is settled by mean of two values, R_{on} and R_{off}, that activate or deactivate the resistances on the valve surfaces. The value of R_{on} is large, and it is chosen to guarantee a negligible flow across the active surfaces, the choice in our numerical experiments is 1×10^6. The value of R_{off}, set to 0, makes the surfaces invisible to the flow. The switching between the activate or deactivate resistances is achieved by mean of the logical variable δ_c^n, which assumes value 1 when the valve closes, 0 when the valve opens, i.e.

$$\delta_c^n = \begin{cases} 1 & \text{if} \quad Q^n < 0, \quad \text{on } \mathcal{S}_c, \quad \text{(valve has to close)}, \\ 0 & \text{if} \quad \Delta p^n > 0, \quad \text{on } \mathcal{S}_c, \quad \text{(valve has to open)}. \end{cases} \tag{4.7}$$

The resistances actually depend on the pressure and velocity computed at the current time step, i.e. $R_i^n = R_i(\mathbf{u}^n, p^n)$. This makes the previous algorithm highly non-linear. In order

to linearize the previous algorithm, a re-computation of the Fluid problem 1 is in order when the value of the resistances changes. In other words, after the (4.4) is solved, the valves status is checked, i.e.

$$\begin{aligned} &\text{Closed valve status} \quad \begin{cases} \Delta p^n > 0 & \text{Not admissible.} \\ \Delta p^n < 0 & \text{Admissible.} \end{cases} \\ &\text{Open valve status} \quad \begin{cases} Q^n < 0 & \text{Not admissible.} \\ Q^n > 0 & \text{Admissible.} \end{cases} \end{aligned} \tag{4.8}$$

This means that if the pressure difference is positive but the valve is still closed, the status of the valve is not admissible and the fluid problem should be re-computed with the new valve status. In the same way, if the flow is negative and the valve is still open, a re-computation of the fluid 1 should be in order. The method is represented by the following flow chart.

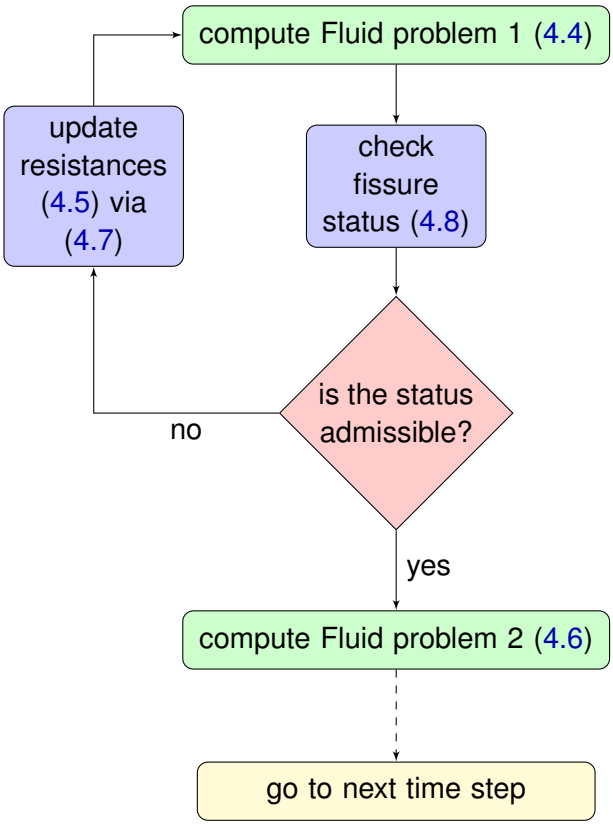

The re-computation of the Fluid model 1 is not at each time step but only when the valve status changes, and in a cardiac cycle this happens only twice, i.e. the re-computation of the equation (4.4) occurs only twice.

REMARK 4.3

Another option to linearize Algorithm 4.1 is to evaluate the resistances at previous time step, i.e. $R_i^{n-1} = R_i(\mathbf{u}^{n-1}, p^{n-1})$. *This introduces a delay in the valve opening and closure, i.e. the valve closes only after the flow is already negative and the valve opens only after the ventricular pressure is greater than aortic pressure.*

4.3 Numerical example RIS - FFI model

We present in this section the numerical simulations associated to the previous section. Two numerical experiments are suggested. The first case corresponds to an idealized situation, i.e. we use a simplified geometry of the aorta. In the second case the aortic geometry was obtained from medical imaging.

4.3.1 Fissured valve geometry and boundary conditions

As previously explained, the valve behavior is described only by two configurations, open and closed (Figure 4.3). Both configurations are represented by two surfaces fixed in space, obtained from 3D FSI simulations ([SAG10]).

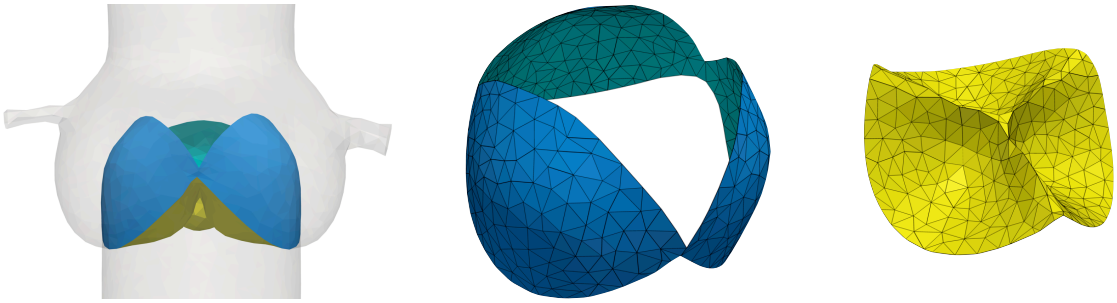

Figure 4.3: *Aortic valve domains: position in the aortic root (left), mesh for open configuration (middle) and mesh for closed configuration (right).*

During the implementation of the RIS model, we have faced two main difficulties. The first one is related to the geometry and the second one arises with the choice of the inlet conditions.

Fissured valve geometry The standard space-continuous finite element approximations of the pressure cannot capture accurately the jump of stresses across the surfaces. This would produce a smearing of the stresses across the interface, which leads to inaccurate results, especially during the closed valve phases. In order to capture a discontinuity of the pressure, while keeping the velocity variable continuous, a crack is introduced in the geometry. The open and closed surfaces are duplicated splitting the mesh into two distinct parts. This introduce a fissure in the computational domain. The continuity of the velocity across the fissure is obtained by fusing together its degrees of freedom. In other words, if we consider a node of the fissure in the proximal surface and the associated node in the distal surface, the same degree of freedom is considered for the velocity. A similar technique could be used for example to simulate boundary conditions of a mathematical torus, in which the computational domain is only represented by a square and the torus is construct by pasting the opposite sides. The velocity variable “see” the mesh as one piece while the pressure variable is computed in two distinct parts (Figure 4.4).

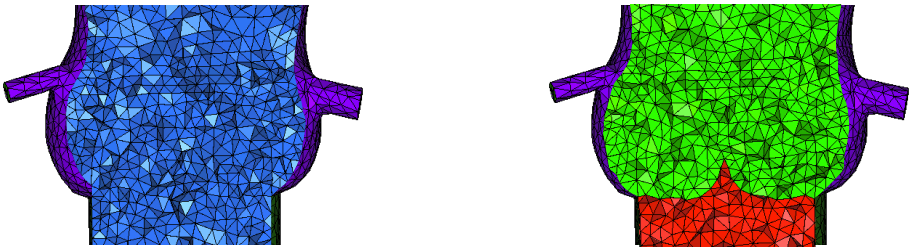

(a) *The mesh view by velocity variable.* (b) *The mesh view by pressure variable.*

Figure 4.4: *Fissured computational domain.*

Inlet conditions The second crucial point is related to the inlet conditions. A flow boundary condition, i.e. Dirichlet condition, is usually imposed to improve the robustness of the numerical simulations. We consider a fluid domain like that one in Paragraph 3.3.1, page 65, which roughly speaking is a straight tube in which one side is the inlet and the other side is the closed valve surface. For this domain, such condition is appropriate during the opening/closing of the valve but are inadequate when the valve is closed.

The fluid incompressibility constraint, makes inlet Dirichlet conditions difficult to handle: when the valve is closed, the flow imposed on Γ_{in} must be zero. This makes necessary to know a priori when the valve should be closed. Indeed if the flow imposed on the inlet is positive, the valve opens and if the flow is negative, instabilities could appear.

As the Dirichlet conditions are inappropriate during the closed valve state, we possibly can use Neumann inlet conditions. The prescription of Neumann-type boundary conditions, both at the inlet and at the outlet by mean of Windkessel model, may be difficult to retrieve physiological values of velocity and pressure at open valve states. The prescription of these boundary conditions is extremely delicate because of the fluid dynamics instabilities that could develop at the inlet or outlet of the fluid domain.

These considerations have motivated the switching between Dirichlet/Neumann conditions at each opening/closure of the valve, made for the RIS model in [AHSG12] and for the mechanical closure of an artificial heart valve in [HNP+06]. The same approach is used for the numerical simulations of this chapter. In Figure 4.5, the input conditions in the principal cardiac phases are reported (see Paragraph 1.3.6 on page 20 for further physiological details). In our example the cardiac cycle lasts for $0.775\ s$, giving an heart rate of about 77 beats per minute. When the valve is open, during the ejection phase $(0.0 - 0.21\ s)$, a plug-flow as Dirichlet boundary condition is imposed on Γ_{in}. The flow reaches a maximum value of $235\ cc/s$. During the isovolumic relaxation $(0.21 - 0.27\ s)$, filling $(0.27 - 0.72\ s)$ and isovolumic contraction $(0.72 - 0.775\ s)$ - i.e. the three cases where the valve is closed - the flow condition switches with a pressure condition. We define it by a function describing the pressure behavior in the left ventricle. Note that, in order to easily switch from Dirichlet to Neumann and from Neumann to Dirichlet, the flow boundary condition is imposed by penalization, i.e.

$$\frac{1}{\epsilon}\mathbf{u} + \boldsymbol{\sigma}(\mathbf{u}, p)\mathbf{n} = \frac{1}{\epsilon}\mathbf{u}_{in} - p_{in}\mathbf{n}, \qquad \text{on} \quad \Gamma_{in}. \tag{4.9}$$

The previous expression can be seen as a Robin boundary condition on Γ_{in} in which the

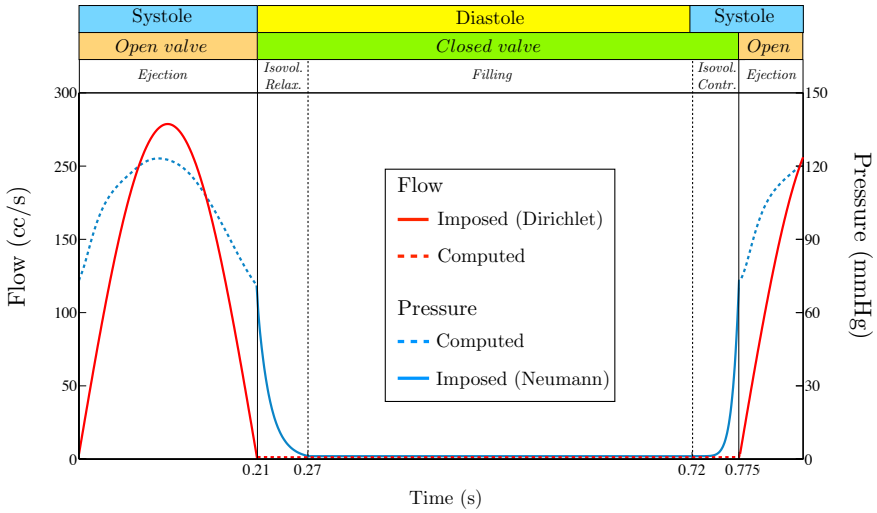

Figure 4.5: *Input condition for RIS valve model. Dirichlet on flow with open valve configuration, Neumann on pressure with closed valve configuration.*

coefficient ϵ varies according to the closure and the opening of the valve. It reaches large values when the valve is closed, e.g. $1 \times 10^{+30}$, and small values when the valve is open, e.g. 1×10^{-30}. For the sake of simplicity, the velocity imposed to obtain inflow condition during ejection is taken as a sinusoidal function and the pressure p_{in} as polynomial function during the other phases. More complex and realistic curves for pressure and flow could be considered as well but for the purpose of this chapter this choice is appropriate.

Parameters definitions The physical parameters used in the two following tests are those typical of newtonian blood flows, $\rho = 1.06\ g/cm^3$ for the density and $\mu = 0.04\ poise$ for the dynamic viscosity. The left and right coronaries, in the aortic sinus, are closed, while the Windkessel equation (3.2), page 66, is solved in the remaining outlets. With respect to the simulations discussed in the previous chapter, some of the Windkessel parameters were adapted to obtain more physiological results. Their values are reported in Table 4.1.

	Γ_a	Γ_b	Γ_c	Γ_{out}
$R_p\ (dyn \cdot s \cdot cm^{-5})$	0.005×10^4	0.19×10^4	0.075×10^4	0.015×10^4
$R_d\ (dyn \cdot s \cdot cm^{-5})$	0.92×10^4	3.27×10^4	1.32×10^4	0.32×10^4
$C\ (cm^5 \cdot dyn^{-1})$	0.95×10^{-4}	0.25×10^{-4}	0.64×10^{-4}	9.00×10^{-4}

Table 4.1: *Windkessel parameters for aorta geometry with RIS valve model.*

The space of discretization is based on $\mathbb{P}_1/\mathbb{P}_1$ finite elements, stabilized with the SUPG method. The stabilization parameters deriving from Nitsche's method are still $\gamma = 2500$ and $\gamma_0 = 1$, fixed with the 2D test case in Section 3.2.2, on page 64. The global simulation time is 8 seconds with a time step $\tau = 10^{-3}\ s$, i.e. a total of 10 cardiac cycles. All cardiac cycles present the same characteristics, except the first one, in which the solution is perturbed by

initial conditions. We show in the next paragraphs the results concerning the two last cardiac cycles. All test cases are obtained solving the coupled model summarized in Algorithm 4.1 and using the master/slave approach presented in Paragraph 3.3.2, on page 67.

We can now suggest two numerical tests. The first test case, performed in the idealized aorta geometry, allows us to validate the RIS model. In the second test case, we use a more realistic aorta to perform numerical examples of stenotic valves.

4.3.2 Idealized aorta test case: validation of the model

We have performed the first simulation in the same aorta geometry adopted for the explicit algorithm test cases. It is described in Section 3.3.1, the geometry used is shown in the middle of Figure 3.4 on page 65. We further add to the aortic root geometry the closed valve position and we have fissured the mesh to let the pressure jump.

Velocity magnitude and pressure distribution Figure 4.6 shows six snapshots obtained solving Algorithm 4.1, on page 97. The first five snapshots are taken in the ninth cardiac cycle and the last one belongs to the tenth cardiac cycle. For each time instant, the velocity magnitude is shown with together the elevated surface representing the pressure distribution in the longitudinal mid plane of the aorta.

The two snapshots on the top of the figure, depict two time instants during the ejection, when the valve is open, i.e. $R_c = 0$ and $R_o \neq 0$. The first shown time instant, $t = 6.306\ s$, occurs during the maximum inflow condition and the second snapshot, at $t = 6.410\ s$, is the last time instant in which the valve is open. Afterward the flow becomes negative, the resistance R_c becomes different from zero and the valve closes. During this two time instants, Dirichlet inflow conditions are imposed.

The two following time instants, $t = 6.420\ s$ and $t = 6.448\ s$, in the middle of the figure, are taken during the isovolumic relaxation. In the second one in particular the pressure in the aorta reaches its maximum value at closed valve, in other words it is in the point of the so-called *dicrotic notch*. Notice the jump in the pressure distribution given on the immersed surface by the resistive valve model. Neumann pressure conditions are prescribed at the inlet.

In the last two snapshots in the bottom of the figure, $t = 6.970\ s$ and $t = 7.028\ s$, the isovolumic contraction and a new ejection phase are reported. In the first one, the ventricular pressure is increasing. Neumann inlet condition are still imposed. In the second one the ventricular pressure has passed the aortic pressure, the inlet condition is switched into Dirichlet condition and a new cardiac cycle has begun.

Proximal and distal curves In Figure 4.7 the two curves are the pressure in the proximal side of the valve surface, simulating the left ventricular pressure, and the pressure computed on the distal side of the closed valve surface, representing the aortic pressure over a complete cardiac cycle. The dotted lines delimit the isovolumic phases, the continuous lines, the ejection and filling. When the valve is open (OV), in the ejection phase, the two

Figure 4.6: *Velocity magnitude (left of each snapshot) and pressure distribution (right of each snapshot) of Algorithm 4.1, in the idealized aorta, during the ninth and tenth cardiac cycle.*

pressures are equal. When the valve is closed (CV) during the other phases, a pressure difference appears. After the aortic valve closes, the smooth downward slope of the pressure waveform is interrupted by a very brief upward movement. This slight rising, caused by the sudden closure of the valve, is named *dicrotic notch*. Even if this is a complex phenomenon, whose origin is reason of discussion in the medical community, it is interesting to observe that the used model can reproduce the dicrotic wave by mean of the valve dynamics.

Figure 4.8 depicts the inlet and the outlet pressures during the opening and the closing of the valve. Notice the physiological increase of the outlet pressure with respect to the inlet pressure, before the valve closes. The dicrotic notch is faded out and a smoother slope takes place, since the effect of the valve closure is less powerful.

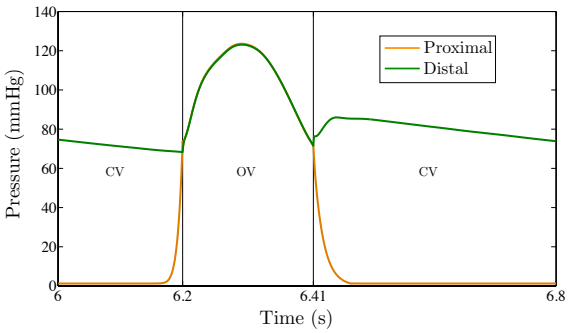

Figure 4.7: *Pressure on the proximal and distal side of the closed valve surface.*

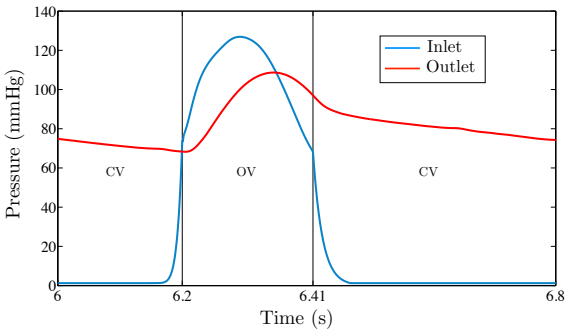

Figure 4.8: *Comparison between pressure in the inlet Γ_{in} and outlet Γ_{out}.*

4.3.3 Realistic aorta test case: application to stenotic valves

In this section, the test cases concern the numerical simulation of the blood dynamics, when the aortic valve presents stenotic leaflets. Here we recall the example tested in [AHSG12], and we extended it for two different stenotic configurations.

Realistic geometry and boundary conditions A new aorta geometry, more realistic, is used to simulate this aortic valve disease. The aortic root includes the same valve mesh, closed and open configurations, used for the previous test cases (Figure 4.3). The geometry of the aortic arch has been acquired from the *Zygote Media Group* [Zyg11] and it is part of a complete heart mesh, including ventricle, atria, valves and the aorta. We refer to the next chapter, Section 6.3.1 for more details about this mesh. The aortic root, the domain Ω_1, is a mesh of $58^{'}151$ tetrahedra and the aortic arch, the domain Ω_2, has $123^{'}939$ tetrahedra. The interface Σ has 264 nodes.

Three different configurations of the valves are tested. In the first one, all the leaflets opens normally, in the second one we suppose that one of the leaflets does not open and the last configuration has two of the three leaflets that do not open (Figure 4.9).

From a computational viewpoint the stenotic leaflets correspond to impose a constant resistance $R_c \neq 0$ on a part of the closed valve surfaces and $R_o = 0$ on the corresponding

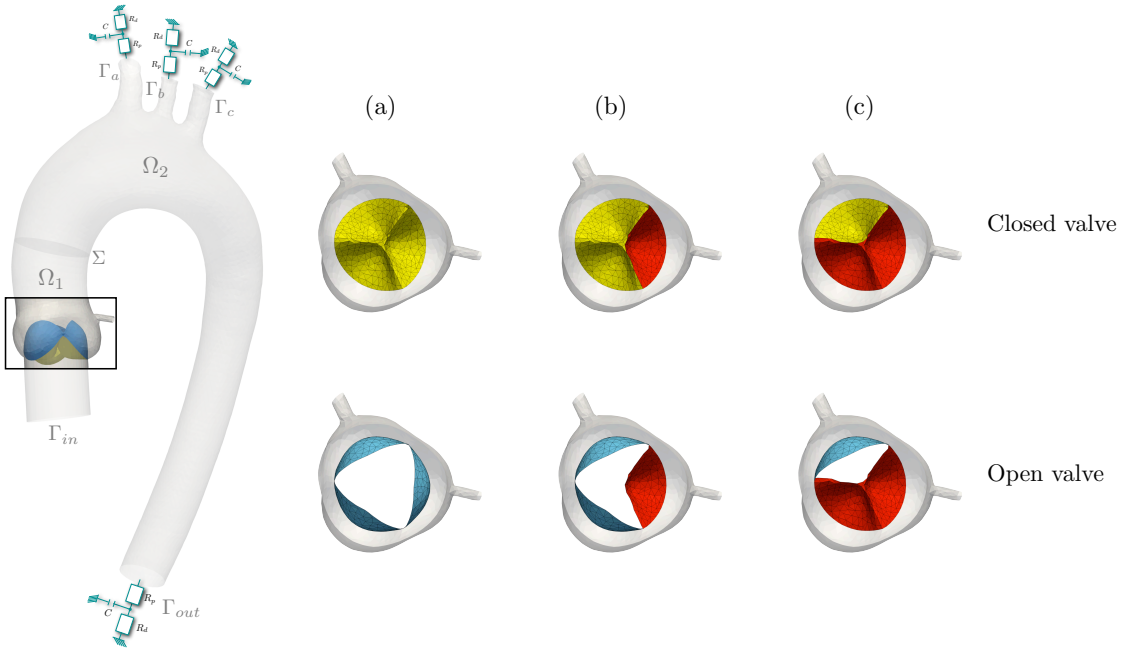

Figure 4.9: *Aortic root and aortic arch sub-domain for normal (a), one stenotic leaflet (b) and two stenotic leaflets (c). Open and closed configurations.*

open valve surfaces, during all the cardiac cycles of the entire simulation. The conditions reproduced here are rather extreme if we consider their medical aspect, since we suppose that one and two leaflets do not open at all. Clearly more realistic stenotic valve geometries, obtained from medical images, can be used as well.

REMARK 4.4
In the same way, we can impose throughout the entire simulation a constant resistance $R_o \neq 0$ on one or two open leaflets, and $R_c = 0$ on the corresponding closed leaflets. With such a choice, the so-called aortic regurgitation can be investigated, i.e. the reverse flow direction during ventricular diastole, from the aorta into the left ventricle. Again, this correspond to extreme conditions, and including the complete ventricular fluid mechanics, the results would be more precise.

The physical parameters adopted for the numerical simulations are the same of the previous example, as well as the inlet Dirichlet/Neumann conditions (Figure 4.5). The parameters used for the Windkessel models are the same reported in Table 4.1.

In the main outlet Γ_{out}, in the descending aorta, back-flow may introduce instabilities particularly at diastole. Back-flow is a physiologic phenomenon arising commonly in both healthy and diseased cardiovascular system. To avoid instabilities the stabilization of [MBH+11], originally proposed by [BGH+09], is added to the weak formulation of the model used for all three cases. It has the form

$$\beta \int_{\Gamma} (\mathbf{u}^{n-1} \cdot \mathbf{n})(\mathbf{u}^{n} \cdot \mathbf{v}), \qquad \text{with } \beta = \begin{cases} 0 & \text{if } \mathbf{u}^{n-1} \cdot \mathbf{n} \geq 0 \quad \text{on } \Gamma, \\ \frac{1}{2} & \text{if } \mathbf{u}^{n-1} \cdot \mathbf{n} < 0 \quad \text{on } \Gamma, \end{cases} \tag{4.10}$$

where $\Gamma = \Gamma_{out}$, with a semi-implicit approach assumed for time discretization.

Velocity vectors and pressure distribution Figures 4.10-4.13 show the velocity vectors and the elevated surface of the pressure distribution in the longitudinal mid plane of the aortic root and part of the aortic arch. These results are presented for the normal and the stenotic valve configurations, in the two last cardiac cycles of the simulation.

Figure 4.10, displays the snapshot in the middle of the systole of the ninth cardiac cycle. Notice the two-stenotic leaflet case (c), in the *vena contracta*, i.e. the cross-sectional area where the flow jet is minimal, the velocity magnitude increases up to $600\ cm/s$. The narrowing of the valve opening is remarkable also in the great increasing of the pressure distribution.

Figures 4.11 and 4.12, are two time instants taken during the closed valve phases. The first one, at $t = 6.695\ s$, in the middle of the filling and the second one, at $t = 6.970\ s$, during the isovolumic contraction. Note that the three test cases present similar velocity magnitude and equal pressure distribution.

Figure 4.13 shows the velocity vectors and the pressure distribution at $t = 7.028\ s$, a time instant in the ejection of the tenth cardiac cycle, before the peak of the inflow condition. We can see that, the case of one stenotic leaflet (b) has qualitatively the same behavior of the normal test case (a), since the flow across the valve is still weak. On the contrary, the two-stenotic-leaflets case (c) already shows a considerable increasing in the velocity magnitude and in the pressure distribution.

Proximal and distal pressure curves The difference between the three cases can be better estimated in Figure 4.14, in which the pressure jumps are illustrated. All curves are computed on the proximal and distal surfaces of the closed valve. The results of the ninth and tenth cardiac cycle are plotted.

In 4.14a-4.14c, the curves of the ventricular and aortic pressure, i.e. proximal and distal pressures, are compared for each test case. The pressures are equals in the open valve configurations, while a pressure difference appears during the closed valve status.

In Figure 4.14d the proximal pressure, i.e. the ventricular pressure, of the normal case is compared with the proximal pressure of the two stenotic cases. The stenotic pressures differ from the normal case in the open valve status (OV), while they are the same during the closed valve configurations, as we could expect. Similarly, 4.14e compares the distal pressure, i.e. the aortic pressure, of the normal and stenotic leaflets configurations. Slight differences appear in the closed valve status of the second stenotic test with respect to the two other test cases.

Figure 4.15 corresponds to the flow pattern and the pressure course of all the test cases, in the three top arteries and in the descending aorta. The flow could not be a complete indicator of the stenosis behavior, while with the pressure curves we can see the different impacts when the RIS model is applied to a stenotic example.

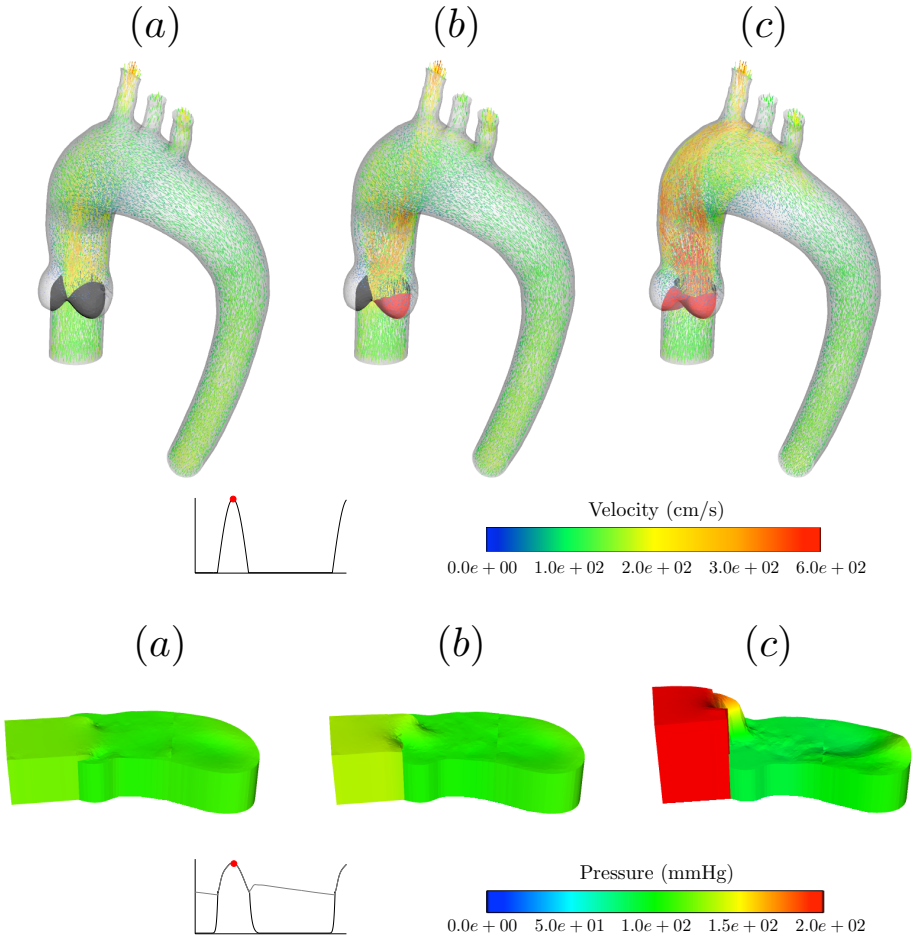

Figure 4.10: *Velocity vectors and pressure distribution for Normal (a), Stenotic 1 (b) and Stenotic 2 (c) at* $t = 6.306\ s$ *(Ejection).*

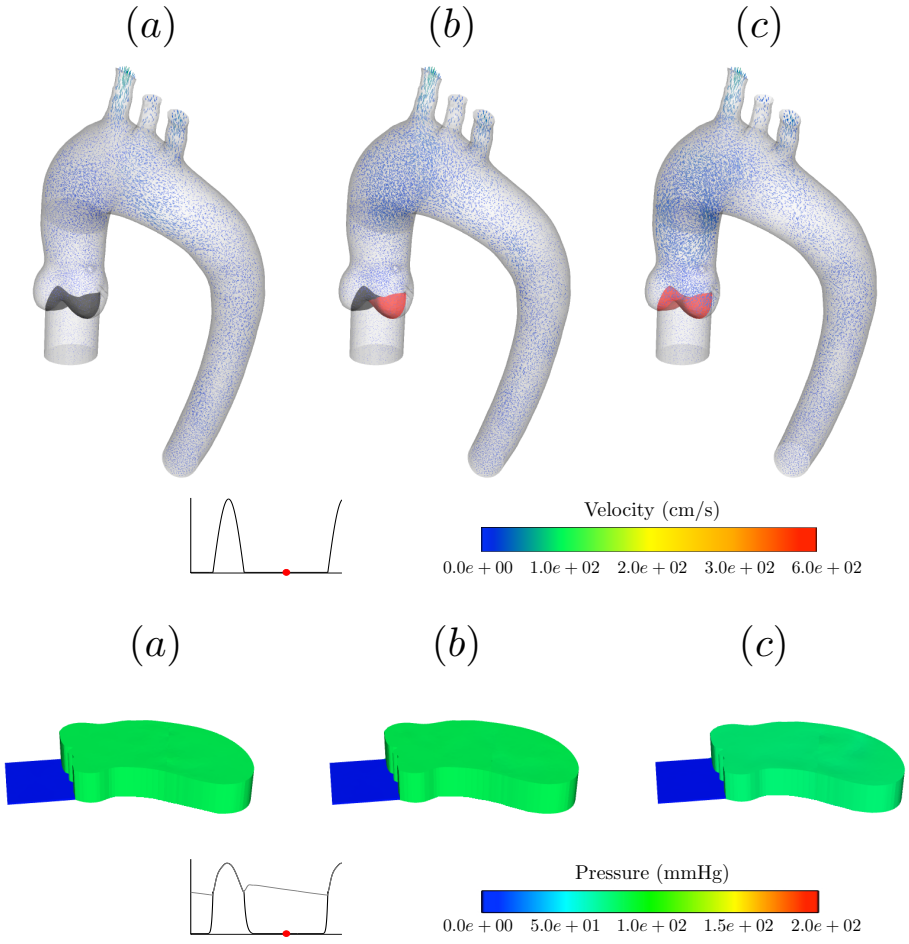

Figure 4.11: *Velocity vectors and pressure distribution for Normal (a), Stenotic 1 (b) and Stenotic 2 (c) at* $t = 6.695\ s$ *(Filling).*

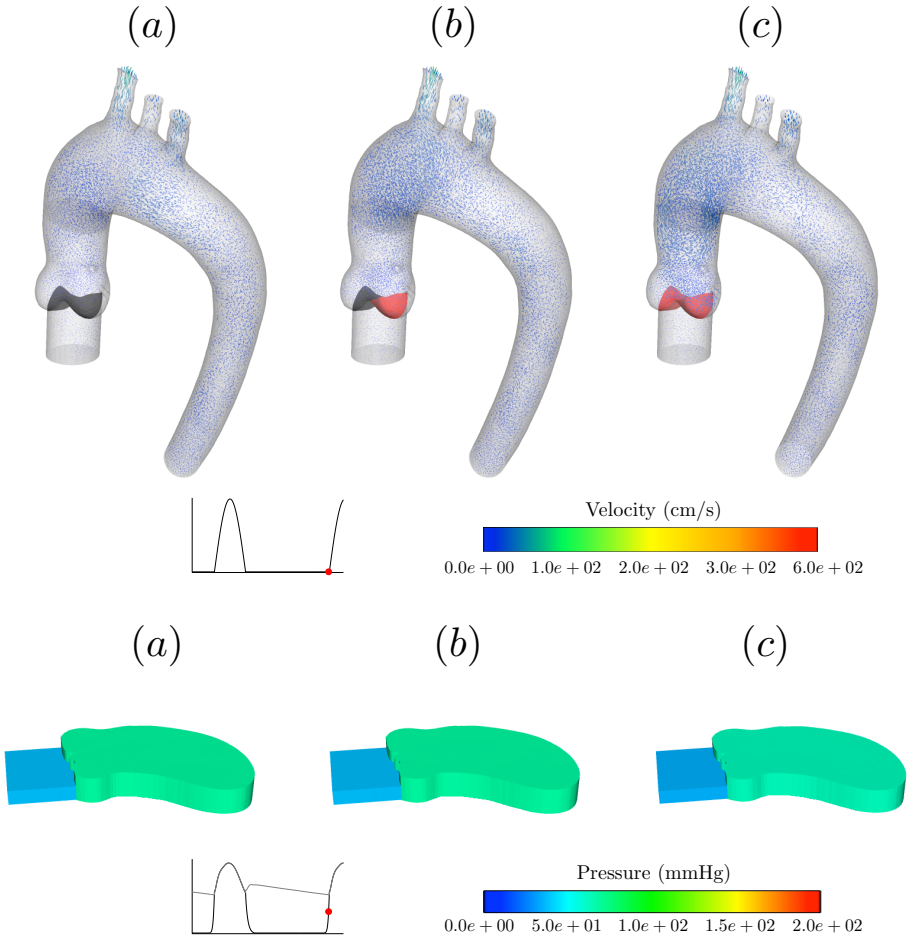

Figure 4.12: *Velocity vectors and pressure distribution for Normal (a), Stenotic 1 (b) and Stenotic 2 (c) at* $t = 6.970\ s$ *(isovolumic Contraction).*

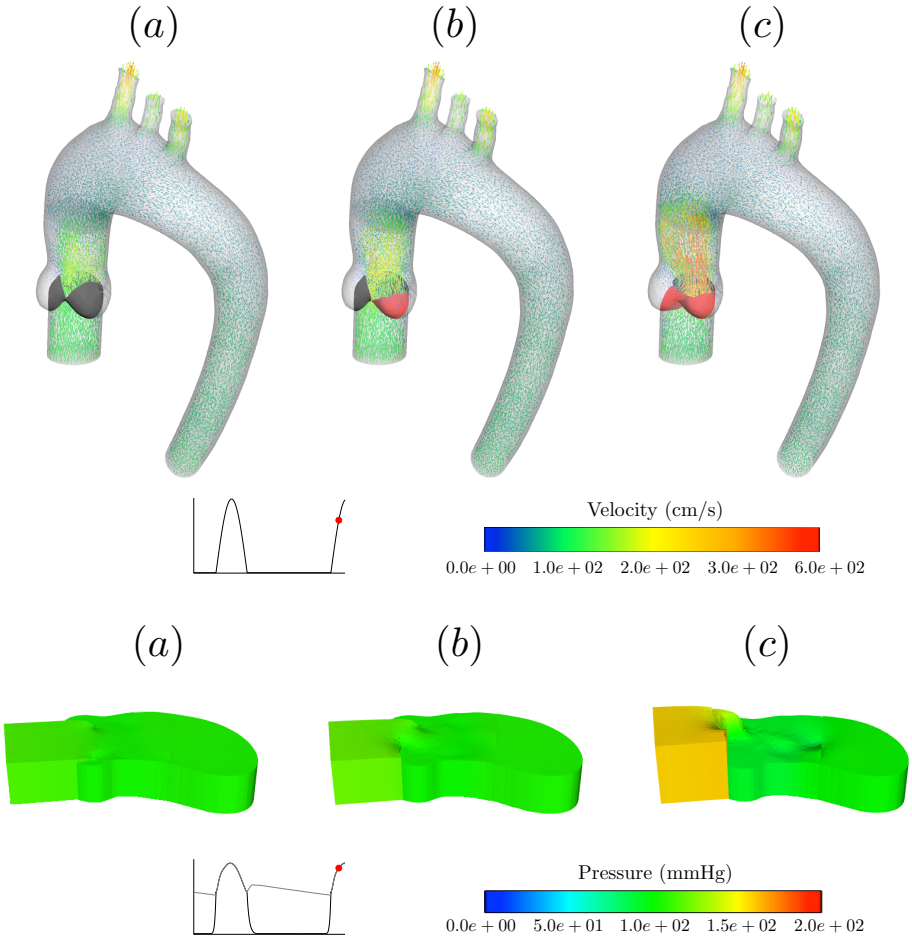

Figure 4.13: *Velocity vectors and pressure distribution for Normal (a), Stenotic 1 (b) and Stenotic 2 (c) at* $t = 7.028\ s$ *(Ejection).*

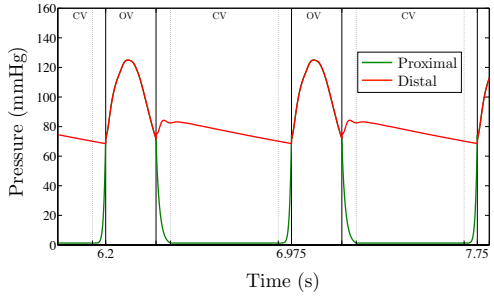

(a) *Normal valve: proximal and distal pressure.*

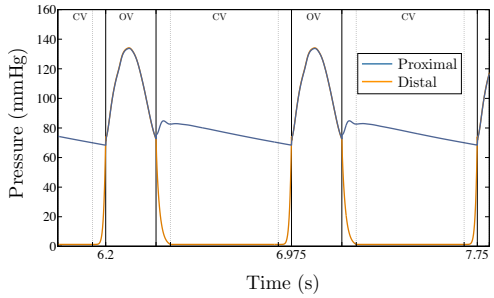

(b) *Stenotic 1 valve: proximal and distal pressure.*

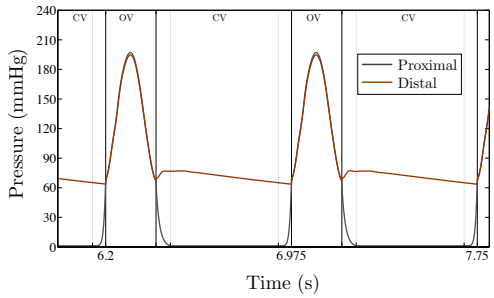

(c) *Stenotic 2 valve: proximal and distal pressure.*

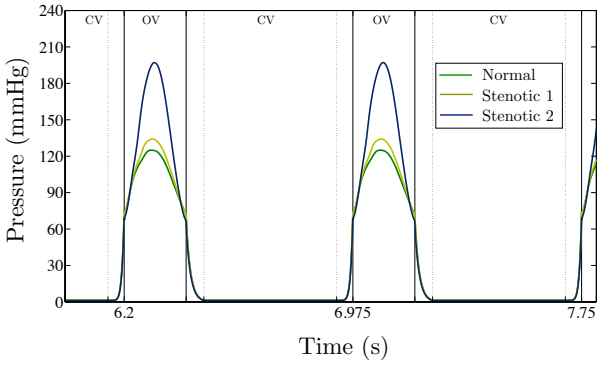

(d) *Proximal pressure: Normal, Stenotic 1, Stenotic 2.*

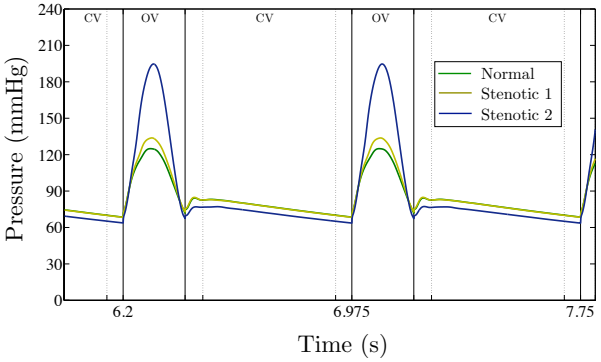

(e) *Distal pressure: Normal, Stenotic 1, Stenotic 2.*

Figure 4.14: *Pressure in the proximal and distal closed surfaces for normal, 1 stenotic leaflet and 2 stenotic leaflets configuration.*

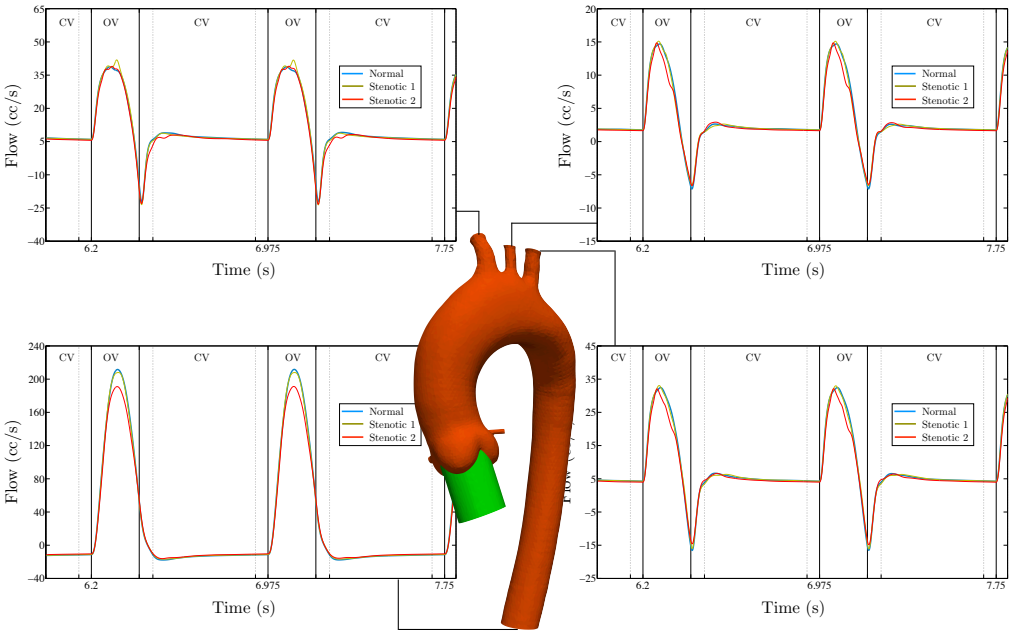

(a) *Flows*.

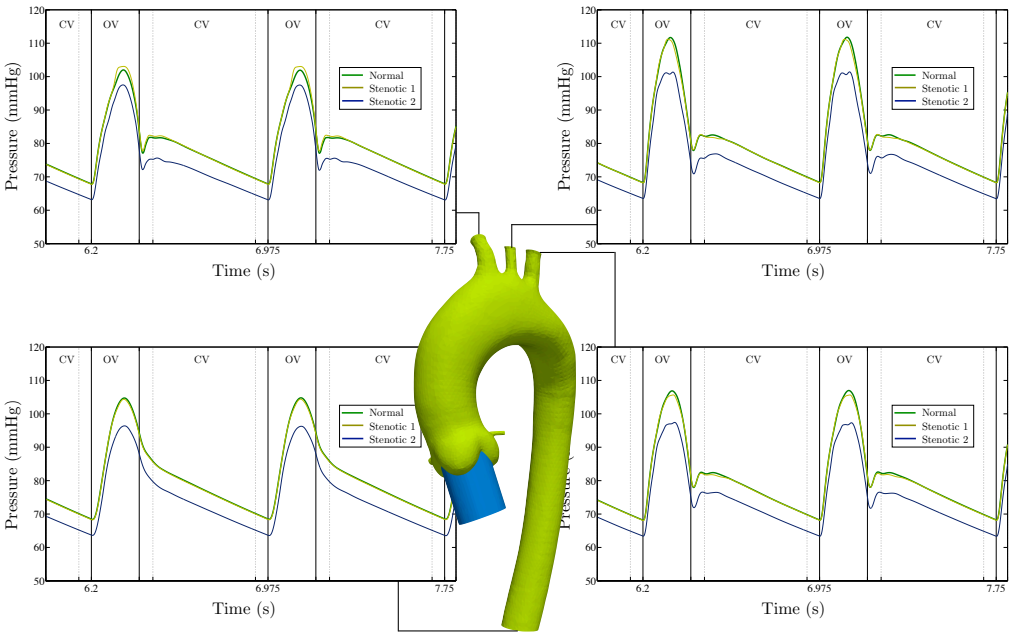

(b) *Pressures*.

Figure 4.15: *Two-fluid and RIS models: real geometry outlets*.

4.3.4 Clinical assessment of stenotic valve with RIS model

In order to asset the degree of a stenosis, clinicians have the use of standard indexes based on blood velocity and pressure measurements, established from simplified fluid mechanics equations. The blood pressure on both sides of the aortic valve can be directly obtained by catheterization. Doppler echocardiography, based on the ultra-sounds, can evaluate the velocity of the blood flow. In general the second one is preferred since is a non-invasive technique.

The most common manner to asset an aortic stenosis is to determine the net pressure gradient, $TPG_{net} = p_{_{LV}} - p_{_A}$, between the left ventricle (LV) and the ascending aorta. If the pressure is measured further down in the cross-sectional area where the flow jet is minimal, i.e. in the vena contracta (VC), the maximum pressure gradient $TPG_{max} = p_{_{LV}} - p_{_{VC}}$ is obtained as well (see e.g. [CdSG+05, GD06]). This method are invasive, since the pressure is computed by cathaterization. Using Doppler, the pressure gradient can be recovered from the measure of the velocity between left ventricle and the vena contracta. Clinicians in general assume that the ventricular velocity can be neglected, taking $\rho \simeq 1000\ kg/m^3$ and the average in time of the velocity in m, the *mean pressure gradient* converted in $mmHg$, is calculated as

$$\overline{TPG} = 4\bar{\mathbf{u}}^2_{_{VC}}. \tag{4.11}$$

However, the standard parameter used by clinicians for the assessment of aortic valve stenosis severity is the so-called aortic valve *Effective Orifice Area* [GPL+04, GK06, vL09]. The EOA is defined as the minimal cross-sectional area of the flow jet. Using catheterization, EOA is evaluated from the Gorlin equation [GG51] as $EOA_{cath} = Q/44.3\sqrt{TPG_{max}}$, where Q is the trans-valvular flow in mL/s and the value 44.3 is an empirical factor that derived from the original equation proposed by Gorlin. Using Doppler, this value is obtained from the application of the continuity equation between the left ventricle and the vena contracta. Assuming that the values of the areas are not modified during systolic ejection, that the section of the ventricle is circular and that velocity profiles are flat, EOA is expressed in cm^2 as

$$EOA = \frac{A_{_{LVOT}} \times \bar{\mathbf{u}}_{_{LVOT}}}{\bar{\mathbf{u}}_{_{VC}}}, \tag{4.12}$$

where $A_{_{LVOT}}$, measured in cm^2, is the cross-sectional area at the left ventricle outflow track, supposed to be constant through the systole. The two velocities $\bar{\mathbf{u}}_{_{LVOT}}$ and $\bar{\mathbf{u}}_{_{VC}}$ are respectively the temporal averages of the velocity at the left ventricle and in the vena contracta. The product $A_{_{LVOT}} \times \bar{\mathbf{u}}_{_{LVOT}}$ is the so-called *stroke volume*, i.e. the volume of blood pumped out from the ventricle in a heart beat. From the previous considerations, the EOA results constant in time as well.

Table 4.2 indicates the grade of a stenosis for the two clinical indexes discussed above. Mild and moderate in general ask for a constant medical monitoring of its progression. The severe stenosis usually requires aortic valve replacement.

A third way to evaluate aortic stenosis is to consider the dissipation of the energy supplied by the left ventricle work. In [GPD+00] the authors propose to derive the amount of

	mild	moderate	severe
$\overline{\mathbf{TPG}}$	$< 20\ mmHg$	$20\ mmHg\ -\ 50\ mmHg$	$> 50\ mmHg$
EOA	$> 1.5\ cm^2$	$1\ cm^2\ -\ 1.5\ cm^2$	$< 1\ cm^2$

Table 4.2: *Classification of aortic stenosis severity by mean of $\overline{TGP}$ and EOA. Guideline of America Heart Association* [BHB+09, Table 3]

energy loss from non-invasive measurements, by the expression

$$\overline{EL} = 4\left(\frac{\overline{Q}}{C_{EL}}\right)^2, \tag{4.13}$$

where $\overline{Q}$ is the mean trans-valvular flow, in mL. The term C_{EL} is the coefficient energy loss, expressed in cm^2 and defined by the relation

$$C_{EL} = \frac{EOA \times A_a}{A_a - EOA}, \tag{4.14}$$

where A_a, in cm^2, indicates the cross-sectional area of the ascending aorta, supposed by always constant. This coefficient can be easily obtained by Doppler and describes a more physical quantity directly linked to the damage caused by the stenosis on the heart work.

To evaluate the severity of the stenosis induced with the RIS valve model, we have derived the three clinical indexes explained above. The mean velocity $\bar{\mathbf{u}}_{LVOT}$ is computed on Γ_{in} and the velocity $\bar{\mathbf{u}}_{VC}$ is computed in a cross-sectional surface next to the open valve mesh configuration. The two time-average velocities, are computed over the systole phase of the last cardiac cycle. We have identified A_{LVOT} as Γ_{in}, it has an area of $2.5635\ cm^2$. The area of the ascending aorta A_a is $4.00834\ cm^2$ and we suppose corresponding to the interface Σ. The mean trans-valvular flow according to [CdSG+05, GPD+00] is computed as $\overline{Q} = \bar{\mathbf{u}}_{VC} \times EOA$. Table 4.3 reports the time-averaged velocities and the values obtained by (4.11)-(4.14), for the two stenotic test cases presented in the Paragraph 4.3.3.

	1 Stenotic leaflet	2 Stenotic leaflets
$\bar{\mathbf{u}}_{LVOT}$	$1.2811\ m$	$1.1745\ m$
$\bar{\mathbf{u}}_{VC}$	$2.1830\ m$	$4.0922\ m$
$\overline{\mathbf{TPG}}$	$19.0401\ mmHg$	$66.9330\ mmHg$
EOA	$1.5044\ cm^2$	$0.7357\ cm^2$
$\mathbf{C_{EL}}$	$2.4084\ cm^2$	$0.9011\ cm^2$
$\overline{\mathbf{EL}}$	$136.3605\ mmHg$	$301.0632\ mmHg$

Table 4.3: *Main clinical indexes for stenosis evaluation in an aortic valve described with a RIS model.*

The mean velocity computed in the LVOT, upstream the valve, is slightly lower for the second stenotic case. On the vena contracta (VC), downstream the valve, the mean velocity is obviously greater for the second stenotic case as consequence of the bigger narrowing of the valve orifice. According both $\overline{TPG}$ and EOA, the first case corresponds to a mild aortic

stenosis. Whereas with the second RIS stenotic valve model, we were able to simulate a severe aortic stenosis. The coefficient of energy loss increase with the increasing of the stenosis severity, i.e. with the decreasing of the EOA, keeping aortic section area constant. As a consequence the second test case presents a greater loss of energy, as we could expect.

4.4 Final remarks

In this chapter we have illustrated some numerical examples of the fluid-fluid model in the ascending aorta with the reduced model for the heart valves presented in [AHSG12]. Within this approach, the aortic valve is modeled by an immersed surface acting as a resistance on the fluid.

The pressure jump across the valve was obtained with the same approach used in [FGM08] to model a stent for a cerebral aneurysm. We introduce a fissured mesh and we paste together the degrees of freedom of the velocity while the pressures degrees of freedom have been kept separate in the proximal and distal valve label. This means to provide the solver of a geometry in which in pre-processing phase the valve labels where doubled. An alternative is to provide a geometry with a non-fissured mesh and then duplicate the degree of freedom of the pressure inside the solver.

The opening or the closure of the valve, i.e. the value of the resistance, is based on very simple fluid dynamics principles. In normal conditions, we choose to set the opening of the valve when $\Delta p > \alpha$ with $\alpha = 0$ and the closure when $Q < \beta$ with $\beta = 0$. However, we can set α and β different from zero to model particular pathologies, such as late or early opening and closure of the valve.

The computation of the resistance make the model non-linear, because the value of the resistance depends on the flow and the pressure at current time step. To linearize the problem two approaches can be used for the evaluation the resistances R_i

- $R_i^n = R_i(\mathbf{u}^n, p^n)$, $i = o, c$, the resistance is updated with the valve status at current time step. This method as the advantage to "predict" the valve status and to change it if not correct, but implies a re-computation of the fluid equation at least two times in a cardiac cycle.

- $R_i^{n-1} = R_i(\mathbf{u}^{n-1}, p^{n-1})$, $i = o, c$, the resistance is updated according the valve status at previous time step. This technique does not need a re-computation of the fluid equation, but produces a delay of δt in the opening/closure of the valve.

We have adopted in this chapter the first approach and we have performed two kinds of numerical experiments

1. The *template of the aorta*, has been used to test the two-fluid coupled model with the RIS valve model. With respect to the simulations presented in Chapter 3, the aortic root domain without closed valve configuration, has been replaced by a fissured domain with closed and open valve configuration, while the aortic arch mesh is

kept unchanged. The staggered algorithm applied is obtained with the explicit coupled scheme with the static pressure and unbalance energy estimation (Algorithm 2.3 on pag. 45). The presence of a resistive immersed surface does not impact the performances of the fluid-fluid model. This is confirmed by the flow and pressure errors on the interface reported in the Table 4.4.

ε_{f_1}	0.0073	ε_{p_1}	0.0185
ε_{f_2}	0.0180	ε_{p_2}	0.0198
ε_f	0.0246	ε_p	0.0064

Algorithm 4.1

Table 4.4: *Interface relative errors: flow* ε_{f_1}, ε_{f_2} *and pressure* ε_{p_1}, ε_{p_2}. *Interface drop errors: flow* ε_f *and pressure* ε_p.

The errors are computed with respect to the reference solution obtained solving (4.1) with a standard finite element discretization of the model in the one-piece domain. The expressions of the errors indicators has been defined in (3.1) on page 62.

2. The *realistic aorta*, whose geometry has been obtained from medical images, was employed to investigate two stenotic valve cases. The RIS model allows a certain flexibility in reproducing also pathological states of the valves. Pathologies, such as regurgitation or stenosis, can be included in the mathematical model simply putting non-zero resistance R_i on the stenotic leaflet, while keeping the same valve geometry with respect to the normal case. This is the choice we have adopted for the examples of Paragraph 4.3.3. An other option could be to consider the pathology directly in the computational geometry, i.e. providing a valve mesh presenting a particular configuration, taken for example from a patient specific model. In this direction an example is reported in [AHSG12], here the RIS model is applied to a patient-specific geometry derived from a computed tomography data set.

In the end we have illustrated how the RIS valve model can reproduce some of the main clinical indexes to recover a valve stenosis. According to clinical evaluation, our examples reproduce a mild and a severe stenosis. This shows how the RIS valve model can be appealing from a computational point of view, particularly for our coupled problems, as well as under a clinical point of view.

In the next chapter we extend the fluid-fluid approach to couple the left ventricle with the aorta. The RIS model for the aortic and mitral valve are considered as well.

Bibliography of Chapter 4

[AGPT09] M. Astorino, J.-F. Gerbeau, O. Pantz, and K.-F. Traoré. Fluid-structure interaction and multi-body contact. Application to the aortic valves. *Comput. Methods Appl. Mech. Engng.*, 198(45-46):3603–3612, 2009.

[AHSG12] M. Astorino, J. Hamers, S. C. Shadden, and J.-F. Gerbeau. A robust and efficient valve model based on resistive immersed surfaces. *Int. J. Numer. Meth. Biomed. Engng.*, 28:937–959, 2012.

[Ast10] M. Astorino. *Interaction Fluide-Structure dans le Systéme Cardiovasculaire. Analyse Numèrique et Simulation*. PhD thesis, Universitè Pierre et Marie Curie, Paris 6, 2010.

[BGH+09] Y. Bazilevs, J.R. Gohean, T.J.R. Hughes, R.D. Moser, and Y. Zhang. Patient-specific isogeometric fluid-structure interaction analysis of thoracic aortic blood flow due to implantation of the Jarvik 2000 left ventricular assist device. *Comput. Methods Appl. Mech. Engng.*, 198:3534–3550, 2009.

[BHB+09] H. Baumgartner, J. Hung, J. Bermejo, J. B. Chambers, A. Evangelista, B. P. Griffin, B. Iung, C. M. Otto, P. A. Pellikka, and M. Quinones. Echocardiographic assessment of valve stenosis: EAE/ASE recommendations for clinical practice. *European Journal of Echocardiography*, 10:1–25, 2009.

[CdSG+05] P. Causin, N. D. dos Santos, J.-F. Gerbeau, C. Guivieand, and P. Métier. An embedded surface method for valve simulation. Application to stenotic aortic valve estimation. *ESAIM*, 14:48–62, 2005.

[CFGM11] A. Caiazzo, M.A. Fernández, J.-F. Gerbeau, and V. Martin. Projection schemes for fluid flows through a porous interface. *SIAM Journal on Scientific Computing*, 33:541–564, 2011.

[DZL07] V. Díaz-Zuccarini and J. LeFèvre. An energetically coherent lumped parameter model of the left ventricle specially developed for educational purposes. *Comput. Biol. Med.*, 37:774–784, 2007.

[FGM08] M. Fernández, J.-F. Gerbeau, and V. Martin. Numerical simulation of blood flows through a porous interface. *Mathematical Modelling and Numerical Analysis*, 42:961–990, 2008.

[FLTV06] L. Formaggia, D. Lamponi, M. Tuveri, and A. Veneziani. Numerical modeling of 1d arterial networks coupled with a lumped parameters description of the heart. *Computer Methods in Biomechanics and Biomedical Engineering*, 9(5):273–288, 2006.

[GD06] D. Garcia and L.-G. Durand. *Aortic Stenosis and Systemic Hypertension, Modeling of*. John Wiley and Sons Inc., 2006.

[GG51] R. Gorlin and S.C. Gorlin. Hydraulic formula for calculation of the area of the stenotic mitral valve, other cardiac valves, and central circulatory shunts. *Journal of the America Heart Association*, 41:1–29, 1951.

[GK06] D. Garcia and L. Kadem. What do you mean by aortic valve area: Geometric orifice area, effective orifice area, or gorlin area? *J Heart Valve Dis.*, 15(5):601–608, 2006.

[GPD+00] D. Garcia, P. Pibarot, J. Dumesnil, F. Sakr, and L.-G. Durand. Assessment of aortic valve stenosis severity, a new index based on the energy loss concept. *Circulation. Journal of the America Heart Association*, 101:765–771, 2000.

[GPL+04] D. Garcia, P. Pibarot, C. Landry, A. Allard, B. Chayer, J. Dumesnil, and L.-G. Durand. Estimation of aortic valve effective orifice area by doppler echocardiography: Effects of valve inflow shape and flow rate. *Circulation. Journal of the America Heart Association*, 7:756–765, 2004.

[HNP+06] D. R. Hose, A. J. Narracott, J. M.T. Penrose, D. Baguley, I. P. Jones, and P. V. Lawford. Fundamental mechanics of aortic heart valve closure. *Journal of Biomechanics*, (39):958 – 967, 2006.

[HPSB03] J. De Hart, G.W.M. Peters, P.J.G. Schreurs, and F.P.T. Baaijens. A three-dimensional computational analysis of fluid-structure interaction in the aortic valve. *Journal of Biomechanics*, 36:103–112, 2003.

[JL06] E. Jung and W. Lee. Lumped parameter models of cardiovascular circulation in normal and arrhythmia cases. *J. Korean Math. Soc.*, 43(4):885–897, 2006.

[KS06a] T. Korakianitis and Y. Shi. A concentrated parameter model for the human cardiovascular system including heart valve dynamics and atrioventricular interaction. *Medical Engineering & Physics*, 28:613–628, 2006.

[KS06b] T. Korakianitis and Y. Shi. Numerical simulation of cardiovascular dynamics with healthy and diseased heart valves. *Journal of Biomechanics*, 39:1964–1982, 2006.

[LDSB10] K.D. Lau, V. Diaz, P. Scambler, and G. Burriesci. Mitral valve dynamics in structural and fluid-structure interaction models. *Medical Engineering & Physics*, 32:1057–1064, 2010.

[MBH+11] M. E. Moghadam, Y. Bazilevs, T.-Y. Hsia, I. E. Vignon-Clementel, and Al. L. Marsden. A comparison of outlet boundary treatments for prevention of backflow divergence with relevance to blood flow simulations. *Computational Mechanics*, 48(3):277–291, 2011.

[MKR+13] G. Marom, H.-S. Kim, M. Rosenfeld, E. Raanani, and R. Haj-Ali. Fully coupled fluid-structure interaction model of congenital bicuspid aortic valves: effect of asymmetry on hemodynamics. *Med. Biol. Eng. Comput.*, (51):839 – 848, 2013.

[NKI+13] T. Noack, P. Kiefer, R. Ionasec, I. Voigt, T. Mansi, M. Vollroth, M. Hoebartner, M. Misfeld, F.-W. Mohr, and J. Seeburger. New concepts for mitral valve imaging. *Annals of Cardiothoracic Surgery*, 2(6):787–795, 2013.

[NWY06] M. Nakamura, S. Wada, and T. Yamaguchi. Influence of the opening mode of the mitral valve orifice on intraventricular hemodynamics. *Annals of Biomedical Engineering*, 34(6):927–935, 2006.

[RFS+12] M.I K. Rausch, N. Famaey, T. O. Shultz, W. Bothe, D. C. Miller, and E. Kuhl. Mechanics of the mitral valve. A critical review, an in vivo parameter identification, and the effect of prestrain. *Biomech Model Mechanobiol*, 13:1053–1071, 2013 12:.

[RKM+99] S. I. Reynertson, R. Kundur, G. M. Mullen, M. R. Costanzo, T. L. McKiernan, and E. K. Louie. Asymmetry of right ventricular enlargement in response to tricuspid regurgitation. *Circulation. Journal of the America Heart Association*, 100:465–467, 1999.

[SAG10] S. Shadden, M. Astorino, and J.-F. Gerbeau. Computational analysis of an aortic valve jet with lagrangian coherent structures. *Chaos*, 20:017–512, 2010.

[SB09] F. Sotiropoulos and I. Borazjani. A review of state-of-the-art numerical methods for simulating flow through mechanical heart valves. *Med Biol Eng Comput*, 47:245–256, 2009.

[SMCCS08] J. Sainte-Marie, D. Chapelle, R. Cimrman, and M. Sorine. Modeling and estimation of the cardiac electromechanical activity. *Computers and Structures*, 84:1743–1759, 2008.

[SSG+04] G. Szabóa, D. Soansb, A. Grafa, C. J. Bellera, L. Waiteb, and S. Hagla. A new computer model of mitral valve hemodynamics during ventricular filling. *European Journal of Cardio-thoracic Surgery*, 26:239–247, 2004.

[TCBV09] M. D. De Tullio, A. Cristallo, E. Balaras, and R. Verzicco. Direct numerical simulation of the pulsatile flow through an aortic bileaflet mechanical heart valve. *J. Fluid Mech.*, 622:259 –290, 2009.

[TW89] J. D. Thomas and A. E. Weyman. Fluid dynamics model of mitral valve flow: Description with in vitro validation. *Journal of the American College of Cardiology*, 13(1):221–233, 1989.

[VCA+10] F. Viscardi, Vergara C, L. Antiga, S. Merelli, A. Veneziani, G. Puppini, G. Faggian, A. Mazzucco, and G. B. Luciani. Comparative finite element model analysis of ascending aortic flow in bicuspid and tricuspid aortic valve. *Artificial Organs*, 34(12):1114–1120, 2010.

[vL09] R. van Loon. Towards computational modelling of aortic stenosis. *Commun. Numer. Meth. Engng.*, 26(3-4):405–420, 2009.

[vLABvdV05] R. van Loon, P. D. Anderson, F. P.T. Baaijens, and F. N. van de Vosse. A three-dimensional fluid-structure interaction method for heart valve modelling. *C. R. Mecanique*, 333:856–866, 2005.

[WM07] E. J. Weinberg and M. R. K. Mofradl. Transient, three-dimensional, multiscale simulations of the human aortic valve. *Cardiovascular Engineering*, 7:140–155, 2007.

[WM08] E. J. Weinberg and M. R. K. Mofradl. A multiscale computational comparison of the bicuspid and tricuspid aortic valves in relation to calcific aortic stenosis. *Journal of Biomechanics*, 41:3482–3487, 2008.

[Zyg11] Zygote Media Group. *3D Human Anatomy for Animation, Illustration, CAD and Software Development*. http://www.zygote.com/, 2011. 3D Science project, http://www.3dscience.com/.

CHAPTER 5

An energy stable time-marching scheme for fluid flows in moving domains

This chapter of the thesis is devoted to the numerical stability of a time discretization scheme for fluids in moving domains, through the so called ALE (Arbitrary Eulerian Lagrangian) formulation. The difficulty comes from those integrals, which are integrated over the moving domain at a given time-step. We show that adding a suitable consistent term we can get a stable energy inequality without fulfilling any Geometric Conservation Laws, that were so far necessary to establish an energy balance for the fluid equations on a moving domain.

Contents

5.1 Introduction

The ultimate goal of this thesis is to present some numerical examples of cardiac hemodynamics, generated by the left ventricle contraction. To reach this aim we present here the mathematical model of fluid problem in moving domains.

Indeed, despite the assumption of fixed domain made in previous chapters, the blood dynamics is in general a phenomenon occurring in computational domains that moves in time. In hemodynamics the *Arbitrary Lagrangian-Eulerian* (ALE) formulation is commonly used for fluid-solid interaction problems in particular for numerical simulations in compliant arteries (e.g. [Ber12, FQV09] and references therein).

The ALE formulations is a popular technique which facilitates the time discretization of partial differential equations on moving domains [DHPRF04, HLZ81]. In the arbitrary Lagrangian-Eulerian description, the computational domain is neither fixed (*Eulerian* framework), nor governed by the fluid motion (*Lagrangian* framework), but its dynamics is driven by the movement of the boundary/interface. Inside the domain the movement can be given by any smooth lift of the movement of interface, this determines its arbitrary definition.

Within this approach, the unsteady Navier-Stokes equations, are expressed with respect to a reference fixed configuration and a so-called ALE map associates at each time t a point in the current computational domain to a point in the reference domain. The most obvious influence of an ALE formulation in flow problems is that the convective term must account for the mesh motion which can increase or decrease the convection effects.

A major difficulty that has to be faced is the fact that a numerical time-discretization scheme for fixed domains does not necessary preserve stability and cannot be translated to moving domains.

In problems with moving domains, some properties can be lost by discretization. To ensure these properties after discretization, several works suggest to consider the so-called *Geometric Conservation Law* (*GCL*) (see [EGP09, TL79] for a review). The GCL is usually necessary to establish an energy balance for the original fluid equations on a moving domain (see [FN99, TM01]). The notion of GCL has been much investigated in the framework of the finite differences (e.g. [TL79, ZRTC93]) and finite volume method (see e.g. [GF00, LF96, ZRTC93]). In the framework of finite element methods we cite [BG04, FN99, FN04] where the unconditional stability is guaranteed through the fulfillment of a GCL condition.

In this chapter we present the fluid equations expressed with the ALE formalism and we derive its discrete energy balance. We shall see that for a backward Euler scheme, a simple correction, inspired by the "Temam's trick" [Tem68, Tem79] , allows us to recover the energy inequality without requiring any Geometric Conservation Laws.

Outline This chapter is organized as follows. In next section we provide the reader with the essential vocabulary of the continuum mechanics (Paragraph 5.2.1) and we present the ALE formalism (Paragraph 5.2.2). The fluid problems in a moving domain described via the ALE map is presented in Section 5.3. Section 5.4 deals with the space and time discretization of the fluid problem in a moving domain (Paragraph 5.4.1) and its energy balance (Paragraph 5.4.2). The chapter ends with some numerical tests (Paragraph 5.5).

5.2 Fundamentals of continuum mechanics

In this section we provide some basic notions about the mathematical modeling of the continuum media. For a more detailed exposition about this topic we refer to [FFGQ09, Gur81].

5.2.1 Lagrangian and Eulerian formalism

Let $\widehat{\Omega}$ be a domain, i.e. a bounded, open and simply connected subset of $\mathbb{R}^3$, with smooth boundary, filled by a continuum medium. The domain $\widehat{\Omega}$ is called the *reference* (or *not-deformed*) *configuration* of the medium under consideration (fluid or solid). In general, $\widehat{\Omega}$ can be the position of the continuum medium in a certain instant t. Any change in time of the configuration of the continuum body is the result of a *motion* defined by a non-linear mapping (Figure 5.1[1]).

$$\begin{aligned} \hat{\boldsymbol{\varphi}} : \widehat{\Omega} \times \mathbb{R}^+ &\longrightarrow \Omega(t) \\ (\hat{\mathbf{x}}, t) &\longmapsto \mathbf{x} = \hat{\boldsymbol{\varphi}}(\hat{\mathbf{x}}, t). \end{aligned} \tag{5.1}$$

The point $\mathbf{x} = \hat{\boldsymbol{\varphi}}(\hat{\mathbf{x}}, t) \equiv \hat{\boldsymbol{\varphi}}_t(\hat{\mathbf{x}})$ represents the position of the *material particle* identified by $\hat{\mathbf{x}}$, while $\Omega(t) \stackrel{\text{def}}{=} \hat{\boldsymbol{\varphi}}_t(\widehat{\Omega})$ denotes the *current* (or *deformed*) *configuration* at time $t \geq 0$.

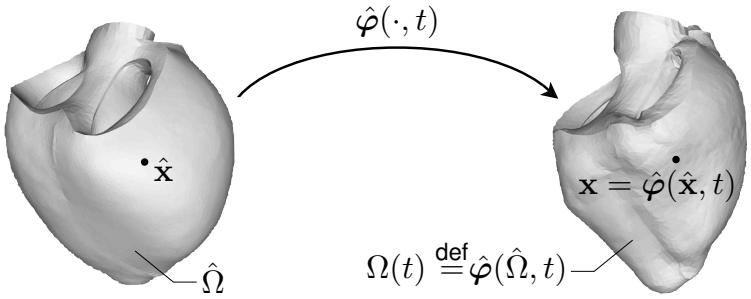

Figure 5.1: *Deformation of a continuum medium.*

For any fixed time $\bar{t} \geq 0$, $\hat{\boldsymbol{\varphi}}_{\bar{t}}(\hat{\mathbf{x}}) \equiv \hat{\boldsymbol{\varphi}}(\hat{\mathbf{x}}, \bar{t})$ defines a *deformation* of the continuum body. In other words, a motion is one-parameter family of deformations, the parameter t being the time. In addition we can define the *displacement* of a material particle $\hat{\mathbf{x}}$ as the vector field

$$\begin{aligned} \hat{\mathbf{d}} : \widehat{\Omega} \times \mathbb{R}^+ &\longrightarrow \mathbb{R}^3 \\ (\hat{\mathbf{x}}, t) &\longmapsto \hat{\mathbf{d}}(\hat{\mathbf{x}}, t) \stackrel{\text{def}}{=} \hat{\boldsymbol{\varphi}}_t(\hat{\mathbf{x}}) - \hat{\mathbf{x}}. \end{aligned} \tag{5.2}$$

Assuming that $\hat{\boldsymbol{\varphi}}_t \in C^1(\widehat{\Omega})$, we can define the time-dependent *deformation gradient* as $\widehat{\boldsymbol{F}}(\hat{\mathbf{x}}, t) \stackrel{\text{def}}{=} \nabla_{\hat{\mathbf{x}}} \hat{\boldsymbol{\varphi}}(\hat{\mathbf{x}}, t)$, where the symbol $\nabla_{\hat{\mathbf{x}}}$ indicates the gradient with respect to the $\hat{\mathbf{x}} = (\hat{x}_1,\ \hat{x}_2,\ \hat{x}_3)$ coordinates. The deformation gradient is a second order tensor field $\widehat{\boldsymbol{F}} : \widehat{\Omega} \times \mathbb{R}^+ \longrightarrow \mathbb{R}^3 \times \mathbb{R}^3$, $\hat{F}_{ij} = \frac{\partial x_i}{\partial \hat{x}_j}$, with $i, j = 1, 2, 3$. We also assume that its determinant $\widehat{J} \stackrel{\text{def}}{=} \det[\widehat{\boldsymbol{F}}(\hat{\mathbf{x}}, t)]$, called the *Jacobian* of the deformation, is everywhere strictly positive. This means that the mapping is orientation preserving.

All physical quantities can be defined alternatively on the reference $\widehat{\Omega}$ or on the current configuration $\Omega(t)$, the choice being a matter of convenience. In order to solve the differential

[1] The images of two domains are taken from a simulation of [Imp13].

equations governing the motion of a continuum medium (fluid or solid) we need to identify the appropriate computational domain where the equations have to be solved and provide suitable boundary conditions. We thus define the two configurations

- *Lagrangian* when we adopt $(\hat{\mathbf{x}}, t)$ as independent variables, we focus on the *material particle* $\hat{\mathbf{x}}$ and its evolution. This coordinate system is usually said *material*.
  This configuration is typically adopted to describe the evolution of a solid, whose displacements are often relatively small. The computational domain is thus taken to be $\widehat{\Omega}$.

- *Eulerian* we observe what happens at a given point $\mathbf{x}$ in the *physical space*, we refer to the $(\mathbf{x}, t)$ pair as independent variables. This second coordinate system is instead termed *spatial*.
  This configuration is preferred to describe the evolution of fluids since the displacements are extremely large and usually irrelevant. The motion of the fluid is observed in a control volume, normally chosen as a fixed, open bounded set $\Omega \subset \mathbb{R}^3$ such that $\Omega \subset \Omega(t)$, for all times t.

In the following, we adopt the usual convention to denote with the superscript $\hat{\cdot}$ a Lagrangian field. For the rest of configurations the superscript is not used.

5.2.2 The ALE formalism

In many cases of practical interest in hemodynamics, such as blood flowing in a compliant artery, the computational domain for the fluid cannot be fixed in time, as it has to follow the displacements of the fluid-wall interface. The Eulerian configuration is not convenient. Yet, the Lagrangian frame is not of help here, since certainly we do not wish to follow the evolution of the blood particles as they circulate along the whole cardiovascular system.

We usually wish to compute the flow field in a domain confined in the area of interest, yet following the movement of the wall interface. It is then necessary to introduce another, intermediate, frame of reference, i.e. an *Arbitrary Lagrangian Eulerian* (ALE). In this frame the computational domain, is not fixed, because of the moving boundary, and is not necessarily a material sub-domain, since its evolution is not governed by the fluid motion, but the computational domain has to follow the motion of the boundary (Figure 5.2).

The ALE description is based on the introduction of an appropriate mapping $\widehat{\mathcal{A}}$ from a reference fixed configuration $\widehat{\Omega}$ (e.g. $\widehat{\Omega} = \Omega(0)$) to the current moving domain $\Omega(t)$

$$\begin{aligned} \widehat{\mathcal{A}} : \widehat{\Omega} \times \mathbb{R}^+ &\longrightarrow \Omega(t) \\ (\hat{\mathbf{x}}, t) &\longmapsto \mathbf{x} = \widehat{\mathcal{A}}(\hat{\mathbf{x}}, t) \end{aligned} \tag{5.3}$$

such that $\Omega(t) = \widehat{\mathcal{A}}(\widehat{\Omega}, t)$ for all $t \geq 0$.

In the ALE formulation we have then the interplay of (at least) two motions: the one of the medium under consideration and that of the computational domain. The former is governed by physical laws, the latter is rather arbitrary, provided that the given law for the domain boundary movement be respected. The ALE map $\widehat{\mathcal{A}}_t(\hat{\mathbf{x}}) \equiv \widehat{\mathcal{A}}(\hat{\mathbf{x}}, t)$ represents the

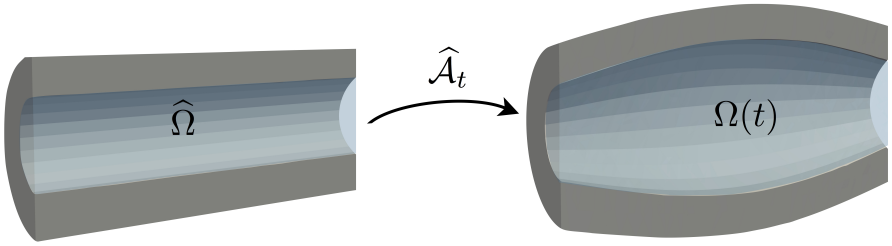

Figure 5.2: *Blood flow in a compliant artery is a typical example of a continuum medium whose evolution is described by an ALE map* $\widehat{\mathcal{A}}_t$.

deformation of the domain at any time $t \geq 0$, we can define then the corresponding *domain velocity* as

$$\hat{\mathbf{w}} \stackrel{\text{def}}{=} \frac{\partial \widehat{\mathcal{A}}(\hat{\mathbf{x}}, t)}{\partial t}, \qquad \forall \hat{\mathbf{x}} \in \widehat{\Omega}. \tag{5.4}$$

For any given function $\hat{f} : \widehat{\Omega} \to \mathbb{R}^d$, $d = 1, 2, 3$ defined in the ALE reference domain $\widehat{\Omega}$, we can write its Eulerian description as $f(\mathbf{x}, t) = \hat{f}(\widehat{\mathcal{A}}_t^{-1}(\mathbf{x}), t)$, $\forall \mathbf{x} \in \Omega(t)$, $t > 0$. In what follows, we use the Eulerian representation of the ALE domain velocity, i.e.

$$\mathbf{w}(\mathbf{x}, t) = \hat{\mathbf{w}}(\widehat{\mathcal{A}}_t^{-1}(\mathbf{x}), t), \qquad \forall \mathbf{x} \in \Omega(t), \quad t > 0. \tag{5.5}$$

In order to use an ALE formulation, we need to introduce the corresponding ALE time-derivative of an Eulerian (scalar or vector) field $f : \Omega(t) \to \mathbb{R}^d$, $d = 1, 2, 3$, as

$$\left.\frac{\partial f}{\partial t}\right|_{\widehat{\mathcal{A}}} = \left.\frac{\partial f}{\partial t}\right|_{\hat{\mathbf{x}}} + \mathbf{w} \cdot \nabla f, \tag{5.6}$$

derived by the application of the chain rule for the composition of functions, we refer to [FFGQ09, Proposition 3.3, page 87] for the proof. The transport term $\mathbf{w} \cdot \nabla f$ accounts for the variation of f caused by the motion of the computational domain.

We can also define the Jacobian of the ALE deformation as

$$\widehat{J}_{\widehat{\mathcal{A}}} \stackrel{\text{def}}{=} \det[\nabla_{\hat{\mathbf{x}}} \widehat{\mathcal{A}}(\hat{\mathbf{x}}, t)]. \tag{5.7}$$

The quantity $|\widehat{J}_{\widehat{\mathcal{A}}}| d\hat{\mathbf{x}}$ can be seen as the infinitesimal volume after the ALE deformation of the reference infinitesimal volume. More precisely we have

$$\int_{\widehat{\mathcal{A}}_t(\widehat{\Omega})} d\mathbf{x} = \int_{\widehat{\Omega}} |\widehat{J}_{\widehat{\mathcal{A}}}| d\hat{\mathbf{x}}. \tag{5.8}$$

It is thus natural to assume that $\widehat{J}_{\widehat{\mathcal{A}}} > 0$, in order to preserve the orientation. In addition, it

can be proved that [FFGQ09]

$$\partial_t \widehat{J}_{\widehat{\mathcal{A}}} = \widehat{J}_{\widehat{\mathcal{A}}} \nabla \cdot \mathbf{w}, \tag{5.9}$$

obtained recasting the so-called *Euler expansion formula* to the ALE mapping.

5.3 The fluid problem in the ALE formalism

When a fluid problem is stated in a moving domain, it is convenient to describe its evolution with an ALE map (5.3).

Let $\Omega(t) \subset \mathbb{R}^3$ be a bounded time-dependent control volume described by an ALE mapping (5.3), i.e. $\Omega(t) \overset{\text{def}}{=} \widehat{\mathcal{A}}_t(\widehat{\Omega})$. The reference domain $\widehat{\Omega}$ being, for example, the control volume at initial time, e.g. $\widehat{\Omega} \equiv \Omega(0)$ (Figure 5.3). Let $\mathbf{n}$ denote the unit outward normal on the boundary $\partial\Omega(t) = \Gamma_D \cup \Gamma_N \cup \Sigma(t)$. The velocity of the fluid domain $\mathbf{w}$ is given by (5.5). For the sake of simplicity, the inlet and outlet surfaces Γ_D and Γ_N are assumed to be fixed, i.e. $\mathbf{w} = \mathbf{0}$ on $\Gamma_D \cup \Gamma_N$ and $\Sigma(t)$ denotes the current configuration of the moving interface.

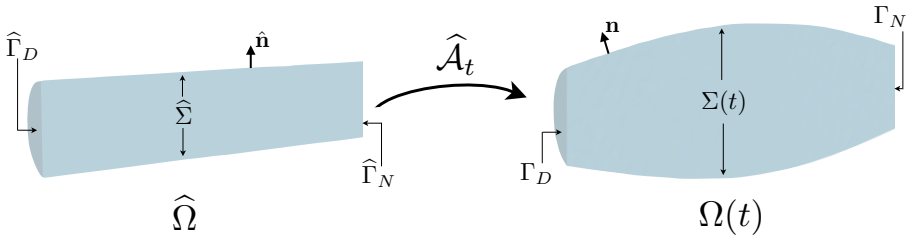

Figure 5.3: *Motion of the computational fluid domain via the ALE map* $\widehat{\mathcal{A}}_t$.

The incompressible Navier-Stokes equations in the ALE formulation reads as follows. Find the velocity $\mathbf{u} : \Omega(t) \times \mathbb{R}^+ \to \mathbb{R}^d$ and the pressure $p : \Omega(t) \times \mathbb{R}^+ \to \mathbb{R}$ of the fluid satisfying

$$\begin{cases} \rho \partial_t \mathbf{u}|_{\widehat{\mathcal{A}}} + \rho(\mathbf{u} - \mathbf{w}) \cdot \nabla \mathbf{u} - \nabla \cdot \boldsymbol{\sigma}(\mathbf{u}, p) = \mathbf{0}, & \text{in } \Omega(t), \\ \nabla \cdot \mathbf{u} = 0, & \text{in } \Omega(t), \\ \mathbf{u} = \mathbf{u}_D, & \text{on } \Gamma_D, \\ \boldsymbol{\sigma}(\mathbf{u}, p)\mathbf{n} = \mathbf{0}, & \text{on } \Gamma_N, \\ \mathbf{u} = \mathbf{w}, & \text{on } \Sigma(t), \end{cases} \tag{5.10}$$

with the initial conditions $\mathbf{u}(0) = \mathbf{u}_0$. The time derivative $\partial_t \mathbf{u}|_{\widehat{\mathcal{A}}}$ is the ALE derivative defined in (5.6). The term $\boldsymbol{\sigma}(\mathbf{u}, p) = -p\mathbf{I} + 2\mu\boldsymbol{\epsilon}(\mathbf{u})$, where $\boldsymbol{\epsilon}(\mathbf{u}) = (\nabla \mathbf{u} + \nabla^T \mathbf{u})/2$, is the fluid stress tensor. While ρ and μ stand for the fluid density and the dynamic viscosity respectively, both assumed to be constant.

REMARK 5.1
The analysis that follows holds also by assuming that $\mathbf{u}\cdot\mathbf{n} = \mathbf{w}\cdot\mathbf{n}$ *with* $\mathbf{n}$ *outgoing normal vector on* $\Sigma(t)$*. This means that the fluid can slip along the interface.*

In order to get an energy equality of the above problem, we multiply the $(5.10)_1$ by $\mathbf{u}$ and integrating over $\Omega(t)$, we get

$$\underbrace{\rho\int_{\Omega(t)}\frac{\partial}{\partial t}\Big|_{\widehat{\mathcal{A}}}\left(\frac{|\mathbf{u}|^2}{2}\right)}_{T_1}+\underbrace{\int_{\Omega(t)}\rho(\mathbf{u}-\mathbf{w})\cdot\nabla\mathbf{u}\cdot\mathbf{u}}_{T_2}+\underbrace{\int_{\Omega(t)}\nabla\cdot\boldsymbol{\sigma}(\mathbf{u},p)\cdot\mathbf{u}}_{T_3}=0. \tag{5.11}$$

With the use of the property (5.8), the first term can be reformulated as

$$\begin{aligned}T_1&=\int_{\widehat{\Omega}}\rho\frac{\partial}{\partial t}\Big|_{\widehat{\mathcal{A}}}\left(\frac{|\hat{\mathbf{u}}|^2}{2}\right)\widehat{J}_{\widehat{\mathcal{A}}}=\frac{\rho}{2}\frac{d}{dt}\int_{\widehat{\Omega}}|\hat{\mathbf{u}}|^2\widehat{J}_{\widehat{\mathcal{A}}}-\frac{\rho}{2}\int_{\widehat{\Omega}}|\hat{\mathbf{u}}|^2\partial_t\widehat{J}_{\widehat{\mathcal{A}}}\\&=\frac{\rho}{2}\frac{d}{dt}\int_{\Omega(t)}|\mathbf{u}|^2-\frac{\rho}{2}\int_{\Omega(t)}|\mathbf{u}|^2\nabla\cdot\mathbf{w},\end{aligned}$$

and the last one was obtained by mean of (5.9) and (5.8). Thus, integrating the second term of (5.11) by parts, knowing that $\mathbf{w}=\mathbf{0}$ on $\Gamma_D\cup\Gamma_N$ and using the boundary condition $\mathbf{u}\cdot\mathbf{n}=\mathbf{w}\cdot\mathbf{n}$ on $\Sigma(t)$, we get

$$\begin{aligned}T_2=&\frac{\rho}{2}\int_{\Sigma}(\mathbf{u}-\mathbf{w})\cdot\mathbf{n}|\mathbf{u}|^2+\frac{\rho}{2}\int_{\Omega(t)}|\mathbf{u}|^2(\nabla\cdot\mathbf{w})+\frac{\rho}{2}\int_{\Gamma_N\cup\Gamma_D}(\mathbf{u}\cdot\mathbf{n})|\mathbf{u}|^2\\=&\frac{\rho}{2}\int_{\Omega(t)}|\mathbf{u}|^2\nabla\cdot\mathbf{w}+\frac{\rho}{2}\int_{\Gamma_D\cup\Gamma_N}\mathbf{u}\cdot\mathbf{n}|\mathbf{u}|^2.\end{aligned}$$

In the end, integrating the term T_3 by parts, we obtain

$$T_3=2\mu\int_{\Omega(t)}|\boldsymbol{\epsilon}(\mathbf{u})|^2+\int_{\Sigma\cup\Gamma_D}\boldsymbol{\sigma}(\mathbf{u},p)\mathbf{n}\cdot\mathbf{u}.$$

Inserting T_1, T_2 and T_3 in (5.11) we obtain the following energy

$$\frac{\rho}{2}\frac{d}{dt}\int_{\Omega(t)}|\mathbf{u}|^2+2\mu\int_{\Omega(t)}|\boldsymbol{\epsilon}(\mathbf{u})|^2+\frac{\rho}{2}\int_{\Gamma_D\cup\Gamma_N}\mathbf{u}\cdot\mathbf{n}|\mathbf{u}|^2=-\int_{\Sigma\cup\Gamma_D}\boldsymbol{\sigma}(\mathbf{u},p)\mathbf{n}\cdot\mathbf{u}. \tag{5.12}$$

After discretization it is possible that some properties can be lost. In the following section we present the time-space fully discretization of the problem (5.10) and we discuss its energy balance.

5.4 An energy stable time-marching scheme for fluid flows in moving domains

5.4.1 Variational formulation and discretization of the fluid problem

Problem (5.10) can be reformulated in a weak form using appropriate test functions, performing integrations by parts and taking into account the boundary conditions. Let $\hat{\mathbf{v}} : \widehat{\Omega} \to \mathbb{R}^d$ and $\hat{q} : \widehat{\Omega} \to \mathbb{R}^d$ be two time-independent smooth functions, such that $\hat{\mathbf{v}} \in [H^1(\widehat{\Omega})]^d$ and $\hat{q} \in L^2(\widehat{\Omega})$. Hence for the ALE fluid problem, we consider as test functions their Eulerian counterparts defined in the two functional spaces

$$\mathcal{X} \stackrel{\text{def}}{=} \{\mathbf{v} : \Omega(t) \to \mathbb{R}^d,\ \mathbf{v} = \hat{\mathbf{v}}(\widehat{\mathcal{A}}_t^{-1}(\mathbf{x}))\}, \quad \forall \hat{\mathbf{v}} \in [H^1(\widehat{\Omega})]^d, \tag{5.13}$$

and

$$\mathcal{M} \stackrel{\text{def}}{=} \{q : \Omega(t) \to \mathbb{R}^d,\ q = \hat{q}(\widehat{\mathcal{A}}_t^{-1}(\mathbf{x}))\}, \quad \forall \hat{q} \in L^2(\widehat{\Omega}), \tag{5.14}$$

and we denote by $\mathcal{X}_\gamma$ the space of the functions in $\mathcal{X}$ vanishing on a part γ of the boundary $\partial\Omega(t)$. Notice that, in contrast to test functions on fixed domains, these functions are time-dependent. However, since $\hat{\mathbf{v}}$ and $\hat{q}$ are independent of t, their Eulerian counterparts have zero ALE time-derivative, i.e. $\partial_t \mathbf{v}|_{\widehat{\mathcal{A}}} = \mathbf{0}$ and $\partial_t q|_{\widehat{\mathcal{A}}} = 0$.

Then the variational formulation of the ALE fluid problem can be obtained by multiplying the fluid equation (5.10) by $(\mathbf{v}, q) \in \mathcal{X}_{\Gamma_D \cup \Sigma} \times \mathcal{M}$, then integrating by parts and taking into account the boundary conditions, we get

$$\begin{aligned} &\rho \int_{\Omega(t)} \frac{\partial \mathbf{u}}{\partial t}\Big|_{\widehat{\mathcal{A}}} \cdot \mathbf{v} + \rho \int_{\Omega(t)} (\mathbf{u} - \mathbf{w}) \cdot \nabla \mathbf{u} \cdot \mathbf{v} + 2\mu \int_{\Omega(t)} \boldsymbol{\epsilon}(\mathbf{u}) : \boldsymbol{\epsilon}(\mathbf{v}) \\ &- \int_{\Omega(t)} p \nabla \cdot \mathbf{v} + \int_{\Omega(t)} q \nabla \cdot \mathbf{u} = 0. \end{aligned} \tag{5.15}$$

With a change of variable and using the propriety $\partial_t \mathbf{v}|_{\widehat{\mathcal{A}}} = \mathbf{0}$, we can rewrite the first integral of the previous formulation as

$$\begin{aligned} \rho \int_{\Omega(t)} \frac{\partial \mathbf{u}}{\partial t}\Big|_{\widehat{\mathcal{A}}} \cdot \mathbf{v} &= \rho \int_{\widehat{\Omega}} \widehat{J}_{\widehat{\mathcal{A}}} \left(\frac{\partial \hat{\mathbf{u}}}{\partial t} \cdot \hat{\mathbf{v}} \right) \\ &= \rho \frac{d}{dt} \int_{\widehat{\Omega}} \widehat{J}_{\widehat{\mathcal{A}}} (\hat{\mathbf{u}} \cdot \hat{\mathbf{v}}) - \rho \int_{\widehat{\Omega}} \widehat{J}_{\widehat{\mathcal{A}}} (\hat{\mathbf{u}} \cdot \hat{\mathbf{v}}) \widehat{\nabla \cdot \mathbf{w}} \\ &= \rho \frac{d}{dt} \int_{\Omega(t)} \mathbf{u} \cdot \mathbf{v} - \rho \int_{\Omega(t)} (\mathbf{u} \cdot \mathbf{v}) \nabla \cdot \mathbf{w}. \end{aligned} \tag{5.16}$$

Owing these remarks we can now present the space discretization of the previous variational formulation. Let $\{\mathcal{T}_h(t)\}_{0 \le h \le 1}$, for every $t > 0$, be a suitable family of triangulations of the domain $\Omega(t)$, with typical diameter h. Let $\mathcal{X}_h \times \mathcal{M}_h$ denote an inf-sup stable and conforming finite element approximation of the spaces $\mathcal{X} \times \mathcal{M}$ and $\mathcal{V}_h = \mathcal{X}_h \cap \mathcal{X}_{\Gamma_D \cup \Sigma}$. The variational formulation of (5.10) reads:
For all $t \in \mathbb{R}^+$, find $(\mathbf{u}_h,\ p_h) \in \mathcal{X}_h \times \mathcal{M}_h$ satisfying the essential boundary conditions and

such that

$$A_{\widehat{\mathcal{A}}}[\mathbf{u}_h;(\mathbf{u}_h,p_h),(\mathbf{v}_h,q_h)]=0, \tag{5.17}$$

for all $(\mathbf{v}_h,\ q_h)\in\mathcal{V}_h\times\mathcal{M}_h$ and we use the shorthand notation

$$\begin{aligned}A_{\widehat{\mathcal{A}}}[\mathbf{u}_h;(\mathbf{u}_h,p_h),(\mathbf{v}_h,q_h)] \overset{\text{def}}{=}\ & \rho\frac{d}{dt}\int_{\Omega(t)}\mathbf{u}_h\cdot\mathbf{v}_h+\rho\int_{\Omega(t)}(\mathbf{u}_h-\mathbf{w}_h)\cdot\nabla\mathbf{u}_h\cdot\mathbf{v}_h\\ &-\rho\int_{\Omega(t)}(\mathbf{u}_h\cdot\mathbf{v}_h)\nabla\cdot\mathbf{w}_h+2\mu\int_{\Omega(t)}\boldsymbol{\epsilon}(\mathbf{u}_h):\boldsymbol{\epsilon}(\mathbf{v}_h)\\ &-\int_{\Omega(t)}p_h\nabla\cdot\mathbf{v}_h+\int_{\Omega(t)}q_h\nabla\cdot\mathbf{u}_h.\end{aligned} \tag{5.18}$$

We can now present the time discretization of the problem (5.17). A semi-implicit Euler scheme is used. Let denote $\delta t\overset{\text{def}}{=}T/N$ the time step size, the interval of interest is $(0,T)$, $N\in\mathbb{N}^+$ is a given integer and $x^n\approx x(n\delta t)$ with $0\leq n\leq N$. The time-space fully discretization problem (5.10) is summarized in the following algorithm.

ALGORITHM 5.1 (Standard ALE formulation)

1. *Find* $(\mathbf{u}_h^n,\ p_h^n)\in\mathcal{X}_h\times\mathcal{M}_h$ *satisfying* $\mathbf{u}_h^n=\mathbf{w}_h^n$ *on* Σ^n *and* $\mathbf{u}_h^n=\mathbf{u}_D^n$ *on* Γ_D*, such that*

$$A_{\widehat{\mathcal{A}},\delta t}[\mathbf{u}_h^{n-1};(\mathbf{u}_h^n,p_h^n),(\mathbf{v}_h,q_h)]=0, \tag{5.19}$$

   for all $(\mathbf{v}_h,\ p_h)\in\mathcal{V}_h\times\mathcal{M}_h$.

2. *Go to next time-step.*

The expression $A_{\widehat{\mathcal{A}},\delta t}[\mathbf{u}_h^{n-1};(\mathbf{u}_h^n,p_h^n),(\mathbf{v}_h,q_h)]$ appearing in (5.19) is given by

$$\begin{aligned}A_{\widehat{\mathcal{A}},\delta t}[\mathbf{u}_h^{n-1};(\mathbf{u}_h^n,p_h^n),(\mathbf{v}_h,q_h)] \overset{\text{def}}{=}\ & \frac{\rho}{\delta t}\left(\int_{\Omega^n}\mathbf{u}_h^n\cdot\mathbf{v}_h-\int_{\Omega^{n-1}}\mathbf{u}_h^{n-1}\cdot\mathbf{v}_h\right)\\ &+\rho\int_{\Omega^n}(\mathbf{u}_h^{n-1}-\mathbf{w}_h^{n-1})\cdot\nabla\mathbf{u}_h^n\cdot\mathbf{v}_h\\ &-\rho\int_{\Omega^n}(\mathbf{u}_h^n\cdot\mathbf{v}_h)\nabla\cdot\mathbf{w}_h^{n-1}+2\mu\int_{\Omega^n}\boldsymbol{\epsilon}(\mathbf{u}_h^n):\boldsymbol{\epsilon}(\mathbf{v}_h)\\ &-\int_{\Omega^n}p_h^n\nabla\cdot\mathbf{v}_h+\int_{\Omega^n}q_h\nabla\cdot\mathbf{u}_h^n+\frac{\rho}{2}\int_{\Omega^n}(\mathbf{u}_h^n\cdot\mathbf{v}_h)(\nabla\cdot\mathbf{u}_h^{n-1}).\end{aligned} \tag{5.20}$$

The last integral in (5.20) is nothing but the standard Temam's trick [Tem68, Tem79].

REMARK 5.2

An alternative scheme can be obtained from the direct discretization of (5.18)*, without a change of variable. But the technique we present in what follows does not apply to this scheme.*

5.4.2 Energy equality of a fluid problem in moving domain

In what follows we will use the quantity (the interior power)

$$E^n_{\widehat{\mathcal{A}}} \overset{\text{def}}{=} \frac{\rho}{2\delta t}\left(||\mathbf{u}^n_h||^2_{\Omega^n} - ||\mathbf{u}^{n-1}_h||^2_{\Omega^{n-1}} + ||\mathbf{u}^n_h - \mathbf{u}^{n-1}_h||^2_{\Omega^{n-1}}\right) + 2\mu||\boldsymbol{\epsilon}(\mathbf{u}^n_h)||^2_{\Omega^n}. \tag{5.21}$$

A first attempt to derive an energy equation for (5.19) brings to the following result.

PROPOSITION 5.1
Let $\mathcal{L}_h\mathbf{u}^n_h$ denote any discrete lifting of $\mathbf{u}^n_h$ from $\partial\Omega^n$ to Ω^n such that $\mathcal{L}_h\mathbf{u}^n_h = \mathbf{u}^n_h$ on $\Gamma_D\cup\Sigma$ and $\mathcal{L}_h\mathbf{u}^n_h = \mathbf{0}$ otherwise. Let $(\mathbf{u}^n_h, p^n_h)$ be solution of Algorithm 5.1. Then we have the following energy balance

$$\begin{aligned} &E^n_{\widehat{\mathcal{A}}} + \frac{\rho}{2}\left[\frac{1}{\delta t}\left(\int_{\Omega^n}|\mathbf{u}^n_h|^2 - \int_{\Omega^{n-1}}|\mathbf{u}^n_h|^2\right) - \int_{\Omega^n}|\mathbf{u}^n_h|^2\nabla\cdot\mathbf{w}^{n-1}_h\right] + \frac{\rho}{2}\int_{\Gamma_N\cup\Gamma_D}(\mathbf{u}^{n-1}_h\cdot\mathbf{n})|\mathbf{u}^n_h|^2 \\ &= A_{\widehat{\mathcal{A}},\delta t}[\mathbf{u}^{n-1}_h; (\mathbf{u}^n_h, p^n_h), (\mathcal{L}_h\mathbf{u}^n_h, 0)], \end{aligned} \tag{5.22}$$

with $E^n_{\widehat{\mathcal{A}}}$ as in (5.21).

Proof. Let's take in (5.19) $\mathbf{v}_h = \mathbf{u}^n_h - \mathcal{L}_h\mathbf{u}^n_h \in \mathcal{V}_h$ and $q_h = p^n_h$, we have

$$\begin{aligned} &\frac{\rho}{\delta t}\left(\int_{\Omega^n}|\mathbf{u}^n_h|^2 - \int_{\Omega^{n-1}}\mathbf{u}^{n-1}_h\mathbf{u}^n_h\right) \\ &+ \rho\left(\int_{\Omega^n}(\mathbf{u}^{n-1}_h\cdot\nabla\mathbf{u}^n_h)\cdot\mathbf{u}^n_h - \int_{\Omega^n}(\mathbf{w}^{n-1}_h\cdot\nabla\mathbf{u}^n_h)\cdot\mathbf{u}^n_h\right) \\ &- \rho\int_{\Omega^n}|\mathbf{u}^n_h|^2\nabla\cdot\mathbf{w}^{n-1}_h + 2\mu\int_{\Omega^n}|\boldsymbol{\epsilon}(\mathbf{u}^n_h)|^2 \\ &+ \frac{\rho}{2}\int_{\Omega^n}|\mathbf{u}^n_h|^2(\nabla\cdot\mathbf{u}^{n-1}_h) - A_{\widehat{\mathcal{A}},\delta t}[\mathbf{u}^{n-1}_h; (\mathbf{u}^n_h, p^n_h), (\mathcal{L}_h\mathbf{u}^n_h, 0)] = 0. \end{aligned} \tag{5.23}$$

The second integral in the previous expression can be decomposed as

$$-\int_{\Omega^{n-1}}\mathbf{u}^{n-1}_h\mathbf{u}^n_h = -\frac{1}{2}\int_{\Omega^{n-1}}|\mathbf{u}^n_h|^2 - \frac{1}{2}\int_{\Omega^{n-1}}|\mathbf{u}^{n-1}_h|^2 + \frac{1}{2}\int_{\Omega^{n-1}}|\mathbf{u}^n_h - \mathbf{u}^{n-1}_h|^2. \tag{5.24}$$

Then, we integrate by parts the third and forth integrals of (5.23). Since Γ_D and Γ_N are fixed, i.e. $\mathbf{w}^{n-1}_h = \mathbf{0}$, we have

$$\begin{aligned} &\rho\left(\int_{\Omega^n}(\mathbf{u}^{n-1}_h\cdot\nabla\mathbf{u}^n_h)\cdot\mathbf{u}^n_h - \int_{\Omega^n}(\mathbf{w}^{n-1}_h\cdot\nabla\mathbf{u}^n_h)\cdot\mathbf{u}^n_h\right) = \\ &-\frac{\rho}{2}\int_{\Omega^n}|\mathbf{u}^n_h|^2(\nabla\cdot\mathbf{u}^{n-1}_h) + \frac{\rho}{2}\int_{\Sigma^n}(\mathbf{u}^{n-1}_h\cdot\mathbf{n})|\mathbf{u}^n_h|^2 + \frac{\rho}{2}\int_{\Omega^n}|\mathbf{u}^n_h|^2(\nabla\cdot\mathbf{w}^{n-1}_h) - \frac{\rho}{2}\int_{\Sigma^n}(\mathbf{w}^{n-1}_h\cdot\mathbf{n})|\mathbf{u}^n_h|^2 \\ &+\frac{\rho}{2}\int_{\Gamma_N\cup\Gamma_D}(\mathbf{u}^{n-1}_h\cdot\mathbf{n})|\mathbf{u}^n_h|^2. \end{aligned} \tag{5.25}$$

Using the property $\mathbf{u}^{n-1}_h\cdot\mathbf{n} - \mathbf{w}^{n-1}_h\cdot\mathbf{n} = 0$ the boundary terms on Σ^n of the previous relation

cancel. Inserting the (5.24) and (5.25) in (5.23) we obtain

$$\begin{aligned}
&\frac{\rho}{\delta t}\left(\int_{\Omega^n}|\mathbf{u}_h^n|^2-\frac{1}{2}\int_{\Omega^{n-1}}|\mathbf{u}_h^n|^2-\frac{1}{2}\int_{\Omega^{n-1}}|\mathbf{u}_h^{n-1}|^2\right)\\
&+\frac{\rho}{2\delta t}\int_{\Omega^{n-1}}|\mathbf{u}_h^n-\mathbf{u}_h^{n-1}|^2-\frac{\rho}{2}\int_{\Omega^n}|\mathbf{u}_h^n|^2\nabla\cdot\mathbf{w}_h^{n-1}\\
&+2\mu\int_{\Omega^n}|\boldsymbol{\epsilon}(\mathbf{u}_h^n)|^2+\frac{\rho}{2}\int_{\Gamma_N}(\mathbf{u}_h^{n-1}\cdot\mathbf{n})|\mathbf{u}_h^n|^2-A_{\widehat{\mathcal{A}},\delta t}[\mathbf{u}_h^{n-1};(\mathbf{u}_h^n,p_h^n),(\mathcal{L}_h\mathbf{u}_h^n,0)]=0,
\end{aligned}$$

which proves the assertion. ∎

The term $A_{\widehat{\mathcal{A}},\delta t}[\mathbf{u}_h^{n-1};(\mathbf{u}_h^n,p_h^n),(\mathcal{L}_h\mathbf{u}_h^n,0)]$ corresponds to the discrete counterpart (variational residual) of the term $\displaystyle\int_{\Sigma\cup\Gamma_D}\boldsymbol{\sigma}(\mathbf{u}_h^n,p_h^n)\mathbf{n}\cdot\mathbf{u}_h^n$, that this the stress power generated on the Dirichlet boundaries (see equation (5.12)).

The expression (5.22) introduce an artificial power in the energy equation which can led to numerical instability.

In order to control the energy, the idea is to add to (5.19) the following consistent term

$$B_{\delta t}[\mathbf{u}_h^n,\mathbf{v}_h]\overset{\text{def}}{=}-\frac{\rho}{2}\left[\frac{1}{\delta t}\left(\int_{\Omega^n}\mathbf{u}_h^n\cdot\mathbf{v}_h-\int_{\Omega^{n-1}}\mathbf{u}_h^n\cdot\mathbf{v}_h\right)-\int_{\Omega^n}(\mathbf{u}_h^n\cdot\mathbf{v}_h)\nabla\cdot\mathbf{w}_h^{n-1}\right]. \tag{5.26}$$

The resulting new scheme is summarized in the Algorithm 5.2.

ALGORITHM 5.2 (New ALE formulation)

1. *Find* $(\mathbf{u}_h^n,\, p_h^n)\in\mathcal{X}_h\times\mathcal{M}_h$ *satisfying* $\mathbf{u}_h^n=\mathbf{w}_h^n$ *on* Σ^n *and* $\mathbf{u}_h^n=\mathbf{u}_D^n$ *on* Γ_D*, such that*

$$A_{\widehat{\mathcal{A}},\delta t}[\mathbf{u}_h^{n-1};(\mathbf{u}_h^n,p_h^n),(\mathbf{v}_h,q_h)]+B_{\delta t}[\mathbf{u}_h^n,\mathbf{v}_h]=0 \tag{5.27}$$

   for all $(\mathbf{v}_h,\, p_h)\in\mathcal{V}_h\times\mathcal{M}_h$.

2. *Go to next time-step.*

The form $A_{\widehat{\mathcal{A}},\delta t}[\mathbf{u}_h^{n-1};(\mathbf{u}_h^n,p_h^n),(\mathbf{v}_h,q_h)]$ has the same expression as in (5.20). The new ALE formulation (5.27) can be re-written in a more compact form summing the integrals of (5.20) and (5.26), i.e.

$$\begin{aligned}
&\frac{\rho}{\delta t}\left[\frac{1}{2}\left(\int_{\Omega^n}\mathbf{u}_h^n\cdot\mathbf{v}_h+\int_{\Omega^{n-1}}\mathbf{u}_h^n\cdot\mathbf{v}_h\right)-\int_{\Omega^{n-1}}\mathbf{u}_h^{n-1}\cdot\mathbf{v}_h\right]+\rho\int_{\Omega^n}(\mathbf{u}_h^{n-1}-\mathbf{w}_h^{n-1})\cdot\nabla\mathbf{u}_h^n\cdot\mathbf{v}_h\\
&-\frac{\rho}{2}\int_{\Omega^n}(\mathbf{u}_h^n\cdot\mathbf{v}_h)\nabla\cdot\mathbf{w}_h^{n-1}+2\mu\int_{\Omega^n}\boldsymbol{\epsilon}(\mathbf{u}_h^n):\boldsymbol{\epsilon}(\mathbf{v}_h)\\
&-\int_{\Omega^n}p_h^n\nabla\cdot\mathbf{v}_h+\int_{\Omega^n}q_h\nabla\cdot\mathbf{u}_h^n+\frac{\rho}{2}\int_{\Omega^n}(\mathbf{u}_h^n\cdot\mathbf{v}_h)(\nabla\cdot\mathbf{u}_h^{n-1})=0.
\end{aligned}\tag{5.28}$$

To get an heuristic explanation of the term (5.26), let us assume that the motion of the

domain is not yet discretized. Multiplying the equation (5.9) by $\hat{\mathbf{u}}^n \cdot \mathbf{v}$ and integrating over $[t^{n-1}, t^n] \times \widehat{\Omega}$, we get

$$\begin{aligned}
0 &= \int_{t^{n-1}}^{t^n} \int_{\widehat{\Omega}} (\hat{\mathbf{u}}^n \cdot \mathbf{v}) \left[\partial_t \widehat{J}_{\widehat{\mathcal{A}}} - \widehat{J}_{\widehat{\mathcal{A}}} \nabla \cdot \mathbf{w}(t) \right] \\
&= \int_{\Omega(t^n)} \mathbf{u}^n \cdot \mathbf{v} - \int_{\Omega(t^{n-1})} \mathbf{u}^n \cdot \mathbf{v} - \int_{t^{n-1}}^{t^n} \int_{\Omega(t)} (\mathbf{u}^n \cdot \mathbf{v}) \nabla \cdot \mathbf{w}(t) \\
&= \int_{\Omega(t^n)} \mathbf{u}^n \cdot \mathbf{v} - \int_{\Omega(t^{n-1})} \mathbf{u}^n \cdot \mathbf{v} - \delta t \int_{\Omega(t^n)} (\mathbf{u}^n \cdot \mathbf{v}) \nabla \cdot \mathbf{w}(t^n) + \mathcal{O}(\delta t^2),
\end{aligned}$$

which shows that

$$\frac{1}{\delta t} \left(\int_{\Omega^n} \mathbf{u}^n \cdot \mathbf{v} - \int_{\Omega^{n-1}} \mathbf{u}^n \cdot \mathbf{v} \right) - \int_{\Omega^n} (\mathbf{u}^n \cdot \mathbf{v}) (\nabla \cdot \mathbf{w}^{n-1}) = \mathcal{O}(\delta t).$$

The (5.26) that has been added to (5.27) in order to get an energy inequality is therefore consistent. It is important to remark that this correction term is weakly consistent, but not strongly consistent, in contrast with the usual Temam's trick. This is not a surprise since (5.26) involves a time discretization by finite difference, which is not strongly consistent, even on a fixed domain.

From (5.27), we have the desired result:

PROPOSITION 5.2
Let $\mathcal{L}_h \mathbf{u}_h^n$ denote any discrete lifting of $\mathbf{u}_h^n$ from $\partial\Omega^n$ to Ω^n such that $\mathcal{L}_h \mathbf{u}_h^n = \mathbf{u}_h^n$ on $\Gamma_D \cup \Sigma$ and $\mathcal{L}_h \mathbf{u}_h^n = \mathbf{0}$ otherwise. Let $(\mathbf{u}_h^n, p_h^n)$ be solution of Algorithm 5.1. Then we have the following energy balance

$$E_{\widehat{\mathcal{A}}}^n + \frac{\rho}{2} \int_{\Gamma_N \cup \Gamma_D} (\mathbf{u}_h^{n-1} \cdot \mathbf{n}) |\mathbf{u}_h^n|^2 = A_{\widehat{\mathcal{A}},\delta t}[\mathbf{u}_h^{n-1}; (\mathbf{u}_h^n, p_h^n), (\mathcal{L}_h \mathbf{u}_h^n, 0)] + B_{\delta t}[\mathbf{u}_h^n, \mathcal{L}_h \mathbf{u}_h^n], \quad (5.29)$$

having $E_{\widehat{\mathcal{A}}}^n$ as in (5.21).

Proof. Taking $\mathbf{v}_h = \mathbf{u}_h^n - \mathcal{L}_h \mathbf{u}_h^n \in \mathcal{V}_h$ and $q_h = p_h^n$ in (5.28) we have

$$\begin{aligned}
&\frac{\rho}{\delta t} \left[\frac{1}{2} \left(\int_{\Omega^n} |\mathbf{u}_h^n|^2 + \int_{\Omega^{n-1}} |\mathbf{u}_h^n|^2 \right) - \int_{\Omega^{n-1}} \mathbf{u}_h^{n-1} \cdot \mathbf{u}_h^n \right] + \rho \int_{\Omega^n} (\mathbf{u}_h^{n-1} - \mathbf{w}_h^{n-1}) \cdot \nabla \mathbf{u}_h^n \cdot \mathbf{u}_h^n \\
&- \frac{\rho}{2} \int_{\Omega^n} |\mathbf{u}_h^n|^2 \nabla \cdot \mathbf{w}_h^{n-1} + 2\mu \int_{\Omega^n} |\boldsymbol{\epsilon}(\mathbf{u}_h^n)|^2 + \frac{\rho}{2} \int_{\Omega^n} |\mathbf{u}_h^n|^2 (\nabla \cdot \mathbf{u}_h^{n-1}) \\
&= A_{\widehat{\mathcal{A}},\delta t}[\mathbf{u}_h^{n-1}; (\mathbf{u}_h^n, p_h^n), (\mathcal{L}_h \mathbf{u}_h^n, 0)] + B_{\delta t}[\mathbf{u}_h^n, \mathcal{L}_h \mathbf{u}_h^n].
\end{aligned}$$

If we decompose now the third integral as in (5.24) and we integrate the forth integral by part as in (5.25), we obtain

$$\begin{aligned}
&\frac{\rho}{\delta t} \left(\frac{1}{2} \int_{\Omega^n} |\mathbf{u}_h^n|^2 - \frac{1}{2} \int_{\Omega^{n-1}} |\mathbf{u}_h^{n-1}|^2 \right) + \frac{\rho}{2\delta t} \int_{\Omega^{n-1}} |\mathbf{u}_h^n - \mathbf{u}_h^{n-1}|^2 + 2\mu \int_{\Omega^n} |\boldsymbol{\epsilon}(\mathbf{u}_h^n)|^2 \\
&+ \frac{\rho}{2} \int_{\Gamma_N} (\mathbf{u}_h^{n-1} \cdot \mathbf{n}) |\mathbf{u}_h^n|^2 = A_{\widehat{\mathcal{A}},\delta t}[\mathbf{u}_h^{n-1}; (\mathbf{u}_h^n, p_h^n), (\mathcal{L}_h \mathbf{u}_h^n, 0)] + B_{\delta t}[\mathbf{u}_h^n, \mathcal{L}_h \mathbf{u}_h^n]
\end{aligned}$$

which is the (5.29). ■

REMARK 5.3
Note that if the system is isolated ($\mathbf{u} = \mathbf{0}$ on $\Gamma_D \cup \Sigma$), the right-hand side of (5.29) *vanishes and then we have an energy estimate.*

To the best of our knowledge this is the first stability result of an ALE scheme in finite element that does not rely on any GCL assumption. It is therefore more general that the result in literature (e.g. [FN99, TM01]) since it does not make strong assumption on the mesh displacement.

5.5 Numerical example

Domain and boundary conditions We consider in this section an adaptation of the large displacement 3D-*balloon-type* example proposed in [FMV13, KFW06], i.e a curved fluid domain surrounded by two interfaces (see Figure 5.4).

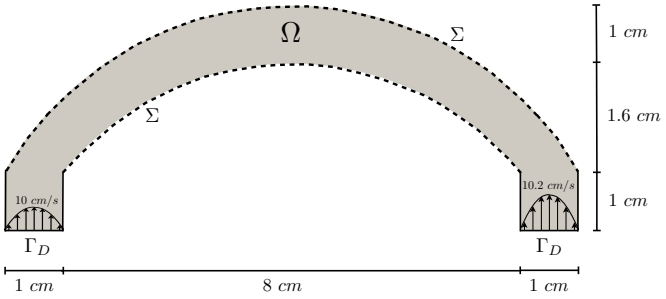

Figure 5.4: *Bended fluid domain surrounded by two interfaces.*

A given displacement is imposed on Σ, while Γ_D is assumed to be fixed, i.e. $\mathbf{w} = \mathbf{0}$. Note that with respect to (5.10) we have $\Gamma_N = \emptyset$. A parabolic velocity profile is prescribed both on the left and right inflow boundaries, with maximal magnitudes $10\ cm/s$ and $10.2\ cm/s$, respectively, to avoid perfect symmetry. Zero velocity is enforced on the remaining fluid boundaries. The fluid physical parameters are given by $\rho = 1.0\ g/cm^3$ and $\mu = 9\ poise$. The fluid is loaded with the volume force $f = (0, -10)^T\ dyne/cm^2$. The fluid equations are discretized in space using continuous $\mathbb{P}_1/\mathbb{P}_1$ finite elements stabilized with a PSPG method. A time-step of $t = 0.005\ s$ is employed for both simulations.

Displacement and velocity magnitude Figure 5.5 shows the fluid velocity magnitude snapshots and the domain deformations in two time instants, $t = 1.5\ s$ and $t = 3.3\ s$, obtained with Algorithm 5.1 and Algorithm 5.2. Notice that the results presents the same behavior for both Algorithms employed.

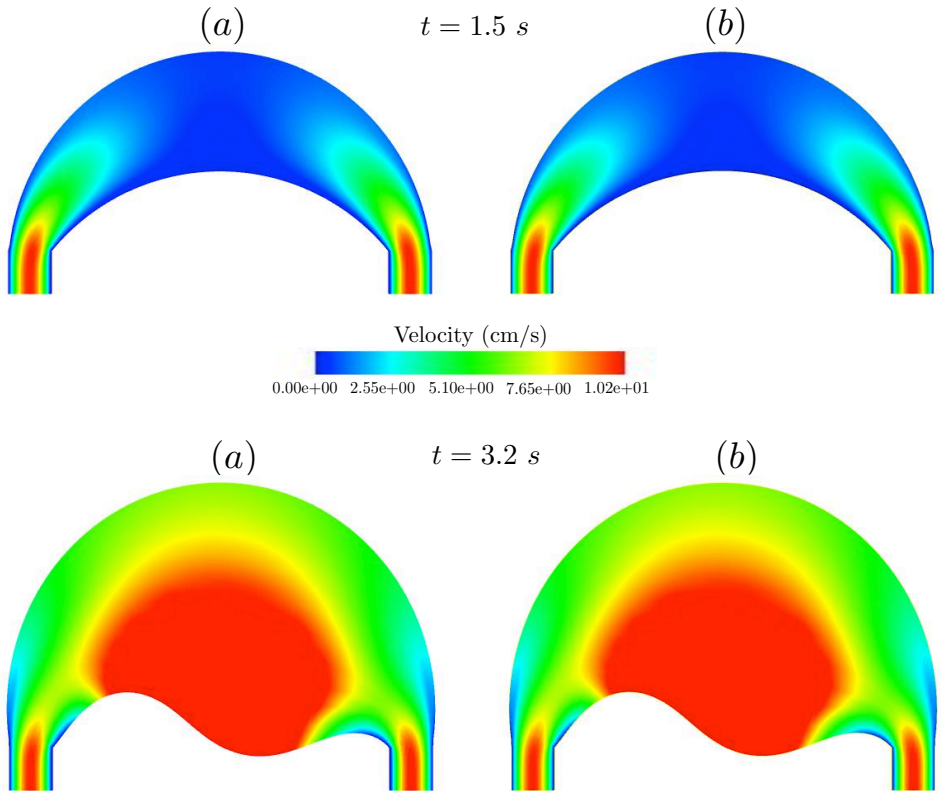

Figure 5.5: *Velocity and displacement obtained with Algorithm 5.1 (a) and Algorithm 5.2 (b).*

Energy study In order to evaluate the impact of the ALE stabilization term (5.26) on the overall stability of the proposed example, we compute the different terms involved in the energy quantity of Algorithm 5.1 and Algorithm 5.2 (Figure 5.6). For the system shown in Figure 5.4, first we compute the physical power

$$E_1 \overset{\text{def}}{=} \frac{\rho}{2\delta t}\left(||\mathbf{u}_h^n||^2_{\Omega^n} - ||\mathbf{u}_h^{n-1}||^2_{\Omega^{n-1}}\right) + 2\mu||\boldsymbol{\epsilon}(\mathbf{u}_h^n)||^2_{\Omega^n} - \int_{\Sigma\cup\Gamma_D} \boldsymbol{\sigma}(\mathbf{u}_h^n, p_h^n)\mathbf{n}\cdot\mathbf{u}_h^n + \frac{\rho}{2}\int_{\Gamma_D} \mathbf{u}_D^{n-1}|\mathbf{u}_D^n|^2. \tag{5.30}$$

We see in Figure 5.6a that the physical energy is indeed dissipated.

To understand the reason for this stability - in spite of the moving domain - we now plot in Figure 5.6b the energy

$$E_2 \overset{\text{def}}{=} E^n_{\widehat{\mathcal{A}}} - \int_{\Sigma\cup\Gamma_D} \boldsymbol{\sigma}(\mathbf{u}_h^n, p_h^n)\mathbf{n}\cdot\mathbf{u}_h^n + \frac{\rho}{2}\int_{\Gamma_D} \mathbf{u}_D^{n-1}|\mathbf{u}_D^n|^2, \tag{5.31}$$

where the $E^n_{\widehat{\mathcal{A}}}$ is given by (5.21). This shows a partial explanation for the stability, which is due to the artificial dissipation introduced by the Euler scheme.

The last figure, Figure 5.6c, shows the energy

$$E_3 \overset{\text{def}}{=} E^n_{\widehat{\mathcal{A}}} - \int_{\Sigma\cup\Gamma_D} \boldsymbol{\sigma}(\mathbf{u}^n_h, p^n_h)\mathbf{n}\cdot\mathbf{u}^n_h + \frac{\rho}{2}\int_{\Gamma_D} \mathbf{u}^{n-1}_D|\mathbf{u}^n_D|^2 + \frac{h^2}{\mu}\int_{\Omega^n}|\nabla p^n_h|^2, \tag{5.32}$$

where $E^n_{\widehat{\mathcal{A}}}$ has the form (5.21). With this new plot, it is clear that the PSPG dissipation dominates and it is the responsible for the overall stability. Figure 5.6c shows that the standard ALE scheme could be unstable in absence of artificial dissipation. Whereas, with the proposed new ALE scheme, the energy is controlled even in absence of artificial dissipation.

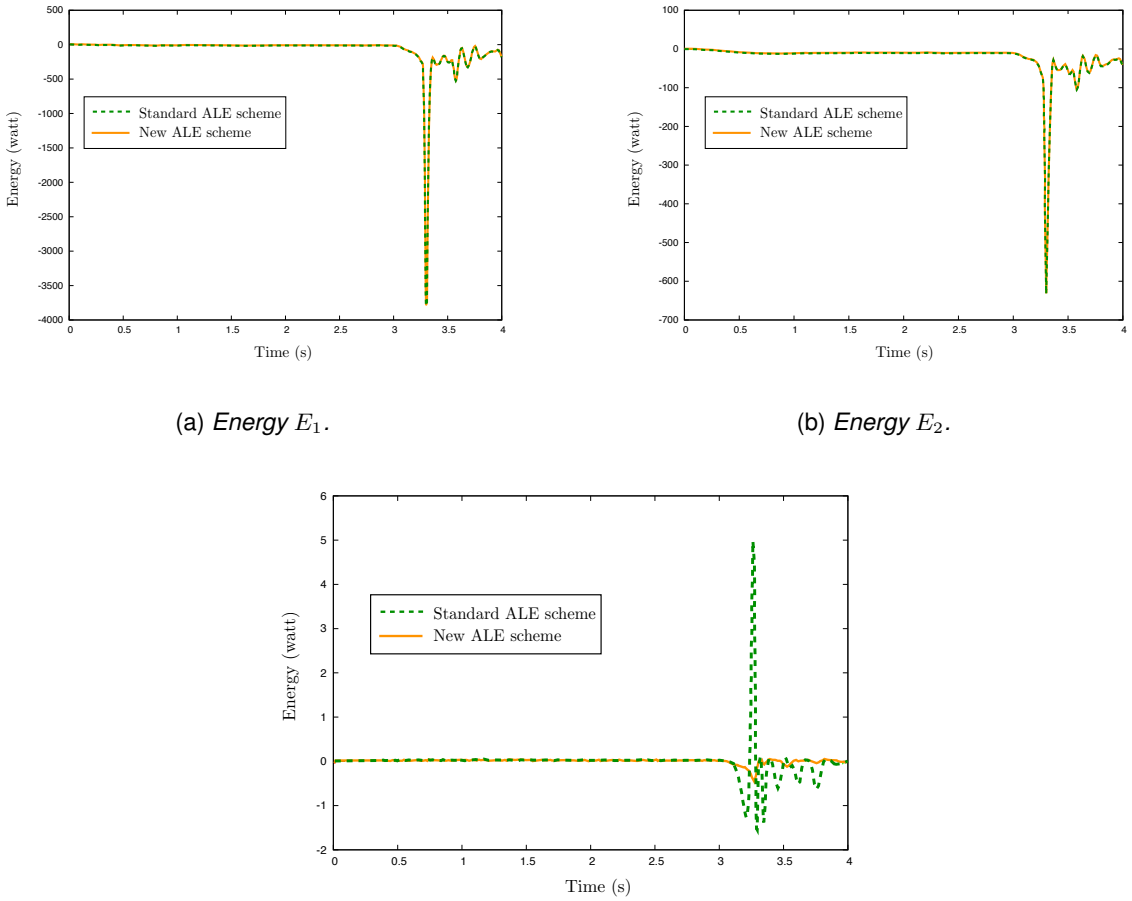

(a) *Energy* E_1. (b) *Energy* E_2.

(c) *Energy* E_3.

Figure 5.6: *Energies obtained with standard ALE formulation (Algorithm 5.1) vs new ALE formulation (Algorithm 5.2).*

5.6 Final remarks

In this chapter we have discussed a technique to get an energy stability for a fluid problem in a moving domain. An ALE formalism has been adopted to account for the dynamic

mesh. Our main contribution is to have proposed the first ALE scheme that can be proved to be stable in the energy norm without special assumption on the mesh movement (in particular without Geometric Conservation Law).

A numerical example - the 3D baloon-type with with large displacements - has been performed. The first observation is that the consistent terms added for the stability did not affect significantly the results obtained with a standard scheme. This effect is due to the Euler and PSPG artificial dissipation as confirmed by plotting the two energies (5.30) and (5.31) (Figure 5.6a and 5.6b). Indeed, we decreased significantly time and space discretization step, i.e the artificial dissipation produced by the Euler scheme and PSPG, the artificial power of the standard ALE could destabilize the simulation, whereas the new ALE scheme guarantees the stability.

Bibliography of Chapter 5

[Ber12] C. Bertoglio. *Problémes Directs et Inverses en Interaction Fluide-Structure. Application á l'hèmodynamique*. PhD thesis, Universitè Pierre et Marie Curie, Paris 6, 2012.

[BG04] D. Boffi and L. Gastaldi. Stability and geometric conservation laws for ale formulations. *Comput. Methods Appl. Mech. Engrg*, 193:4717–4739, 2004.

[DHPRF04] J. Donea, A. Huerta, J.-Ph. Ponthot, and A. Rodríguez-Ferran. The derivation of the equations for fluids and structure. In E. Stein, R. De Borst, and T. J.R. Hughes, editors, *Encyclopedia of Computational Mechanics*, volume 1, chapter 14. John Wiley & Sons, 2004.

[EGP09] S. Étienne, A. Garon, and D. Pelletier. Perspective on the geometric conservation law and finite element methods for ALE simulations of incompressible flow. *Journal of Computational Physics*, 228(7):2313 – 2333, 2009.

[FFGQ09] M. Fernández, L. Formaggia, J.-F. Gerbeau, and A. Quarteroni. The derivation of the equations for fluids and structure. In L. Formaggia, A. Quarteroni, and A. Veneziani, editors, *Cardiovascular Mathematics. Modeling and simulation of the circulatory system*, volume 2, chapter 3. Springer, 2009.

[FMV13] M. A. Fernández, J. Mullaert, and M. Vidrascu. Generalized Robin-Neumann explicit coupling schemes for incompressible fluid-structure interaction: stability analysis and numerics. Research Report RR-8384, INRIA, http://hal.inria.fr/hal-00875819/PDF/RR-8384.pdf, 2013.

[FN99] L. Formaggia and F. Nobile. A stability analysis for the arbitrary lagrangian eulerian formulation with finite elements. *East-West J. Numer. Math.*, 7(2):105–131, 1999.

[FN04] L. Formaggia and F. Nobile. Stability analysis of second-order time accurate schemes for ALE-FEM. *Comput. Methods Appl. Mech. Engrg.*, 193:4097–4116, 2004.

[FQV09] L. Formaggia, A. Quarteroni, and A. Veneziani. *Cardiovascular Mathematics*, volume 2. Springer, 2009.

[GF00] H. Guillard and C. Farhat. On the significance of the geometric conservation law for flow computations on moving meshes. *Comp. Meth. Appl. Mech. Engrg.*, 190(11-12):1467 – 1482, 2000.

[Gur81] M. E. Gurtin. *An Introduction to Continuum Mechanics*, volume 18 of *Mathematics in Science & Engineering*. Academic Press, 1981.

[HLZ81] T.J.R. Hughes, W.K Liu, and T.K. Zimmermann. Lagrangian-Eulerian finite element formulation for incompressible viscous flows. *Comput. Methods Appl. Mech. Engrg.*, 29:329–349, 1981.

[Imp13] A. Imperiale. *Méthodes d'assimilation de la donnée image pour la personnalisation de modéles mécaniques*. PhD thesis, Universitè Pierre et Marie Curie, Paris 6, 2013.

[KFW06] U. Küttler, C. Förster, and W. A. Wall. A solution for the incompressibility dilemma in partitioned fluid–structure interaction with pure dirichlet fluid domains. *Computational Mechanics*, 38(4-5):417–429, 2006.

[LF96] M. Lesoinne and C. Farhat. Geometric conservation laws for flow problems with moving boundaries and deformable meshes, and their impact on aeroelastic computations. *Comp. Meth. Appl. Mech. Engrg.*, 134(1–2):71 – 90, 1996.

[Tem68] R. Temam. Une méthode d'approximation de la solution des équations de Navier-Stokes. *Bulletin de la Société Mathématique de France*, 96:115–152, 1968.

[Tem79] R. Temam. *Navier-Stokes Equations*, volume 2. Studies in Mathematics and its Applications. North-Holland Publishing Co., Amsterdam, 1979.

[TL79] P.D. Thomas and C.K. Lombard. Geometric conservation law and its application to flow computations on moving grids. *AIAA J.*, 17:1030–1037, 1979.

[TM01] P. Le Tallec and J. Mouro. Fluid structure interaction with large structural displacements. *Comput. Meth. Appl. Mech. Engrg.*, 190:3039–3067, 2001.

[ZRTC93] H. Zhang, M. Reggio, J.Y. Trepanier, and R. Camarero. Discrete form of the GCL and its implementation in CFD codes. *Computers and fluids*, 22(1):9–23, 1993.

CHAPTER 6
Numerical examples in cardiac hemodynamics

The goal of this chapter is to simulate the blood dynamics within the left ventricle and the thoracic aorta. The contraction/relaxation dynamics of the myocardium are modeled through a given displacement obtained from a electro-mechanical model of the heart. This displacement is imposed on the ALE Navier-Stokes model in the left ventricle. The mechanics of the mitral and aortic valve are simulated introducing fissured surfaces in which RIS models are applied. The dynamics of the blood in the ventricle is coupled with the blood flow in the aorta with a fluid-fluid staggered scheme. In the outlets, 0D-Winkessel models are employed to account for the discarded part of the cardiovascular system.

Contents

6.1 Introduction

The numerical simulations of the blood flow in the heart is a problem of outstanding difficulty, due to the multi-physics aspect involved [NNN+11]. One of the objectives of this thesis is to address the hemodynamics in the left ventricle coupled to the hemodynamics in the aorta, using our 3D-3D coupling algorithm. This interaction is relevant from a clinical perspective since pathologies of the aorta and pathologies of the myocardium can have a mutual influence. In this chapter, we present some preliminary results, close to physiological conditions.

Different kinds of approaches can drive numerical simulations of fluid dynamics in the heart (see [KNZ11] and reference therein). In the immersed boundary method,

[MP00, VCMP08], the immersed solid is accounted for in the surrounding fluid by adding body forces to the governing fluid equations. Body forces are distributed on all nodes of the fluid mesh via a discrete Dirac measure.

Another approach consists of solving the structure in a conventional Lagrangian framework and to couple it to the fluid with an FSI algorithm [COS05, WHS+02, WSKH04]. This type of method is the one who resolves the complex properties of the cardiac structure and the delicate interaction of fluid and structure. With this approach, it is possible to model the total heart function by integrating cardiac anatomy, electrical activation, mechanics, metabolism and fluid mechanics together.

A third way is to consider only the fluid dynamics of the heart, without solving the coupled fluid-structure problem, either by imposing wall displacements [DPB05, NWY06], for example obtained from another computation, or using the moving geometry obtained from medical imaging [CMN14, SMR+09]. Even if this method has some limitations – electrical activation and other physiological properties cannot be included, Lagrangian movements is difficult to obtain from medical imaging – it may lead to realistic simulations without requiring the solution of a difficult FSI problem.

In most of the existing works, the influence of valves has been simulated using boundary conditions with lumped parameter models. To the best of our knowledge, only Peskin's group performed numerical simulations of the fluid-structure in the heart with flexible valves [GHMP07], but without coupling the left ventricle and the aorta.

In this chapter, we present our first numerical simulations of the ventricle-valves-aorta system. Due to the complexity of a coupled fluid-structure interaction method, as first step in this direction, we simulate the left ventricle dynamics by an imposed external displacement obtained from a mechanical simulation. Here, the hemodynamics in the ventricle is coupled with the hemodynamics in the aorta via our staggered explicit algorithm, investigated in Chapters 2 and 3. The mitral and aortic valves are modeled with the RIS method, discussed in Chapter 4. The stabilized ALE formulation analyzed in Chapter 5 is used to model the left ventricle movement. All simulations are performed in a realistic aorta-heart geometry.

Outline This chapter is organized as follows. In the next section we present the coupled problem between two fluids, one in a moving domain and described with an ALE formalism and the second one in a fixed domain. Section 6.3 deals with some numerical simulations obtained in a realistic heart geometry (illustrated in Paragraph 6.3.1) whose contraction is induced by displacements derived from a electro-mechanical simulation of the heart (sketched in Paragraph 6.3.2). In Paragraph 6.3.4 we discuss the obtained results.

6.2 The fluid dynamics model: from the ventricle to the aorta

In this section we present the mathematical model adopted to simulate the blood flowing from the left ventricle towards the aorta. The dynamics of the blood in the left ventricle is modeled by Navier-Stokes equations in the ALE formalism. We consider two resistive immersed surfaces models to account for the heart valves (see Chapter 4 for more details).

The dynamics of the blood in the aorta is coupled with a fluid-fluid interaction problem (see Chapter 2 for more details).

Two interfaces are present in the following model. The interface between the two domains in which we enforce the coupled fluid-fluid transmission conditions (see (2.31) on page 45) and the interface represented by the ventricle wall were the realistic displacements are imposed. In what follows the first one is denoted by Σ_{FFI}, while the second interface is indicated as $\Sigma_{\text{ALE}}(t)$.

Let $\Omega_1(t) \subset \mathbb{R}^d$ be a moving domain and let be $\mathcal{S}_{i,j}(t) \subset \mathbb{R}^{d-1}$ co-dimensional surfaces representing the heart valves, where the subscript $i = o, c$ stands for the open and closed configuration, and $j = m, a$ for mitral and aortic valves. The immersed surfaces are time-dependent, as well. Hence the first computational sub-domain is $\Omega_1(t) \overset{\text{def}}{=} \Omega^f(t) \cup [\mathcal{S}_{j,o}(t) \cup \mathcal{S}_{j,c}(t)]$, where $\Omega^f(t)$ is the blood fluid domain. The domain $\Omega_1(t)$ is separated from a fixed domain Ω_2 by the interface Σ_{FFI}, i.e. $\Sigma_{\text{FFI}} \overset{\text{def}}{=} \partial\Omega_1(t) \cap \partial\Omega_2$, supposed to fixed. Then let define $\Gamma_1(t) \overset{\text{def}}{=} \partial\Omega_1(t) \backslash [\Sigma_{\text{FFI}} \cup \Sigma_{\text{ALE}}(t)]$ and $\Gamma_2 \overset{\text{def}}{=} \partial\Omega_2 \backslash \Sigma_{\text{FFI}}$. The sketch of the computational domains is shown in Figure 6.1.

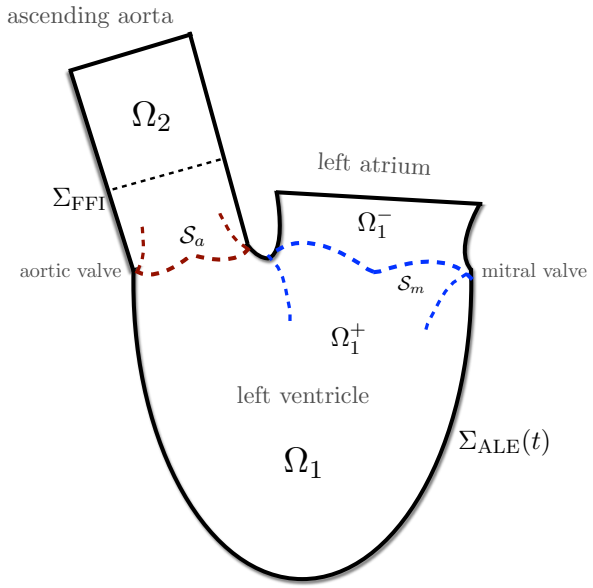

Figure 6.1: *Sketch of the ventricle-valves-aorta domains.*

If we combine the fluid-fluid model (2.2)-(2.4), with the fluid equation (4.1) for valves model and the Navier-Stokes equation (5.10) in the ALE formalism, our problem reads now:

Find the velocity $\mathbf{u}_1 : \Omega_1(t) \times \mathbb{R}^+ \to \mathbb{R}^d$ and the pressure $p_1 : \Omega_1(t) \times \mathbb{R}^+ \to \mathbb{R}$ such that

$$\begin{cases} \rho \partial_t \mathbf{u}_1|_{\widehat{\mathcal{A}}} + \rho(\mathbf{u}_1 - \mathbf{w}_1) \cdot \nabla \mathbf{u}_1 - \nabla \cdot \boldsymbol{\sigma}(\mathbf{u}_1, p_1) + \sum_{i,j} R_{i,j}(\mathbf{u}_1 - \mathbf{w}_1)\delta_{\mathcal{S}_{i,j}} = \mathbf{0}, & \text{in} \quad \Omega_1(t), \\ \nabla \cdot \mathbf{u}_1 = 0, & \text{in} \quad \Omega_1(t), \\ \mathbf{u}_1 = \mathbf{0}, & \text{on} \quad \Gamma_1(t), \end{cases} \tag{6.1}$$

and find the velocity $\mathbf{u}_2 : \Omega_2 \times \mathbb{R}^+ \to \mathbb{R}^d$ and the pressure $p_2 : \Omega_2 \times \mathbb{R}^+ \to \mathbb{R}$, such that

$$\begin{cases} \rho \partial_t \mathbf{u}_2 + \rho \mathbf{u}_2 \cdot \nabla \mathbf{u}_2 - \nabla \cdot \boldsymbol{\sigma}(\mathbf{u}_2, p_2) &= 0, & \text{in} \quad \Omega_2, \\ \nabla \cdot \mathbf{u}_2 &= 0, & \text{in} \quad \Omega_2, \\ \mathbf{u}_2 &= \mathbf{0}, & \text{on} \quad \Gamma_2. \end{cases} \tag{6.2}$$

The solutions in the two sub-domains are coupled through the usual kinematic and kinetic conditions:

$$\begin{cases} \mathbf{u}_1 &= \mathbf{u}_2, & \text{on} \quad \Sigma_{\text{FFI}}, \\ \boldsymbol{\sigma}(\mathbf{u}_2, p_2) \cdot \mathbf{n}_2 &= -\boldsymbol{\sigma}(\mathbf{u}_1, p_1) \cdot \mathbf{n}_1, & \text{on} \quad \Sigma_{\text{FFI}}, \end{cases} \tag{6.3}$$

with $\mathbf{n}_1$, $\mathbf{n}_2$ the outward-pointing unit normal vectors on $\partial\Omega_1(t)$ and $\partial\Omega_2$ respectively. The velocity of the domain $\Omega_1(t)$ is defined as $\mathbf{w} \overset{\text{def}}{=} \partial_t \widehat{\mathcal{A}}(\hat{\mathbf{x}}, t)$, for all $\hat{\mathbf{x}} \in \widehat{\Omega}_1$, the Lagrangian counterpart of $\Omega_1(t)$. For each surface $\mathcal{S}_{i,j}(t)$, we denote by $\delta_{\mathcal{S}_{i,j}}$, the Dirac measure and by $R_{i,j}$, the associated resistance, representing the dissipation due to the presence of the immersed surface. Note that the second fluid problem (6.2) is written in a total Eulerian formalism.

REMARK 6.1

It's worth noticing that with the ALE formulation (6.1), the valves move with the fluid mesh, i.e $R_{i,j}(\mathbf{u}_1 - \mathbf{w})\delta_{\mathcal{S}_{i,j}}$. The movement of the resistive surfaces $\mathcal{S}_{i,j}(t)$ is not related to a physical velocity of the valves. Compared to the deformation of the heart, the deformation of the resistive surfaces is relatively moderate and this approximation is reasonable in the framework of this simplified model.

The time splitting and the space discretization are based on the Nitsche's interface method discussed in Chapter 2. The discretization of the Fluid sub-problem 1 has to account for the time-dependent moving domain and for the pressure discontinuity on the immersed surfaces. Hence, both velocity and pressure approximations will be continuous at inter-element boundaries, while the pressure will be discontinuous on the faces of the immersed surfaces $S_{i,j}(t)$.

Let be $\{\mathcal{T}_{1,h}(t)\}_{0<h\leq 1}$ and $\{\mathcal{T}_{2,h}\}_{0<h\leq 1}$ two families of regular finite element triangulation for $\Omega_1(t)$ and Ω_2 respectively, with diameter h. The triangulation $\{\mathcal{T}_{1,h}(t)\}_{0<h\leq 1}$ is conforming on the immersed surfaces representing the valves.

Let $\mathcal{X}_{1,h}$ denote an inf-sup stable, conforming finite element approximation of the spaces (5.13) in $\Omega_1(t)$. Then we denote with $\mathcal{M}_{1,h}$ a finite element approximation of (5.14) discontinuous on the immersed surfaces, to let the pressure jump (we refer to [FGM08] for a

detailed analysis on discontinuous pressure space). Let $W_{2,h} \times Q_{2,h}$ be an inf-sup stable and conforming finite element approximation of $[H^1(\Omega_2)]^d \times L^2(\Omega_2)$.

Then let be $\mathcal{V}_{1,h} = \mathcal{X}_{1,h} \cap \mathcal{X}_\Gamma$, with $\Gamma = \partial\Omega_1(t) \backslash \Sigma_{\text{FFI}}$, where $\mathcal{X}_\Gamma(\Omega_1(t))$ is the space of the $\mathcal{X}-$functions vanishing on a part Γ of $\partial\Omega_1(t)$. We define also the space $V_{2,h} = W_{2,h} \cap [H^1_{\Gamma_2}(\Omega_2)]^d$, where $H^1_\gamma(\Omega_2)$ is the space of $H^1(\Omega_2)-$functions vanishing on a part γ of $\partial\Omega_2$.

As regards the time discretization, a backward Euler scheme is used and the non-linear terms are linearized with a standard semi-implicit approach. Let $\delta t \stackrel{\text{def}}{=} T/N$ denote the time step size, the interval of interest is $(0, T)$, $N \in \mathbb{N}^+$ is a given integer and $x^n \approx x(n\delta t)$ with $0 \leq n \leq N$. The resulting fully discretized explicit scheme is presented in Algorithm 6.1.

ALGORITHM 6.1 (Explicit staggered scheme with RIS model and ALE formulation)

1. *Find* $(\mathbf{u}^n_{1,h},\, p^n_{1,h}) \in \mathcal{X}_{1,h} \times \mathcal{M}_{1,h}$ *satisfying the essential boundary conditions and such that*

$$\begin{aligned} &A_{1,\widehat{\mathcal{A}},\delta t}[\mathbf{u}^{n-1}_{1,h}; (\mathbf{u}^n_{1,h}, p^n_{1,h}), (\mathbf{v}_{1,h}, q_{1,h})] + B_{1,\delta t}[\mathbf{u}^{n+1}_1, \mathbf{v}_{1,h}] \\ &+C_1[\mathbf{u}^{n-1}_{1,h}; (\mathbf{u}^n_{1,h}, \mathbf{u}^{n-1}_{2,h}), \mathbf{v}_{1,h}] + \frac{\gamma\mu}{h}\int_\Sigma (\mathbf{u}^n_{1,h} - \mathbf{u}^{n-1}_{2,h}) \cdot \mathbf{v}_{1,h} \\ &+ \int_\Sigma \boldsymbol{\sigma}(\mathbf{u}^{n-1}_{2,h}, p^{n-1}_{2,h}) \cdot \mathbf{n}_2 \mathbf{v}_{1,h} + \sum_{i,j} R^n_{i,j} \int_{\mathcal{S}_{i,j}} (\mathbf{u}^n_{1,h} - \mathbf{w}^n_{1,h}) \cdot \mathbf{v}_{1,h} = 0, \end{aligned} \tag{6.4}$$

   for all $(\mathbf{v}_{1,h},\, q_{1,h}) \in \mathcal{V}_{1,h} \times \mathcal{M}_{1,h}$. *With the resistances*

$$R^n_{c,j} = R_{\text{off},j}(1-\delta^n_{c,j}) + R_{\text{on},j}\delta^n_{c,j} \quad \textit{and} \quad R^n_{o,j} = R_{\text{on},j}(1-\delta^n_{c,j}) + R_{\text{off},j}\delta^n_{c,j}, \quad \textit{for} \;\; j = m, a;$$

2. *Find* $(\mathbf{u}^n_{2,h},\, p^n_{2,h}) \in W_{2,h} \times Q_{2,h}$ *satisfying the essential boundary conditions and such that*

$$\begin{aligned} &A_{2,\delta t}[\mathbf{u}^{n-1}_{2,h}; (\mathbf{u}^n_{2,h}, p^n_{2,h}), (\mathbf{v}_{2,h}, q_{2,h})] + S(p^n_{2,h}, q_{2,h}) \\ &+C_2[(\mathbf{u}^{n-1}_{2,h}, \mathbf{u}^{n-1}_{1,h}); (\mathbf{u}^n_{2,h}, \mathbf{u}^n_{1,h}), \mathbf{v}_{2,h}] + \frac{\gamma\mu}{h}\int_\Sigma (\mathbf{u}^n_{2,h} - \mathbf{u}^n_{1,h}) \cdot \mathbf{v}_{2,h} \\ &- \int_\Sigma \boldsymbol{\sigma}(\mathbf{u}^{n-1}_{2,h}, p^{n-1}_{2,h}) \cdot \mathbf{n}_2 \mathbf{v}_{2,h} - \int_\Sigma (\mathbf{u}^n_{2,h} - \mathbf{u}^n_{1,h}) \cdot \mathbf{n}_2 q_{2,h} = 0 \end{aligned} \tag{6.5}$$

   for all $(\mathbf{v}_{2,h},\, p_{2,h}) \in V_{2,h} \times Q_{2,h}$.

3. *Go to next time-step.*

In the sub-problem 1, the form $A_{1,\widehat{\mathcal{A}},\delta t}[\mathbf{u}_{1,h}^{n-1};(\mathbf{u}_{1,h}^{n},p_{1,h}^{n}),(\mathbf{v}_{1,h},q_{1,h})]$ is defined as

$$\begin{aligned}A_{1,\widehat{\mathcal{A}},\delta t}[\mathbf{u}_{1,h}^{n-1};(\mathbf{u}_{1,h}^{n},p_{1,h}^{n}),(\mathbf{v}_{1,h},q_{1,h})] \overset{\text{def}}{=} & \frac{\rho}{\delta t}\left(\int_{\Omega^n}\mathbf{u}_{1,h}^{n}\cdot\mathbf{v}_{1,h}-\int_{\Omega^{n-1}}\mathbf{u}_{1,h}^{n-1}\cdot\mathbf{v}_{1,h}\right)\\ &+\rho\int_{\Omega^n}(\mathbf{u}_{1,h}^{n-1}-\mathbf{w}_{1,h}^{n})\cdot\nabla\mathbf{u}_{1,h}^{n}\cdot\mathbf{v}_{1,h}\\ &-\rho\int_{\Omega^n}(\mathbf{u}_{1,h}^{n}\cdot\mathbf{v}_{1,h})\nabla\cdot\mathbf{w}_{1,h}^{n}+2\mu\int_{\Omega^n}\boldsymbol{\epsilon}(\mathbf{u}_{1,h}^{n}):\boldsymbol{\epsilon}(\mathbf{v}_{1,h})\\ &-\int_{\Omega^n}p_{1,h}^{n}\nabla\cdot\mathbf{v}_{1,h}+\int_{\Omega^n}q_{1,h}\nabla\cdot\mathbf{u}_{1,h}^{n}.\end{aligned}$$

With respect to the form (5.20) of Chapter 5, the last integral, the Temam's trick, is now included in $C_1[\mathbf{u}_{1,h}^{n-1};(\mathbf{u}_{1,h}^{n},\mathbf{u}_{2,h}^{n-1}),\mathbf{v}_{1,h}]$ which has the expression (2.13). The term $B_{1,\delta t}[\mathbf{u}_{1,h}^{n},\mathbf{v}_{1,h}]$ is the weakly consistent term (5.26), introduced in Chapter 5 to get the energy equality in a moving domain. As regards the second fluid problem, the form $A_{2,\delta t}[\mathbf{u}_{2,h}^{n-1};(\mathbf{u}_{2,h}^{n},p_{2,h}^{n}),(\mathbf{v}_{2,h},q_{2,h})]$ has the same expression as in (2.23), and the term $C_2[(\mathbf{u}_{2,h}^{n-1},\mathbf{u}_{1,h}^{n-1});(\mathbf{u}_{2,h}^{n},\mathbf{u}_{1,h}^{n}),\mathbf{v}_{2,h}]$ is defined in (2.14). The pressure stabilization term $S(p_{2,h}^{n},q_{2,h})$ has the form (2.30).

6.3 Numerical simulations

In this section, first we discuss some aspects of the computational mesh and of the imposed displacement. Then we present the heart-valves-aorta numerical simulations when the contraction of the left ventricle is induced by imposed realistic displacements.

6.3.1 Towards a finite element mesh of a complete heart geometry

The numerical simulations presented in this chapter and in Section 4.3.3 of Chapter 4 have been performed employing finite element meshes, which are part of a complete heart geometry. The original geometry of the heart has been acquired by Zygote Media Group [Zyg11]. This geometry has been obtained from the post-processing of highly resolved CT (Computer Tomography) data. A joint work of accurate re-modeling and re-meshing have been performed by students of M∃DESIM and REO teams at Inria making use of the software 3-Matic [Mat13] and Gmsh [GR09].

The heart mesh has the same dimension as for an adult healthy man. It has a realistic spatial orientation and location in order to be matched with other physiological structures, as lungs, bones or a thorax mesh.

The volumetric mesh of the two ventricles has been combined with the surface mesh of the two atria. The volumes are constituted by tetrahedra and the surfaces by triangles. The ventricles mesh has been used to perform biomechanical simulations of the heart and the atria meshes are employed to obtain realistic electrocardiograms. The complete heart mesh has allowed to take in consideration the field of the cardiac fibers on the entire geometry and simulate the complete electrical activity of the heart.

We aim to drive the analysis towards the coupling of the blood dynamics with the others model performed with this geometry. In this perspective we have included the aorta and the heart valves. The aorta present also a volumetric thick structure while the valves are just thin surfaces. They were re-modeled and re-meshed in order to be adapted with the rest of the geometry. A final geometry including ventricles, atria, valves and aorta is obtained and illustrated in Figure 6.2. From this geometry we extract the computational mesh used for our simulations. It is present in Section 6.3.3 and illustrated in Figure 6.4.

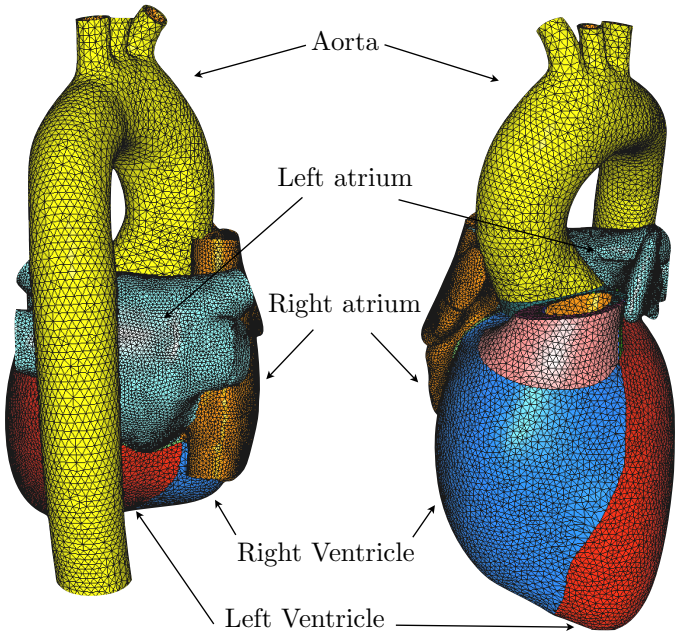

Figure 6.2: *Complete heart mesh: back view (left) and front view (right).*

6.3.2 The electro-mechanical model of the heart

The imposed displacements employed in this chapter are the result of biomechanical simulations in both the ventricular cavities of the heart geometry illustrated above. The simulations have been performed by the Inria team M∃DISIM. The reader can find an exhaustive and detailed exposition of the model and the obtained numerical results in [SMCCS08] and [Imp13, Chapter 1], here we sketch its guideline.

In the above mentioned works, the kinematic of the heart is described in a total Lagrangian formalism by the equation of the elastodynamics

$$\hat{\rho}_s \partial^2_{tt} \hat{\mathbf{d}}_s - \nabla_{\hat{\mathbf{x}}} \cdot (\widehat{\boldsymbol{F}}_s \widehat{\boldsymbol{\Sigma}}) = \mathbf{0}, \quad \text{in} \quad \widehat{\Omega}_s, \tag{6.6}$$

where $\hat{\mathbf{d}}_s$ and $\hat{\rho}_s$ are the displacement and the density of the solid. The term $\widehat{\boldsymbol{F}}_s = \nabla_{\hat{\mathbf{x}}} \hat{\boldsymbol{\varphi}}_{s,t}$ is the deformation gradient of the solid and the symmetric tensor $\widehat{\boldsymbol{\Sigma}}$ is called second Piola-Kirkoff tensor. This is related to the displacement through an appropriate constitutive law (see, e.g. [Tal94]) that take into account the nature of the material of the cardiac muscle.

The second Piola-Kirckoff tensor is additively decomposed in two parts (see also on this topics in [GK10, NP04]), i.e. $\widehat{\boldsymbol{\Sigma}} = \widehat{\boldsymbol{\Sigma}}_{pas} + \widehat{\boldsymbol{\Sigma}}_{act}$, with $\widehat{\boldsymbol{\Sigma}}_{act}$ active and $\widehat{\boldsymbol{\Sigma}}_{pas}$ passive stress-strain. The first tensor is the purely mechanical part and is derived from an elastic potential. This one has been chosen of exponential type and exhibits a transverse isotropic character, i.e. the mechanical properties are the same along a plane.

The second tensor defined as $\widehat{\boldsymbol{\Sigma}}_{act} = \sigma_{1D}(u)\boldsymbol{f} \otimes \boldsymbol{f}$, is the strain drawn by the interplay between the electrical excitation u and contraction forces. It indicates the active tissue response along the direction $\boldsymbol{f}$ of the fibers composing the cardiac muscle. This active part of the strain tensor is considered to be purely anisotropic, since its property depends on the fibers direction. In this model the electrical excitation is considered as an external stimulus.

In each cavity, left and right ventricle, a two R-C block Windkessel model takes into account for the neglected part of the cardiovascular system. The first block corresponds to the arterial pressure while the second block to the distal pressure. The opening/closure of the valve is dictated by an Ohm's law-like that relates the blood flow and the pressure in the ventricle, atrium, and arteries by mean of constant resistance coefficients. A mid-point scheme is adopted for the time discretization of the tensors and other internal variables, thus ensuring a correct energy balance of the complete discretized system (see [CTMS12, Gon00]).

The simulations are performed for both right and left ventricle, but in Figure 6.3 we illustrate just the contraction of the left ventricle, which is that one used in our fluid simulations. The physiological parameters follow the standard known values of an healthy heart. The magnitude of the displacement and the ventricular volume over a cardiac cycle are depicted as well. In this simulation an entire cardiac cycle fires for $0.8\ s$. Before the actual employment of the displacements a linear interpolation in time has been performed in order to adapt the results of the mechanical simulations into the fluid solver.

REMARK 6.2
We note that according to the electro-mechanical simulations, Figures 6.3b and 6.3c, the cardiac cycle starts during the passive filling of the left ventricle, after the atria contraction.

6.3.3 Computational domain for fluid modeling and boundary conditions

Domain and displacement The computational domain for the fluid model is split in two non-overlapping sub-domains as illustrated in Figure 6.4. With respect to the simulations of the previous chapter, the ventricle domain has replaced the aortic root domain. The aortic arch domain is unchanged.

Fissured surfaces are introduced in the domain $\Omega_1(t)$ to catch the pressure jump across the valves during closed status. Whereas the degrees of freedom of the velocity are matched together to have continuity across the fissure, further details are given in Section 4.3.1, page 99. The mitral valve has been considered in its open and closed configurations (Figure 6.5a) while the aortic valve only in the open configuration (Figure 6.5b).

The ventricular wall mesh is the interface $\Sigma_{\text{ALE}}(t)$ between the fluid and the solid. In the green parts of the domain, corresponding to the left atrium and the aortic root, the fluid displacement $\hat{\mathbf{d}}_f$ is implicitly given in the mesh update step of the ALE problem by solving

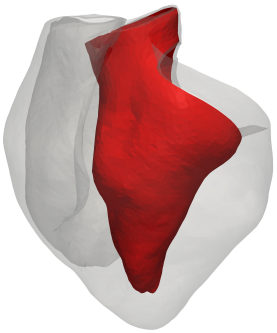

(a) *Deformation of the left ventricle at t*= $0.283\ s$. *Left side view.*

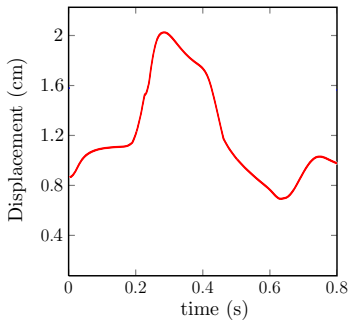

(b) *Mean displacement on the left cavity wall.*

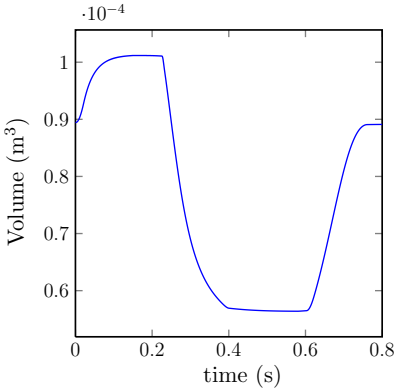

(c) *Volume of the left cavity.*

Figure 6.3: *The electro-mechanical model of the heart. Courtesy of M∃DISIM team. Simulations results from* [Imp13].

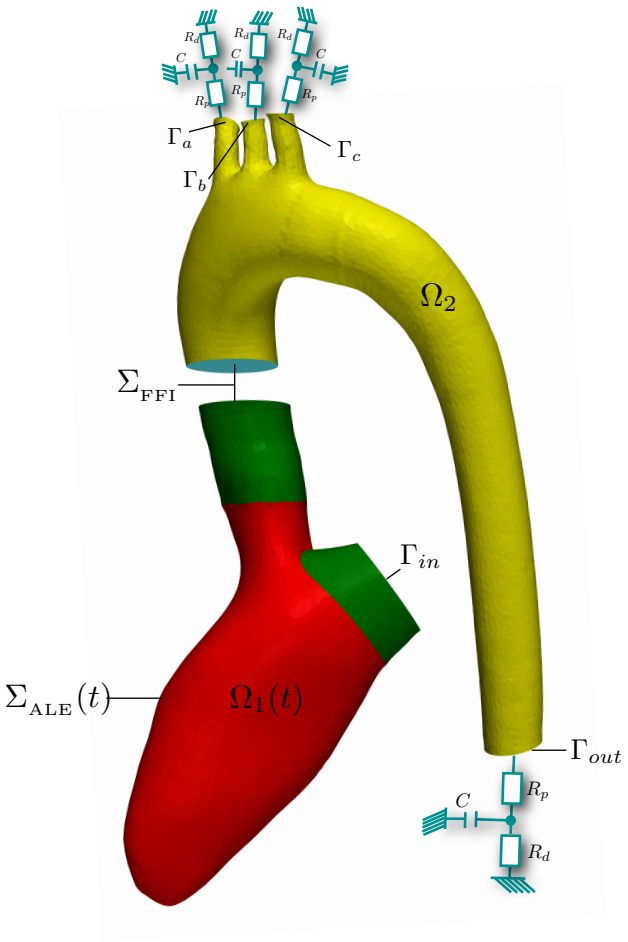

Figure 6.4: *Computational fluid domain.*

the harmonic extension problem

$$\begin{cases} -\boldsymbol{\Delta}\hat{\mathbf{d}}_f &= \mathbf{0}, & \text{in} \quad \widehat{\Omega}_1, \\ \hat{\mathbf{d}}_f &= \mathbf{0}, & \text{on} \quad \widehat{\Sigma}_{\text{FFI}} \cup \widehat{\Gamma}_{in}, \\ \hat{\mathbf{d}}_f &= \alpha\hat{\mathbf{d}}_s, & \text{on} \quad \widehat{\Sigma}_{\text{ALE}}, \end{cases} \tag{6.7}$$

where $\hat{\mathbf{d}}_f(0) = \hat{\mathbf{d}}_{f,0}$. The term $\hat{\mathbf{d}}_s$ is the displacement coming from the mechanical simulation described in Paragraph 6.3.2 and imposed on the ALE interface, the red part on Figure 6.4.

As preliminary test to set up all the tools presented in the thesis, the displacement applied on the ventricle wall, $\hat{\mathbf{d}}_s$ has been scaled with a coefficient $\alpha = 0.2$. This let to avoid too strong distortions of the mesh. The extension problem (6.7) defines the displacement filed in the fluid domain, compatible with the solid displacement at the fluid-solid interface $\Sigma_{\text{ALE}}(t)$. The (6.7) is arbitrary, others laws could be considered as well. Note that the extension problem is computed in the non-deformed configuration with a Lagrangian formalism. It's worth noticing that the unphysical choice of the scaling parameters α, is related to choice

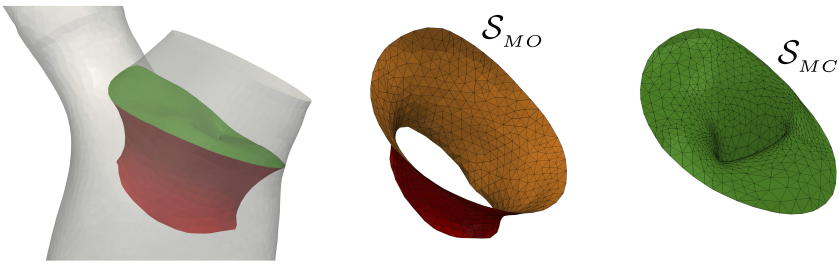

(a) *Mitral valve: position in the left ventricle (right), open surface (middle) and closed surface.*

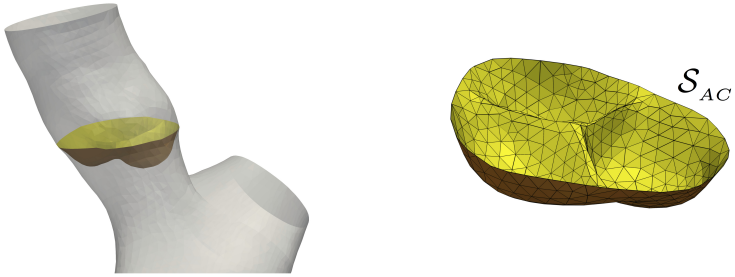

(b) *Aortic valve: position in the left ventricle (right) and closed surface (left).*

Figure 6.5: *Heart valves meshes.*

of the harmonic extension which is known to give very distorted mesh for large boundary displacement. We choose to fix the inlet Γ_{in} and we impose zero displacement in the fluid-fluid interface as well, since the Σ_{FFI} is coupled with the Ω_2 which is a fixed domain. Notice that as observed in the Remark 6.1, the extension problems is applied to all domain $\widehat{\Omega}_1$ even included in the immersed resistive surfaces.

The coupling between the two domains is achieved via master/slave approach that handles the communications between the two fluid solver. At each time step, the velocity and the stress tensor is exchanged between the two fluid domains. We have introduced this approach in Section 3.3.2, of the Chapter 3.

The fluid-solid interface $\Sigma_{\text{ALE}}(t)$ is made by $3\,019$ nodes and The fluid-fluid interface Σ_{FFI} has 264 nodes. The domain $\Omega_1(t)$ is made of $137\,186$ tetrahedral elements while Ω_2 has $125\,068$ tetraedra.

Valves resistances and physical parameters In Chapter 4 the opening and closure of the aortic valve was determined according activation/deactivation parameters with constant value, i.e. $R_{\text{on}} = 1 \times 10^6$ and $R_{\text{off}} = 0$. In this chapter the resistances vary according to the following expressions. For the mitral valve we set

$$\begin{cases} R_{\text{on},m} = 1e04 + 1e06 \cdot \exp(-\exp(-\alpha_m \cdot (t - T_{c,m}))), & \delta_{c,m} = 1 \text{ (closed)}, \\ R_{\text{off},m} = 0 & \delta_{c,m} = 0 \text{ (open)}. \end{cases} \tag{6.8}$$

and t is the time after the closing condition is started, i.e. when the flow though the mitral valve is negative. In the same way for the aortic valves we let the resistances changing as

$$\begin{cases} R_{\text{on},a} &= 1e05 + 1e06 \cdot \exp(-\exp(-\alpha_a \cdot (t - T_{c,a}))), & \delta_{c,a} = 1 \text{ (closed)} \\ R_{\text{off},a} &= 0, & \delta_{c,a} = 0 \text{ (open)}. \end{cases} \tag{6.9}$$

and t is the time after the closing condition is started, i.e. when the flow though the aortic valve is negative. The logical variables $\delta_{c,m}$ and $\delta_{c,a}$ assume value 1 when a negative flow acts on the immersed surface and value 0 when the valve is subjected to a positive pressure difference (see (4.7) on pag. 97). The two time-constant $T_{c,m} = 0.24$ and $T_{c,a} = 0.58$ and the two values $\alpha_m = 40$ and $\alpha_a = 50$, determining the slope of the R_{on}-curves, have been fixed according the contraction of the ventricle. Their course over one cardiac cycle is displayed in Figure 6.6. This means that the valves close gradually owing an increasing of the resistance when the closed configuration is in order. This is in contrast with the simulations of Chapter 4 where a sudden closing has characterized the aortic valve. Note that we consider a constant value for R_{off}. We can also express this parameter with a time-depending decreasing function to simulate a slower opening of the valve.

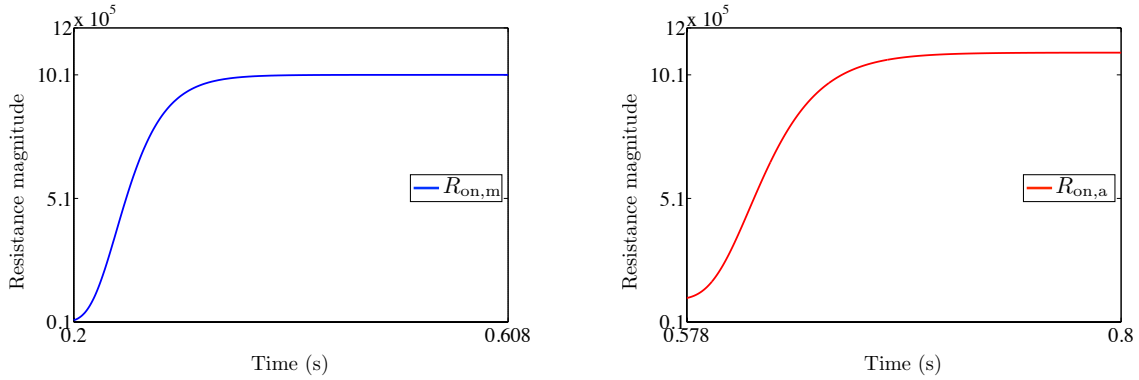

(a) *Mitral valve.* (b) *Aortic valve.*

Figure 6.6: *Course of the resistance activation parameters for closed valves status in the ventricle-aorta test case.*

The standard parameters of newtonian blood flow have been employed for the simulations which follow. The flow density is $\rho = 1.06\ g/cm^3$ and the dynamic viscosity is $\mu = 0.04\ poise$. On the surface Γ_{in} representing a cut inside the left atrium, we impose a constant pressure of $P_{in} = 15\,000\ dyn/cm^2$ that is approximately $11.25\ mmHg$. On the three top arteries and in the descending aorta, the effects generated by the neglecting portion of the cardiovascular system are modeled by the 0D-Windkessel model [VC06, WLW09]

$$CR_d \frac{\mathrm{d}P_p}{\mathrm{d}t} + P_p = Q(R_d + R_p) + CR_pR_d \frac{\mathrm{d}Q}{\mathrm{d}t}.$$

In Table 6.1 we report the parameters defining the above ODE and employed for the simulations of this chapter. Their dimensions are in cgs.

	Γ_a	Γ_b	Γ_c	Γ_{out}
R_p $(dyn \cdot s \cdot cm^{-5})$	0.005×10^4	0.19×10^4	0.07×10^4	0.01×10^4
R_d $(dyn \cdot s \cdot cm^{-5})$	0.9×10^4	3.30×10^4	1.30×10^4	0.1×10^4
C $(cm^5 \cdot dyn^{-1})$	0.95×10^{-4}	0.25×10^{-4}	0.64×10^{-4}	9.00×10^{-4}

Table 6.1: *Windkessel parameters used for aorta with imposed realistic displacement on the ventricle wall.*

We add the outflow stabilization term (4.10), on page 105, on all the outlets of the domain Ω_2 and on Γ_{in} as well. This term has been introduced in [BGH+09, MBH+11] to avoid possible instability in the simulations caused by physiological back-flow phenomena. The time step is $0.001\ s$, and 2 cardiac cycles were run.

6.3.4 Cardiac blood simulations with imposed displacements

Figures 6.7-6.11 illustrate the velocity streamlines and the elevated surface of the pressure distribution in the longitudinal mid plane of the left ventricle and part of the aortic arch. These results represent 8 time instants of the second cardiac cycle. In the first cardiac cycle the solution is perturbed by the initial condition and is left out.

Figure 6.7 is a snapshot during the filling, when the mitral valve is open while the aortic valve is closed. The pressure jumps appears between the left ventricle pressure and aortic root.

Figures 6.8 represent two consecutive instants of time during the isovolumic contraction. The mitral valve closes due to backflow and a pressure jumps appear on the immersed surfaces between the left atrium and left ventricle as well.

As the pressure in the ventricle keeps growing, the aortic valves opens due to a positive pressure difference, letting the blood flowing in the aorta. This is the case of the two time instants during the ejection, illustrate in Figure 6.9.

In Figure 6.10 two snapshots during the isovolumic relaxation are shown. The left ventricle is relaxing making the pressure to decrease. Due to the back-flow, the aortic valves closes.

As the pressure in the ventricle keeps decreasing, the mitral valve opens due to a positive pressure difference, letting a new filling phase re-start. This is the snpashot reported in Figure 6.11. Notice the good agreement of the solution along the fluid-fluid interface.

In the end, in Figure 6.12a the flow in the aorta is displayed. While Figure 6.12b illustrates the aortic pressure and the pressure in the left atrium and in the left ventricle. We can remark the weak flow power due to the scaled displacement imposed in the ventricular wall. Moreover the two isovolumic phases are smaller than the physiological one.

6.4 Final remarks

This chapter deals with the numerical simulations of the blood dynamics in the left ventricle, where RIS models have been integrated for both aortic and mitral valves. This has

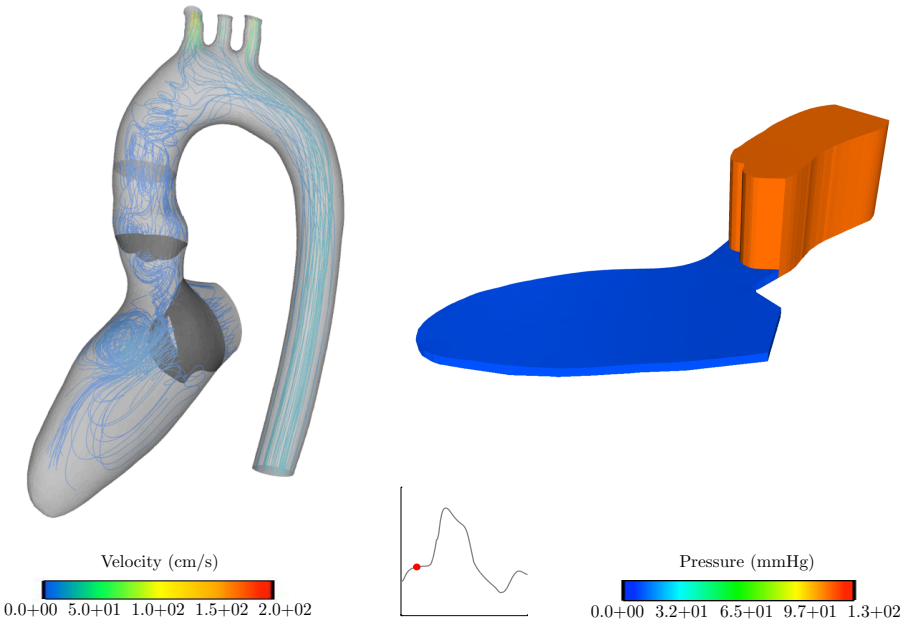

(a) $t = 900\ s$.

Figure 6.7: *Velocity streamlines and pressure distribution (Filling).*

been coupled via a staggered explicit scheme with the blood dynamics in the aorta, here Windkessel models account for the neglected part of the cardiovascular system. From a mathematical standpoint, an explicit fluid-fluid staggered scheme is considered and the stability of ALE formulation in Fluid problems 1 is reached adding a suitable weakly consistent term (see Chapter 5)

To induce the contraction of the ventricular wall, we impose a scaled displacement coming from an electro-mechanical simulation carried out in the same ventricular geometry. The displacements are not calculated simultaneously with the fluid problem but they have been *a priori* computed in a part of the geometry and for the rest an harmonic extension has been employed. Hence, some issues arise:

1. The displacements have been scaled to avoid tetrahedra with negative measure.
2. Non-physiological fluid flow is generated in the left ventricle.
3. The Windkessel parameters has been sensitively increased to obtain satisfactory pressures.

With the results presented in this chapter, some interesting considerations can be pointed out:

1. The RIS method is a strong and robust method for heart valves. The resistance magnitude can be easily handled to adapt the valve model to the particular problem.

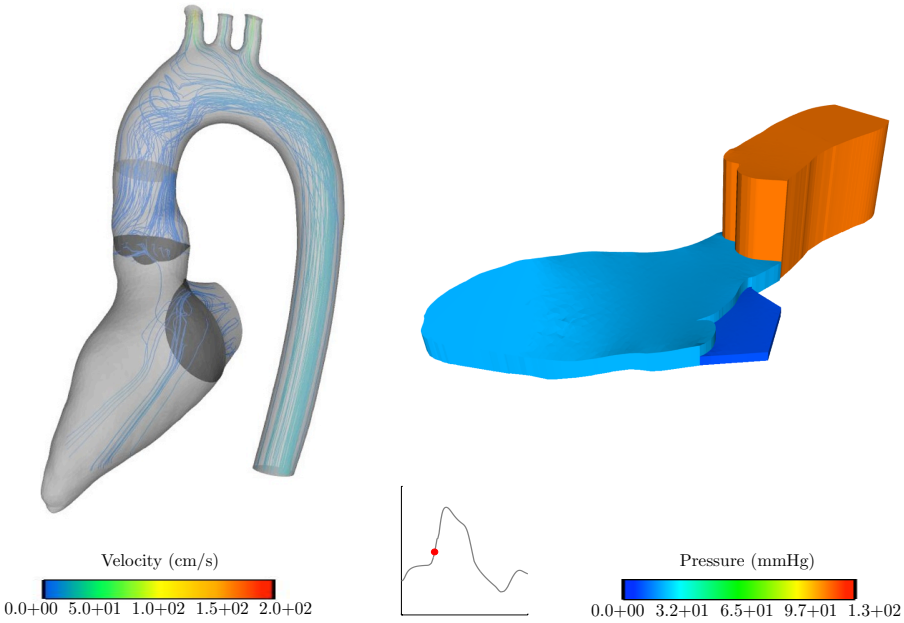

(a) $t = 1010\ s$.

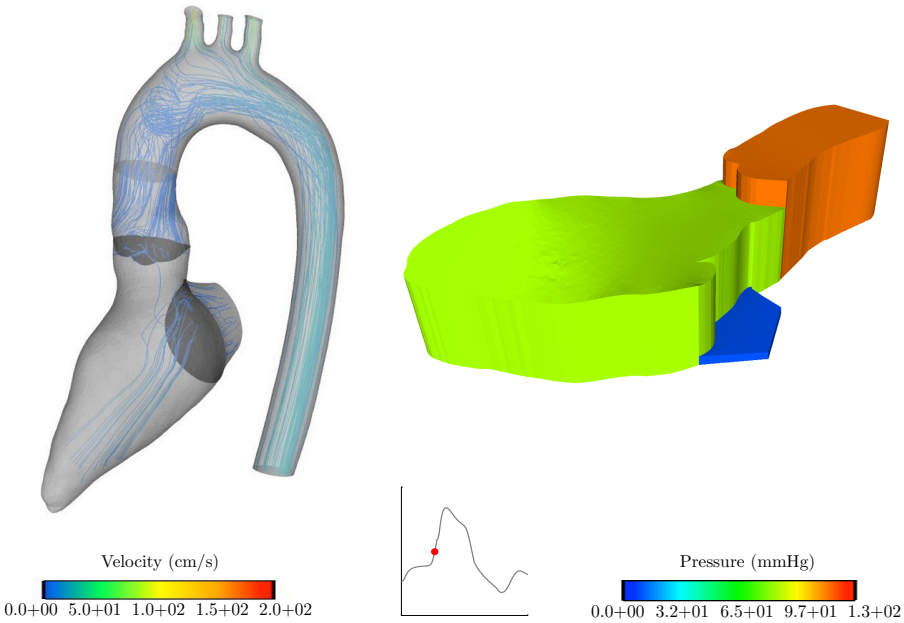

(b) $t = 1011\ s$.

Figure 6.8: *Velocity streamlines and pressure distribution (Isovolumic contraction).*

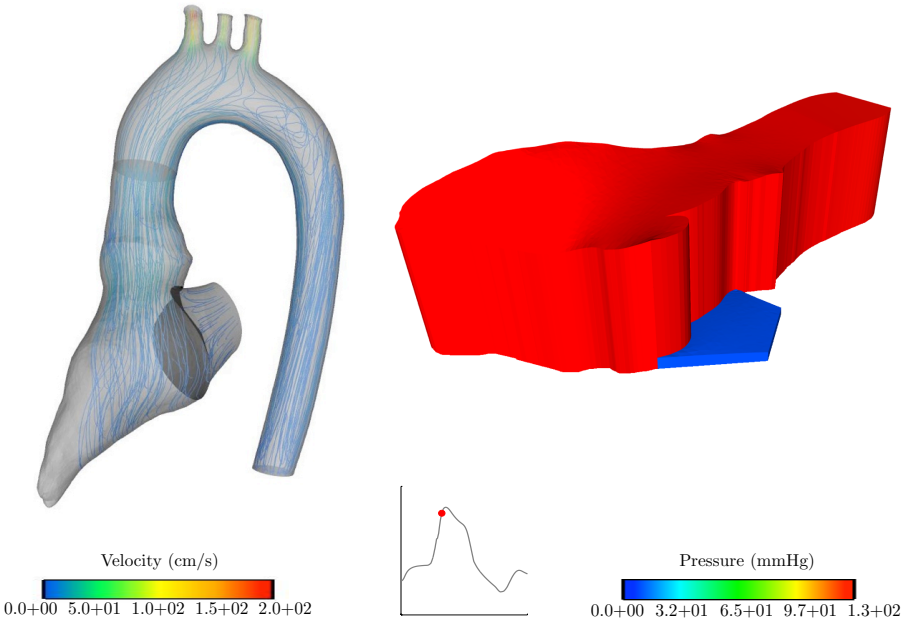

(a) $t = 1058\ s.$

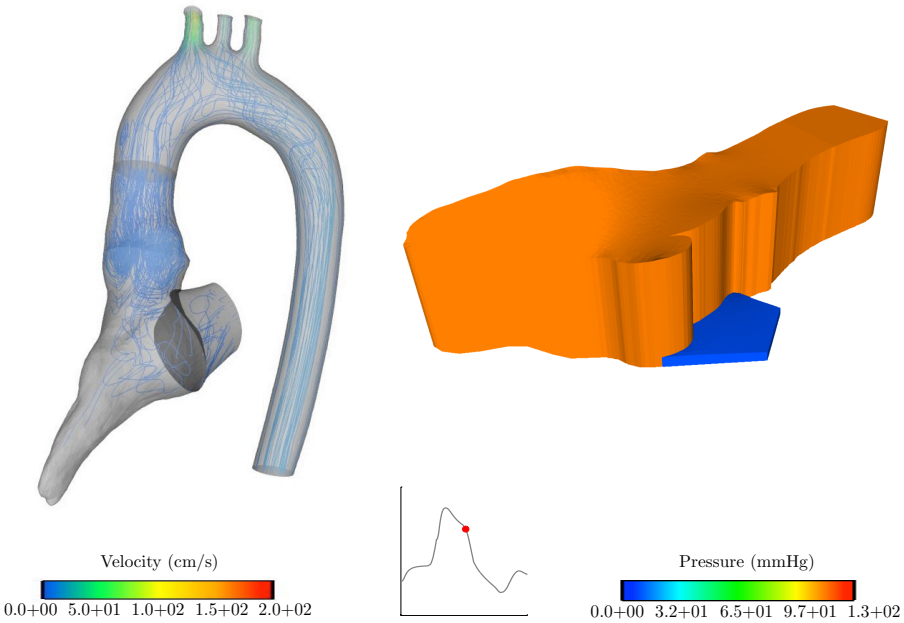

(b) $t = 1210\ s.$

Figure 6.9: *Velocity streamlines and pressure distribution (Ejection).*

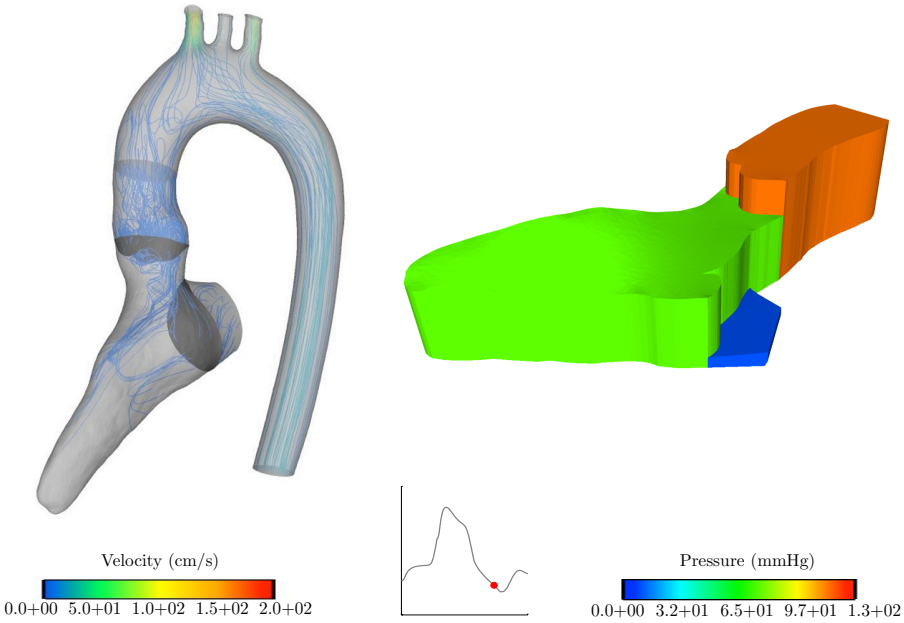

(a) $t = 1386\ s$.

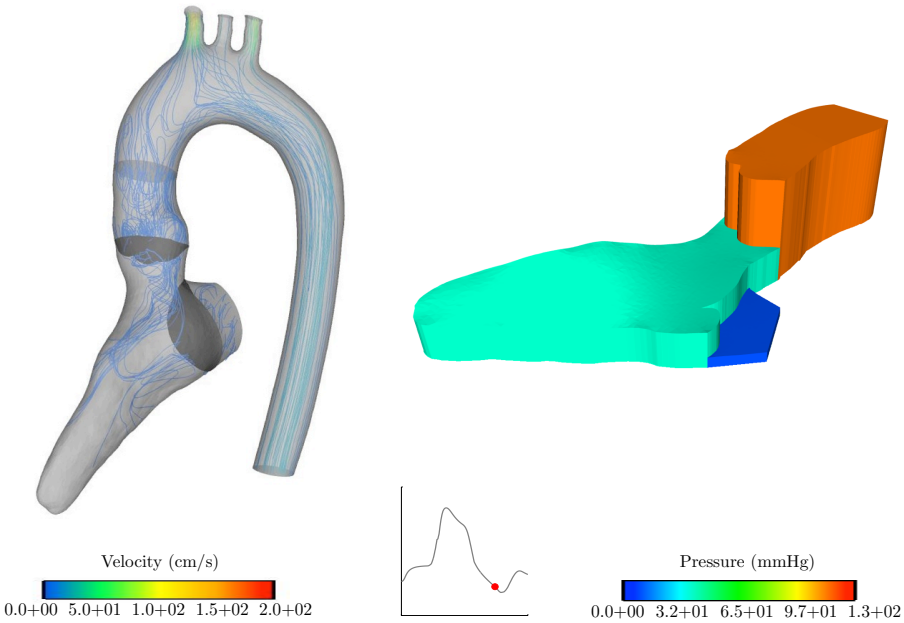

(b) $t = 1392\ s$.

Figure 6.10: *Velocity streamlines and pressure distribution (Isovolumic relaxation).*

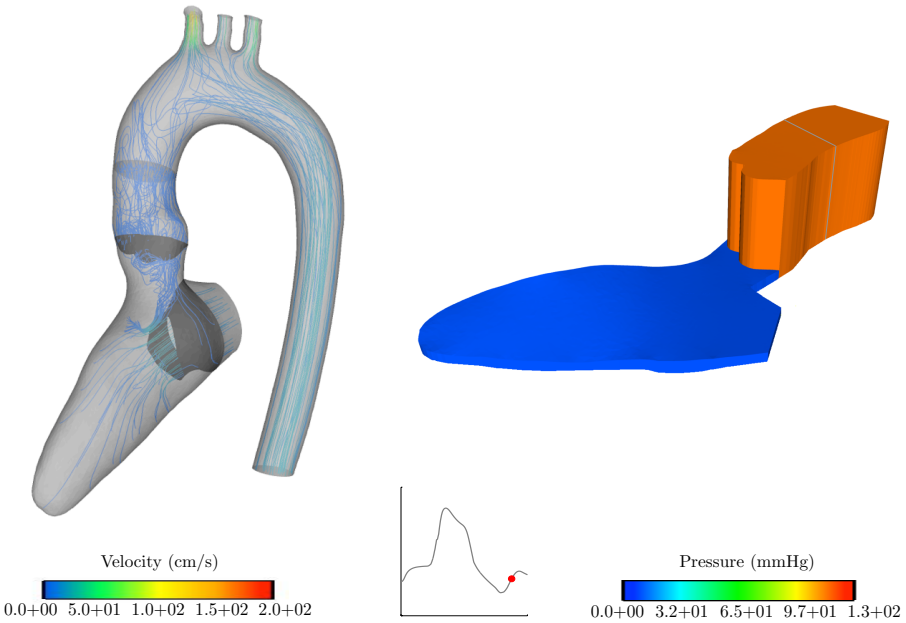

(a) $t = 1500\ s$ *(Filling).*

Figure 6.11: *Velocity streamlines and pressure distribution (Filling).*

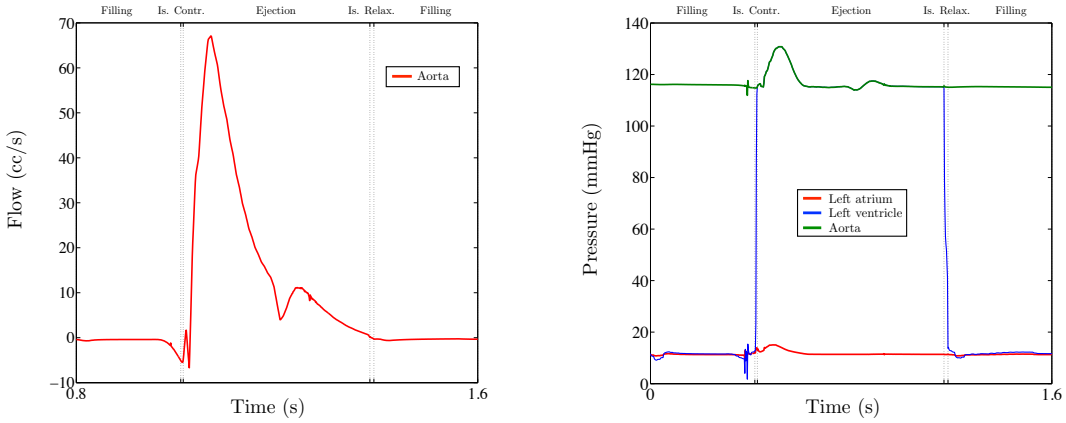

(a) *Flow.* (b) *Pressures.*

Figure 6.12: *Course of the aortic flow and atrial, ventricular and aortic pressures obtained imposing an external displacement on ventricular wall.*

2. Two different RIS valve models can be easily managed.

3. The fluid-fluid coupled problem has shown a certain reliability in coupling more complex fluid problem.

We plan to use the RIS model for the numerical simulations of cardiac fluid-structure interaction problems where a precise description of the leaflet bio-mechanics is not required and the fluid-fluid coupled problems is a good tool to take into account the blood dynamics in the aorta. A fluid-structure interaction problem can be consider to model the blood dynamics in the aorta, as well.

Although this topic is still controversial, it is likely the turbulence model has to be considered in the ventricle (see e.g. [CMN14]).

The final goal of heart modeling is to simulate the total heart function by integrating cardiac anatomy, electrical activation, mechanics, metabolism and fluid mechanics together, from a mathematical standpoint as well as in the computational framework. This will be the natural continuation of this work.

Bibliography of Chapter 6

[BGH+09] Y. Bazilevs, J.R. Gohean, T.J.R. Hughes, R.D. Moser, and Y. Zhang. Patient-specific isogeometric fluid-structure interaction analysis of thoracic aortic blood flow due to implantation of the Jarvik 2000 left ventricular assist device. *Comput. Methods Appl. Mech. Engng.*, 198:3534–3550, 2009.

[CMN14] C. Chnafa, S. Mendez, and F. Nicoud. Image-based large-eddy simulation in a realistic left heart. *Computers & Fluids*, 94(0):173 – 187, 2014.

[COS05] Y. Cheng, H. Oertel, and T. Schenkel. Fluid-structure coupled CFD simulation of the left ventricular flow during filling phase. *Annals of Biomedical Engineering*, 33(5):567–576, 2005.

[CTMS12] D. Chapelle, P. Le Tallec, P. Moireau, and M. Sorine. An energy-preserving muscle tissue model: formulation and compatible discretizations. *Journal for Multiscale Computational Engineering*, 10(2):189–211, 2012.

[DPB05] F. Domenichini, G. Pedrizzetti, and B. Baccani. Three-dimensional filling flow into a model left ventricle. *J. Fluid Mech.*, 539:179–198, 2005.

[FGM08] M. Fernández, J.-F. Gerbeau, and V. Martin. Numerical simulation of blood flows through a porous interface. *Mathematical Modelling and Numerical Analysis*, 42:961–990, 2008.

[GHMP07] B.E. Griffith, R.D. Hornung, D.M. McQueen, and C.S. Peskin. An adaptive, formally second order accurate version of the immersed boundary method. *J. Comput. Phys.*, 223(1):10–49, 2007.

[GK10] S. Göktepe and E. Kuhl. Electromechanics of the heart: a unified approach to the strongly coupled excitation-contraction problem. *Computational Mechanics*, 45:227–243, 2010.

[Gon00] O. Gonzalez. Exact energy and momentum conserving algorithms for general models in nonlinear elasticity. *Comput. Methods Appl. Mech. Engrg.*, 190:1763–1783, 2000.

[GR09] C. Geuzaine and J.-F. Remacle. Gmsh: A 3-d finite element mesh generator with built-in pre- and post-processing facilities. *International Journal for Numerical Methods in Engineering*, 79(11):1309–1331, 2009.

[Imp13] A. Imperiale. *Méthodes d'assimilation de la donnée image pour la personnalisation de modéles mécaniques*. PhD thesis, Universitè Pierre et Marie Curie, Paris 6, 2013.

[KNZ11] S.S. Khalafvand, E.Y.K. Ng, and L. Zhong. CFD simulation of flow through heart: a perspective review. *Computer Methods in Biomechanics and Biomedical Engineering*, 14(1):113–132, 2011.

[Mat13] Materialise. *3-Matic version 8*. http://biomedical.materialise.com/3-matic, 2013.

[MBH+11] M. E. Moghadam, Y. Bazilevs, T.-Y. Hsia, I. E. Vignon-Clementel, and Al. L. Marsden. A comparison of outlet boundary treatments for prevention of backflow divergence with relevance to blood flow simulations. *Computational Mechanics*, 48(3):277–291, 2011.

[MP00] D. M. McQueen and C. S. Peskin. A three-dimensional computer model of the human heart for studying cardiac fluid dynamics. *SIGGRAPH Comput. Graph.*, 34(1):56–60, 2000.

[NNN+11] D.A. Nordsletten, S.A. Niederer, M.P. Nash, P.J. Hunter, and N.P. Smith. Coupling multi-physics models to cardiac mechanics. *Progress in Biophysics and Molecular Biology*, 104(1–3):77 – 88, 2011.

[NP04] M. P. Nash and A. V. Panfilov. Electromechanical model of excitable tissue to study reentrant cardiac arrhythmias. *Progress in Biophysics & Molecular Biology*, 85:501–522, 2004.

[NWY06] M. Nakamura, S. Wada, and T. Yamaguchi. Influence of the opening mode of the mitral valve orifice on intraventricular hemodynamics. *Annals of Biomedical Engineering*, 34(6):927–935, 2006.

[SMCCS08] J. Sainte-Marie, D. Chapelle, R. Cimrman, and M. Sorine. Modeling and estimation of the cardiac electromechanical activity. *Computers and Structures*, 84:1743–1759, 2008.

[SMR+09] T. Schenkel, M. Malve, M. Reik, M. Markl, B. Jung, and H. Oertel. MRI-based CFD analysis of flow in a human left ventricle: Methodology and application to a healthy heart. *Annals of Biomedical Engineering*, 37(3):503–515, 2009.

[Tal94] P. Le Tallec. Numerical methods for nonlinear three-dimensional elasticity. In *Handbook of numerical analysis*, volume III, pages 465–622. North-Holland, 1994.

[VC06] I. Vignon-Clementel. *A coupled multidomain method for computational modeling of blood flow*. PhD thesis, Stanford University, 2006.

[VCMP08] E. J. Vigmond, C. Clements, D. M. McQueen, and C. S. Peskin. Effect of bundle branch block on cardiac output: A whole heart simulation study. *Progress in Biophysics and Molecular Biology*, 97(2–3):520 – 542, 2008.

[WHS+02] H. Watanabe, T. Hisada, S. Sugiura, J. Okada, and H. Fukunari. Computer simulation of blood flow, left ventricular wall motion and their interrelationship by fluid-structure interaction finite element method. *JSME International Journal Series C*, 45(4):1003–1012, 2002.

[WLW09] N. Wetserhof, J.-W. Lankhaa, and B. E. Wetserhof. The arterial Windkessel. *Med. Biol. Eng. Comput.*, 47:131–141, 2009.

[WSKH04] H. Watanabe, S. Sugiura, H. Kafuku, and T. Hisada. Multiphysics simulation of left ventricular filling dynamics using fluid-structure interaction finite element method. *Biophys. J.*, 87(3):2074–2085, 2004.

[Zyg11] Zygote Media Group. *3D Human Anatomy for Animation, Illustration, CAD and Software Development*. http://www.zygote.com/, 2011. 3D Science project, http://www.3dscience.com/.

CONCLUSIONS

What, what was that you tried to say?
Everything in its right place.

"Everything In Its Right Place" by Radioahead.

CHAPTER 7
Obtained results and perspectives

The main findings and conclusions we have drawn from this work are given in this last chapter. Innovative tools developed in this thesis bring to new questions and further objective. A list of conclusions and perspectives by chapter is proposed.

Contents

7.1 General conclusion

Many cardiovascular diseases are due to disorders which affect the heart functioning. The mathematical problems that arise on this subject are numerous, this justifies a wide literature on this field. In this thesis we tried to contribute to this vast project whose ultimate aim is to produce simulations - with reasonable computing time and realistic results - that can help physicians to understand the functioning of the cardiovascular system.

We hope with this thesis to have offered innovative results and relevant reflections in order to shed light on the multiphysic problems arising in the cardiovascular system. This interdisciplinarity represents a difficulty for this subject and it requires knowledge in different areas.

This thesis has been the occasion to develop and use techniques or tools based on a variety of mathematical theories. Some objective, pointed out in the introduction and in the overall chapters of the thesis, have been achieved:

1. **Models coupling**: we have presented several fluid-fluid coupling strategies validated by a large number of numerical experiments.

2. **Solver coupling**: a master/slaves code - started with the beginning of this thesis - has been developed and used to perform all the simulations presented.

3. **Finite element solver**: with this thesis we have widely contributed to a collaborative code to solve different aspects of the cardiovascular system.

4. **Geometry**: several 2D/3D geometries have been managed and we have contributed to create a finite element mesh of a complete heart.

5. **Cardiovascular numerical simulations**: exhaustive numerical experiments have been performed to validate the numerical methods discussed and several numerical simulation have been performed giving satisfactory results.

The topics dealt in this work has been gathered in two parts. The first one introduces the fluid-fluid coupled problem and its numerical validation, the second one mainly deals with numerical examples on cardiac hemodynamics. In the following we summarize the main achieved results and the further perspective for each chapter.

7.2 Part I: Fluid-Fluid Interaction problem

7.2.1 Chapter 2 and Chapter 3

Conclusions This two chapters deal with several loosely coupled strategies for fluid-fluid interaction problems coupling the incompressible Navier-Stokes equations. Basically, this approach extends the loosely coupled schemes introduced in [BF09, BF13] for FSI problems, based on the Nitsche's interface method, to fluid-fluid interaction problems.

The methods rely on explicit Robin-Robin treatment of the interface coupling and on a suitable weakly consistent artificial compressibility on the interface. A specific formulation of the convective terms lead to different formulation: static pressure (standard and skew-symmetric) and total pressure formulations.

The energy stability has been proved for each formulation. Energy stability cannot a priori be guaranteed for the standard static pressure formulation (Algorithm 2.3 on page 45). It can be recovered with a static pressure skew-symmetric formulation (Algorithm 2.4 on page 50) and with the total pressure formulation (Algorithm 2.6 on page 52). Unfortunately, the skew-symmetric formulation is not consistent with the original coupled problem. For the total pressure formulation, an a priori energy estimate guaranteeing the stability of the splitting (Algorithm 2.6) has been derived. Exhaustive numerical examples have shown the accuracy of the proposed methods in an idealized aorta geometry.

The methods and the results presented in these chapters have generated the manuscript [FGS14] submitted for publication in *SIAM Journal on Scientific Computing* in 2013.

Perspectives Additional numerical examples could be performed: for example numerical simulations of a computational domain split in more than 3 sub-domains considering also Algorithm 2.4 and Algorithm 2.6.

The current developments are aimed at blood flow modeling, a major concern is with the extension to FSI problems. In such cases, there are additional boundary terms arising over

the FSI interface. In this case we can use Algorithm 2.3, which is based on static pressure and give very good results (even if we were not able to prove its stability). Otherwise, if the total pressure formulation (Algorithm 2.6) is used in a FSI context, the load should be explicitly computed via face-wise integration. In-deep analysis on this aspect can be pointed out.

Code coupling has been an important motivation of this chapter and of this work. In the simulations of Chapter 3 a computation saving of about 30% has been noticed when using a staggered scheme, compared to a monolithic solution over one cardiac cycle. Further analysis on this aspect should be in order.

7.3 Part II: Toward cardiac hemodynamics

7.3.1 Chapter 4

Conclusions A reduced model for heart valves, recently developed in [Ast10, AHSG12], has been discussed in this chapter. It consists of modeling the valves by the 3D shape of the open/closed configuration acting as resistance in the fluid. A new dissipative term is added in the Navier-Stokes equations. The mechanics of the valve is therefore neglected in favor of a simplified two-state representation, where the active configuration (open or closed) evolves in time according to the local fluid dynamics conditions. At the discrete level, a particular finite element formulation, originally proposed in [FGM08], is adopted to accurately capture the pressure jump across the valve and to avoid unphysical results. The discontinuity on the geometry is obtained introducing a fissure in the computational mesh.

In the framework of the cardiovascular compartments coupling, the RIS model is a prototype for left ventricle hemodynamics discussed in the Chapter 6. Various experimental tests have been performed to illustrate the efficiency and the flexibility of the RIS model in the framework of the coupled fluid-fluid problem. In particular, we have presented numerical simulation on an idealized aorta and on an aorta geometry derived from medical imaging.

Perspectives The valve resistances assume only two values, a great number (closed status) or zero (open status). As done in Chapter 6 (see (6.9) and (6.8) on page 149), it can be interesting carry out more numerical experiments with different values of the resistances. For instance, we can use a time-increasing function for R_{on} - which closes the valve - and time-decreasing function for R_{off} - which opens the valve.

Different values on the resistances can be also employed to simulate particular pathological cases. In fact, the RIS valve model seems to allow a certain flexibility in reproducing also pathological states of the valves. Pathologies such as stenosis or regurgitation can be easily included either in the mathematical model or directly in the computational geometry. In this chapter we use a great value of the resistance to simulate the stenotic leaflet, while keeping the same valve geometry with respect to the normal case. In this perspective, it can be interesting to present additional numerical examples in order to consider the pathology directly in the computational geometry, i.e. providing a valve mesh from a patient specific model.

7.3.2 Chapter 5

Conclusions The goal of this chapter was to obtain a provably stable algorithm for fluid flow in moving domain described with an ALE formalism. Without requesting any Geometric Conservation Law ([EGP09, FN99, TL79]), the stability is reached adding a weakly consistent term, (5.26) on page 131, to the original discretized formulation. The stabilization technique proposed is related to the particular time discretization adopted.

A numerical example with large displacements (Section 5.5) has been performed in which the ALE non-stabilized and stabilized scheme (Algorithm 5.1 vs. Algorithm 5.2) are compared. The consistent terms added for the stability did not affect significantly the results obtained with a standard scheme. The stability of the standard ALE formulation, is due in practice to the artificial dissipation introduced by the Euler scheme and the PSPG term (Figure 5.6a and 5.6b on page 135). In fact, by decreasing the effect of these dissipations (Figure 5.6c) , the new ALE formulation remains stable whereas the standard scheme could be unstable.

Perspectives As first example we proved the importance to add the ALE stabilization term (5.26). Further numerical examples remain to be performed.

7.3.3 Chapter 6

Conclusions This last chapter presents numerical simulations of the ventricle-valves-aorta blood dynamics. A staggered explicit scheme, presented in Chapter 2, has been employed to couple the fluid model in the ventricle with the fluid model in the aorta. The ALE stabilized formulation for moving domain, analyzed in Chapter 5, has been employed in Fluid problem 1. RIS models, discussed in Chapter 4 have been integrated to simulate the behavior of both aortic and mitral valves.

To induce the left ventricle contraction we use realistic displacement imposed on the ventricular wall, coming from a electro-mechanical simulation carried out in the same ventricular geometry. The displacements are not calculated simultaneously with the fluid problem but they have been *a priori* computed in a part of the geometry and for the rest an harmonic extension has been employed ((6.7) on page 148). Hence, a scale coefficient was needed to avoid to much distortion of the mesh elements.

Perspectives The use of an imposed displacement joint to the harmonic extension has shown its physiological limits in the numerical example illustrated. Analytical displacement or a realistic displacement applied on all the boundary of Fluid 1, can generate more realistic fluid flow in the aorta or in the ventricle. Further investigations on the parameters (e.g. valves resistances, Windkessel parameters) can be performed as well.

It is interesting to couple more than 2 fluids in the example of this chapter. In other words the fluid dynamics in the left ventricle can be coupled with the fluid dynamics in the aortic root - with RIS valve model - and this last one coupled with the aortic arch blood flow.

The FSI problem in such example is the next step. In term of mathematical model and software development, a next challenge can be to consider a FSI problem in the left ventricle

in which the heart valves are accounted via RIS methods. By mean of suitable fluid-fluid schemes, this can be coupled with an FSI problem in the aorta where Windkessel models account for the discarded part of the cardiovascular system. All numerical examples can be supported through an accurate mathematical analysis.

Bibliography of Chapter 7

[AHSG12] M. Astorino, J. Hamers, S. C. Shadden, and J.-F. Gerbeau. A robust and efficient valve model based on resistive immersed surfaces. *Int. J. Numer. Meth. Biomed. Engng.*, 28:937–959, 2012.

[Ast10] M. Astorino. *Interaction Fluide-Structure dans le Systéme Cardiovasculaire. Analyse Numèrique et Simulation*. PhD thesis, Universitè Pierre et Marie Curie, Paris 6, 2010.

[BF09] E. Burman and M. A. Fernández. Stabilization of explicit coupling in fluid-structure interaction involving fluid incompressibility. *Comput. Methods Appl. Mech. Engrg*, 198:766–784, 2009.

[BF13] E. Burman and M.A. Fernández. An unfitted Nitsche method for incompressible fluid-structure interaction using overlapping meshes. Research Report RR-8424, Inria, 2013. http://hal.inria.fr/hal-00918272.

[EGP09] S. Étienne, A. Garon, and D. Pelletier. Perspective on the geometric conservation law and finite element methods for ALE simulations of incompressible flow. *Journal of Computational Physics*, 228(7):2313 – 2333, 2009.

[FGM08] M. Fernández, J.-F. Gerbeau, and V. Martin. Numerical simulation of blood flows through a porous interface. *Mathematical Modelling and Numerical Analysis*, 42:961–990, 2008.

[FGS14] M. Fernández, J. Gerbeau, and S. Smaldone. Explicit coupling schemes for a fluid-fluid interaction problem arising in hemodynamics. *SIAM Journal on Scientific Computing*, 36(6):A2557–A2583, 2014.

[FN99] L. Formaggia and F. Nobile. A stability analysis for the arbitrary lagrangian eulerian formulation with finite elements. *East-West J. Numer. Math.*, 7(2):105–131, 1999.

[TL79] P.D. Thomas and C.K. Lombard. Geometric conservation law and its application to flow computations on moving grids. *AIAA J.*, 17:1030–1037, 1979.